To the Graduate Council:

I am submitting herewith a dissertation written by Hassan Bodaghi entitled "A Study and Comparison of Polymer Films Formed from Isotropic and Liquid Crystalline Solutions." I have examined the final copy of this dissertation for form and content and recommend that it be accepted in partial fulfillment of the requirements for the degree of Doctor of Philosophy, with a major in Polymer Engineering.

John F. Fellers

John F. Fellers,
Major Professor

We have read this dissertation
and recommend its acceptance:

J. E. Spruiell

Edward L. Clark

Larry C. Wadsworth

Accepted for the Council:

Burmikel

Vice Provost
and Dean of the Graduate School

A STUDY AND COMPARISON OF POLYMER FILMS FORMED FROM ISOTROPIC AND LIQUID CRYSTALLINE SOLUTIONS

A Dissertation

Presented for the

Doctor of Philosophy

Degree

The University of Tennessee, Knoxville

Hassan Bodaghi

December 1984

ACKNOWLEDGEMENTS

The author is very indebted to professor J.F. Fellers, his advisor for his wisdom and guidance during the course of this research. His continuing support and encouragement made it possible to complete this dissertation. Gratitude is extended to Dr. J.L. White for his support and recommendation in this program.

The cooperation of several individuals were essential to the completion of this work. I express my sincere thanks to these individuals for their generous help on several matters: to Dr. Colin L. Browne, of Celanese Fiber Company for sending material and his consultation in this research study; to Dr. Toshio Kitao of Kyota University of Industrial Arts and Textile of Japan for permission to present data from SAXS analysis of PPTA films; to Dr. J. S. Lin of the National Center for Small Angle X-ray at Oak Ridge National Laboratory for his helpful comments and suggestions regarding SAXS analyses; and finally, to the faculty of the Polymer Engineering Department; Joseph E. Spruiell, Donald C. Bogue, and Edward S. Clark for their instruction, support and discussions that have helped me achieve my academic goal.

Financial assistance provided by the Office of Naval Research, Celanese Fiber Company, and the Polymer

Consortium of The University of Tennessee are gratefully acknowledged.

The author wishes to thank Tommy Thompson and his co-workers in the mechanical shop, Ted Long and his co-workers in the electrical shop, and both A. Carter and Aileen Cagle in the facilities group.

Above all, I thank my loving wife Trisha for her devotion, encouragement, and help, my sons Kirk and Dustin for the warmth they bring into my life, and my parents Mohammad and Marzeyeh for their continuing love and understanding.

ABSTRACT

Various cellulose triacetate (CTA) and poly (p-phenylene terephthalamide) (PPTA) films have been prepared by extrusion of isotropic and anisotropic solutions through an annular die. The extrudate was given a uniaxial drawdown into a coagulation bath or biaxially expanded using a lubricated mandrel and a coagulant recycle blow-up process.

The films were characterized by Small Angle X-ray Scattering (SAXS), mass density, scanning electron microscopy (SEM), differential scanning calorimetry (DSC), Small Angle Light Scattering (SALS), Wide Angle X-ray Scattering (WAXS), and birefringence. The latter two methods were used to characterize the molecular orientation produced with processing conditions. Films extruded without drawdown exhibit some polymer chain orientation in the machine direction. This is increased by uniaxially drawing down films. Films produced using an oil coated mandrel and a coagulant recycle blow-up process show approximately equal biaxial orientation. Density and SAXS measurements indicate a void content increasing with increasing solution concentration.The volume fraction of voids was computed from the invariant analysis of SAXS and from mass density measurements. The void volume fraction increased with increased solution concentration

and decreased with increased drawdown ratio. Fibrillar structure was observed for "peeled" uniaxial films. This is increased with an increase in solution concentration. Biaxial films did not peel, apparently due to biaxial orientation developed in them. SEM locates micron size voids in the cross-sections of films produced from high solution concentrations. SAXS indicates much smaller void sizes which are roughly prolate ellipsoids for uniaxial films and oblate ellipsoids for the biaxially oriented films. Various techniques are used to estimate average void size and void size distribution. The mechanical properties of films were also measured. The uniaxial films exhibit highly anisotropic mechanical properties, while the biaxial films show fairly high modulus and tensile strength in all directions. Heat treatment under tension contributed greatly to enhancement of orientation and mechanical properties. Annealing also resulted in a significant decrease in voids and increased surface smoothness. A general comparison has been made between CTA films and PPTA films. The mechanical properties of these films are also compared to some commonly available commercial films.

TABLE OF CONTENTS

CHAPTER			PAGE
I.	INTRODUCTION		1
II.	BACKGROUND AND REVIEW OF LITERATURE		4
	A.	Liquid Crystals	4
		Structure and Classifications	4
		Synthetic Macromolecular Liquid Crystals	9
		Rheology of Liquid Crystals	22
	B.	Survey of Processing	39
		Synthetic Fibers	40
		Formation of Tubular Film	51
		Mandrel Process	53
		Formation of Film from Solution	57
	C.	Birefringence and Orientation	60
		Flow Birefringence	60
		Orientation Representation	63
	D.	Experimental Techniques for Investigation of Crystalline Orientation and Morphology	77
		Pole Figures	78
		Small Angle X-Ray Scattering (SAXS)	81
	E.	Structure Development and Solid State Crystal Structure	93
		Morphology and Orientation	116
		Mechanical Properties	130
	F.	Diffusion and Permeation Behavior of Polymer Films	136
III.	EXPERIMENTAL METHODS AND PROCEDURES		146
	A.	Materials	146
		Polymers	146
		Solvents and Non-Solvents	146
	B.	Preparation of Solutions	147
		PPTA-H_2SO_4 Solutions	147
		Cellulose Triacetate Solutions	153
	C.	Film Processing	156
		Kevlar® Film Extrusion Process	156
		CTA Film Extrusion Process	162
	D.	Film Characterization	171
		Scanning Electron Microscopy (SEM)	171
		Mass Density	174

CHAPTER PAGE

Differential Scanning Calorimetry (DSC) 175
Qualitative Small Angle X-Ray Scattering (SAXS) 175
Quantitative Small Angle X-Ray Scattering 176
Polarized Light Microscopy 179
Small Angle Light Scattering (SALS) . . 179
Wide Angle X-Ray Scattering (WAXS) . . 181
Pole Figures and Orientation Functions 181
Birefringence 185
Tensile Mechanical Property Measurements 185

IV. STRUCTURE DEVELOPMENT IN PPTA/H_2SO_4 FILMS . . 187

A. Processing Conditions 187
B. Void Characterization 191
Scanning Electron Microscopy 191
Density 198
Qualitative Small Angle X-Ray Scattering 201
Quantitative Small Angle X-Ray Scattering 204
C. Molecular Orientation 228
Qualitative Wide Angle X-Ray Scattering 228
Pole Figures and Orientation Functions 230
D. Discussion 240

V. STRUCTURE DEVELOPMENT OF CTA FILMS 250

A. Processing Conditions 250
B. Void Characterization 256
Scanning Electron Microscopy 256
Density 269
Small Angle X-Ray Scattering - Quantitative 272
C. Molecular Orientation and Crystallinity 295
Birefringence 295
Wide-Angle X-Ray Scattering 302
Differential Scanning Calorimetry . . . 310
D. Small Angle Light Scattering 324
E. Discussion 333

CHAPTER		PAGE
VI.	MECHANICAL PROPERTIES OF THE FILMS	344
	A. PPTA Films	344
	Initial Modulus	350
	Tensile Strength	353
	Percent Elongation to Break	357
	Discussion	358
	B. CTA Films	360
	Initial Modulus	364
	Tensile Strength	368
	Elongation to Break	374
	Discussion	375
VII.	COMPARISON OF CTA FILMS TO PPTA FILMS	378
	A. Processing Conditions	378
	B. Void Characterization	380
	C. Molecular Orientation	384
	D. Mechanical Properties	385
VIII.	CONCLUSIONS AND RECOMMENDATIONS	392
LIST OF REFERENCES		397
APPENDIXES		412
A.	PREPARATION OF DENSITY GRADIENT COLUMN	413
B.	POLE FIGURES AND DETERMINATION OF BIAXIAL ORIENTATION FACTORS	425
C.	MEASUREMENT OF BIREFRINGENCE	430
D.	COMPUTER PROGRAM	434
VITA		440

LIST OF TABLES

TABLE		PAGE
II.1.	White and Spruiel's Biaxial Orientation for Different Types of Orientation in a Film	73
II.2.	Scattering Functions for Various Particle Shapes	87
II.3.	List of Observed Reflections for Poly (p-Phenylene Terephthalamide) Fibers after Northolt (211)	97
II.4.	Spacings of Cellulose Triacetate I	105
II.5.	Spacings of Cellulose Triacetate II	106
II.6.	Unit Cell Dimensions of Cellulose Triacetate I and II	109
III.1.	Dimensions of Reservoir, Die and Mandrel	159
IV.1.	Summary of Experimental Runs and Their Process Conditions	189
IV.2.	Densities and Average Thickness for Prepared Films	199
IV.3.	Void Fraction "ϕ" Estimated from Density Data	202
IV.4.	Void Sizes Determined by Guinier Plots	213
IV.5.	Void Size Distribution Based on Method of Jellinek et al.	222
IV.6.	Summary of Void Size Determined by Debye et al. Technique	227
IV.7.	Biaxial Orientation Factors for PPTA Films	237
V.1.	Summary of CTA Films Prepared in This Study	253

TABLE		PAGE
V.2.	Average Thickness and Densities for CTA Films	270
V.3.	Void Fractions Measured from SAXS (ϕ) Invariant	285
V.4.	Void Dimensions Determined by Guinier Method	293
V.5.	Void Sizes Measured Using Debye and Bueche Technique	299
V.6.	Birefringence of CTA Films	301
V.7.	Heat of Fusion and Melting Temperature for CTA Films	322
VI.1.	Mechanical Properties of PPTA Films	348
VI.2.	Mechanical Properties of CTA Film	363
VII.1.	Mechanical Properties for Uniaxially Oriented Films and Fibers	386
VII.2.	Mechanical Properties for Biaxially Oriented and Casted Films	388
VII.3.	Mechanical Properties of Some Common Commercially Available Films (230)	390

LIST OF FIGURES

FIGURE		PAGE
II.1.	The Three Liquid Crystal States; Nematic, Smectic, and Cholesteric	7
II.2.	Viscosity Versus Concentration	25
II.3.	Three Regions of Flow Behavior for Liquid Crystals	30
II.4.	A Schematic Representation of the Bulk Structure of Polymer Liquid Crystals (I) Polydomain System, (II) Degraded Polydomain System; where Continuous Phase Exists Predominately, and (III) Monodomain Continuous Phase	38
II.5.	The Tubular Film Blowing Process Developed by Aoki et al. (13)	59
II.6.	Uniaxial Orientation Illustration and a Range of Values of Hermans-Stein Orientation Factors	68
II.7.	White and Spruiell's Coordinate System for Biaxial Orientation Functions	71
II.8.	Different States of Orientation in Films and White and Spruiell's Biaxial Orientation Factors	74
II.9.	Graphical Representation of Orientation, the Orientation Triangle Diagram (White and Spruiell)	76
II.10.	Experimental Schematic of a Goniometer for Orienting a Sample in the X-Ray Beam	79
II.11.	Position of Plane Normal by Spherical Coordinates	80
II.12.	(a) The Northolt Model for PPTA's Unit Cell and (b) The c-Axis Projection of the Northolt Model	99

FIGURE		PAGE
II.13.	C-axis Projections of the Crystal Structures of PPTA	101
II.14.	Structure Development of Liquid Crystalline vs. Conventional Folded Chain Polymers . . .	112
III.1.	Dry Box Used for Preparation of PPTA/H_2SO_4 Solutions	151
III.2.	Ross Planetary Mixer	155
III.3.	Mandrel Process for Producing Biaxially Oriented PPTA Film	157
III.4.	Wet Film Extrusion of Set-Up with Coagulant Recycle	163
III.5.	Current Die Design	165
III.6.	Circular Tube for Blowing CTA Films	168
III.7.	Schematic of Coagulant Blow-Up Film Extrusion	169
III.8.	Principle of the Scanning Electron Microscope	172
III.9.	SEM Sample Mounting Technique	173
III.10.	Diagram of 10 Meter Small Angle X-Ray Scattering	177
III.11.	Small Angle Light Scattering	180
III.12.	Sample Holder Attachment for Obtaining WAXS Patterns	182
III.13.	Sample Mounting for Pole Figures	184
IV.1.	SEM Photomicrographs for Cross-Sections and Surface of Sample 1)Extruded Film	192
IV.2.	SEM Photomicrographs for Cross-Sections and Surface of Sample 2)Uniaxial Low Drawdown Film	193
IV.3.	SEM Photomicrographs for Cross-Sections and Surface of Sample 3)Uniaxial High Drawdown Film	194

FIGURE		PAGE
IV.4.	SEM Photomicrographs for Cross-Sections and Surface of Sample 4)Mandrel Processed Film	195
IV.5.	SEM Photomicrographs for Cross-Sections and Surface of Sample 5)Annealed Mandrel Film	196
IV.6.	SAXS Qualitative Film Patterns of 1)Extruded 2)Uniaxial Low Drawdown 3)Uniaxial High Drawdown 4)Mandrel Processed 5)Annealed Mandrel Film	203
IV.7.	SAXS Intensity Contour Plot for Three Directions Relative to Sample 1) Extruded Film	205
IV.8.	SAXS Intensity Contour Plot for the Beam Normal to the Extrusion Plane of Sample 2) Uniaxial Low Drawdown Film	206
IV.9.	SAXS Intensity Contour Plots for Three Directions Relative to Sample 3) Uniaxial High Drawdown Film	207
IV.10.	SAXS Intensity Contour Plots for Three Directions Relative to Sample 4) Mandrel Processed Film	208
IV.11.	SAXS Intensity Contour Plots Normal to the Extrusion Plane for Sample 4)Mandrel Processed and Sample 5)Annealed Mandrel Films	209
IV.12.	Guinier Plots for Sample 1)Undrawn Film . .	214
IV.13.	Guinier Plots for Sample 2)Uniaxial Low Drawdown Film	215
IV.14.	Guinier Plots for Sample 3)Uniaxial High Drawdown Film	216
IV.15.	Guinier Plots for Sample 4)Mandrel Processed Film	217

FIGURE		PAGE
IV.16.	Jellinek-Solmon-Funkuchen Plots of Through View for Film 3	219
IV.17.	Jellinek-Solmon-Funkuchen Plots of Edge View for Film 3	220
IV.18.	Jellinek-Solmon-Funkuchen Plots of End View for Film 3	221
IV.19.	Debye-Bueche Plots of Through View for Sample 1)Undrawn Film	224
IV.20.	Debye-Bueche Plots of Edge View for Film One	225
IV.21.	Debye-Bueche Plots of End View for Film One	226
IV.22.	Schematic of Typical WAXS Patterns Taken Normal to the Extrusion Plane of; 1. Extruded 2. Uniaxial Low Drawdown 3. Uniaxial High Drawdown 4. Mandrel Processed 5. Annealed Mandrel Film	229
IV.23.	Pole Figures for Extruded PPTA Film a. 200 Reflection b. 006 Reflection	231
IV.24.	Pole Figures for Uniaxially Low Drawdown PPTA Film a. 200 Reflection b. 006 Reflection	232
IV.25.	Pole Figure for Uniaxially High Drawdown PPTA Film a. 200 Reflection b. 006 Reflection	233
IV.26.	Pole Figures for Mandrel PPTA Film a. 200 Reflection b. 006 Reflection	234
IV.27.	Pole Figures for Annealed Mandrel PPTA Film a. 200 Reflection b. 006 Reflection	235
IV.28.	Orientation Triangle for PPTA Films	239

FIGURE		PAGE
V.1.	Extrusion Rate Calibration	255
V.2.	SEM Photomicrographs for Sample 1; a)End View b) Edge View c) Surface	257
V.3.	SEM Photomicrographs for Sample 2; a)End View b) Edge View c) Surface	258
V.4.	SEM Photomicrographs for Sample 3; a)End View b) Edge View c) Surface	259
V.5.	SEM Photomicrographs for Sample 4; a)End View b) Edge View c) Surface d) Peeled . . .	260
V.6.	SEM Photomicrographs for Sample 5; a)End View b) Edge View c) Surface	261
V.7.	SEM Photomicrographs for Sample 6; a)End View b) Edge View c) Surface d) Peeled . . .	262
V.8.	SEM Photomicrographs for Sample 7; a)End View b) Edge View c) Surface	263
V.9.	SEM Photomicrographs for Sample 8; a)End View b) Edge View c) Surface	264
V.10.	SEM Photomicrographs for Sample 9; a)End View b) Edge View c) Surface	265
V.11.	SEM Photomicrographs for Sample 10; a)End View b) Edge View c) Surface	266
V.12.	SAXS Intensity Contour Plots for Three Directions Relative to Sample 1	273
V.13.	SAXS Intensity Contour Plots for Three Directions Relative to Sample 2	274
V.14.	SAXS Intensity Contour Plots for Three Directions Relative to Sample 3	275
V.15.	SAXS Intensity Contour Plots for Three Directions Relative to Sample 4	276
V.16.	SAXS Intensity Contour Plots for Three Directions Relative to Sample 5	277
V.17.	SAXS Intensity Contour Plots for Three Directions Relative to Sample 6	278

FIGURE PAGE

V.18. SAXS Intensity Contour Plots for Three Directions Relative to Sample 7 279

V.19. SAXS Intensity Contour Plots for Three Directions Relative to Sample 8 280

V.20. SAXS Intensity Contour Plots for Three Directions Relative to Sample 9 (a,b,c) and Sample 10 (d,e,f) 281

V.21. Radial Average of Intensity Versus Scattering Angle for Sample 5 287

V.22. Intensity Versus Scattering Angle for End View of Sample 5 288

V.23. Intensity Versus Scattering Angle for Edge View of Sample 5 289

V.24. Guinier Plot for Through View of Sample 5 . 290

V.25. Guinier Plot for End View of Sample 5 . . . 291

V.26. Guinier Plot for Edge View of Sample 5 . . . 292

V.27. Debye-Bueche Plot for Through View of Sample 5 296

V.28. Debye-Bueche Plots for End View of Sample 5 297

V.29. Debye-Bueche Plots for Edge View of Sample 5 298

V.30. WAXS Patterns with the Beam Normal to the Plane of the Films; a)Sample 1, b)Sample 3 c)Sample 4, d)Sample 5, e)Sample 6 f)Sample 7, g)Sample 8 303

V.31. WAXS Patterns with the Beam Normal to the Plane of the Films for; h)Sample 9 i)Sample 10 305

V.32. WAXS Patterns for Sample 6; a)Uniaxial Film, b)Hydrolyzed Uniaxial Film 307

V.33. WAXS Patterns for Sample 7; a)Biaxial Film, b)Hydrolyzed Biaxial Film 308

FIGURE		PAGE
V.34.	WAXS Patterns for Sample 8; a)Biaxial and Annealed Film, b)Hydrolyzed Biaxial and Annealed Film	309
V.35.	DSC Thermogram for Film 1	311
V.36.	DSC Thermogram for Film 2	312
V.37.	DSC Thermogram for Film 3	313
V.38.	DSC Thermogram for Film 4	314
V.39.	DSC Thermogram for Film 5	315
V.40.	DSC Thermogram for Film 6	316
V.41.	DSC Thermogram for Film 7	317
V.42.	DSC Thermogram for Film 8	318
V.43.	DSC Thermogram for Film 9	319
V.44.	DSC Thermogram for Film 10	320
V.45.	SALS Patterns for Film 1; a)V_v, b)H_v	325
V.46.	SALS Patterns for Film 2; a)V_v, b)H_v	326
V.47.	SALS Patterns for Film 3; a)V_v, b)H_v	327
V.48.	SALS Patterns for Film 4; a)V_v, b)H_v	328
V.49.	SALS Patterns for Film 5; a)V_v, b)H_v	329
V.50.	SALS Patterns for Film 6; a)V_v, b)H_v	330
V.51.	SALS Patterns for Film 7; a)V_v, b)H_v	331
V.52.	SALS Patterns for Film 8; a)V_v, b)H_v	332
VI.1.	Stress-Strain Curves for Film 1 as a Function of Film Direction	345
VI.2.	Stress-Strain Curves for Film 3 as a Function of Film Direction	346
VI.3.	Stress-Strain Curves for Film 4 as a Function of Film Direction	347

FIGURE		PAGE
VI.4.	Radial Plots of Modulus as a Function of Film Direction for; 1. Extruded 2. Uniaxial Low Drawdown 3. Uniaxial High Drawdown	351
VI.5.	Radial Plot of Modulus as a Function of Film Direction for; 4. Mandrel Processed 5. Annealed Mandrel Film	352
VI.6.	Radial Plots of Tensile Strength as a Function of Film Direction for; 1. Extruded 2. Uniaxial Low Drawdown 3. Uniaxial High Drawdown 4. Mandrel Processed	354
VI.7.	Radial Plots of Tensile Strength as a Function of Film Direction for; 1. Extruded 4. Mandrel Processed 5. Annealed Mandrel Films	355
VI.8.	Typical Stress-Strain Curves for Uniaxially Drawn Films as a Function of Film Direction	361
VI.9.	Typical Stress-Strain Curves for Biaxially Expanded Films as a Function of Film Direction	362
VI.10.	Radial Plots of Modulus as a Function of Film Direction for Films 1 to 4	365
VI.11.	Radial Plots of Modulus as a Function of Film Direction for Films 5, 7, and 8	367
VI.12.	Radial Plots of Modulus as a Function of Film Direction for Films 9 and 10	369
VI.13.	Radial Plots of Tensile Strength as a Function of Film Direction for Films 1 to 4	370
VI.14.	Radial Plots of Tensile Strength as a Function of Film Direction for Films 5, 7, and 8	371

FIGURE		PAGE
VI.15.	Radial Plots of Tensile Strength as a Function of Film Direction for Films 9 and 10	372
A.1.	Schematic of the Filling of a DGC	414
A.2.	DGC Calibration Curve Used for Density Measurements of CTA Films	421
A.3.	DGC Calibration Curve Used for Density Measurements of Kevlar Film Samples 2-5 . .	422
A.4.	DGC Calibration Curve Used for Density Measurements of Kevlar Film Sample 1	423
B.1.	Three-Dimensional View of a Pole Figure . .	426
C.1.	Illustration of Gaertner Polariscope and Compensator	431

CHAPTER I

INTRODUCTION

The existance of liquid crystals have been known for nearly a century. Polypeptides, aromatic polyamides and cellulose derivatives are the major classes of polymers which exhibit liquid crystalline character in solutions (102,151,190) and are relatively recent discoveries.

Cellulose and its derivatives have played a major role in the plastic and fiber industry for nearly a century but lost their dominance with the discovery of truly synthetic polymers. During the past decade, recognition of the liquid crystalline character of some aromatic polyamides (29,102,103) and cellulose derivatives (132,190) by DuPont investigators has created considerable interest in these polymers and their fabrication into products.

The inventions by Kwolek, Morgan and their co-workers at DuPont (19,20,32,102,103,133) of super high modulus and tensile strength fibers from poly (p-phenylene terepthalamide), PPTA and commercialization of Kevlar® led various research teams to search for new liquid crystalline polymer systems(3,41,88,132,162) and investigate their structure in the quiescent state (3,29,

128,190) as well as in flow (13,128,134,162). Panar and Wilcox (132) made filaments from various liquid crystalline cellulose derivative dopes and found their mechanical properties superior to those made from isotropic dopes.

Several investigations have been carried out in our own laboratory on the properties of liquid crystalline polymers (13), and cellulose derivatives in solution (127,128,129).

Recent work from here (4) shows that hydroxypropycellulose, found to be lyotropic in other studies (29,127,128), is also thermotropic. Ethyl cellulose has been shown to be shown to be thermotropic too (177). A number of other investigators have also described the formation of liquid crystalline solutions of cellulose triacetate (115,136) and other cellulose derivatives (3,4,51).

However, the interest in liquid crystalline polymers has been primarily to produce high modulus fibers. Few attempts have been reported to develop more complex processing procedures and products. One by Tennessee Eastman investigators (89,90) described the injection molding of liquid crystalline polyesters. Other works are from our own laboratory at the University of Tennessee. These involve the wet spinning of fiber (73) and the fabrication of films (12,63) from liquid crystalline

PPTA/H_2SO_4 solutions. An earlier fabrication study (12) involved a vertically downward tubular process with air inflation to produce a biaxially oriented film. This process was unstable and developed only a low level of biaxial orientation. The more recent investigation (63) used a lubricated mandrel and developed significant levels of biaxial orientation, i.e., orientation in the transverse as well as the machine direction in PPTA or Kevlar® films.

As indicated in the above paragraphs, most of the work cited earlier on liquid crystalline cellulose and its derivatives have dealt with fibers, as was the case with polyamides. In this research project our main goals are twofold; first, to produce various films such as uniaxial and biaxial from isotropic and liquid crystalline solutions of PPTA and cellulose triacetate (CTA). Secondly, the films are studied by characterizing the structural variation of the produced films with processing conditions. In this second area an emphasis will be made on a general comparison of films made from PPTA with those produced from CTA.

CHAPTER II

BACKGROUND AND REVIEW OF LITERATURE

A. Liquid Crystals

The study of liquid crystals first began with the research of Reintzer (150) who observed that several cholesterol esters did not render themselves as transparent liquid upon melting, but exhibited colors over a range of temperature before becoming transparent. Materials showing such behavior were termed by Lehmann (107) as "Flowing Crystals" (1889), "Crystalline Liquids" (1890), and finally "Liquid Crystals " (1904).

Liquid crystals (sometimes named mesophases, mesomorphic phases, or anisotropic fluids) are intermediate between ordinary fluids, which are endowed with only short-range order or structure, and crystalline solids, which ideally have perfect order both with respect to the position and the orientation of their component molecules. Relaxation of the condition for perfect ordering in various ways gives rise to mesophases of different sorts.

Structure and Classifications

Polymer liquid crystals can be classified by phase transitions from isotropic to anisotropy, or by structure. According to molecular order, liquid crystals were

classified by Friedel (64) in 1922, as nematic, smectic and cholestric. The cholesteric liquid crystals have a one dimensional order with layers forming a superimposed twist. The cholesteric state is usually thought of as a twisted or helical nematic. Nematic liquid crystals, such as Kevlar, have the simpler one dimensional order. This state can be thought of as a collection of rigid rods which have an average alignment in the long direction but little alignment or order in the transverse direction. Smectic liquid crystals have a layered structure of two dimensional order (64). Variations exist within the smectic state involving twisting or tilting within the liquid crystals. As many as eight smectic phases have been tenatively indentified. However, except for three that have been reasonably well characterized, considerable uncertainty still exists about the exact nature of the molecular ordering in these phases. The three best understood smectic phases are known as, smectic A, B, and C phases. All three appear to have a common feature,one degree of translational ordering, resulting in a layered structure. As a result of this partial translational ordering, the smectic phases are much more viscous than either the cholesteric or nematic phase.

Within the layers of a smectic A mesophase the molecules are aligned parallel to the layer normal and are uncorrelated with respect to center of mass position,

except over very short distances. Thus, the layers are individually fluid, with a substantial probability for inter-layer diffusion as well (53).

In the smectic C order, the long axis of molecules are tilted in the layer plane. Tilt angles of up to 45° have been observed and in some materials the tilt angle has been found to be temperature dependent. As in the smectic A phase, the layers are individually fluid and inter-layer diffusion can occur, although most likely with some what lower probability (53).

In addition to layered structure, x-ray data indicate ordering of the constituent molecules within the layers of the smectic B phase. In contrast to the smectic A and C phases, the layers are no longer fluid and the mechanical properties of the smectic B are quite different from those that would be expected for a material having full three dimensional order. However, it has been suggested that the smectic B phase may in fact be a plastic crystal (53). Examples of the nematic, cholesteric and smectic states are shown in Figure II-1.

Liquid crystals may also be classified according to the phase transition from isotropy to anisotropy. Isotropic materials which become anisotropic through purely thermal processes are called thermotropic liquid crystals. Materials showing thermotropic liquid crystal phase are usually organic substances with molecular structures typified by

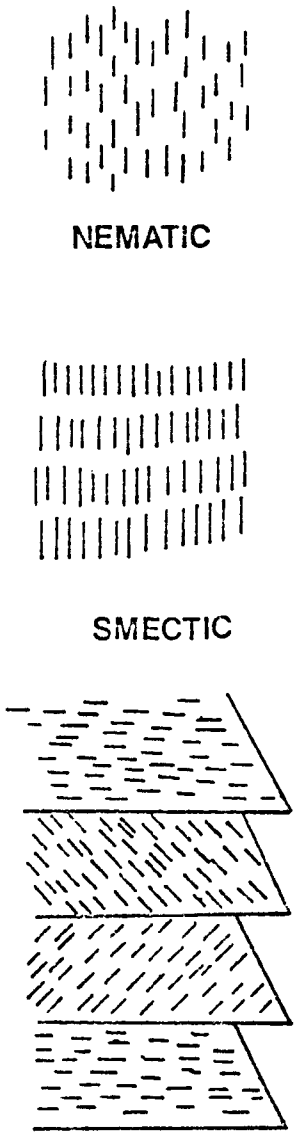
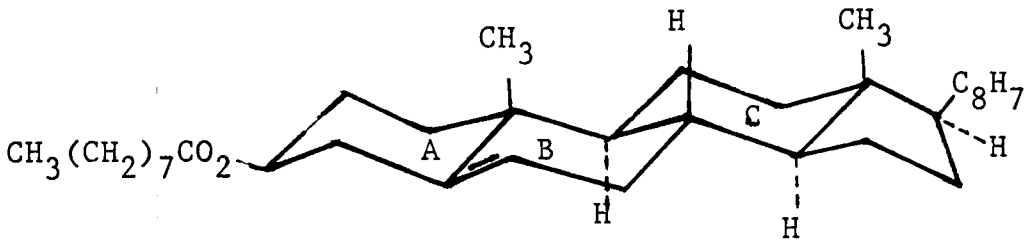
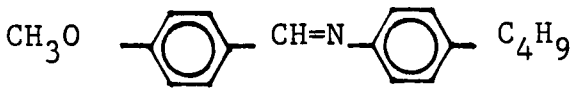


Figure II. 1. The three liquid crystal states; Nematic, Smectic, and Cholesteric.

those of cholesteryl nonanoate and N-(P-methoxybenxylidene) -p-n-butylaniline (MBBA) shown below.



Cholestery Nonanoate



(MBBA)

Axial ratios of 4-8 and molecular weight of 200-500 gm/mol are typical for thermotropic liquid crystal mesogens. In this type of liquid crystals, every molecule participates on an equal basis in the long range ordering.

Solutions of rod-like entities in a normally isotropic solvent often form liquid crystal phases for sufficiently high solute concentration. These anisotropic solutions mesophases are called lyotropic liquid crystals. The rod-like entities are usually large compared with typical thermotropic liquid-crystal mesogens. The actual ratios are seldom greater than ≈15. Deoxyribonucleic acid (DNA) and many synthetic polypeptides form lytropic mesophases when dissolved in an appropriate solvent in suitable concentration (42,148).

Synthetic Macromolecular Liquid Crystals

Polypeptides. Synthetic polypeptides were the earliest macromolecules found to reveal liquid crystalline in character. In 1950 Elliot and Ambrose (60) observed poly (γ-benzyl-L-glutamate), P γ BLG to form spherulites of the cholesteric N_c state in concentrations above 15 wt. percent. Later, in 1956 the investigations by Robinson (151) with P γBLG confirmed Elliott and Ambrose results. Robinson et al (151,152) found that the critical concentration of Pγ BLG was dependent on molecular weight. They reported that by increasing the molecular weight the critical concentration decreased.

Dupre and Hammersmith (59) noted that P γ BLG formed the nematic state in 1:4 CH_2 CL_2/dioxane, and the cholesteric state in CH CL_3, dioxane, M-creosol, CH_2CL_2, dichloroacetic acid, benzene, and dimethyl formamide (DMF). First they (59) reported that P γ BLG formed a smectic state in benzene, but later optical and structural studied (59,135) did not confirm it. However, structures of synthetic polypeptides which exhibited liquid crystalline characteristics are as follow (123,151,174,183,193),

$$\left(\begin{array}{c} O \\ \| \\ C \\ | \\ CH \\ | \\ R \end{array} - NH\right)_n \quad \text{where} \quad R=(CH_2)_4 - \begin{array}{c} O \\ \| \\ C \end{array} - CH_2$$

for poly (E-carbobenzyloxy-L-lysine) (183)

R= CH_2 - COOH for poly (glutamic acid) (174)

R= (CH_2)- $COOCH_2$- 

for poly (γ-benzyl-L-glutamate)(151)

R= $CH_2 - \overset{O}{\overset{\|}{C}} - OCH_2$ - 

for poly (β-benzyl-L-aspartate)(151)

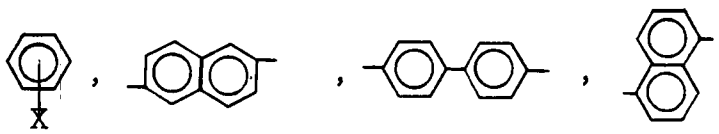
R= $(CH_2)_2 - \overset{O}{\overset{\|}{C}} - R'$

for poly (γ-alkyl-L-glutamate)(123,151,193)
where R is methyl (P γ MLG), ethyl (P γ ELG), bulyl, hexyl, cyclohexyl, or propyl.

Aromatic polyamides. Aromatic polyamides were first developed by DuPont scientists, from the early sixties to the mid-seventies (102,103,192). These polymers have structures of the form:

$$\leftarrow\overset{O}{\overset{\|}{C}} - R - \overset{O}{\overset{\|}{C}} - NH - R' - NH\rightarrow_n$$

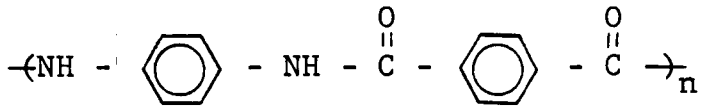
where R and R' may be as follow:



and X= Cl, F, H or R'= SO_3 H, etc.

Patents issued to Kwolek (102) in 1972 involve the polymerization and processing of poly (p-phenylene terephtalamide) PPTA or better known as Kevlar®. Based on infrared and nuclear magnetic resonance studies it is

believed that the structural formula of PPTA is



These polyamides exhibit the nematic liquid crystalline state in concentrations 9-10 wt. percent in one hundred percent H_2SO_4 for polymer molecular weights of around 40,000 (127). The concentration needed to induce the onset of anisotropy was found to be inversely proportional to molecular weight as noted by Papkov (134) for poly (p-benzamide).

Schaefgen et al. (159), Arpin and Strazielle (14) and Kwolek (103), investigated dilute solutions of p-linked amides. Schaefgen et al. (159) found the intrinsic viscosity- molecular weight relationship, using Mark-Howink equation ,"a" values of 1.7, 1.08 for low and high molecular weight poly (p-benzamide) were obtained respectively. These values suggested a semi-rigid model for p-linked aromatic chains. Kwolek (102,103) and Arpin et al. (14) reported similar results.

Kwolek (102,103) observed anisotropic solutions by dissolving PPTA in 100 percent sulfuric acid at appropriate concentrations. By plotting viscosity as a function of polymer concentration, she verified the transition from an isotropic solution to an anisotropic solution for poly (p-benzamide) in HF. A phase diagram presented for PPTA

and H_2SO_4 indicates a need for acid concentration of at least 99 percent SO_3 to produce optically anisotropic solutions.

In the early seventies Blades (32) in his patents discusses degradation problems associated with PPTA/H_2SO_4 dopes. Degradation is usually a reduction in molecular weight. To prevent this degradation problem, he suggested use of a sulfuric acid concentration of 99.8 percent to keep moisture content down and to reduce hydrolysis. Since the elevated heat of solution causes degradation the mixing temperature should be kept below 90°C.

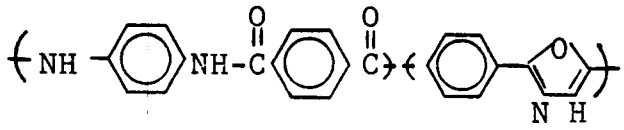
Blades (32) also discusses the melting temperature of PPTA/H_2SO_4 at various concentrations. It was found that as polymer concentration increases the melting temperature will increase. The temperature at which the solutions begin to change from an anisotropic state to an isotropic state where determined. For various concentrations such as 17, 21, 25 percent the temperatures of 80°—100°, 82°—140°, 110°-120° C were found respectively.

Recent papers of Flood et al. (63) show phase diagrams for PPTA in sulfuric acid. They plotted temperature as a function of polymer concentration and indicate the temperature at which the transition from the anisotropic to isotropic state take place.

Other investigators (28,133) of PPTA/H_2SO_4 solutions observed the existence of birefringent spheres within the

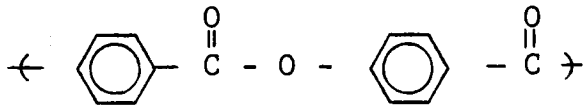
transition regions and nematic or thread like structures in wholly anisotropic solutions. Further, the existence of negative spherulites in the transition regions of PPTA and CL-PPTA solutions is reported by Onogi et al. (127) and Aoki et al. (12). These suggest that the macromolecules are present in a circumferential or tangential manner in relation to the spherulite radius. Observations of wholly anisotropic solutions are in good agreement with Panar and Beste (133) that is, nematic crystals were observed.

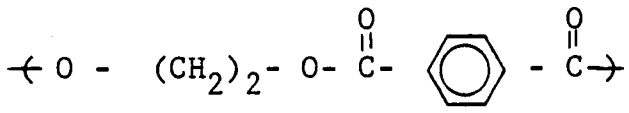
Recently, Silver and Black (163) of Monsanto prepared a liquid crystalline copolymer, so called poly (P-didulfanotophenylene) - (Terepthalamide)- co-poly (phenylene- 1,3,4 oxadia zole). They indicated that the phenylene -1,3,4 oxadia zole (PO_x) units in ratios from 10:90 to 30:70 appeared to have a synergistic effect on the liquid crystalline character. Increasing the ratio of (PO_x) units above 30 percent inhibited the liquid crystal formation. The copolymer structure is as follow:

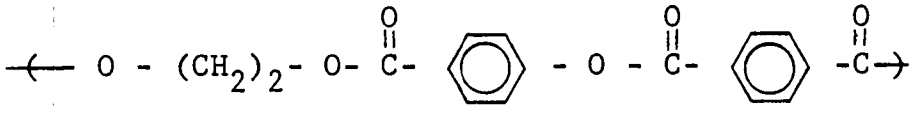


The anisotropic state for the aromatic polyamides in general has been reported to be the nematic by many investigators (102,103,122,133,193).

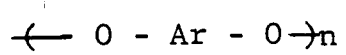
Polyesters. One of the other classes of polymers which exhibits liquid crystalline characteristics are partial aromatic copolyesters. Kuhfuss and Jackson (88, 106) of Tennessee Eastman, developed copolymers by acidolysis of poly (ethylene terepthalate), PET, with poly (acetoxy benzoic acid) and by reacting PET copolyester with methyl-P-hydoxy benzoate. Its polymeric structure includes the following (88,106);

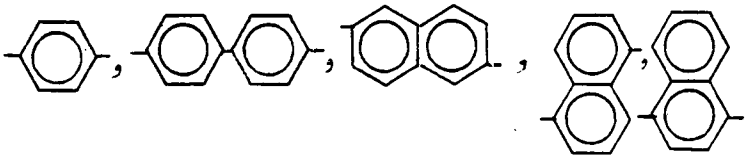






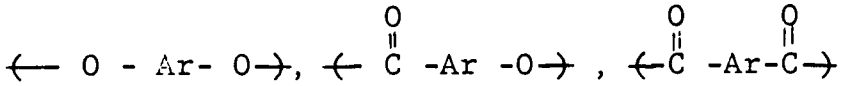
McFarlane et al. (113) of Tennessee Eastman, have prepared other partially aromatic copolyesters synthesized from PET (polyethylene terphthalate), parahydroxybenzoic acid, terephthalic acid, and acetylated quinones of the following form;

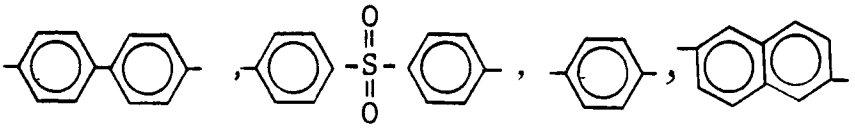


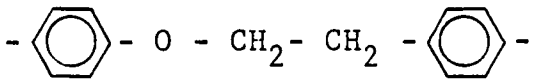
Where Ar= 

Investigators at DuPont, namely Pletcher (145) and Kleinschuster (100), have developed similar classes of aromatic copolyesters to those of Eastman polyesters which exhibit liquid crystalline characteristics.

Recently, researchers of Celanese, namely Calundann (41), Warner (188,189) and Wissbrun (198), have studied thermotropic aromatic copolyesters based on structures of the type:



where Ar= 

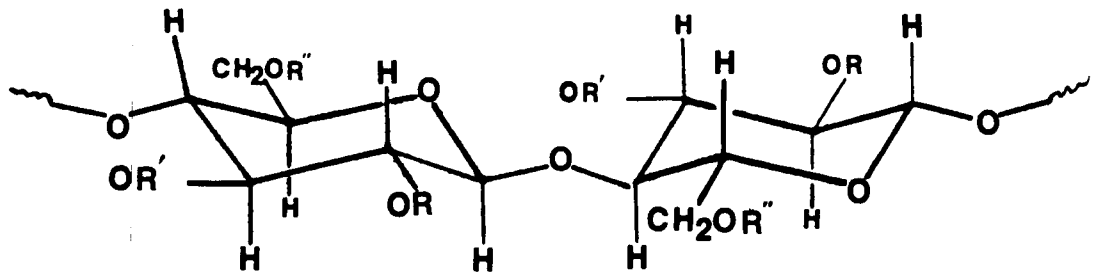


However, thermotropic aromatic polyesters form the nematic state in the melt (88,106,145,198) and the aromatic copolyesters do not form lyotropic liquid crystals (127).

Cellulose Derivatives. One of the most recent classes of polymers found to exhibit liquid crystalline characteristics are cellulose and its derivatives. In 1969 first Samuels (156) reported studies on solution cast films of hydroxylpropyl cellulose, in which he

indicated that the polymer exists in the solid state as a collection of rigid rods or crystalline microfibrils. However, Werbowj and Gray (190) first reported liquid crystalline characteristics of hydroxypropyl cellulose solutions. In the same period, the liquid crystalline nature of a variety of cellulose derivative solutions was reported by Panar and Willcox (132) in 1977.

Some examples and the general repeating structure of the cellulose derivatives are shown below (29);



where $R'' = \overset{O}{\overset{\|}{C}}- CH_3$, $R = R' = H$

for cellulose acetate (CA)

$R = R' = H$, $R'' = CH_2 - CH_3$

for ethyl cellulose (EC)

$R'' = CH_2 - \underset{O}{\underset{|}{CH}} - CH_3$ $\quad\quad$ $-CH_2 - \underset{OH}{\underset{|}{CH}} - CH_3$ $\quad$ and $\quad R' = R = CH_2 - \underset{OH}{\underset{|}{CH}} - CH_3$

for hydroxypropyl cellulose (HPC)

$$R = R' = R'' = \overset{O}{\overset{\|}{C}} - CH_3 \text{ for cellulose triacetate (CTA)}$$

$$R = \overset{O}{\overset{\|}{C}} - CH_3,\ R' = H,\ R'' = \overset{O}{\overset{\|}{C}} - (CH_2)_2 - CH_3$$

for cellulose acetate butyrate (CAB).

Werbowj and Gray (190) reported that HPC formed a lyotropic cholesteric mesophase in water. This later was confirmed and extended by Onogi et al. (128). They reported that the cholesteric mesomorphic state was formed in the concentration range of 53-70 wt. percent. Solutions with concentrations greater than 70 wt. percent showed negatively birefringent spherulitic domains of dimensions 25-80 microns (134,127). Bheda, Fellers and White (29) studied hydroxypropyl cellulose in various solvents such as dichloracetic acid (DCA), water, acetic acid, dimethylacetamide (DMA) and ethanol. They observed that the critical concentration (C*) for the on set of anisotropy in HPC solutions decreased as solvent acidity increased from a low of 21 wt. percent in DCA to a high of 42 percent for ethanol and water. Shimamura et al. (162) carried out studies of HPC in the melt. They found that the cholesteric state was formed in the HPC melts in temperature ranging from 160°C- 205°C.

Cellulose triacetate and other cellulosic derivatives have also been studied by Bheda et al. (29). They reported

that cellulose triacetate formed positively birefringent spherulitic domains in solutions, while ethyl cellulose as well as HPC formed negatively birefringent spherulitic. Cellulose acetate was found to form no well defined structures in solution.

Recently, cellulose acetate was investigated in 30 different solvents by Aharoni (3). He reported the critical concentration decreases with increasing acid strength in moderate to strong acids. Weakly acidic, neutral, or basic solvents followed a different C*-solvent relation, C* decreased with the increasing molar volume of the solvent. The same C* solvent relationship for acid solution was reported by Bheda et al. (29) in their studies of cellulose derivatives.

A comparative study of the thermotropic mesomorphic tendencies and rheological characteristics of three cellulose derivates: ethylene and propylene oxide and an acetate butyrate ester are reported in a more recent paper by Suto, White and Fellers (177). They noted that hydroxypropyl cellulose and ethyl cellulose are thermotroic liquid crystals, while cellulose acetate butyrate behaves in a manner similar to a vetrifying isotropic melt such as polystyrene.

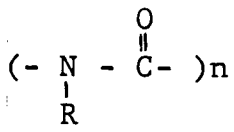
Gel formation and liquid crystalline order in cellulose triacetate solutions have been carried out by Meeten and Navard (115). They dissolved CTA in

trifluoroacetic acid. Below a critical concentration of 34 g/100 ml a clear isotropic solution was formed. Solutions more concentrated than this were in the cholesteric liquid crystalline state. A gel phase was formed when water was added to the solution if the polymer concentration was above a critical value. Morever, their experimental observations were not inconsistent with the Pincus-de Gennes theory (144). According to their theory, polymer solutions in dilute solutions exist as flexible random coils, and the isotropic- to anisotropic transition is accompanied by a coil-to-helix conformation change.

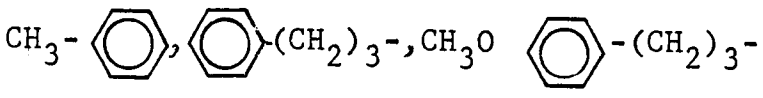
Patel and Gilbert (136) carried out studies of mesomorphic solutions of cellulose triacetate in trifluroacetic acid halogenated solvent mixtures including phase separations and factors affecting the cholesteric pitch. The formation of liquid-crystalline solutions of CTA in various mixtures of TFA with CH_2Cl_2, 1,2,-dichloroethane (1,2-DCE), and $CH\ Cl_3$. They also reported the effect of solvent composition, temperature, polymer concentration, time, and magnetic field on the pitch of the cholesteric structures, and the flow properties of the solutions of CTA in various TFA-CH_2Cl_2 mixtures at constant volume fraction of CTA. Their results indicate that the order of solvent powers in TFA- CH_2Cl_2 TFA- 1,2-DCE TFA -$CH\ Cl_3$, which is the order of decreasing acidity

of the solvent systems, with TFA-CH_2 Cl_2 as solvent, the one-fourth power of the pitch varies inversely with the CTA concentration, and increases linearly with temperature. The pitch was found to increase exponentially with time and increases faster the more acidic the solvent. In a magnetic field a cholesteric to nematic transition occurs. They also noted that a minimum in solution viscosity occurs at 34 percent w/v of CH_2 Cl_2 for solution in TFA- CH_2 Cl_2.

Other polymers which exhibit liquid crystalline characteristics. In 1976, Millich (118) first reported the liquid crystalline nature of the polyisoscynates. The rigid rod-like characteristics of these macromolecules has been realized and known since 1963 (40). These polymers have a structural unit of the following type:



Where R can be an alkyl groups such as $4 \leqslant R \leqslant 12$ carbon units long or other structures like

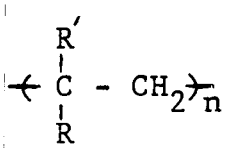


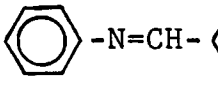
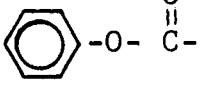
Burchard (40) noted that poly (n-butyl isocynate) had rod-like character from the high value he obtained for the Mark-Houwink experiment of dilute solution viscosity

measurements. Later investigations of other researchers (39,93,206) on dilute solutions of poly (n-butyl isocynate) and poly (n-hexyl isocynate) substantiated Burchard's observation.

Aharoni et al. (4,5,6) carried out work involving concentrated solutions of poly (alkyl or arylalkyl isocynates) in trichloroethylene or chloroform. They reported that solutions between 25-50 percent w/v formed the nematic state and solutions above 50 percent w/v formed anisotropic gels. They also found that the poly (alkyl isocynates) such as Poly (n-hexyl isocynate), poly (n-octyl isocynate),poly (n-undecyl isocynate), poly (n-butyl isocynate), and poly (n-nonyl isocynate) undergo thermotropic transitions to the nematic state in addition to lyotropic transitions (5,6).

One other class of polymers observed to show liquid crystalline character are acrylate or vinyl based polymers. These polymers have a repeating unit of the form (33,95,161,193);

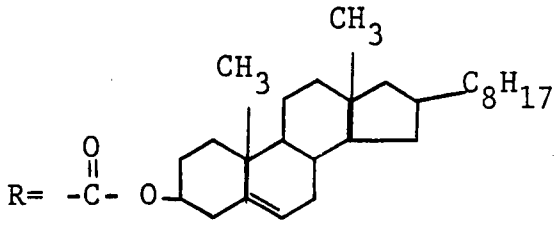


where R= N ≡ C-  -N=CH-  -O- C(=O)- and R'= H

For poly (benzylidene-p-cyanoaniline acrylate)

R= CH_3- $(CH_2)_{15}$ - O - C(=O)- and R' = H

for poly (hexyldecyl acrylate)



and R'= H for poly (cholesterol acrylate)

Schibaev et al. (161) noted that poly (hexyl decyl acrylate) formed anisotropic gels at 0.3 - 0.35 percent concentrations in C_7-C_{12} n-type alcohols or C_{10}- C_{16} n-type hydrocarbons. They also reported that the smectic state was formed by the polymer in alcohol solutions and the nematic state in hydrocarbon solutions.

Poly (benxylidene-p-cyanoanitine acrylate) and remaining polymers of this type with mesogenic side group (33) have been reported to form nematic, cholesteric or smectic states in solutions or melts.

Rheology of Liquid Crystals

The major use of the synthetic macromolecular liquid crystalline systems is fabrication of high strength fibers and films. The higher strength of the fabricated products can be directly attributed to the orientation of the macromolecular chains. Rheology is the study of the response of materials under mechanical stimulus and offers an insight into the supermolecular arrangement upon the mechanical response. Since all the fabrication processes

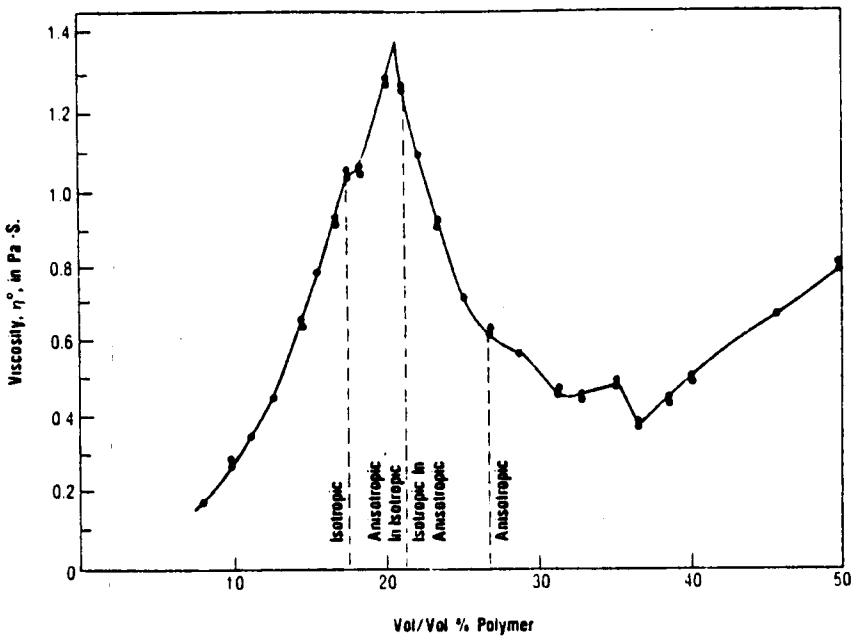
require the material to go through some kind of a stress field, the study of rheology is fundamental towards controlling the mechanical properties of the fabricated products.

The rheological studies have mainly been performed on solutions of synthetic polypeptides which are known to exist as rigid rods and aromatic polyamides which are believed to exist as extended chains in solutions. Since a few pioneers (22,147) already have reviewed earlier work on the rheological features of LCP's, in this section the emphasis will be on update experimental results in this area. For the rheology of the rod-like LCP's, readers can refer to a recent paper published by Wissbrun (146). He discussed the rheological findings and mechanisms with the frame work based on three region flow curve proposed by Onogi and Asada (129).

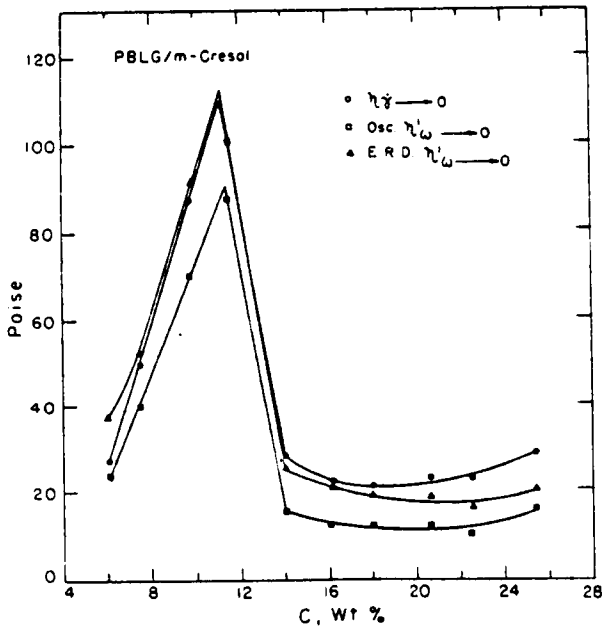
The effects of concentrations upon material functions. One of the striking features of rheology for liquid crystalline polymers in a solvent is that the viscosities do not show a monotonic increase with solute concentration, and this feature has been thought to be related to the phase transition from the isotropic to mesomorphic phase. In one of the earliest studies in this interest, Hermans (78) reported that the viscosity goes through a maximum, and this maximum point can be associated with

the phase transition. Even though this association has been published by many authors, and is well-known, this identification began to be thought to be impossible on physical grounds by some authors (5,7,8,110) recently.

Aharoni (5,7,8) repeatedly reported that the maximum peak in viscosity appeared not at the point where the anisotropic phase first makes its appearance, but substantially within the biphasic range, where isotrpic and anisotropic phase coexists, through the combined results of isothermal viscosity measurements and cross-polarized light microscopy for several lyotropic LCP's including polyisocyanide (PIC), poly (n-hexylisocyanate) (PHIC), poly (50 percent n-hexyl + 50 percent propyl) isocyanate (PHPIC) in toluene, and poly (50 percent n-buthyl + 50 percent p-anisole-3-propyl) isocyanate (PBAPIC) in TCE. His works indicate the onset of the mesogenic phase may be related not to the concentration (C) at maximum viscosity but to a shoulder shown in front of the peak in the viscosity-concentration curves, as illustrated in Figure II-2a. He also divided the biphasic region into two parts: isotropic matrix containing anisotropic inclusion and anisotropic matrix containing isotropic inclusion. The phase inversion from isotropic matrix to anisotropic matrix was also observed to occur at a concentration higher than the concentration at peak viscosity



a. Viscosity and phase transformations of PHIC (M_w = 70,000) in toluene, as a function of concentration.



b. Limiting Viscosity values vs. concentration for PBLG solutions.

Figure II.2. Viscosity versus concentration.

with no irregularity. Aharoni also suggested that the exact location of the concentration at the peak viscosity depends on the solvent and solute viscosity and on the volume fraction at the concentration. In another paper, Aharoni (8) reported that the concentration of onset of anisotropy and attainment of full anisotropy were dependent on the magnitude and the sign of polymer-solvent interaction parameter; the smaller the interaction parameter, the lower the values of these concentrations.

Recently, in the viscosity-concentration study for cellulose derivative (CDA), Dayan et al. (51) reported that the critical concentration (C) is correspondent to the appearance of an anisotropic phase.They explained the discrepancy with the Aharoni's result to be due to the fact that the mesomorpic solution obtained with this cellulose derivative was not nematic as shown in Aharoni's result but cholesteric. However, the biphasic regime was not reported to be seen in their system.

For the theoretical treatment of appearance of the shoulder in the viscosity-concentration curve, Matheson (110) published a good explanation of this presence and related this shoulder to the onset of anisotropic phase. However, his theory was thought to be limited to the monodisperse systems only, because the biphasic interval was assumed to contain two phases with the same viscosity.

Aharoni also has made a more detailed attempt to describe the entire course of the viscose-concentration curve. However, he did not have available to him a theory for the rheology of the anisotropic phase. As an extension of Doi-Edwards rigid rod solution theory, Doi (56) suggested that with increasing concentration, the order parameter (S) would continue to increase and the viscosity decreases accordingly. Doi noted that his theory, however, applies separately to the isotropic and anisotropic phases but not the biphasic region.

For the thermotropic LCP's, there are similar phenomena to the viscosity- concentration relation of lyotropic polymers. Jackson and Kuhfuss (88) found that on first incorporation of p-hydroxybenzoic acid (HBA) into PET the melt viscosity increases because of partial replacement of flexible ethylene glycol linkage by the rigid HBA unit, and then it decreases as the anisotropic phase appears.

Measurements of the normal stress differences at different concentration have been reported to show similar tendency to those of viscosities. After Baird (23) found that normal stress coefficient increases with increasing concentration and then goes through a maximum similar to the behavior of the viscosity, Kiss and Porter (99) made a plot of normal stress difference (N) versus

concentration for PBLG/m-cresol system at low shear rate and at high shear rate so that it located in the positive region of N for all concentrations. It is striking that this curve not only is similar to that of viscosity vs concentration, but also shows the concentration (C) at maximum normal stress identical to the concentration (C) at maximum viscosity. They also observed the same trends in the plot of the limiting dynamic viscosity vs. concentration at low frequency using two different experiments (OSC and ERD). Even though they did not obtain the same value for each experimental method, the concentration (C) at maximum dynamic limit viscosity was reported to be the same for different methods, and to steady shear viscosity result, as illustrated in Figure II-2b. However, for the PCBZL, the agreement in the values of C given by different techniques was observed to be fair but not as good as in the case of PBLG solution. The relation between G' and C was also found to be almost similar to that between η and C. They obtained good quantitative agreement between oscillatory G' and ERD G' at most concentration. Values of concentrations (C) at maximum G' for two different experimental methods were observed to agree well with each other and with C in ERD method.

General aspects of flow behavior for LCP. For the general flow behavior of liquid crystals, Asada and

Onogi (129) reported that the dependence of the viscosity on the shear rate for typical liquid crystal seemed to be represented by a curve schematically shown in the Figure II-3, where the entire behavior was divided into three regions according to shear rate. After they proposed three region flow behavior, Wissbrun (196) collected lots of viscosity-shear rate data to review the flow behavior. It was not found to be difficult to discern all three regions, even though some thermotropic liquid crystal did not show Region I or III. He thought that both Region I and III would be revealed if measurements are carried out in a wider region of shear rate.

Investigations of rheological properties of polymeric liquid crystals have been concerned mostly with concentrated solutions above a certain critical concentration (C), which is classified as lyotropic, of rigid or semi-rigid molecules, rod-like helical molecules, and cellulose derivatives. For the helical polypeptides (PBLZ, PCBZL), Kiss and Porter observed a well-defined low shear Newtonian plateau with ending of shear thinning in all case. For some cases they also found a second Newtonian plateau. Even though they did not eliminate the doubt of error, above a certain intersect point in-plot, all curves were observed to align in order of concentration. From these observation Kiss and Porter suggested that at high shear

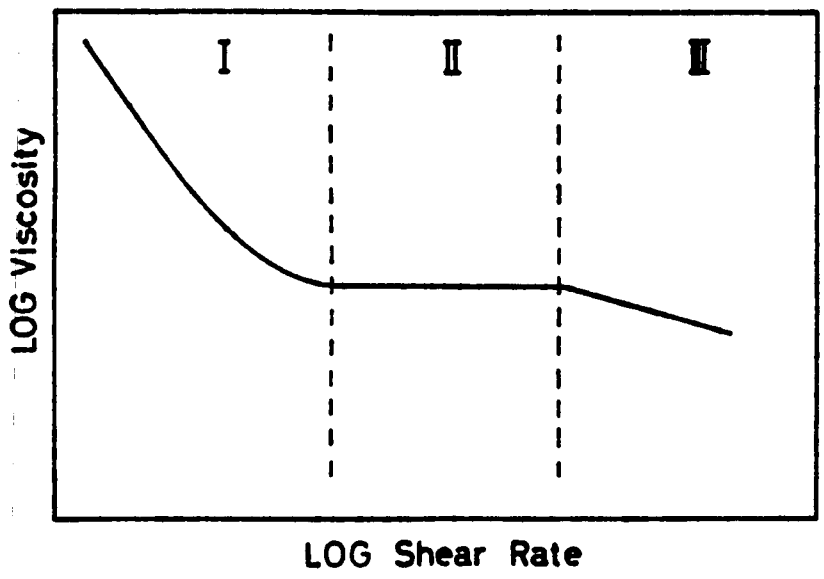


Figure II.3. Three regions of flow behavior for liquid crystals.

rate the shear-induced orientation dominated that induced by volume filling requirements. They also found abrupt onset of a negative normal stress in higher concentration than critical concentration (C). However, as noted by Wissbrun in his review paper (196), the agreement of the rheological experimental results for this lyotropic polymer has not been concluded among several investigators.

For polyamides, these ambiguous situations also show up. Baird's (23) findings for PPTA are that shear thinning begins several decades of shear rate lower for anisotropic solution than for an isotropic one of the same viscosity. In his researches, he also found that the normal stress difference is dependent on the shear rate. He (196) also reported that at low shear rate small changes in Mw give large changes in the normal stress coefficient, and the normal stress coefficient was observed to be Mw dependent.

For the wholly aromatic polyamides such as poly (3,8- phenanthridinonediyl terephthalamide) (DAP-T), Kaneda's (94) finding is that the viscosity for extrusion from the spinneret to be dependent on the dimension of hole: with a finer nozzle the viscosity is reduced. They also observed that cold-drawing did not make any difference for the mechanical properties of the spun DAP-T. On the other hand, the annealing was observed to increase these properties. They also found the higher straightened

molecules from the beginning of the spinning with x-ray pattern.

For the solutions of cellulose derivatives, Navard and Haudin (125) obtained the anisotropic-isotropic phase transition critical temperature for the cellulose-NMMO (N-methyl morpoline N-oxide) solution using the plot of ln η vs. 1/T, which should be a straight line within the same phase. This critical temperature was confirmed by means of the optical microscope under cross polarizers. They also assured the common fact that the difference of viscosities between two phases decrease with increasing of shear rate. It was proved that the transition occurred in a very short temperature range, and they also found that below the transition temperature the extrudate swell rate was lower than 1.2.

Using absorption spectrum experiments for hydroxy propyl cellulose (HPC) in water, Onogi et al. (128) found that the walls influenced the orientation of the layers for the HPC solutions and also found that in the thicker cell, the structure near the walls is highly oriented. By comparison of the build-up and decay of the birefringence and stress for the isotropic and anisotropic single phase of HPC/H_2O solution, they observed that the one-phase solution in quiescent state consists of cholesteric liquid crystalline structure existing in domains with oriented

structures at solid boundaries. In flow,this cholesteric structure was found to be transformed to an oriented nematic structure. At the same time, domain boundaries disappeared. However their observations in elongational flow are that there are no domain structures and much higher orientation are obtained than shear flow when comparisons are made at either the same deformation rate or difference in principal stresses. Therefore, they asserted quantitatively that the elongational flow is about three times more effective at the same deformation rate.

In another intensive rheological study for cellulose derivatives, Dayan et al. (51) found that at low concentration of HPC/H_2O and CA/TFA solutions,the slopes in the plot of shear stress and shear rate is approximately 1.0 (newtonian plateau) and then decreased linearily with concentration, until the value of slope decreases drastically at the critical concentration (C). A further increase of the polymer concentration was found to cause an increase of the value of slope. Therefore, they suggested that the power law can be used to demonstrate the appearance of the anisotropic phase. They also found that the variation of the values of the slopes with concentration was greater in high molecular weight samples.

In the comparative rheological studies for the melt of cellulose derivatives including EC, CAB and HPC, whose solution is known to show the liquid crystalline phase, Suto et al. (177) found that HPC and EC are thermotropic liquid crystals, while CAB behaves in a manner similar to a varifying isotropic melt such as PS using various characterizing methods. They also observed two different swell phenomena for CAB and HPC or EC; for CAB extrudate swell ratio increases from 1.1 with increasing shear stress whereas those values for EC or HPC were less than 1.1 regardless of values of shear stresses. They suggested the low die swell ratio for the latter to be related to the slow decay of birefringence, and the fact that the orientation developed in the flow does not recover in the emerging extrudate.

For the thermotropic polymers, there have been a lot of extensive investigations for the copolyester of p-phydoxybenzoic acid and polyester (HBA/PET). Wissbrun (198) observed that melt rheology of HBA/PET system is quantitatively indistinguishable from that of isotropic polymer at high temperature. However, he measured dynamic properties from which a relaxation time was found to be much higher than that of PET. Jerman and Baird (93) found that shear viscosity for this copolyester is dependent on shear rate and lower than that of homopolymer. The low viscosity was thought to be due to the domains

of rod-like molecules where all molecules have a common orientation, even though they did not associate this phenomenon with the structural change.

For the extrudate swell of this copolyester, Jerman and Baird (93) observed two significant features that even when the extrudate contracts, die swell ratio increases with decreasing capillary length, and the die swell ratio is less than 1.0. The extrudate swell ratio was found to decrease with the increasing of apparent shear strain rate. They also observed this ratio to be extremely temperature dependent; with increasing temperature, it increases. It was suggested that the lack of die swell could be attributed to the presence of yield stress, which inhibits elastic recovery of the extrudate, even though they did not make sure whether there was a yield stress. For another possible reason for the lack of extrudate swell ratio was thought to be due to the negative values of the normal stress differences.

In the recent paper published by Wissbrun and Griffin (197), the rheological features of thermotropic aliphatic aromatic polyester in the nematic phase were compared with those in isotropic phase. Their results indicate that the general features of the nematic phase are much more complicated, showing that the complex viscosity is strongly shear thinning, the storage modulus

(G') is concave and upward, and compliance (J') and relaxation time (t) is larger. They also found the oscillatory flow behavior of the nematic phase to be dependent on the shear history.

Structure of liquid crystalline flow. Obviously, the rheology of the liquid crystalline polymer melts or solutions is quite complicated. Since several investigators implicated the presence of a certain kind of structure in these systems through lots of anormalous experimental findings, it has been known that rheological studies alone cannot tell the full story of deformation mechanism of polymer liquid crystalline system, because the systems usually form complicate superstructure or texture. Rheological properties generally depend strongly on the bulk structure or the texture of a specimen. For instance, the yielding phenomena for liquid crystalline polymers were known to be due to the existence of a bulk structure in the specimen being tested. The bulk structure may be deformed during test, and this change may occur over a time scale long compared to that of the test, giving rise to deformation history effect. Thus, the texture of bulk structure is a determining factor for the rheological properties of liquid crystals. Disregard of the texture often seems to cause misunderstanding or disagreement among investigators. This is the reason why some investigators have been

utilized rheo-optical techniques for studying liquid crystalline system (128,129,177). However the textures or the bulk structures of single phase of polymer liquid crystalline solution in general were known to be difficult to characterize in a simple manner.

In one of the most noticiable review articles on the rheology of the liquid crystalline polymer, Wissbrun (196) already has reviewed the three types of distinct mechanisms proposed for the shear thinning region at low shear rate (Region I in Onogi and Asada's nomenclature), which is thought to be responsible for anormalies such as negative normal stress, yielding phenomena, and history dependence. One of these three distinct mechanisms is plastic flow of piled domains. The basis for this proposed mechanism is supported by rheo-optic experiments (128,129). The rheo-optic observations carried out by Onogi and Asada (129) are primarily measurements of the variation with shear rate of light transmitted between cross polars with the polarization direction parallel to or at 45° to the flow direction. From the results of this experiment, the structure of a liquid crystal in the quiescent state was described as a piled polydomain structure resembling to a polycrystalline texture of crystalline polymer as illustrated in Figure II-4.

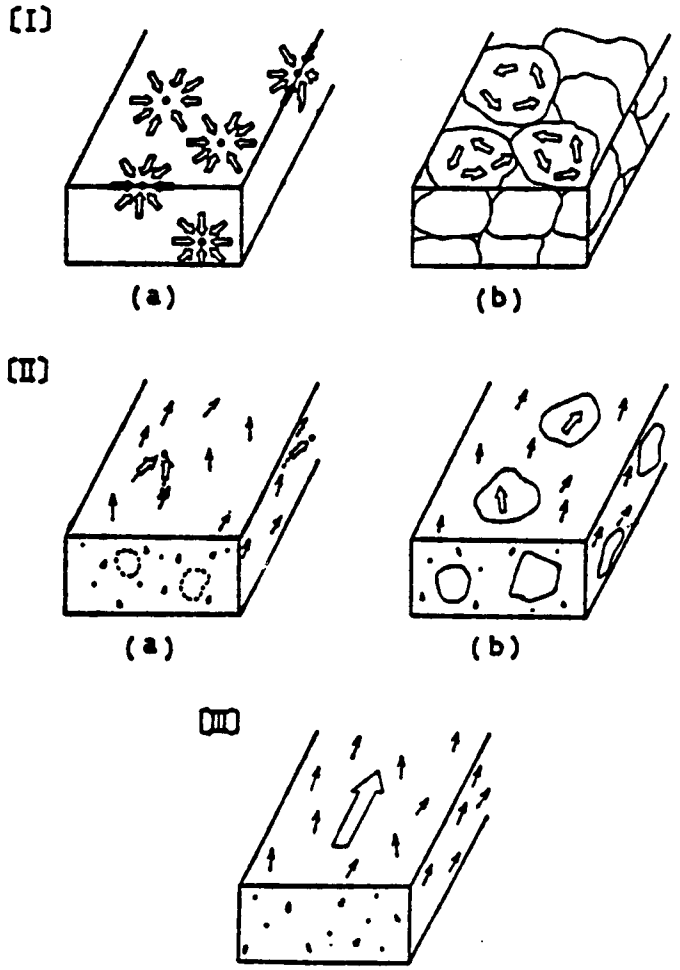


Figure II.4. A schematic representation of the bulk structure of polymer liquid crystals (I) polydomain system, (II) degraded polydomain system; where continuous phase exists predominately, and (III) monodomain continuous phase.

The nature of such a bulk structure which depends mostly on the preparation procedure, is thought to be responsible for the rheological properties of this material at low shear rate flow region. This bulk structure of liquid crystals in the quiescent state is considered to form under the influence of a wall effect. Such bulk texture, however, is thought to be apt to be broken mostly in the Region I. On the other hand, the monodomain continuous phase structure is attained only at very high shear rates belonging in Region III. The flow properties of the Region III are said to be least dependent on the sample history.

B. Survey of Processing

Many of the polymer liquid crystals reviewed in the earlier section of this chapter are lyotropic in character. To convert such materials to fibers or films, one has to resort to either dry spinning or wet spinning. However many of the liquid crystal forming polymers dissolve only in certain solvents which have high boiling points, thus leaving wet spinning as the only viable method. The wet spinning process consists of extruding the polymer solution into a liquid bath containing low molecular weight liquid miscible with solvent, but not dissolving the polymer.

Synthetic Fibers

Polypeptides. Ballard, Griffiths, and Walson (24) at Courtaulds first developed a method for producing artifical fibers from liquid crystal polymers. The polypeptides such as poly (γ-methyl-L-glutamate) and poly (γ-methyl-D-glutamate) were used. These polypeptides were in the form of an α helix and formed a cholesteric mesophase. Upon wet spinning, a fiber in the α crystalline form was obtained. After a subsequent drawing of these resulted fibers, the α configuration form converted to the fully extended chain or β configuration form (25). A fifteen fold improvement of maximum spinning speed in the case of anisotropic solutions over isotropic solutions has been reported. However, no improvement in the mechanical properties was observed.

Aromatic polyamides. The spinning studies of aromatic polyamides fibers can be found as early as 1961 (81), one of the earliest patents describing a wet spinning process involving aromatic polyamides in King's patent (97). One of the polymers he used was poly (m-phenylene isophthalamide) or MPD-T. He spun the fiber from a 18 percent solution of MPD-T, dimethylacetamide (DMA) and calcium chloride. Various amounts of calcium thiocyanate in DMA was used to coagulate. Following coagulation, the fiber was drawn over a hot plate (300 1/4C) for further crystallization. Fiber

mechanical properties of 150-180 grams per denier (gpd) for the modulus, ≃ 10gpd tensile strength and 10- 13 percent elongation to break were obtained.

A dry jet process was described by Morgan of Monsanto (122). In this fabrication process the extruded fiber is spun through a gaseous medium 1/8- 1¼ inches into a coagulation bath. Polymers such as poly (m-phenylene-isophthalamide) and poly (4 - 4 - diamin benzanilide terepthalamide) were used in this process. Dimethyl formamide and dimethyl acetamide containing ≃ 10 percent metal salts were used as solvents. Following the coagulation in dialkyamide and H_2O an orientation step was set in which the fiber was relaxed or stretched in a hot water bath.

The wet spinning studies of anisotropic aromatic polyamide dopes was initiated by Kwolek (102). A solution of PPTA/H_2SO_4 is spun through a thick percious metal die into an aqueous coagulation bath near 40°C. The coagulant was water, methanol, and ethylene glycol. Following the coagulation, the fibers were taken up around rollers on a bobbin and washed with cool water. Annealing of fibers was done at different temperatures. She reported (102) that fibers fabricated from such process exhibited greatly enhanced mechanical properties.

Dry jet spinning as shown by Blades (32) leads to greatly enhanced mechanical properties similar to

Kwolek's except a jet-dry spinning induced higher level of orientation. The total process consisted of dry jet spinning, washing of the coagulated fibers, followed by heat treatment under tension at 525°C. The filamets however exhibit little drawing under these conditions. The heat treatment improves the tensile strength to a great extent as high as 32 gpd, modulus as high as 950 gpd, and elongation to break of about 3 percent. This leads one to believe this to be a process where orientation occurs during spinning and is greatly improved by annealing without drawing.

No significant modification of the solution spinning method has been reported since then.Of considerable importance, however, is the fact that papers on poly (p-benzamide) (PBA), PPTA and poly (chloro-p-phenylene terephthalamide) (Cl-PPTA) have been published by Morgan and co-workers(9,15,19,103,122,133) and Ciferri et al. (46). Kwolek (103) showed that relatively small changes in PBA dope solids can greatly increase the anisotropic phase in the spin dope and produce a dramatic reduction in solution viscosity of the dope, but a dramatic increase in tensile strength and modulus of fibers. Ciferri et al. (46) showed that except at very small draw ratios, the modulus of the as-spun fiber by wet spinning from the anisotropic

PBA/dimethyl acetamide -LiCl solution is almost constant as the draw ratio is increased and the air gap in the so called dry-jet wet spinning appeared to play a minor role in the modulus of the as-spun fiber. However, there is the effects of draw ratio on the modulus of as-spun fiber as shown by Kwolek (103) where an anisotropic PBA/ tetramethylurea -LiCl solution is dry spun under different take-up velocities. The importance of postspinning heat treatment was also shown by these authors.

Except in the above solution systems, other solutions in which anisotropic solution can be formed, which are useful for dry and wet spinning, include strong acids. That the anhydrous HF solvent can form high weight percent polymer anisotropic solutions (20 percent) at very low bulk viscosity for PBA and PPTA was also shown. Wet spinning of such anisotropic solutions can also give HM/HS fibers.

Totally aromatic rigid rod polymers which consist of aromatic and hetrocyclic units have also been reported (199). Spinning was performed using 5 - 10 percent of these polymers in methanesulfuric, chlorosulfonic or polyphosphoric acids. These polymers such as poly (p-phenylene-benzobisthiazole) can reach a modulus as high as 250 Gpa.

In view of poor solubities and high melting temperature of rigid polymers, solution spinning of

polyterephthalamide of p-aminobenzylhydrazide (X-500), which is semirigid compared to the above p-linked polyamides, has been reported (46). Solutions of X-500 in dimethylsulfoxide (DMS) do not form anisotropic solution. However, some evidence indicates that the rigidity of X-500 in DMSO is close to the value at which a nematic phase can spontaneously occur (46). Ciferri et al. (46) reported wet spinning of X-500 in DMSO using water at 18°C as a coagulating agent. About 5-10 cm^3 solution is extruded from a cylinder-piston unit to a spinneret die of 0.1 mm diameter through an adjustable length of tubing. The filament is collected at the end of the coagulating bath (90cm long) by a set of rollers, continues into a washing bath (90 cm long) and a second set of rollers and, after about 1m in air, is wounded by a bobbin. Their as-spun fiber is then passed a thermomechanical treatment at different temperatures, ranging from 200° to 400°C, and different draw ratios. It was shown that a high elastic modulus (about 15 Gpa) has already occurred during coagulation at very low draw ratios, and there is the effect of air gap or draw ratio on the modulus of the as-spun fiber. The postspinning heat treatment can increase the modulus value to about 67 Gpa.

Cellulose derivatives. The Panar and Willcox patent (132) discloses the fiber and film formation from a

variety of cellulose derivatives in different solvents, most of them wet spun. Typically better mechanical properties are obtained from the fibers spun from anisotropic dopes. For some cellulose derivatives such as ethyl-cellulose, dry spinning is preferred over wet spinning for obtaining high strength fibers. Generally, coagulation bath temperatures of 0 to 5°C are preferred.

Cellulose triacetate fibers of tensile strength of more than 7 grams per denier were obtained (132). After thermal treatment at 240°C for two minutes and subsequent hydrolysis the tensile strength greatly increased to 11 grams per denier. Another important development is the solution spinning of cellulose in aqueous solutions of a cyclic amine oxide, such as N-methylmorpholine N-oxide to yield fibers with strength of the order of 1 Gpa (132). This system was reported later by Chanzy and Peguy (43) to form a cholesteric lyotropic mesophase. Solution birefringence occurred in the concentration range of 20-55 percent and depended on the temperature of the solution, the water content of the solvent system, and the molecular weight of cellulose. They also showed that this anisotropic cellulose solution could be readily oriented during extrusion or casting to give fibers or films which upon coagulation in water or methanol exhibit high orientation.

It was noted that the highly anisotropic phases of

solutions of cellulose and its deriveratives all have a cholesteric structure. To date no details except the work done by White and co-workers (127,128,129) about processibilities and methods to convert the cholesteric mesophase to nematic structure can be found in the open literautre. The development of high level of birefringence and orientation during the flow of solutions of hydroxylpropylcellulose (HPC) and cellulose acetate butyrate were done by Onogi et al. (127,128) and Bheda et al. (29) respectively. As shown by Onogi et al., the isotropic solution of HPC showed a steady state birefringence in seconds after applying a steady shear and the birefringence decayed to zero in seconds after cessation of steady flow. However, for anisotropic solutions, it took some minutes to achieve a steady state birefringence and about 15 percent of the birefringence still remains after 30 minutes following cessation of flow. They concluded that the cholesteric structure is transferred to a nematic structure during flow, and decreasing of birefringence after cessation of flow is due to recovery of the cholesteric structure. They also performed gravity spinning in which HPC solutions were extruded from a die by using a Harvard infusion/withdraw pump. On line measurement of diameter profile and birefringence showed that for an isotropic solution (30 percent), the spinning solution continues to deform along the length of spinline

and birefringence rises to a steady state value within 75 cm from the die exit. But for the anisotropic solution spinning, all changes in diameter and birefringence occurred within several centimeter from the die, the velocity gradients abruptly go to zero within 5 cm from the die. They indicated that elongational flow is several times more effective at the same deformation rate to orient the anisotropic HPC fibers but the long relaxation time of anisotropic solution should also be considered.

Recently, Bheda et al. (29) extensively studied fiber formation and characterization of liquid crystalline cellulose derivatives. Fibers were made from solutions via dry jet wet spinning process. In the dry jet wet spinning of CAB in DMA the concentration of 35 percent, 40 percent, 45 percent, and 50 percent was made where 35 percent solutions were isotropic and 45 percent, 50 percent solutions were completely anisotropic, the 40 percent solution was biphasic. Fibers were also spun from solutions of CT in trifluoracetic acid of concentration 25 percent and 30 percent. The 25 percent solution was isotropic and the 30 percent solution was anisotropic. They reported there is a marked difference in the spinnability of isotropic and anisotropic solutions (29). The isotropic solutions for both polymers (CAB and CT) were extremely difficult to spin where the isotropic filaments failed at very low

take-up speeds. The other solutions (anisotropic) were spun to the maximum take-up speeds the spin line could support.

Shimamura et al. (162) carried out studies of structure development and characterization of liquid crystalline cellulose derivatives in continuous extrusion and melt spinning. They reported that extruded filaments have skin-care structures with highly oriented outer layers. This was believed to be due to the orientation achieved during flow in the die and reservoir.

Polysters. Aromatic polyesters which form mesophases were first melt spun into fibers by Tennessee Eastman (106,113) and DuPont investigators (100,159). The basic structure of these polyesters are benzene rings attached at para positions through ester groups. Standard poly (ethylene terephthalade) (PET) melt spinning technology appears to have been used. The history of the preparation of thermotropic liquid crystal polyesters was shown by Jackson and his co-workers (90,200). It was indicated by Jackson (89) that the high melting points of this basic structure can be reduced to a melt processable range by introduction of flexible aliphatic units in the polymer chain, by modification of the rigid rod structures with substitutes on the aromatic rings or with certain other rod-like modifying components, and by

introducing links into the polymer chain.For example, poly (ethylene terephthalate-co-p-benzoate) (PET/PHB) was found to behave as nematic melt at 275°C as the PHB concentration is above 30 mol percent. These liquid crystalline copolyesters are characterized by long relaxation times so that the polymer chain retain its orientation during processing to yield HM/HS fibers or molding products.

Recently, there have been some reports on the studies of melt spinning conditions to form the HM/HS fibers. Acierno et al (1) studied the influence of draw ratio and operation conditons on the elastic modulus of two samples to PET/PHB 30 mol percent and 60 mol percent p-oxybenzoate. These polymer melts were extruded at temperature ranging from 225-285°C into air at room temperature. The filaments were then taken-up at different draw ratios up to 3000 at a distance of about 1.5 m from the extruded die. They found that 70/30 (PET/PHB) is amorphous in the melt state andyields a maximum modulus on the order of 3 Gpa. The melt of 40/60 (PET/PHB) exhibits nematic mesophase at about 265°C. The elastic modulus of this polymer spun at 225°C and 245°C, where some small degree of crystallinity likely persists due to the short sequence of p-hydroxybenzoic acid residues, reaches to about 32 Gpa. However, considerable lower moduli were

observed by spinning this 40/60 system above 260°C is due to the superposition of a small degree of crystallinity to the mesophase. A melt spinning of semi flexible homo-polyester containing both rigid and flexible segments in the repeating unit was also studied (1). These polyesters were spun at temperatures showwhat lower, or higher than those corresponding to the range of stability of the mesophase, or within the range of the stable mesophase. They showed that their semiflexible polymers exhibit poor spinnability at temperatures corresponding to the existance of the single phase and that the mechanical properties of fibers spun from both the nematic and smectic phase of these polymers are poor. It seems from their results that semiflexible chains do not adopt a chain extension conformation in the nematic phase so that there is large variation of the director orientation as compared with that formed from rigid thermotropic polymers.

Zachariades et al. (207,208) studies the 20/80 mole ratio of OET/PHB. They found that this copolyester forms a nematic mesophase at about 295°C, and on further heating, the PHB domains remained clearly discernible. At 328°C, where the PHB domains is fused in the surrounding mesophase, the melt viscosity decreased noticably. Melt spinning was performed in the temperature range from 295°C to 340°C. They found that because of PHB domains in the melt, which remain undeformed as temperature is

lower than 328°C, the oriented morphologies exhibit lower mechanical properties.

Ide and Ophir (86) studied the orientation development during melt spinning of a thermotropic polymer produced by melt polymerization of p-acetoxybenzoic acid (60 mole percent), 2,6-naphthalene diacetate (20 mole percent) and terephthalic acid (20 mole percent). This polymer was extruded at 340°C through a capillary rheometer at widely different shear rates. A skin-core morphology was found for the gravity spinning extrudate. The extrudate rearranges to a flat velocity profile so that the fluid element near the surface must be stretched and those near the center must be compressed. This elongational strain mechanism together with the yield stress behavior and large shear strain in the entrance region as shown by Shimamura et al. (162) play an important rule in the formation of skin-core structure. In their melt spinning studies, they found that the orientation of the filament as indicated by the changes of modulus is not a direct function of elongational stress.

Formation of Tubular Film

A tubular film process is a procedure by which thin thermoplastic films are produced. Typically, polymer melt is extruded through an annular die, where air is blown into

the tube through the die with pressure slightly higher than the ambient to provide a moving bubble of melt. The molten polymer tube exiting from the die is drawn upward by a take-up device. Usually an air cooling ring is installed around the bubble. It cools the hot bubble rapidly and solidifies the film at a certain distance from the die exit. This cooling ring also helps to shape and stabilize the expanded bubble. In a tubular blown-film process, dies are varied by designs for pressure drops through the die. The pressure drop can be described as the pressure at which the die system operates as indicated by pressure gage on the adapter. The die output must be balanced. The ratio of the final bubble diameter to the die diameter is called the blow-up ratio (B). The most common blow-up ratio for commercial films seems to be in the range of $1 < B < 3$.

In early patents (160) methods of film blowing were described in which a screw extruder is used to extrude the molten polymer upward through an annular die into take-up device. In the same year another patent (184) was issued involving tubular film processing where the film was extruded downward with air being applied from below the film and not through the die.

Cheney and Hughes (44) were issued a patent describing a tubular blown film process in which air pressure is applied through a so called "centrally located distributor".

This was done to improve temperature control while it still induced orientation into the blown film.

The dynamics of the tubular film process due to the expansion of the bubble have been paid great attention by various investigators (10,72,117,138). In 1965, Alfrey (10) developed force balance equations using the theory of mechanical equilibrium of shells of rotation symmetry. Further development of the dynamics of this process were made by Pearson and Petrile (138), Han (72), Han et al. (72), and Middleman (117).

Pearson et al. (138) and Han (72) have made kinematic studies of blown films as well as dynamic investigations. Basic experimental studies of kinematics are reported by Ast (17), Farber and Dealy (62), and Han and Park (72). Farber and Dealy (62) used motion picture techniques to follow the deformation history. Han and Park studied the effects of variation of the air pressure within the bubble of biaxial extension.

Mandrel Process

A mandrel process can be used to produce biaxially oriented films. A tubular film is extruded through an annular die over a mandrel expanding the film to a desirable radius. The film is cooled as it passes over the mandrel while it is being drawn and then solidified.

In the early sixties Richie and Scalora (153) described a mandrel process. They introduced a spreader in order to facilitate take up of the film. A circular shape of film bubble was changed to elliptical by a spreader prior to film take up. Recently a similar mandrel process was developed by Gerow (65). He found that bubble instability occurs when the mandrel distances are greater than half the mandrel diameter with blow-up ratios in excess of 3:1. Other variable such as mandrel shapes, mandrel temperatures, extrution rates, and take-up speeds have been considered. He reported that the optimum mandrel distance should be half the mandrel diameter with blow-up ratios ranging from 2.5 to 1. In the case of polyethylene he noted that optimum mandrel temperatures were found to be in the range of 150° to 200°C. These temperatures provided higher film modulus and prevented stickage of the film to the mandrel surface. Lower extrusion rates were also found to give better film properties.

Fallwell (61) and Cichelli (45) carried out mandrel process experiments. Cichelli's experiment involved a mandrel with a gradual increase of radius and air as a lubricant. Fallwell's experiment was some-what similar to that of Cichelli.

More recently Flood, White and Fellers (63) described a new mandrel process for making equal biaxially oriented

films from liquid crystalline solutions of poly (p-phenylene terephthalamide) (PPTA). In this process the film is extruded through an annular die over an oil-coated mandrel, drawn in the coagulation bath and finally taken-up at the other end of the bath. The purpose of the oil is to reduce friction and induce biaxial elongational flow in the solution.

They produced a variety of films ranging from uniaxially to biaxially oriented. The uniaxial films are highly anisotropic with tensile strength of order 1.2 x 10^8 Pa in the machine direction and 7.5 x 10^6 Pa in transverse direction. Uniaxially drawn films which were coagulated in water has tensile strengths in the machine direction as high as 2.8 x 10^8 Pa. The elongation to break for these films was in the range of 3 -12 percent.

The biaxial films produced using a mandrel have shown more balanced mechanical behavior. Tensile strength in both machine and transverse directions of 5.2 x 10^7 Pa were observed. The elongation to break were in the range of 7 -11 percent in the machine direction and 4 -8 percent in the transverse direction. It is important to note that none of the films in their studies were heat treated as the case of Kevlar fibers discussed earlier. More detailed information on apparatus including process analysis is also given by Flood et al. (63) elsewhere.

Since the extrusion of a tubular film over a mandrel involves drawing, which induces orientation in the machine and radial direction, studies of kinematics and dynamics of this process is of considerable interest. Wessling and Alfrey (191) and Wessling (192) carried out studies on biaxial stretching of elastic and viscous tubes using a rotational symmetric mandrel. Similar studies have been reported by Gutteridge (69), where elastic and visco-elastic models were considered in the stretching of films over a conical mandrel.

In Wessling's and Alfrey's studies, a thin walled tube of vulcanized rubber was drawn slowly over a conical mandrel for the elastic case. The material properties equation and equilibrium equations were combined to obtain the elastic model. A variety of conditons for stretching of tubes over conical mandrels were investigated. However, they noted there is no operating conditions which will produce uniform biaxial stretching in the elastic case. For the viscous case, they found a wide range of biaxial stretching patterns dependent on viscosity, friction and velocity ratio.

In Gutteridge's studies of film-stretching using both an elastic and visco-elastic rheological model, the constitutive equation was combined with the equations of equilibrium in order to define the elastic and visco-elastic models. Gutteridge (69) found that under isothermal

and limited stretching conditions, a high degree of equal biaxial extension can be obtained. By using a visco-elastic material at a low temperature and applying a linearly decreasing temperature profile, an elastic material can produce equal biaxial extension over a variety of stretching conditions.

Formation of Film from Solution

Most of the work cited earlier on liquid crystalline polymers such as polyamides and cellulose derivaties have dealt with fibers. In 1915, a patent issued to Cohoe (48) described the extrusion of a cellulose solution through an annular die and coagulating it to produce sausage casing. Bradenbergers (37) was issued two patents involving the manufacture of viscose cellulose films by extrusion of the solution through a slit shape die. Panar and Willcox (132) in their patent applications made passing reference to film but only described fiber formation from liquid crystalline solutions of cellulose derivatives.

Some of the early patents of DuPont (178) are involved with producing films via casting the solutions and separation of films from the solvents. Hill and Kwolek (81) used such a process whereby film was made from 15 percent solutions of poly (m-phenylene isophthalamide), MPD-I, dissolved in dimethyl formamaide and lithium chloride. Mechanical properties of the films were found

to be as follow; tensile strength of 1.2×10^4 psi, modulus of 5×10^5 psi, and elongation to break, 3-5 percent. These properties were obtained for samples prepared at 20°C. For hot rolled films the machine direction properties were higher. Modulus of 9×10^5 psi, tensile strength of 3×10^4 psi, and a 10 percent elongation were observed. Film casting from solutions of poly (m-phenylene isophthalamide) dissolved in dimethylacetamide and lithim chloride also were reported by Sweeny (178).

Tubular film formation from aromatic polyamides has been described in a Japanese patent (119). A dry-jet wet spinning method was used followed by a coagulant to solidify the film. Film blow up ratios were claimed to be three times the original diameter. The coagulant was water at room temperature. PPTA films of high strength of order of 4×10^4 psi tensile strength in both MD and TD were claimed to be obtained. Unblown PPTA film was found to be weak and brittle.

Recently at The University of Tennessee, Aoki et al. (12) investigated the characterization and continuous isotropic and anisotropic PPTA/H_2SO_4 solutions to form ribbons and blown films. Ribbons were made using a slit die and blown films were prepared using an apparatus shown in Figure II-5. The main objective of this apparatus was to radially expand the extrudate through the dies

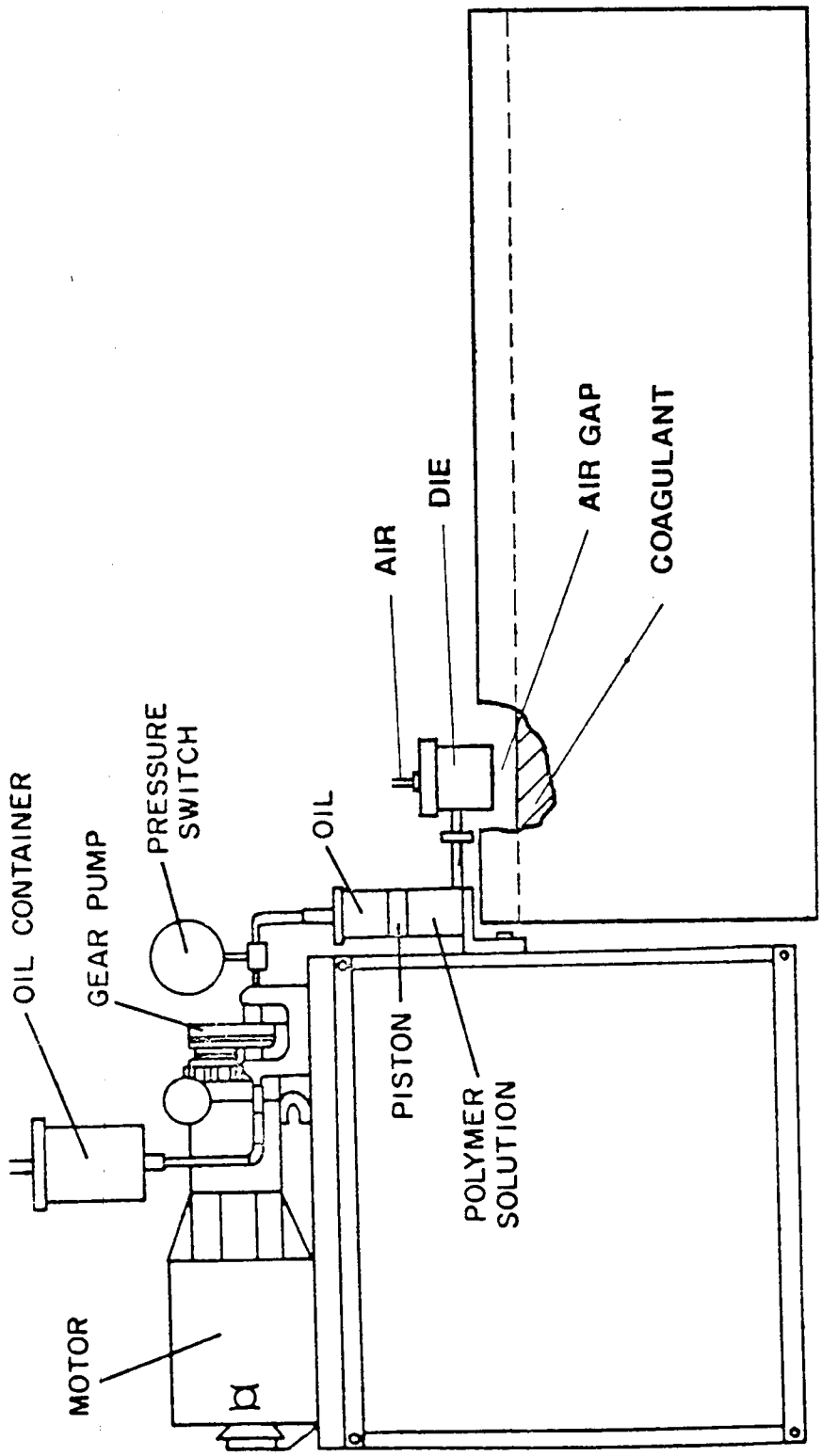


Figure II.5. The tubular film blowing process developed by Aoki et al. (13).

annular gap with pressurized nitrogen gas introduced from the outlet of the die. Thus the emerging tube may be continuously drawn biaxially via radial expansion and simultaneous winding tension. However the blown films demonstrated preferential orientation in the machine and transverse directions.

C. Birefringence and Orientation

Macromolecules tend to orient upon application of a stress field. They are anisotropic i.e., the properties they possess along the chain axis are different from those perpendicular to it. Advantage is taken of one such property, refractive index to quantify the orientation of the macromolecules. The difference of principal refractive indices is called the birefringence and can be fairly easily determined experimentally.

Flow Birefringence

The development of molecular orientation during flow has been studied for over a century (38,48,112). Most studies were confined to dilute solutions involving biological and rigid macromolecules, and to limited extent flexible hydrocarbon polymers. Early experiments of Brewster (38) showed that application of stresses produced birefringence. Other investigators (108,112,143) later showed that the development of birefringence is

governed by the stress-optical or "rheo-optical law" which relates the birefringence to the difference in principle stresses existing during the flow.

$$\Delta n_{ij} = n_i - n_j = C(\sigma_i - \sigma_j) \qquad (1)$$

Where Δn is birefringence, n is the refractive index. Tensor σ_i and σ_j are the principal stresses along the i and j directions respectively.

Kuhn and Grun (209) first investigated the optical properties of statistically linked long chain molecules composed of optically anisotropic links. They noted that a stretched network of flexible chains could be characterized by two principal refractive indices corresponding to the directions of polarization respectively, // and $\perp$ to the extension direction. Treloar (185) in studies of vulcanized rubber reported that the birefringence is a simple function of the principal extension and proportional to the difference between the two corresponding principal stresses.

Lodge (108), Philippoff (142,143) and others (2, 175,185) studied concentrated solutions of flexible chain polymers. Lodge (108) was the first to suggest that the rheo-optical law may be applied to polymer solutions and melts. In the case of shear flow he noted that

$$\Delta n = C(\sigma_{11} - \sigma_{22}) \cos 2x_{opt} = 2C\ \sigma_{12}/\sin 2x_{opt} \qquad (2)$$

Where σ_{12} is the shear stress and x_{opt} is the optical extinction angle which is defined as the angle between the principal axes of the stress tensor and flow direction. Philippoff (142,143) verified the validity of the "Rheo-optical law" on a series of polymer solutions. He described that birefringence can be successfully used to measure normal stresses in shear flow. Matsumoto and Bogue (111) also carried out a detailed experimental verification of the validity of the stress optical relation in polystyrene under non-isothermal conditions.

Oda, et al. (210) reported that it is implicit in the theory of birefringence of flexible polymer chains that the stress optical constant "C" should be proportional to $(\alpha_{//} - \alpha_{\perp}) \times \Delta^{o}$. Thus in unaxial extension

$$f = (C/\Delta^{o})\sigma_{//} \qquad (3)$$

is a good approximation, independent of polymer type, giving $C/\Delta^{o} \simeq 2 \times 10^{4}$ brewsters. They varied this for on-line birefringence measurements on fiber spinlines and vitrified polystyrene fibers.

There have been very few studies on the rheo-optics of polymer liquid crystalline solutions (16,83,165). These studies are involved with the flow birefringence of isotropic and liquid crystalline solutions of aromatic polyamides (83), polypeptides (16) and hydroxpropyl-cellulose (128). These studies are qualitative in nature and limit themselves to shear flow.

Recently, studies on flow birefringence in elongational and shear flow of HPC in H_2O was reported by Onogi, White and Fellers (128). The behavior in the isotropic and anisotropic phases have been found to be significantly different. The elongational rates in the isotropic solutions were found to be constant, whereas in the anisotropic solutions they increased monotonically. A maximum in the birefringence along the spinline has been observed in anisotropic solutions. It is noted that to induce a certain degree of orientation, elongation rates are three times more effective than shear rates.

They reported that the "universal const" noted by Oda et al. (210) for flexible chains (C/Δ^o) were found to be 4×10^5 brewsters for isotropic and 500×10^5 brewsters for anisotropic solutions in shear flow. These values were 60×10^5 and 900×10^5 brewsters respectively in the elongational flow. These high values of C/Δ^o were attributed to the case of orientation of HPC molecules when subjected to flow.

Orientation Representation

Maxwell's displacement vector D is given (130) by

$$D = \varepsilon_o \underset{\sim}{E} + \underset{\sim}{P} \qquad (4)$$

This form of D is useful when we wish to connect the

phenomenalogical with the mechanistic view of D. Here P is called polarization vector and caused by the sum of all the contribution to polarization from all bonds, segments, molecules, etc.

ε_o is dielectric constant of vacuum, and $\underset{\sim}{E}$ is the electric field strength. The electric dipole moment $\underset{\sim}{P}$ established under the influence of the field is as follow

$$\underset{\sim}{P} = \alpha E' \tag{5}$$

in which α is polarizability, and E' is effective electric field. In an anisotropic medium

$$D_k = \sum_j \varepsilon_{kj} E_j \tag{6}$$

$$P_k = \sum_j \alpha_{kj} E'_j \tag{7}$$

Here ε_{kj}, α_{kj} are dielectric and polarizability tensors respectively. For polymers both ε_{kj} and α_{kj} are generally coaxial. In the case of fiber symmetery,

$$d_{kl} = \sum_m \sum_n l_{km} l_{en} d_{mn} \tag{8}$$

Whereas in the chain axis coordinates:

$$d = \begin{Bmatrix} \alpha_1 & 0 & 0 \\ 0 & \alpha_2 & 0 \\ 0 & 0 & \alpha_3 \end{Bmatrix} \tag{9}$$

In which α_1 and α_2 are the polarizability parallel and perpendicular to the polymer chain, l_{km} and l_{en} are the directional cosines. If we take $\alpha_{//}$ and $\alpha_{\perp}$ to be average polarizabilities parallel and perpendicular to fiber axis then,

$$\alpha_{//} = \alpha_1 \text{Cos } \phi_{1,//} + 2\,\alpha_2 \text{Cos } \phi_{2,//} \quad (10)$$

$$\alpha_{\perp} = \alpha_1 \text{Cos } \phi_{1,\perp} = 2\,\alpha_2 \text{Cos } \phi_{2,\perp} \quad (11)$$

Consider the orthogonal axes

$$\text{Cos}^2 \phi_{2,//} = 1/2\ (1-\text{Cos } \phi_{1,//}) \quad (12)$$

$$\text{Cos}^2 \phi_{2,\perp} = 1/2\ (1-\text{Cos } \phi_{1,\perp}) \quad (13)$$

$$\text{Cos}^2 \phi_{1,\perp} = 1/2\ (1-\text{Cos } \phi_{1,//}) \quad (14)$$

then

$$\overline{\alpha_{//} - \alpha_{\perp}} = (\alpha_1 - \alpha_2)\ (\text{Cos}^2 \phi_{1,//} - \text{Cos}^2 \phi_{1,\perp}) \quad (15)$$

$$= (\alpha_1\ \alpha_2)\ \left(\frac{3\ \text{Cos}^2 \phi_{1,//} - 1}{2}\right)$$

which leads to the Hermans orientation function

$$f_H = \frac{\overline{\alpha_{//} - \alpha_{\perp}}}{\alpha_1 - \alpha_2} = 1/2\ (3\ \overline{\text{Cos}^2}\ \phi - 1) \quad (16)$$

Hermans et al (77) have related this to the birefringence in the following manner

$$f_H = 1/2\ (3\ \overline{\text{Cos}^2}\ \phi - 1) = \Delta n\ /\ \Delta^{o} \quad (17)$$

Where Δn is the difference between the principal refractive index parallel ($n_{//}$) and perpendicular ($n_{\perp}$) to the stretch direction or birefringence, ϕ is the angle between the preferred direction and polymer chain axis, and Δ^{o} is the maximum or intrinsic birefringence.

The value of Δ^{o} must be known to use the above equation. The Lorenz-Lorentz equation relate the

refractive index to the polarizability.

$$\frac{n^2-1}{n^2+2} = \frac{4\ \pi NP}{3\ \ M}\ \alpha \qquad (18)$$

In which N is Avagadro's number and M is the molecular weight per structural unit. For small values of $n_{//} - n_{\perp}$, the previous equation after some manipulations reduces to

$$\Delta^{o} = 2\ \pi\ /9\ \frac{NP}{M}\ \left(\frac{n^{-2}+2}{\bar{n}}\right)(\alpha_{//} - \alpha_{\perp}) \qquad (19)$$

$\alpha_{//}$ and $\alpha_{\perp}$ may be evaluated theroetically by considering an extended chain structure and adding the bond polarizabilities, which are second order tensors (68).

For crystalline uniaxially oriented samples Stein (173)generalized the Hermans equation for the three crystallographic axes to specify the degree of orientation with respect to the reference direction. These are called the Hermans-Stein orientation functions given by,

$$f_j = 1/2\ (3\ \overline{\mathrm{Cos}^2}\ \phi_{j,z} - 1) \qquad (20)$$

Where $\overline{\mathrm{Cos}}\ \phi_{j,z}$ is the average value of the cosine squared of the angle between the polymer chain and the j-crystallographic axis (j=a,b,c). The f_j factors are determined from wide angle x-ray diffraction experiments. Hence,

$$\overline{\mathrm{Cos}^2}\phi_{j,z} = \frac{\int_o^{1/2} I_{hkl}(\phi_{j,z})\ \mathrm{Cos}^2\ \phi_{j,z}\ \mathrm{Sin}^2\phi_{j,z}\, d\ \phi_{j,z}}{\int_o^{1/2} I_{hkl}(\phi_{j,z})\ \mathrm{Sin}^2\ \phi_{j,z}\ d\phi_{j,z}} \qquad (21)$$

In which I_{hkl} ($\phi_{j,z}$) is the intensity diffracted from the (hkl) planes which are normal to the j-crystallographic axis. From the above observation the range of the orientation function for the three states of orientation can be seen in Figure II-6.

When the crystallographic axes are orthogonal;

$$\overline{\text{Cos}^2 \phi_{c,z}} + \overline{\text{Cos}^2 \phi_{b,z}} + \overline{\text{Cos}^2 \phi_{a,z}} = 1 \qquad (22)$$

from which it follows that,

$$f_c + f_b + f_a = 0 \qquad (23)$$

The three orientation factors are not independent, only two of them are required to characterize the orientation. The orthogonality relationship in this case demands c,a,b crystal axes are perpendicular.

The amorphous orientation function for semi-crystalline polymers may also be calculated. The total birefringence (Δn) is related to both crystalline and amorphous orientation functions through;

$$\Delta n = X \Delta^{o}_{cry} f_{cry} = (1-X) \Delta^{o}_{am} f_{am} + \Delta n_{form} \qquad (24)$$

in which f_{am} and f_{cry} are Hermans-Stein orientations functions of the amorphous and crystalline phases, X is crystallinity, Δ^{o}_{cry} and Δ^{o}_{am} are intrinsic birefringence of perfectly oriented crystalline and amorphous material respectively.

Stein (173) appears to be the first one to be concerned with biaxial orientation. He defined biaxial

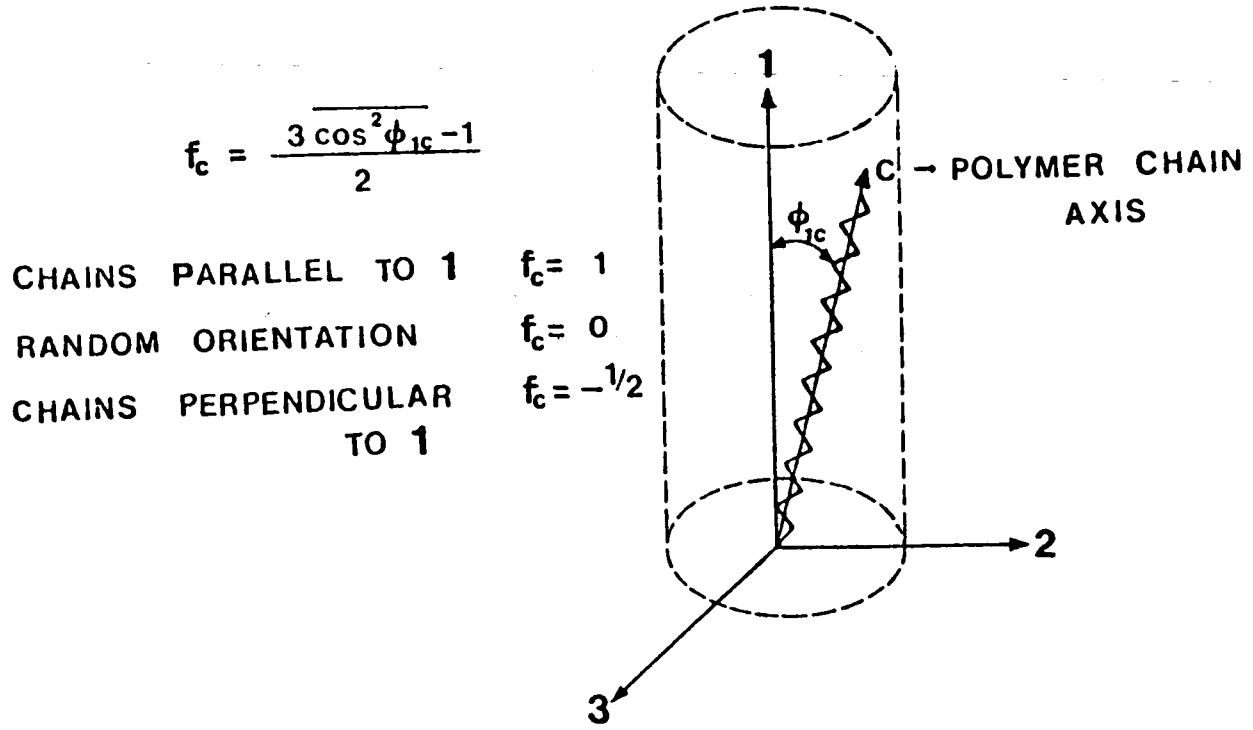


Figure II.6. Uniaxial orientation illustration and a range of values of Hermans-Stein orientation factors.

orientation factors as follow,

$$f_{\alpha,a} = 2\,\overline{\cos^2}\,\alpha_a - 1 \qquad (25)$$

$$f_{\alpha,b} = 2\,\overline{\cos^2}\,\alpha_b - 1 \qquad (26)$$

$$f_{\alpha,c} = 2\,\overline{\cos^2}\,\alpha_c - 1 \qquad (27)$$

from orthogonality

$$f_{\alpha,a}(1-f_{a,z}) + f_{\alpha,b}(1-f_{b,z}) - f_{\alpha,c}(1-f_{c,z}) = 0 \qquad (28)$$

Stein's angle α_j is the eulerian longitude angle between the crystallographic axis and an axis in the plane of the film for each given crystal axis. The range of values of Stein's biaxial orientation function is +1 to -1. If all the axes lie in the plane of the film it gives a value of +1, when axes are random with respect to the plane of the film (uniaxial) the value is 0, and a value of -1 indicates that the axes lie in the plane perpendicular to the plane of the film. Stein also developed a method for determining the birefringence of a biaxially oriented sample with orthorhombic symmetry.

$$\Delta n_{13} = X\left\{\Delta n_{ac} f_a + \frac{f_{2a}(1-f_a)}{3} + \Delta n_{bc}\left[f_b + \frac{f_{2b}(1-f_b)}{3}\right]\right\} \qquad (29)$$

$$\Delta n_{23} = 2/3\ X\left[\Delta n_{ac}(1-f_a) f_{2a} + \Delta n_{bc}(1-f_a) f_{2b}\right] \qquad (30)$$

Where f_a, f_b are uniaxial orientation factors for the a and b crystallographic axes, respectively.

Nomura et al. (126) described two orientation factors in which the first of these is approached as the Hermans-Stein uniaxial orientation function but the second function is defined as follow,

$$f_{22}^{j} = \overline{\text{Sin}^2}\,\phi_{j,z}\;\overline{\text{Cos}^2}\,\beta_{j} \qquad (31)$$

Because of the difficulty of understanding the physical meaning of these orientation factors and the bias toward the machine direction, Wilchinsky (234) suggested that orientation be simply specified in terms of $\overline{\text{Cos}^2}\,\phi_{c,z}$, $\overline{\text{Cos}^2}\,\phi_{c,x}$ and $\overline{\text{Cos}^2}\,\phi_{c,y}$ (three orientation functions).

White and Spruiell (233) developed a method for defining biaxial orientation factors based upon the anisotropy of the polarizability tensors, which was defined as a second rank tensor with nine components. They used the angles between crystallographic axes and the polymer chain, machine and transverse directions rather than Euler's angles.

Two equations were obtained for general analysis using the coordinates system shown in Figure II-7.

$$f_z^{B} = 2\,\overline{\text{Cos}^2}\,\phi_{c,z} + \overline{\text{Cos}^2}\,\phi_{c,y} - 1 \qquad (32)$$

$$f_y^{B} = 2\,\overline{\text{Cos}^2}\,\phi_{c,y} + \overline{\text{Cos}^2}\,\phi_{c,z} - 1 \qquad (33)$$

Where the subscript "c" is the chain direction and the

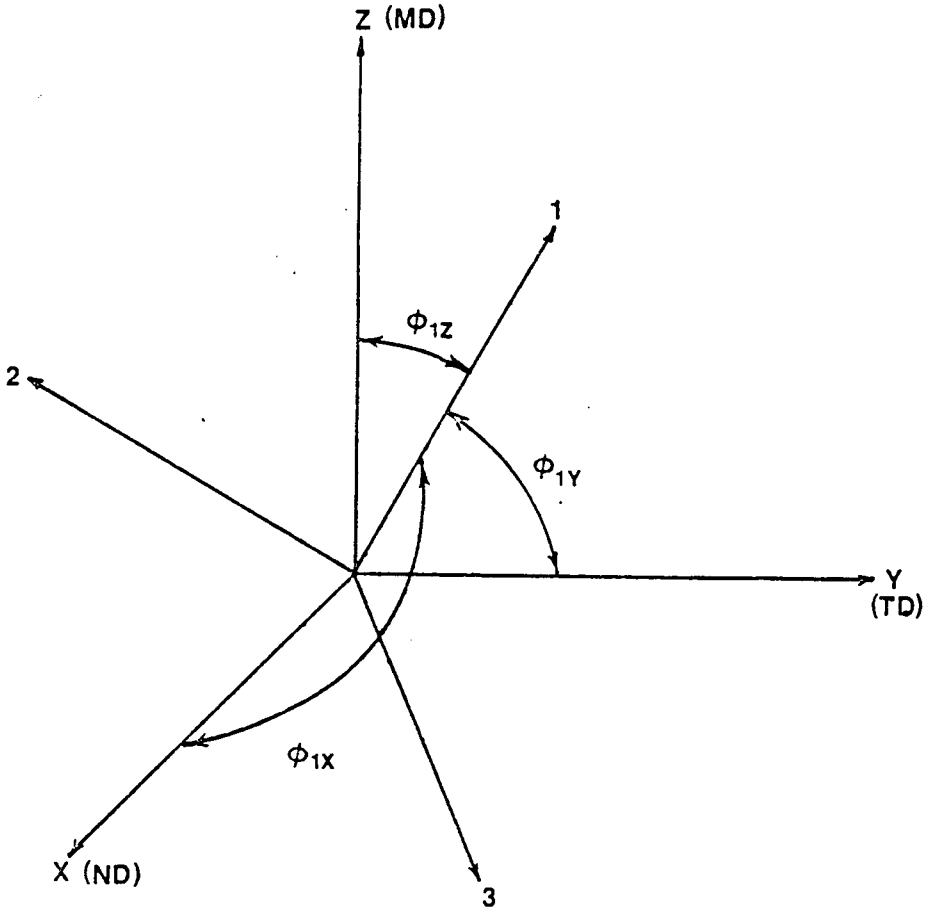


Figure II.7. White and Spruiell's coordinate system for biaxial orientation functions.

subscripts z and y refer to the reference direction (ie., machine and transverse direction respectively). For semi-crystalline polymers they described two biaxial orientation factors for each crystallographic axis.

a-axis

$$f_z^B = 2\,\overline{\cos^2}\,\phi_{a,z} + \overline{\cos^2}\,\phi_{a,y} - 1 \qquad (34)$$

$$f_y^B = 2\,\overline{\cos^2}\,\phi_{a,y} + \overline{\cos^2}\,\phi_{a,z} - 1 \qquad (35)$$

b-axis

$$f_z^B = 2\,\overline{\cos^2}\,\phi_{b,z} + \overline{\cos^2}\,\phi_{b,y} - 1 \qquad (36)$$

$$f_y^B = 2\,\overline{\cos^2}\,\phi_{b,y} + \overline{\cos^2}\,\phi_{b,z} - 1 \qquad (37)$$

c-axis

$$f_z^B = 2\,\overline{\cos^2}\,\phi_{c,z} + \overline{\cos^2}\,\phi_{c,y} - 1 \qquad (38)$$

$$f_y^B = 2\,\overline{\cos^2}\,\phi_{c,y} + \overline{\cos^2}\,\phi_{c,z} - 1 \qquad (39)$$

In case of orthogonality,

$$\overline{\cos^2}\,\phi_{a,z} + \overline{\cos^2}\,\phi_{b,z} + \overline{\cos^2}\,\phi_{c,z} = 1.0 \qquad (40)$$

$$\overline{\cos^2}\,\phi_{a,y} + \overline{\cos^2}\,\phi_{b,y} + \overline{\cos^2}\,\phi_{c,y} = 1.0 \qquad (41)$$

Thus only four crystalline orientation factors are independent. The values of these orientation functions are represented in Table II-1 and Figure II-8. The special cases of isotropy where the orientation factors are zero and three various types of uniaxial orientation and also

TABLE II.1. WHITE AND SPRUIELL'S BIAXIAL ORIENTATION* FOR DIFFERENT TYPES OF ORIENTATION IN A FILM

Orientation	f_1^B	f_2^B
Isotropic	0	0
Uniaxial Machine Direction	$\frac{3\overline{\cos^2\phi}_{c1}-1}{2}$	0
Chains Parallel to MD	+1	0
Uniaxial Transverse Direction	0	$\frac{3\overline{\cos^2\phi}_{c2}-1}{2}$
Chains Parellel to TD	0	+1
Equal Biaxial (planar or) Non-Planar (Same as Uniaxial Normal Direction	$\frac{1-3\overline{\cos^2\phi}_{c3}}{2}$	$\frac{1-3\overline{\cos^2\phi}_{c3}}{2}$
Chains Parallel to ND	-1	-1
Planar	$\overline{\cos^2\phi}_{c1}$	$\overline{\cos\phi^2}_{c2}$
Planar Equal Biaxial	+ 1/2	+ 1/2
Planar Equidirection (random about ND)	+ 1/2	+ 1/2

* $\overline{\cos^2\phi}_{c1} + \overline{\cos^2\phi}_{c2} + \overline{\cos^2\phi}_{c3} = 1.0$

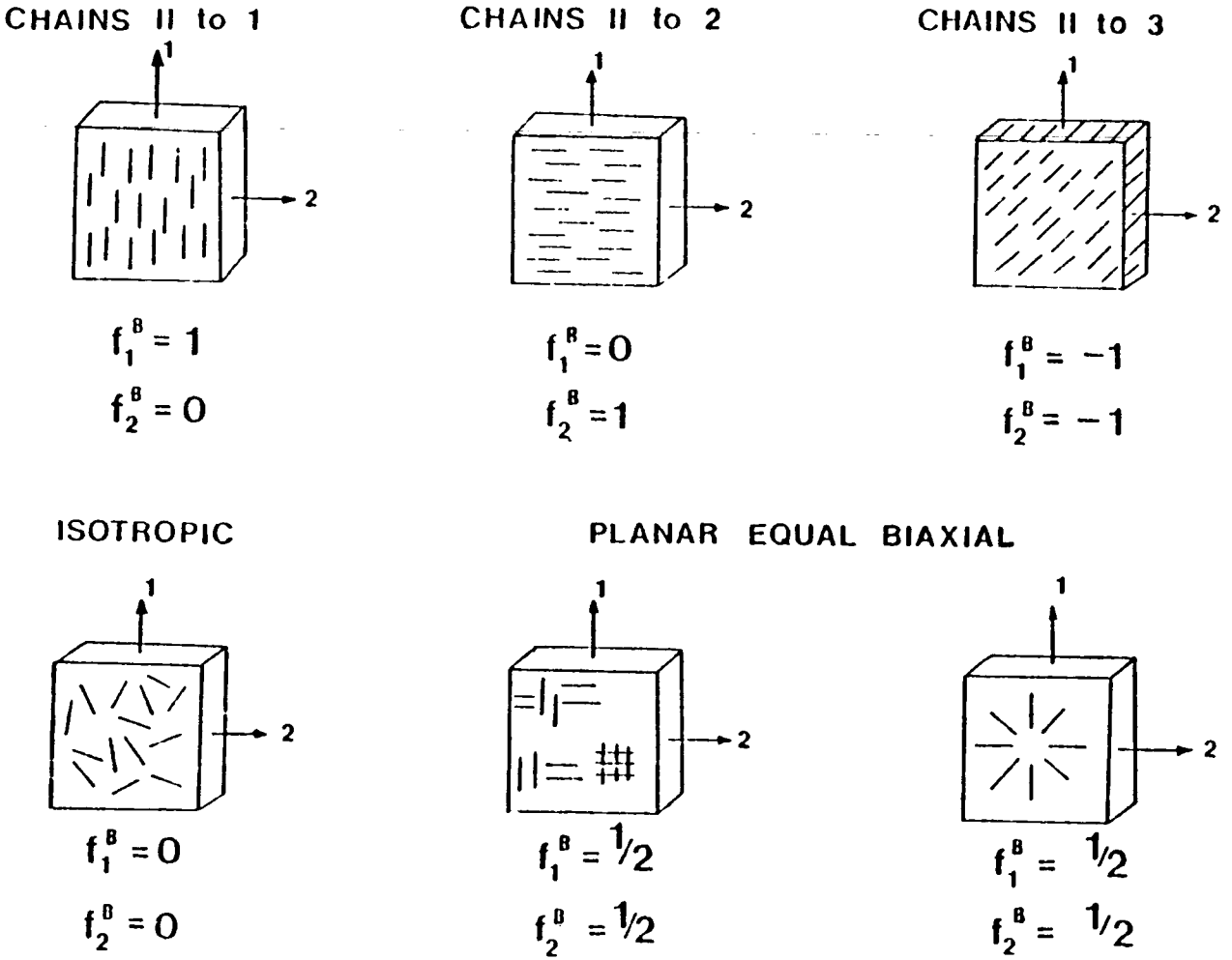


Figure II.8. Different states of orientation in films and White and Spruiell's biaxial orientation factors.

planar orientation are considered. It is important to note in the uniaxial case these orientation factors reduce to the well known Hermans orientation factor. For planar orientation f_z^B and f_y^B may vary from 0.0 to 1.0. As macromolecules tend toward orientation parallel to the film normal f_z^B and f_y^B become negative. Their proposed orientation distribution function triangle diagram is shown in Figure II-9.

White and Spruiell (233) also derived the total birefringence Δn_{zx} and Δn_{yz} for both two-phase semi-crystalline and amorphous polymers respectively as follow,

$$\Delta n_{z,x} = X\left[{}^{oC}\Delta_{ca} f^B_{Z,c} + {}^{oC}\Delta_{ba} f^B_{z,b}\right] + (1-X)\left[{}^{o}\Delta_a f_Z^B\right] + \Delta n_{form} \tag{42}$$

$$\Delta n_{y,x} = X\left[{}^{oC}\Delta_{ca} f^B_{y,c} + {}^{oC}\Delta_{ba} f^B_{y,b}\right] + (1-X)\left[{}^{o}\Delta_a f^B_y\right] + \Delta n_{form} \tag{43}$$

In which X= volume fraction crystallinity, ${}^{oC}\Delta$ = intrinsic crystallite birefringence $({}^{oC}\Delta_{ca} = n_c - n_a, {}^{oC}\Delta_{ba} = n_b - n_a)$

Δn_{form} = intrinsic amorphous birefringence, and Δn_{form} = form birefringence. For amorphous polymers,

$$\Delta n_{z,y} = {}^{o}\Delta_a f_z^B \tag{44}$$

$$\Delta n_{y,x} = {}^{o}\Delta_a f_y^B \tag{45}$$

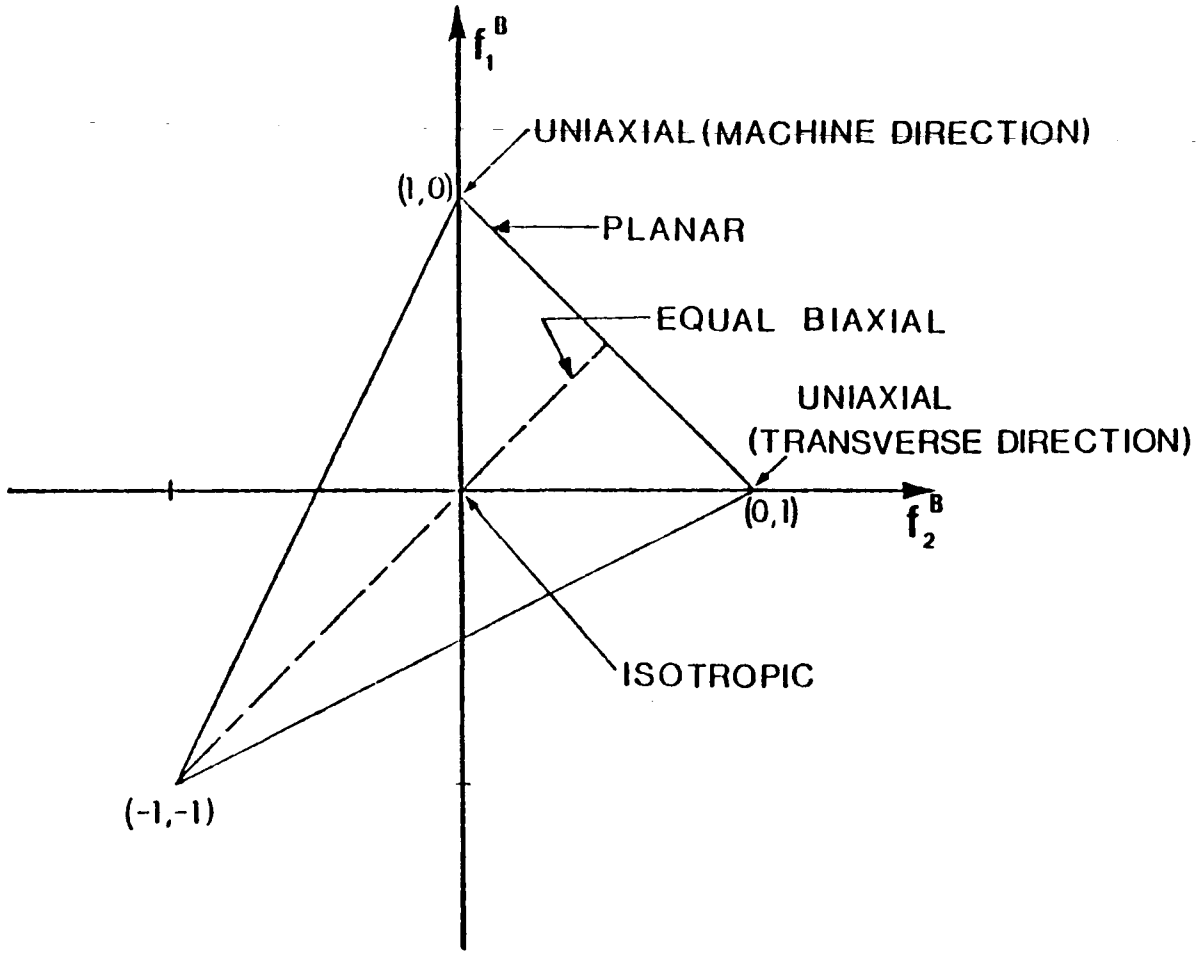


Figure II.9. Graphical representation of orientation, the orientation triangle diagram (White and Spruiell).

D. Experimental Techniques for Investigation of Crystalline Orientation and Morphology

The most powerful methods for investigation of the structure and morphology of crystalline polymer film are diffraction techniques. Wide angle x-ray scattering (WAXS) gives information about crystallographic structure and orientation. Small angle x-ray scattering (SAXS) is useful in determining the morphology of domains with dimensions from 20 Å up to more than a thousand units. Crystallites (20-500 Å), amorphous periodicities (20-2000 Å), chain folding periodicities (50-300 Å), and voids (20-2000 Å) can be studied by this technique (24, 26).

Optical methods yield information on super structure. Light scattering is useful for the investigation of spherulitic structure. Polarized light can be used on these films to determine birefringence which yields information on orientation (203).

Surface and internal characteristics of films can be studied by scanning electron microscopy (SEM) and transition electron microscopy (TEM)(28).

Pole Figures

The pole figure is one of the very important tools to interpret crystalline orientation and morphology in both a quantitative and a qualitative way. Pole figures give a three dimensional orientation distribution of the crystals in a polycrystalline sample, that is the spacial distribution of poles normal to certain crystallographic planes.

The experimental schematic of a goniometer for orienting a specimen in the x-ray beam and its corresponding spherical coordinates ϕ and α are shown in Figure II-10 and II-11 respectively. Pole figures from several planes are needed to determine the experimental values of $\overline{\text{Cos}^2\phi}$ for the computation of orientation functions as outlined in the preceeding section. Diffracting (hkl) planes perpendicular to a crystallographic axis are used in the above case. The $\overline{\text{Cos}^2\phi}$ values are thus obtained by averaging $\overline{\text{Cos}^2\phi}$ over the entire surface of the coordinate sphere. If ϕ is the angle between a chosen crystallographic direction and a reference direction, this average is expressed mathematically as follows,

$$\overline{\text{Cos}^2\phi} = \frac{\int_0^{\pi}\int_0^{2\pi} I(\phi,\alpha)\ \text{Cos}^2\phi\ \text{Sin}\phi\ d\alpha\ d\phi}{\int_0^{\pi}\int_0^{2\pi} I(\phi,\alpha)\ \text{Sin}\phi\ d\alpha\ d\phi} \qquad (46)$$

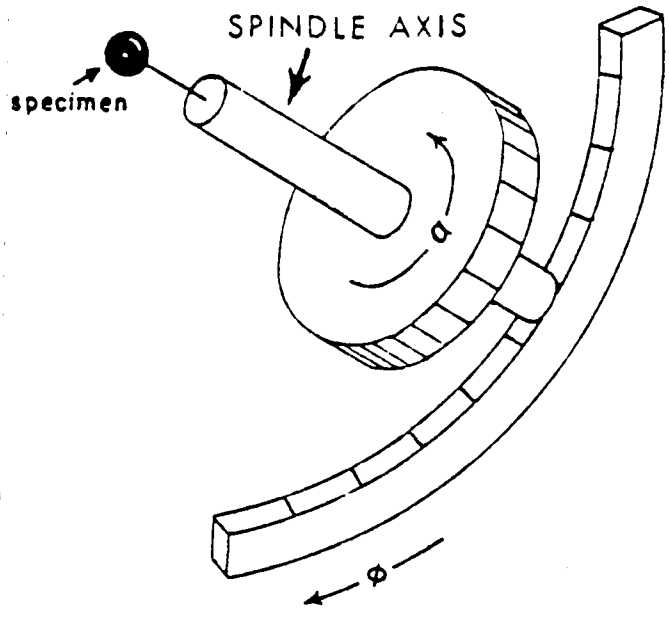


Figure II.10. Experimental schematic of a goniometer for orienting a sample in the x-ray beam.

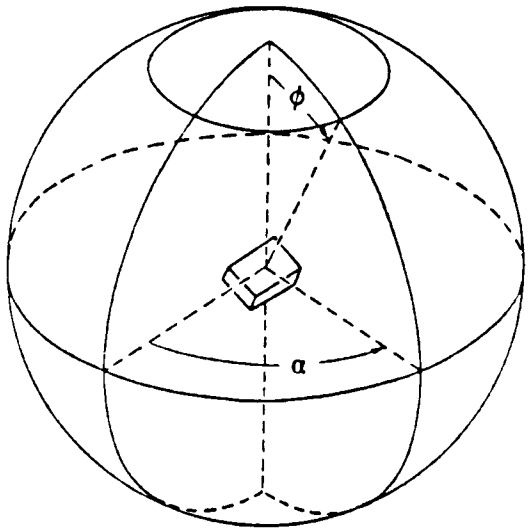


Figure II.11. Position of plane normal by spherical coordinates.

Where I (ϕ,α) is the x-ray intensity diffracted from planes perpendicular to the chosen crystallographic direction. It is important to note that Wilchinsky (234) described a procedure for the situation where there are not diffracting planes perpendicular to the crystallographic axes.

Small Angle X-Ray Scattering (SAXS)

An inhomogeneous system may scatter in either a diffuse or a discrete manner. Guinier (71) showed that a single particle of colloidal dimensions can produce a characteristic diffuse small angle scattering pattern and that many identical particles at sufficiently large and irregular distances from each other will produce a total scattering that is simply the sum of the scattering of the individual particles. It is of prime importance to realize that a diffuse small angle scattering pattern is never subject to an unequivocal structural interpretation on the basis of x-ray data taken along. Specimens which show identical scattering curves may be designated scattering equivalent system (146). In principle the following types of ambiguity must be considered in the interpretation of diffuse small angle scattering; a) it is not possible to distinguish the scattering by a system of particles in space from the scattering by a

complementary system of micropores in a solid continum, b) it is not possible to differentiate without some degree of uncertainity the effects due to particle shape from those due to polydispersity. It is often difficult to determine to what extent the scattering curve is determined by the isolated particles and to what extent by the interparticle interferences (9).

Evidence now shows that the best interpretation of diffuse scattering from solid polymers is in terms of microvoids or intermediate space. Much detailed theory was presented by Porod (146) to show that when the matter is dense enough to cause interparticle interference, the reciprocity rule dictates that the rest of the scattering curve is caused by the interstices or voids. Statton (171) proposed that voids must be considered the cause of the scattering; this was later quantitatively confirmed by Hermans, Heikens and Weidinger (77). In 1962, a review of diffuse small angle scattering by Statton (171) extended to all polymers the interpretation that the most probable cause of the scattering is voids. In a variety of ways it was shown that the inhomogeneity of electron density is microvoids. He reported that the microvoids are small regions in the polymer which are usually less than 100 $\mathring{A}$. In particular Statton (171) makes the following points, 1) it is normal to find intense diffuse scatter in the

small angle patterns of synthetic as well as natural fibers, and very weak scattering is the exception rather than the rule, 2) a fiber treatment that produces a decrease in the diffuse scatter is accompanied by an increase in density, 3) the degree of crystallinity is unrelated to the diffuse scatter as is shown by large variations in the amount of diffuse scatter with no change in the crystalline fraction and, conversely, by observation of large changes in the crystalline fraction with no appreciable change in the intensity of the diffuse scatter, 4) most commercial materials show a level of diffuse scatter, 5) microvoids are a logical consequence of the fact that long chain polymers cannot efficiently fill all space. Thus the voids maybe unfilled spaces around polymer chains, around fibrils, or between lamellae.

The amount of diffuse x-ray scattering given by a fiber depends profoundly upon the method used to form the fiber. Large void contents are promoted by those fiber spinning procedures that result in rapid precipitation of the fibers from solution for example, wet, dry, and dispersion spinning. Such a high level can be subsequently reduced by the annealing effects of thermal after treatments. Relatively small numbers of microvoids are produced by solidification of a viscious polymer from its melt, by

slow evaporation of a polymer solution, or by spinning procedures that permit a slower precipitation from solution (9).

If discrete interferences appear in the small angle x-ray scattering patterns of oriented polymers, they are usually observed in only one direction, most commonly on the meridian. The meridional reflections denote some degree of large-scale periodic character in the structure parallel to the stretch direction. In terms of the "fringed micelle" model the long period spacing obtained from the first order meridional reflection can be most usefully interpreted as the mean distance between the center of successive crystalline regions along the fiber axis (9, 171). This initial interpretation seems also valid for the newer concept of chain folding within the crystalline regions(71).

An important feature of the long period meridional spacings of polymer meterials is the dependence on the crystallization and annealing temperatures. Many significant studies of this long spacing phenomenon have been made (9,28) with the final long period spacing depending on both the time and temperature of annealing.

Moreover, there are various techniques for the analysis of SAXS, especially those related to void size, shape and distribution such as the following.

Scattering functions. Based on x-ray diffraction studies (71), the x-ray intensity from one scattering particle is given by

$$I = Ie\ n^2\ \exp\ (-S^2\ R_d{}^2) \qquad (47)$$

where Ie is the intensity of x-ray scattered by one electron

n is the number of electron in a particle

$S = \frac{2\ \sin\ \varepsilon}{\lambda}$ (λ is wave length, ε is scattering angle)

R_d = electronic radius of gyration of the particle.

The scattered intensity from M particles is represented by,

$$I = Ie\ M\ n^2\ \exp\ (-S^2 R_d{}^2) \qquad (48)$$

in which M is number of particles in the system, and exp $(-S^2R_d{}^2)$ is called "scattering function" denoted as ψ which reflects the shape of the particles in the scattering system.

For the system where the particle concentration is quite small and there is no interaction between particles, the scattering functions were already determined by Fournet, Kratty and others (9,70,104). Then assuming that the void fraction is not so large, we may compare the experimental results with theoretical scattering intensity curves drawn for some specific particles such as spheres, oblate or prolate ellipsoids, cylinders or disks.

When the concentration of particles is high we have to consider the interaction between particles. It makes the

relation much more complicated. Some functions are summarized in Table II-2.

Guinier analysis. Guinier (71) first showed that for a dilute, monodisperse system in which the particles assume all orientations with equal probability the scattered intensity can be written by a power series as follows:

$$I(S) = I(0)\left[1-1/3\ S^2R^2+\cdots\right] \tag{49}$$

Where I (0) is the intensity scattered at zero angle, which is proportional to the total number of electrons in the system irradiated, and R is called the electronic radius of gyration which is the root mean square of the distances of all the electrons from the electronic center of gravity of the representative particle

$$R = \left\{\frac{\sum_k f_k\ r_k^2}{\sum_k f_k}\right\}^{1/2} \tag{50}$$

In which f_k is the scattering factor of the kth electron, and is a distance r_k from the electronic center of gravity. To a good approximation the above equation may be written as:

$$I(S)=I(0)\ \exp\ (-1/3\ S^2R^2) \tag{51}$$

or in terms of the angular distribution as

$$I(S) = I(0)\ \exp\ \left(-\frac{16\ \pi^2\ \mathrm{Sin}^2\theta}{3\ \lambda^2}\ R^2\right) \tag{52}$$

which is the familiar law of Guinier. In logarithmic form the equation 51 becomes,

TABLE II.2. SCATTERING FUNCTIONS FOR VARIOUS PARTICLE SHAPES

Shape of particle	Scattering function
Sphere of uniform electron density and radius R	$\left[\frac{3\,\mathrm{Sin}2\pi\,SR-2\pi\,SR\,\mathrm{Cos}\,2\pi\,SR}{(2\pi\,SR)^3}\right]^2$
Ellipsoids of revolution of volume V and axes, a,a,av	$\int_0^{\pi/2}\phi\left(\frac{2\,S\,av}{\mathrm{Sin}^2\alpha+V^2\mathrm{Cos}^2\alpha}\right)\mathrm{Cos}\phi\,d\phi$ where $\phi(X)=\left[\frac{3\mathrm{Sin}\,X-X\,\mathrm{Cos}\,X}{X^3}\right]$, $a=\arctan(V\tan\phi)$
Cylinders of volume V and length 2H	$\frac{\mathrm{Si}\,(4\pi\,SH)}{2\pi\,SH}-\frac{\mathrm{Sin}^2\,2\pi\,SH}{(2\pi\,SH)^2}$ where $\mathrm{Si}(X)=\int_0^x\frac{\mathrm{Sin}\,t}{t}\,dt$
Flat disks of radius R and volume V	$\frac{2}{(2\pi\,SR)^2}1-\frac{1}{2\pi\,SR}J_1(4\pi\,SR)$ where J_1 is the Bessel Function of order 1

* In this table $S=\varepsilon/\lambda$

$$\log I(S) = \log I(0) - 1/3\, S^2 R^2 \qquad (53)$$

$$\left(S = \frac{4\pi \sin\theta}{\lambda}\right.,\ \theta = \text{scattering angle})$$

When the law of Guinier is closely obeyed by an actual system equation (51) states that a plot of the intensity curve I (S) versus S will be Gaussian, and equation (53) states that a plot of log I (S) versus S^2 will be linear over a large angular range with an ordinate intercept of log I (0) and a slope of $-1/3\ R^2$. The law of Guinier is valid at small " θ " and is based on presuming a dilute system of randomly oriented particles. However, it is important to note that when the logarithmic plot becomes nonlinear with increasing angle as a result of departures from spherical shape or monodispersity, the limiting slope as S approaches zero is still related to the mean radius of gyration of the particles by this fundamental law.

For particles of ellipsoid shapes which are all oriented in the same way in space we can treat the scattering in a manner similar to the above discussion of Guinier analysis such that,

$$I(S) = I(0) \exp(-R_d^2\, S^2) \qquad (54)$$

Where R_d is called average inertial distance, and particle actual dimensions can be calculated using a procedure given by Guinier (71).

Jellinek, Solomon, and Fankuchen's analysis. For a system which contains spherical particles in a monodisperse distributions we can use a simple Guinier plot to analyze the particle size and then to estimate the fraction of scattering particles (71). For a polydisperse system of spherical particles in which there is a distribution of particle sizes, the scattering at small angles may better be represented as (164).

$$I(\theta) = I(0) \int_0^\infty R^3 W(R) \exp(-S^2R^2/3)\, dR \qquad (55)$$

Where W (R) is a particle size distribution function and $S = \frac{4\pi \sin\theta}{\lambda}$. We may estimate this following Jellinek et al (91) as a series of particles of different discrete sizes as,

$$I(\theta) = I(0) \sum A_i \exp(-S^2R_i^2/3) \qquad (56)$$

According to the reciprocity between the dimensions of inhomogeneity and the angular extent of the small angle scattering. The tangent at highest scattering angle of the plot of log I (θ) against S^2 gives the size of the smallest group of particles or voids. The intercept at $S^2 = 0$ is proportional to the weight fraction of the particles. The next particle group is obtained from repeating the plot using,

$$\frac{I(\theta)}{I(0)} - A_i e^{-S^2R_i^2/3} \quad \text{versus } S^2 \qquad (57)$$

the quantities R_i and A_i give void size and relative

Statton (172) has applied this procedure to characterization of void distribution in PET fibers. Bonart and Hoseman (36) determined the thickness distribution of the fibrils in a drawn polyethylene fiber.

Debye and Bueche method. Debye and Bueche (52) have analyzed the scattering intensity of an electromagnetic wave. The scattering intensity I is given by

$$I = \iint \eta_1 \eta_2 \exp \left[ik (r.s) \right] d\tau_1 d\tau_2 \qquad (58)$$

where

η_1 is local fluctuation of polarizability (electron density) in a volume element $d\tau_1$

η_2 is a similar quantity in another volume element $d\tau_2$

$k = 2\pi / \lambda$, λ is wave length

$$S = \underline{S}_o - \underline{S}' \qquad (59)$$

($\underline{S}_o$, incident beam Vector and $\underline{S}'$ scattered beam vector)

$S = 2 \sin\theta = 2 \sin \varepsilon/2$ (ε:scattering angle)

r: displacement vector drom $d\tau_1$ to $d\tau_2$

$$\langle \eta_1, \eta_2 \rangle = \alpha (r) \bar{\eta}^2 \qquad (60)$$

at r = 0

$$\langle \eta_1, \eta_2 \rangle = \bar{\eta}^2 \qquad (61)$$

for larger r

$$\langle \eta_1, \eta_2 \rangle \longrightarrow 0 \qquad (62)$$

Then,

$$I \propto \bar{\eta}^2 V \int \gamma(r) \exp(i k (r.s) dr \quad (63)$$

Where V is scattering volume and γ (r) is called the "correlation function". If the density distribution is isotropic and γ (r) is governed only by r

$$I \propto \bar{\eta}^{-2} V \int \gamma(r) \frac{\text{Sin } (k.s.r)}{(k.s.r)} 4 \pi r^2 dr = \bar{\eta}^{-2} V W, \quad (64)$$

Where W is called the "correlation volume".

The intensity of the scattered beam is,

$$I = \frac{\pi^2}{\alpha^2} \cdot \frac{\pi^2 V W}{\lambda^4 R^2} \frac{1 + \text{Cos}^2 \theta}{2} I_o, \quad (65)$$

Where R is the distance between sample and detector.

If the correlation function γ (r) is a simple function of r, such as

$$\gamma (r) = e^{-r/a} \quad (66)$$

The scattered intensity is represented as

$$I \propto V \bar{\eta}^2 W \frac{8 \pi a^3}{(1+ K^2 S^2 a^2)^2} \quad (67)$$

Therefore the plot of $(I)^{-\frac{1}{2}}$ against S^2 is linear. The value of "the correlation length" may be obtained from a slope-intercept ratio, i.e.,

$$a = \frac{\lambda}{2\pi} \left(\frac{\text{slope}}{\text{intercept}}\right)^{\frac{1}{2}} \quad (68)$$

"The correlation length" a, is related to the average pore diameter $\bar{R}_d$ by,

$$\bar{R}_d = 3a/2 \ (1-c) \quad (69)$$

where C is volume fraction of the voids which can be determined from specific volume measurements.

Invariant analysis. The volume fraction of voids can be calculated using invariant analysis (35). The total intensity in the small angle range is called the invariant and designated by "Q"

$$Q = \int I(\bar{S})\, dV_s \tag{70}$$

Where $\bar{S}$ is the diffraction vector and dV_s is a volume element in reciprocal space. For a cylindircally symmetric distribution of scattered intensity Q is given in terms of the intensities measured on the detector plane by,

$$Q_d = \frac{\pi \iint S_2\, I(S_2, S_1)\, d S_2\, d S_1}{I(0)\,(CT)\,(TM)} \tag{71}$$

and

$$Q = \frac{1}{(a\lambda)^3}\, Q_d \tag{72}$$

Where S_1 and S_2 are the coordinates on the dector plane in perpendicular and horizontal directions respectively, $I(S_2, S_1)$ is the measured intensity at coordinates S_2, S_1 for some fixed counting time (CT), I (0) is the intensity of the incident beam, and TM is the sample transmission factor. The latter quantity corrects the measurements for absorption in the sample. Also "a" is the sample to detector distance and λ is the wavelength of radiation.

Following the arguments of Kratky and Miholic (104) it can be shown that the mean square fluctuation of the electron density is given by,

$$\overline{(\rho - \bar{\rho})^2} = K\, Q_d \tag{73}$$

where $K = 1/(ie\ N^2\ d\ a\ \lambda^3)$

Here ie is the Thomson scattering constant for a free electron (7.9×10^{-26}), N is Avogadro's number, and d is the specimen thickness.

For a two phase system the mean square electron density fluctuation can be written (24) as,

$$\overline{(\rho - \bar{\rho})^2} = (\rho_1 - \rho_o)^2\ W_1\ W_o \qquad (74)$$

where ρ_o = polymer electron density

ρ_1 = void electron density

W_0 = volume fraction of polymer

W_1 = volume fraction of void

for void we may put $\rho_1 = 0$ which leads to

$$\overline{(\rho - \bar{\rho})^2} = \rho_o^2\ W_1(1-W_1) \qquad (75)$$

Here ρ_o is given by

$$\rho_o = \frac{d'}{M\ Z\ N} \qquad (76)$$

where d' is density, N is avogadro's number (6.02×10^{23}), M is molecular weight and Z is the atomic number.

E. Structure Development and Solid State Characterization of Polymer Liquid Crystals

Crystal Structure

In the wet spinning process, in which polymer dope enters the coagulation bath, the rate of cooling of the polymer dope partially determines the final fiber structure. It is

during this cool down period that the dope has the opportunity to crystallize under stress. The maximum rate of crystallization is dependent on the speed and temperature in which crystallization occurs. Maximum crystal growth rates for polymers are generally in the 10^2- 10^4 nm/ s ranges (201). However, such rates can increase by a couple of orders of magnitude to $\simeq 10^6$ nm/s under stress. For example,Pennings and Pijers (134) observed that the rate of crystallization of polyethylene in solution increased by about 1.5 orders of magnitude on stirring. The crystallization rate is also enhanced by the rodlike nature of the macromolecules which allows them to readily form extended-chain crystal nuclei under stress.

The basic process of polymer crystallization under stress is row nucleation because the presence of nuclei along the rows confined crystal growth to a plane perpendicular to the orienting stress field (96). Under high stress fields these crystals form columns parallel to the stress field and are usually called "shish kebabs" (96). This shish kebab structure consist of a central fibrillar core of aligned extended-chain macromolecules. Crystal lamellae grow on these fibrillar nuclei in planes perpendicular to the fibril and to the stress direction (96,105,139,140). Shish kebabs predominantly have been studied in stirred polyethylene solutions; however other

investigators (91) have also shown similar crystal growth processes occuring in oriented polymer melts. In general, it is assumed that stress- induced fibers that are produced from polymer melts possess a shish-kebab type structure (202). However, the crystallization processes of rod-like macromolecules may not be analogous to those processes that occur in more flexible chain macromolecules. In PPTA/H_2SO_4 liquid crystalline dopes, extended-chain, fibrillar-nucleating sites readily form under stress in the form of nematic liquid crystalline threads (120,181). Subsequent crystal growth perpendicular to the orienting stress field would involve the stacking of the rod like macromolecules in which no chain folding occurs (120, 181). Indeed, Takahaski et al. (181) have reported that rows of lamellae form perpendicular to the shear direction of shearing PPTA/H_2SO_4 (15 wt percent PPTA) dopes. PPTA molecules within the lamellae are aligned parallel to the shear direction. These workers also observed that fibrillar rather than crystalline rows of lamellae occur at higher shear stresses.

It is important however, to note that if indeed there are any significant shear forces imposed on the exterior of the fibrous dope in the spinneret orifice and the resultant shear strains are still present upon dope solidification, the observations of Takahaski et al. (181) suggest that the resulting fiber consists of a

highly oriented fibrillar skin and a crystalline core of row lamellae.

After crystallization of the polymer dope, a subsequent fabrication of fibers or films is reported to play a critical role in the final properties of the material (121). Fibers coagulated in water or alcohol are found to exhibit various polymorphic crystal structures.

Determination of the PPTA unit cell. Northolt (211) has reported an x-ray study of poly (p-phenylene terepthalamide) fibers. He found that all the reflections observed in x-ray diffraction photographs of well-oriented fibers could be satisfactorily indexed by assuming a monoclinic (pseudo-orthorhombic) unit cell with dimensions a=7.87 $\mathring{A}$, b= 5.18 $\mathring{A}$ and C (fiber axis) = 12.9 $\mathring{A}$, γ being approximately 90°, Northolt classified 44 reflections as being above the background and was able to determine their intensities visually. These reflections are listed in Table II-3 along with their respective indices and values of $Sin^2\ \phi$ hkl calculated by means of the following equation (79) for an orthorhombic system,

$$Sin^2\ \phi_{hkl} = \frac{\lambda^2}{4a^2} h^2 + \frac{\lambda^2}{4\ b^2} k^2 + \frac{\lambda^2}{4\ c^2}\ l^2 \qquad (77)$$

which can be written as,

$$Sin^2\ \phi_{hkl} = Ah^2 + Bk^2 + Cl^2 \qquad (78)$$

Where A= 0.0096, B= 0.0221, C=0.0036 for an orthrohombic

TABLE II.3. LIST OF OBSERVED REFLECTIONS FOR POLY (p-PHENYLENE TEREPHTHALAMIDE) FIBERS AFTER NORTHOLT (211)

hkl*	I^{**}_{obs}	$Sin^2\phi_{hkl}$	hkl*	I_{obs}	$Sin^2\phi_{hkl}$
002	m	0.0144	020	vw	0.0884
004	s	0.0576	021	w	0.0920
005	vw	0.0900	022	m	0.1028
006	s	0.1296	023	w	0.1208
104	w	0.0672	024	w	0.1460
106	s	0.1392	025	vw	0.1784
011	vw	0.0257	121	w	0.1016
012	vw	0.0365	310	m	0.1085
013	w	0.0545	311	vw	0.1121
014	w	0.0797	220	w	0.1268
015	w	0.1121	221	w	0.1304
016	w	0.1517	222	w	0.1412
110	vs	0.0317	223	vw	0.1592
111	s	0.0353	224	vw	0.1844
112	w	0.0461	400	w	0.1536
113	w-m	0.0641	402	w	0.1680
114	w	0.0893	321	w-m	0.1784
116	vw	0.1613	132	w	0.2229
200	vs	0.0384	420	w-m	0.2420
202	w	0.0528	510	vw	0.2621
211	s	0.0641	330	vw	0.2853
213	w	0.0929	620	w	0.4340

*I (hkl) and I ($\bar{h}$kl) are taken together.

**Visually estimated intensities; vs=very strong, s=strong, m=medium, w=weak, vw=very weak.

unit cell having the dimensions given by Northolt (211) using CuK α radiation and λ =1.5418 Å.

The Northolt model for PPTA unit cell and the c-axis projection of this model is shown in Figure II-12. The initial model for PPTA has a space group of $P2_1/n$ as determined by extinctions and comparisons of poly (p-phenylene oxide), and poly (p-phenylene sulphate) WAXS patterns to PPTA's WAXS patterns.

Tadokoro (179) also suggested an orthorhombic unit cell with the same dimensions as Northolt for PPTA. Hancock et al. (73) found in wet spun coagulated PPTA fiber that the WAXS reflection is different from Northolt's prediction where the strong (110) reflection is missing and extra reflections at 5.0 Å and 7.6 Å spacings are present. They suggested that this phenomenon might be associated with a polymorphic form. This result has recently been confirmed and developed in the work of Haraguchi, Kajiyama and Takayanagi(76). They (76) discuss the effect of the coagulant on the crystalline structures of uniplanar PPTA films. It was found that water as a coagulant has an effect on the film regardless of the solution concentration. Based on their x-ray and infrared studies they verified that the resulting crystalline structure is different from the Northolt (211) and Tadakoro (179) model which they called "modification I". This new structure was called "modification II".

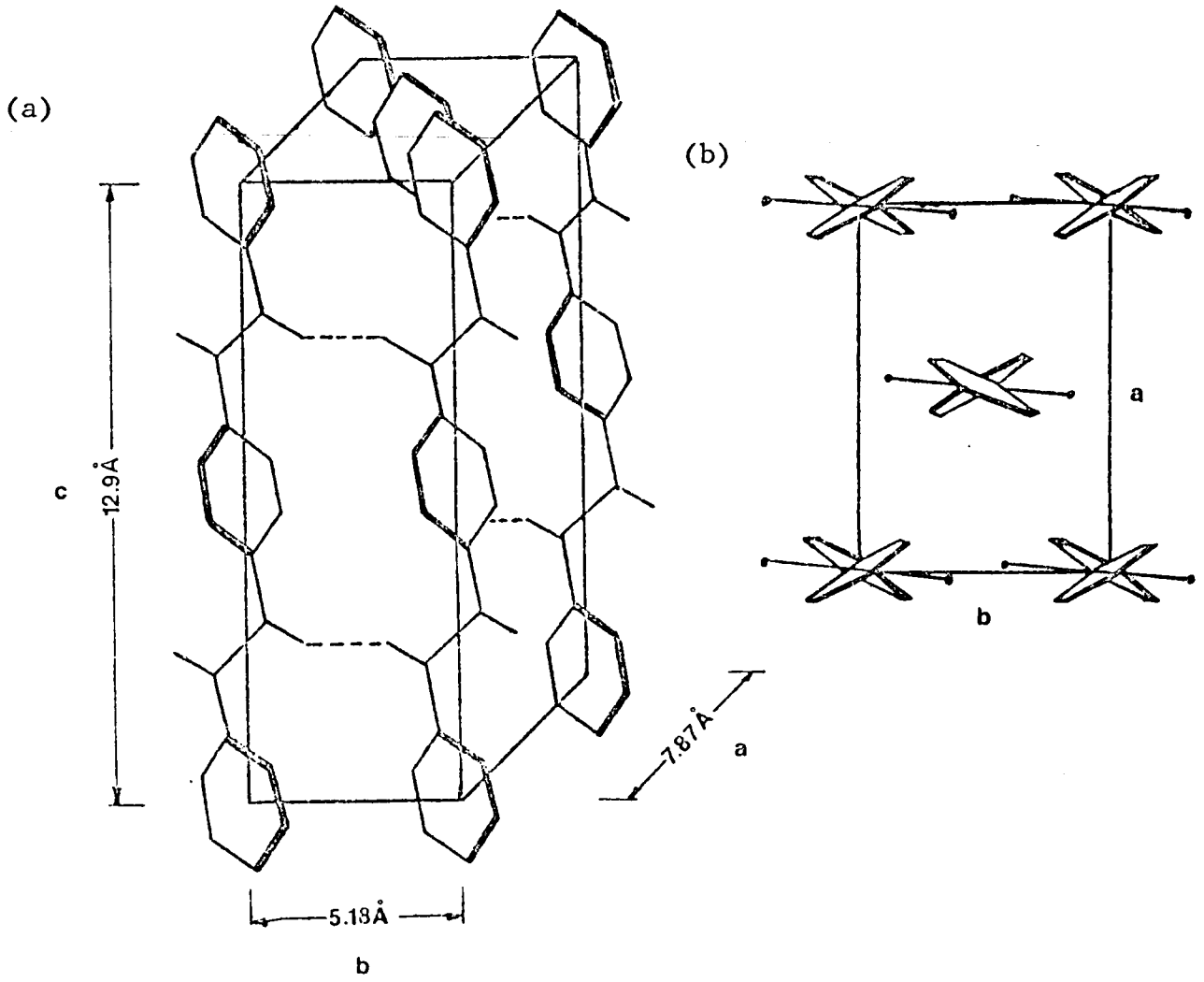
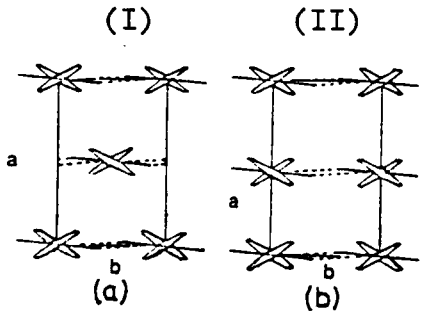


Figure II.12. (a) The Northolt model for PPTA's unit cell and (b) The c-axis projection of the Northolt model.

There are some differences in WAXS patterns of modification II. In this case, the strong (110) reflection is absent, the Bragg spacing of the (200) reflection is somehow larger by 0.01nm, some reflections with spacings between 2.0 Å and 3.2 Å do not appear, and a strong inner reflection with a Bragg spacing of 5.1 Å is observed. C-axis projections of the crystal structure of PPTA for both modifications are presented in Figure II-13.

Infrared studies (76) indicated that the absorption bands at 720 and 730 cm^{-1} were sensitive to crystal modification. The absorption band at 730 cm^{-1} was found to be sensitive to modification II whereas the absorption band at 730 cm^{-1} was sensitive to modification I.

PPTA thin films coagulated with water usually show the crystalline structure of modification II. This is an orthorhombic structure with a=8.0 Å , b= 5.1 Å , and c= 12.9 Å . It is a nonequilibrium more irregular structure. However, films which are coagulated with organic liquids exhibit structure of type I (76), Aoki et al. (31), and Flood, White and Fellers (63) in their WAXS measurements on the films coagulated in water also found some reflections corresponding to Haraguchi, et al. Modification II films coagulated in alcohol (63) showed reflections described by Northolt and correspond to the orthorhombic unit cell he proposed.



Modification I has the unit cell dimensions a = 7.87Å, b = 5.18Å, and c = 12.9Å. Modification II was reported by Northolt and has the dimensions a = 8.0Å, b = 5.1Å, and c = 12.9Å.

Figure II.13. C-axis projections of the crystal structures of PPTA.

Panar et al. (131) studied extensively the crystalline structure of PPTA fibers. Equatorial and meridional scans of PPTA fibers were obtained from an x-ray diffractometer. The meridional scan showed no evidence of an amorphous halo. The equatorial pattern was analyzed for the existence of an underlying oriented amorphous component. Their results indicated that there can be, at most, a small amorphous fraction. A heavily exposed WAXS diffraction pattern of PPTA fiber exhibits no amorphous halo. It detects, however, a small fraction which they believed to be due to a few percent of an unoriented crystalline component as it was revealed by the pair of sharp rings. They further plotted the meridional peak width times the cosine of the diffraction angle as a function of the square of the order. A linear relationship between the parameters was obtained which indicated that the scattering is consistent with a one-dimensional paracrystalline structure.

Determination of CTA unit cell. The various crystalline modifications of cellulose have been studied by many investigators and characterized by numerous methods nearly a century ago, but by comparison the crystalline structure of cellulose triacetate has recieved relatively little attention. In early 1930, Hess and Trogus (80) studied the kinetics of esterification of cellulose and

the formation of crystalline structure. Their results showed two polymorphic crystalline forms of cellulose triacetate, related to the cellulose source and the esterification technique. However, consideration of this field by other investigators (75,84) has cast doubts on the validity of polymorphic crystalline forms interpreted for cellulose triacetate.

Stoll (176) in studies of the crystalline structure of commercial cellulose triacetate fibers described that use of heat promotes crystallization and it can be controlled readily to give a very fast rate of crystallization, resulting in a short time treatment with negligible degradation. It also avoids chemical treatments, which by swelling or other means may introduce ambiguity into the crystal structure or reduce the lateral order to a point where structural interpretations become impossible. In fact, heat treating increased the lateral order to a degree that allows unequivocal conclusions to be drawn and unit cell calculations to be attempted.

Two different crystalline structures are reported for cellulose triacetate namely, structure I and structure II. The dependence of the structure of cellulose triacetate can be summarized as follows: heterogeneous acetylation of cellulose I (usually Ramie, cotton, and wood pulp are utilized as sources of cellulose I) yields triacetate I, b) homogeneous acetylation always results in triacetate

II, c) any type of acetylation of cellulose II (Fortisan is utilized as a source of cellulose II) also yields triacetate II, d) heterogeneous acetylation of cellulose IV (rayon use as a source for cellulose IV) prepared from cellulose II yield triacetate II, and heterogeneous acetylation of IV sometimes yield triacetate I (80,168).

Doulmadge (58) proposed an orthorhombic unit cell with a=24.5 Å, b= 10.43 Å , and c= 11.65 Å for cellulose triacetate. Sprague, Riley and Noether (168) made proposals for unit cell dimensions of cellulose triacetate I and cellulose triacetate II crystals. They measured diffraction spacings of cellulose triacetate I and II. These and similar data by other investigators are listed in Table II-4 and II-5. Observation of their fiber WAXS diagrams lead to conclusions that the unit cell length in the fiber direction is the same for both forms of cellulose triacetate. A value of 10.5 Å is found. Note its similarities to native and regenerated cellulose. Based on these observations, the relative positions of the diffraction arcs on the equator and the layer lines which indicate two axes of the base plane (the lateral directions) are perpendicular to the fiber direction, they suggested the unit cell should be either tetragonal, orthorhombic or monoclinic.

The methods of synthesis of cellulose triacetate I and II and the cellulose structure obtainable from them

TABLE II.4. SPACINGS OF CELLULOSE TRIACETATE I

Sprague et al (168)			Hess and Trogus (80)		
E_1	Intensity	d, Å	No.	Intensity	d, Å
E_1	v.s.	11.58	A_0	v.s.	11.5
			A_1	m.s.	7.72
E_2	s.	5.50	A_2	m.s.	6.09
E_3	m.	4.35	A_3	v.w.	5.42
E_4	w.	3.98	A_4	m.s.	4.31
E_5	w.	3.36	A_5	s.	3.95
E_6	w.	2.73			
I_1	w_1	7.73	I_0	s.	5.27
I_2	m.	4.99			
II_0	s.	5.31	II_0	m.s.	5.18
II_1	w.	4.75			
II_2	s.	3.99			
II_3	m.	3.65			
II_4	w.	3.14			
III_0	v.s.	3.50	III_0	v.s.	3.42
III_1	w.	3.03			
III_2	w.	2.90			
III_3	w.	2.63			
IV_0	w.	2.71	IV_0	w.	2.60

TABLE II.5. SPACINGS OF CELLULOSE TRIACETATE II

Sprague et al(130)			Hess and Trogus(125)			Happey (127)	
No.	Intensity	d,A	No.	Intensity	d,A	Intensity	d,A
E_1	v.s.	10.55		v.s.	10.43	v.v.s.	10.6
E_2	v.s.	8.46		v.s.	8.62	v.s.	8.41
E_3	v.s.	6.82		s.	6.67	v.s.	6.70
E_4	v.s.	5.31		s.	5.12	diff.s.	5.35
E_5	s.	4.80		m.s.	5.83	m.	4.75
E_6	m.s.	4.16		m.w.	4.18	m.	4.30
E_7	s.	3.87		w.	3.83		
E_8	s.	3.79					
E_9	v.w.	3.52					
E_{10}	w.	3.39				m.s.dif.	3.35
E_{11}	v.w.	2.69					
E_{12}	v.w.	2.27					
I_1	w.	9.46					
I_2	m.	7.35	I_1	w.	7.61		
I_3	m.	6.54	I_2	w.	6.79		
I_4	s.	5.11	I_4	s.	5.12		
I_5	s.	4.84					
I_6	m.	4.18	I_3	v.w.	4.29		
I_7	w.	3.95					
I_8	m.	3.66					
I_9	m.	3.32					

TABLE II.5. (continued)

Sprague et al(130)			Hess and Trogus(125)			Happey (127)	
No.	Intensity	d,A	No.	Intensity	d,A	Intensity	d,A
II_0	m.	5.24	II_o	s.	5.43	v.s.	5.2
II_1	s.	4.75	II_1	m.s.	4.88		
II_2	s.	4.43	II_2	m.s.	5.54		
II_3	m.	3.90	II_3	w.	3.95		
II_4	m.	3.75					
II_5	m.	3.45					
II_6	m.	3.29					
III_0	m.	3.52	III_0	m.s.	3.52		
III_1	s.	3.32	III_1	s.	3.36		
IV_0	w.	2.66					

by saponification suggested a similarity of rearrangement between triacetate II and cellulose II, and triacetate I and cellulose I. The relative position of the anhydroglucuse chain atoms for each pair might be rather similar, the spacing between the chain increasing to accomodate the acetyl side groups.

Cellulose triacetate II showed considerably more diffraction arc than triacetate I in the same range of spacings. This was interpreted as several spacings in triacetate I either are very nearly equal or are multiples of one another.

Based on the above assumptions, dimensions of the base plane for triacetate I and II have been obtained. The dimensions of the proposed unit cells are presented in Table II-6. Zugenmaier (231) and Stipanovic et al. (232), recently proposed an orthrohombic unit cell for CTA I. Their proposed cell dimensions are also shown in Table II-6.

Spinning of cellulose and its derivatives from liquid crystalline solutions also have been reported in literature. Oriented cellulose films and fibers from a mesophase system is reported by Chanzy and co-workers (43,132) while Panar and Willcox in 1976 in a 1976 German patent described the solution spinning of fibers from liquid crystalline solutions of cellulose derivatives. Little information concerning structures of these materials

TABLE II.6. UNIT CELL DIMENSIONS OF CELLULOSE TRIACETATE I AND II

Dimension	Sprague et al. (168) CTA-I	Sprague et al. (168) CTA-II	Zugenmaier (131) CTA-I	Stipanovic et al. (132) CTA-I
a (Å)	22.6	25.8	44.3	23.63
b (Å)	10.5	10.5	13.45	6.27
c (fiber axis, Å)	11.8	11.45	10.47	10.43
β	79°	66.4°	90°	90°
No. of cellulose units	4	4	8	2
Calculated density (g/cc)	1.39	1.34	-	-

produced from mesophases are available in the open literature. Bheda, Fellers and White recently studied wet spinning of liquid crystalline solutions of cellulose acetate butyrate and cellulose triacetate. Their WAXS patterns exhibited three spacing which are somewhat diffuse reflections at 3.10 Å, 4.25 Å, and 5.47 Å for cellulose acetate butyrate (CAB). They noted that CAB solidified from the melt forms a glass with an amorphous halo at 5.45 Å. The only pathway to form a solid state crystalline CAB fibers is via the spinning of a liquid crystalline solution. In the case of cellulose triacetate (CTA) fibers they observed x-ray reflections at 3.74 Å, 4.06 Å, 5.43 Å, and 11.64 Å. These spacings were found to correspond to values described by Spraque. Riley, and Noether (168) for the triacetate structure modification I.

Switching now to melt fabrication techniques, the melt spinning of fibers using aromatic polyesters is the most noticable development. The technology would appear to be analogous to that of conventional melt spinning of poly (ethylene terephthalate), PET.

A basic character of crystallization of polyesters from a nematic melt is reported by Warner and Jaffe (188). The Avrami analysis was undertaken as a means to reveal information on the growth geometry and the rate constant. The Avrami plot gave an exponent of about 2 which suggests rod-like growth from sporadic nuclei, and is well within

the range typical of semicrystalline polymers. Unlike low molecular weight nematogens, gross reorganization was not observed during crystallization. The molecular ordering in the solid is very poor, resembling that of the melt, and can be modeled well by close packed rods. That is to say, there is only a very small drop in entropy upon crystallization as would also be the case in crystallization of conventional (flexible) polymers from oriented melts.

A model of two polymers PET and an anisotropic polyester, from the melt into the solid phase given by Ronald (155) is shown in Figure II-14. In this manner, liquid crystal fiber properties such as 10-30 g/d tensile strength and ≈ 500 g/d modulus can be attained. PET, on the other hand, has typical properties of 8 g/d tensile strength and 100 g/d modulus after drawing (155).

It is believed that the mesophase of rigid chain polymeric liquid crystals is nematic (46,155,196), ie., the director of the molecular units tends to a local parallel arrangement. Since the molecular units are linked into continuous polymer chains, this is tantamount to saying that the chains form near-parallel configurations in the molten or solution mesophases. This is confirmed by the structure of extruded filaments, where the elongational flow fields readily impose a very high orientation in the melt, which on subsequent cooling to a solid gives rise to fiber-like x-ray patterns.

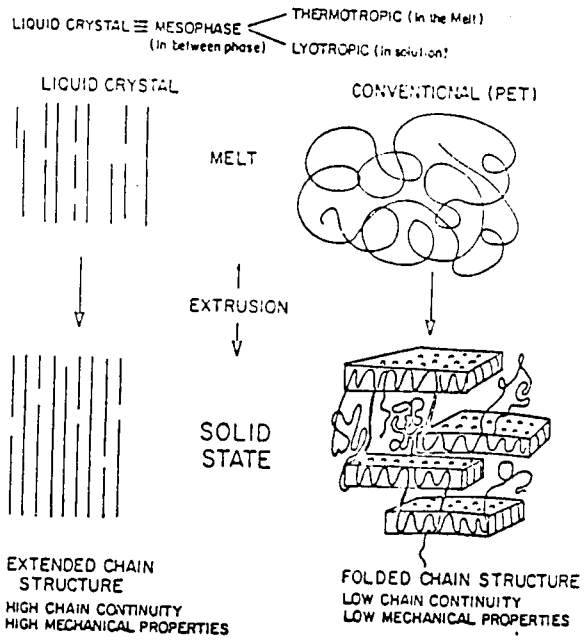


Figure II.14. Structure development of liquid crystalline vs. conventional folded chain polymers.

Many of the rigid chain thermotropic (1,34,86) and lyotropic (63,120,131) polymers that have been synthesized exhibit sharp x-ray diffraction lines that can be associated with crystallites with three dimensional order.

However, from thermal analysis of thermotropic polymers two recognizable transitions are usually observed (149). A Tg type of process at about 100°C and a crystalline melting process Tm over 200°C. The Tg process is accompanied by a change from a very rigid solid to a more flexible solid, while the Tm is associated with a change to a birefringent mesophasic melt of very low viscosity (34). The attainment of a rigid state in the interval between Tg and Tm can be attributed to the presence of the crystallites linking together the rigid chains. In this sense, the crystals form an exactly analogous function to those in conventional crystalline polymers. However, when it comes to the detailed nature of the crystals, there are important distinctions that need to be considered.

Blundell (34) carried out extensive studies on the nature of crystallites that form during solidification of aromatic polyesters, which are typical of rigid chain liquid crystal polymers. He examined two thermotropic polymers having different degree of stiffness using x-ray diffraction and thermal analysis. Two sets of

experiments were considered. In one set, the polymers were heated to 260°C in order to melt then immediately quenched into liquid nitrogen to freeze in the melt structure. For the second set, the polymer was cooled at room temperature from the melt, in order to allow three dimensional crystallites to form. His comparison of quenched and slow-cooled specimens indicates the presence in the quenched material of microcrystals that are too small to give clear x-ray lines. This was proposed to be due to the very low surface energy associated with the nematic chain morphology as explained by Samulski and Dupre (158). He also found that enthalpy and entropy of fusion are much lower than in conventional polymers and are related to the molecular design of the thermotropic polymers.

The structure of liquid crystalline copolyesters fibers recently were studied by Blackwell et al. (31) and Acierno et al (1). Blackwell et al. prepared fibers from ρ -hydroxybenzoic acid (B),2 6- dihydroxy naphthalene (N), and therepthalic acid (P). X-ray data for fibers prepared with B/N/P ratios of 60/20/20, 50/25/25, and 40/30/30 showed variations in the positions and intensities of the maxima suggestive of a truly random copolymer structure rather than extensive block copolymer character. All three fiber diagrams showed intense

equatorials at d=4.43 Å and 2.57 Å and an intense off-equatorial at d= 3.26 Å . These were believed to arise from stacking of the benzene and naphthalene rings. Some of the weak inner reflections were remarkably sharp and were interpreted to be due to relatively large crystallites. Three strong meriodionals were also observed. Two in the region of d=3 Å and one at d=2 Å .The separation between the first two maxima decreased from 0.52 to 0.33 Å as the proportion of B increases from 40 to 60 percent. Furthermore, they have predicted the intensity distribution on the meridian of the x-ray patterns by modelling random chains by a linear sequence of points separated by distance corresponding to the lengths of B, N, and residues. It was found that the positions of the maxima in the averaged squared Fourier transforms of random monomer sequences are in good agreement with those for the three observed strong meridional intensities, and the calculations reproduce the observed shifts in the positons of these meridionals as the monomer ratio is varied.

Copolyester fibers prepared by Aciero et al. (1) exhibited similar crystalline structures to those of pure poly (p-hydroxybenzoic acid) and that obtained by Wissbrun (197). The fiber produced from poly (ethylene terepthalate-co-p-oxybenzoate) containing 30 mol percent p-oxybenzoate after annealing revealed extensive

crystallization. The strongest reflections observed at 5.0, 3.91 and 3.43 Å correspond closely to those for pure PET samples (5.10, 3.83, and 3.43 Å). Other sample from poly (ethylene terephthalate-co-p-oxybenzoate) containing 60 percent p-oxybenzoate after annealing exhibited spacings at 4.48, 4,24 and 3.73 Å, very close to those observed by Wissbrun(197).

Morphology and Orientation

The processing of both classes of polymeric liquid crystals into products with unique properties has realized considerable success in the case of fibers and films. To achieve substantial properties of interest in the solid state, various steps in the fabrication process have been reported to be crucial. Among those, the solidification step (coagulation for lyotropic and cooling for thermotropic systems) must occur in such a way as to preserve orientation developed by flow stresses. Furthermore, the morphology of the final product is determined by the rate of cooling the polymer dope. Each of the lyotropic and thermotropic liquid crystalline fibers and films will be reviewed in turn.

Lyotropic fibers and films. It is well known that wet spun fibers are generally much more porous and contain more complex void structures than their melt spun counterparts (73,101,171). This has been verified by

electron microscopy (101) and small angle x-ray scattering (171). This porosity and the presence of such voids may account for the low elongation to break and tensile strength in wet spun fibers and probably must be minimized to provide better mechanical properties.

The coagulation process created radial heterogeneity in the fiber due to skin formation (131). This skin may have drastic effects on the fiber properties. The effects attributable to the skin are due to differences in crystallinity rather than molecular orientation.

The effects of the coagulation process on the resulting fiber properties and structure have been examined by Knudsen (101). He reported that as the bath temperature is lowered, the fiber properties improved. Zwick and Van Bochave (212) concluded that slowing down coagulation provided optimum values of strength and stiffness.

Wet spinning of aliphatic and aromatic polyamides is reported by Hancock, Spruiell and White (73). This involves wet spinning of nylon 6, nylon 66, Nomex®, and Kevlar® solutions in a $HCOOH/H_2O$ and $NAOH/H_2O$ coagulation bath. Their study revealed that fiber diameter decreased with decreasing pH, and increasing pH increased the void fraction. In an alkaline bath, the reaction between OH^- and HCOOH causes very rapid coagulation rates, resulting in a fiber of large diameter with high void fraction and

a central hallow core. The reaction and diffusion rate decreases as the OH^- concentration is decreased. Such behavior results in a smaller diameter of the fiber.

Hancock, White and Spruiell (74) have studied the mechanism of the formation of fluted void superstructure in the coagulation of wet spun fibers and application to membranes. They observed different superstructures for wet spun fibers under various conditions. Three main characteristic fiber types were identified, i)hollow cores, ii) radial fluted voids, and iii) relatively compacted structures. The first type of voids was observed in very few cases, whereas the second and third type of void structure were observed in a wide range of solvent-coagulant systems.

The origin of the fluted structure has been traced to interfacial characteristics of the solvent-coagulant. Two types of behavior were observed. First, there is a slow movement of a smooth interface and in the second the interface breaks up in finger-like intrusions. The fingering at the interface leads to fluted fibers. The fingering between any solvent- coagulant pair has been found to be affected by the polymer. It was found that fingering is associated with heats of solution.

It has been noted that high viscosities may prevent fingering and fluted fiber structures. However, in the case of Kevlar^R dissolved in H_2SO_4 and coagulated in

water, no fluted structures were observed despite the unfavorable heat of solution.

Recently the wet spinning of liquid crystalline solutions of cellulose derivatives have been studied by Bheda, Fellers and White (29). They observed distinct superstructure; i) an outer skin, ii) a fibrillar structure and iii) an inner core. Skin core superstructures were simillar to those of Hancock, Spruiell and White (73,74). Fibrillar structures are usually not seen in undrawn wet spun fibers, however, they noted that it must be associated with the liquid crystalline spinning solutions and the "dry jet" procedure.

They concluded the crystalline polymers cellulose triacetate, ethyl cellulose, and hydroxypropyl cellulose yield better defined structures in the anisotropic phase The extent of structure developed is dependent upon long range order of crystallinity of the polymer. The structure in the anisotropic phase is also dependent upon the quality of the solvent. Better solvents tend to yield better defined structure.

Aoki et al. (12) have produced ribbons and blown films from isotropic and anisotropic solutions of PPTA/ H_2SO_4 and carried out the structural characterization of the produced ribbons and films. Their SEM photomicrographs indicate a scale like structure for films made from low concentration of 2 percent solution. This roughness or

scale structure diminishes when films were made from higher concentration. High concentration samples appear as a bundle of fibrils.

In the case of blown tubular film, preferential orientation to the machine direction and transverse direction was observed. Wide angle x-ray diffraction studies of samples coagulated in water indicated the orientation of the (110) planes are located in the transverse direction. Based on the known model of PPTA's unit cell (211), it was suggested that the b-axis tends to become oriented perpendicular to the machine direction. Annealing at 400-500 C^{o} for 10 minutes resulted in sharpened and increased diffraction intensity. Some of the annealed samples showed a new diffraction ring at 7.63 $\mathring{A}$ spacing. This reflection is not predicted by Northolt (211) but it was observed by Hancock et al. (73) as it was discussed in an earlier section. It was also found that orientation increased with annealing.

Flood, White and Fellers (63) studied the orientation of films using WAXS measurements. Pole figures of extruded PPTA film from an annular die with no applied draw force exhibit some c-axis orientation in the machine direction, while the a-axis orientation shows a symmetric orientation about this axis. As draw down increased polymer chain orientation in the machine direction is increased.

Extruded films drawn over a lubricated mandrel show biaxial orientation with the c-axis being approximately equally distributed between the machine and the transverse direction. The a-axis orientation is concentrated on the normal direction of the films. Moreover, biaxial orientation factors were evaluated from the pole figures and values of f_{1c}^{B}= 0.3 and f_{2c}^{B}=0.1 for the extruded film, f_{1c}^{B}= 0.47 and f_{2c}^{B} =0.13 for extruded films with drawdown ratio and f_{1c}^{B}= 0.25 and f_{2c}^{B}= 0.28 for extruded films drawn over the mandrel are obtained.

The SEM photomicrographs exhibit complex void structure near the center of the extruded film cross section produced with little drawdown. Smaller voids were found to be elongated and perpendicular to the machine direction. For the uniaxially drawn down films and those stretched over the lubricated mandrel, the voids have a much lower stage of development and were not visible by SEM.

Qualitative small angle x-ray analysis are reported by Dobb and his co-workers (54,55) for characterization of microvoids in polyaromatic fibers (Kevlar 29 and 49). They also studied supramolecular structure of these fibers using a combination of electron diffraction and electron microscope dark-field image techniques (54). Void size and size distribution of microvoids were estimated. It was found that the presence of voids will effect the

mechanical properties of fibers. They noted that voids tend to reduce both the potential lateral and tensile strengths of a fiber. Moreover, when the voids have a length to width ratio greater than unity the effect will be greater on the lateral than on the tensile properties thus contributing to a low compressional strength. Since such features are located predominatly around the periphery of the fibers then one would expect the low compressional strength to have the most effect on the bending characteristics. In addition to the relatively small effect of the voids on the tensile strength arising from the effective reduction in cross-sectional area, a more marked contribution were found to arise from the observed long (up to 16 μ m) macrocracks lying at small angles to the fiber direction. Fracture would be facilitated by propagation of these cracks over extensive lengths to the weak outer layers of the fiber.

The complex molecular structure of these fibers has been shown to consist of a unique system of radially oriented by axially pleated sheets, each sheet composed of an array of extended molecular chains stabilized laterally by hydrogen bonds (55). From electron diffraction and electron microscope dark-field image techniques they found the angle between adjacent components of the pleat is 170°. These workers claim that this supermolecular structure leads to a periodic banding along the fiber

axis with periodicities of approximately 250 to 500 nm. Periodicities in the 200-1000 nm range,which have been associated with this pleat structure have been observed by electron and optical microscopy (54,121,164,218) electron diffraction (26) and chemical degradation (18). Shorter periodicities of about 20 nm have also been reported from small angle x-ray analysis,electron microscopy and chemical degradation studies (29,166,167). The latter periodicities have been associated with defect layers.

In conventional polymers an alternation of crystalline and disordered (amorphous) regions gives rise to x-ray scattering at small angles which is identified as the long period. The scattering is usually in the form of one or more discrete maxima. In PPTA, discrete scattering maxima corresponding to the defect period have not been usually observed using CuK α radiation. However, the absence or extreme weakness of the meridional x-ray scattering at small angle reported by Panar et al. (131) in PPTA fibers is consistent with a limited amount of material in the defect layers and/or with a small difference in electron density between the defect layer and the rest of the fiber. The high crystallinity of their fiber indicated that the observation by Dobb et al. (55) seems to be consistent with a higher level of defects in the weaker fiber. The higher defect level is presumably either sufficient to decrease

the electron density of the defect layer relative to more perfect zones or to broaden the defect layers and thus permit a detectable level of scattering.

However, this meridional small angle x-ray scattering in PPTA fibers has been detected using techniques involving soft (low-energy) radiation from carbon and aluminum sources (131). The defect spacing of 35 nm higher than the value obtained by Dobb et al. (54) is reported.

Fibrillar structure and skin core superstructure seen by Hancock et al. (74) and by Bheda, Fellers and White were also studied by Panar et al. (131). In their studies of morphology of PPTA fibers they reported that their fully crystalline fibers has a fibrillar morphology with the individual fibrils having a high proportion of extended chains passing through periodic defect layers. They added that the major distinction between PPTA and concential fiber lies in the high level of extended chains passing through the defect layers of the former structure. The fibrils reported to be about 600 nm in cross section and being joined by tie bundles, groups of chains which wander from one fibril to an adjacent one. Fracture and crack propagation leading to fiber spliting and fibrillation and reported in detail elsewhere (120).

Another important morphological feature of liquid crystalline material is the skin-core superstructure observed by various investigators (86,131,174). The skin-core

differentiation is related to the orientation and perfection of chain packing across the fibers. Examination by Panar et al. revealed that the skin portion can be nulled when it is parallel to the polarization direction of either the polarizer or analyzer of the microscope. The core, however, can not be nulled at any angle. Such observations were explained in which the surface fibrils are uniformly axially oriented while the fibrils in the core are imperfectly packed and ordered.

Thermotropic fibers and films. As it was mentioned earlier liquid crystalline polymers orient readily during flow, and this property is exploited in spinning high modulus fibers from lyotropic solutions. In such fibers the molecules are thought to be highly aligned along the fiber axis. However, when viewed with polarized light, it is found that the fibers exhibits a series of fine bands running perpendicular to the fiber axis (164). This same banded structure has recently been observed in a range of thermotropic polymers oriented by shear (57,86). Although the detailed analysis of the supermolecular organization within thermotropic liquid crystalline polymers is not fully completed, it is clear that the banded structure observed for these materials is remarkably similar to that reported in lyotropic polymer systems. It is therefore apparent that such structures are a general feature of

liquid crystalline polymers which have been oriented by flow. However, from information in the open literature it is not yet clear whether their formation is induced directly by flow or whether they represent some stage of a relaxation process (57,98).

Recently Viney et al. (187) and Donald et al. (57) in their studies have claimed that observation of sheared thermotropic polymers using polarized light microscopy and transmission electron microscopy indicated that the banded structure arises from a serpentine trajectory of the molecules about the shear axis. The orientation of the molecules thus changes smoothly with position along the shear axis, such that the orientation lies constant along lines perpendicular to this axis. Such a smooth variation is in contrast to the sharp changes in orientation proposed in the "radial pleated sheet" model for Kevlar fibers (54).

Donald and Windle (57) in their more recent paper confirmed that the "segregation" of molecular orientations implicit in the banded structure model does indeed occur. In addition, they found that the period of the banded structure is decreased markedly with increase in shearing temperature.

Zachariades and Logan (207) studied orientation and morphology of the thermotropic aromatic copolyester of poly (ethylene terephthalate) and 80 mole percent

p-acetoxybenzoic acid. Fibers and films of various type were made. The structural features of both the oriented films and the drawn fibers found were to be the same. The banded structure was found as reported by Donald and his co-workers (57,187).

The development of the ordered bands perpendicular to the shear direction in the oriented films which were prepared by shearing the low melt viscosity mesophase at 335 C^{o} were similar to those observed in the oriented films of the random PHBA/PET 60/40 copolyester prepared by shearing the mesophase at 290°C (207) and with other thermotropic polymers (57). The observation of ordered bands or domain-like interfaces perpendicular to the shear direction is an optical effect observed also with low-molecular weight nematic liquid crystals in the presence of electric and magnetic fields or under mechanical stress conditions (195). The separation of the bands in thermotropic material may very from 1 to 100 μ m. This is dependent on the fiber or film thickness and the frequency of the applied field.

Another morphological feature similar to those of lyotropic material is the fibrillar structure seen in a thermotropic system (195). SEM photomicrographs indicated that the anisotropic morphologies of the films and fibers were fibrillar. The electron diffraction patterns from a selected area indicated that only the straight fibrillar

morphologies which were prepared below 328°C show discrete equatorial and meridional arcs consistent with the spacing of the rigid PHBA domains and the pure PHBA homopolymer(207,208). The diffraction patterns of the fibrillar morphologies, which were prepared from the higher temperature mesophase at 330°C, showed diffuse equatorial and wider meridional arcs. The loss of order in the fibrillar morphologies from the higher temperature mesophase is believed to be due to the loss of the three-dimensional order of the PHBA segments, the randomization of the semirigid chains of randomly distributed PHBA and PET units and flexible PET chain segments, and some relaxation (207,208).

Orientation development in thermotropic liquid crystal polymers is reported by Ide and Ophir (86). The extrudates were drawn down and taken up at various ratios. Samples with virtually no draw down did not show any molecular orientation although it was extruded with a high shear rate. With increasing drawdown ratio the orientation was found to increase as do the tensile strength and modulus. For gravity spinning, an extrudate skin-core morphology was observed. More detailed study of the development of structure during injection molding process of thermotropic copolyester is also given by Ide and Ophir (86). Injection-molded articles also showed distinct skin and core morphology. This orientation

difference as explained by elongational flow history. The molten polymer injected into the cavity reaches the flow front and goes through "fountain flow", where it experiences a strong elongational flow, the oriented melt is deposited near the wall. The portions at the center are injected late and can not reach the flow front. Thus the portions near the wall are highly oriented (skin) but the middle portions are not oriented (core).

The same structure development mechanism during injection molding is also reported by Baird and Wilks (21). They found that their injected molding articles exhibited little shrinkage in the surface layer due to the high orientation of 40/60 (Pet/PHB) molecules on the outer skin.

Furthermore the extrudate rearranges to a flat velocity profile so that the fluid element near the surface must be stretched and oriented while those at the center must be compressed. Such elongational strain mechanism together with the yield stress behavior and large shear strain along the entrance of the die as indicated by Shimamura et al. (162) would seem responsible for the skin-core differentiation. They (162) added in their melt spinning studies that filament orientation is not a direct function of elongational stress.

In contrast to orientation development in aromatic thermotropic copolyester as a function of shear and

elongational flow, Ide and Ophir (86) found that high molecular orientation is readily obtained by elongational flow but not with shear flow. Specifically extraordinary orientation is obtained with small elongational strains, but shear strain or shear rate found to have little effect.

Some cellulose derivatives can form thermotropic liquid crystals as reported in the review article by Gilbert et al. (66). However, the development of the structure and orientation during melt spinning of a cholesteric cellulose derivatives as described by Shimamure, White and Fellers (162) are in analogy to the case of lyotropic systems discussed earlier.

Mechanical Properties

In recent years, considerable interest has developed in the study and use of polymers that exhibit liquid crystalline order in solution or in the melt. These polymers however, can potentially produce materials with a high degree of orientation and excellent mechanical properties. Several successful technologies based on these characteristics of rod like polymers have been developed, and the technology of aramide fibers spun from anisotropic solutions attracted a great deal of attention (46,102,193).

On the other hand the technology of thermotropic

On the other hand, the technology of thermotropic polymers is still in the phase of development. At the present time the interest in this class of polymers is due to their simple processing and relatively high melting temperature. Most of the development has been in the area of plastics. Research in the area of fibers and injection mold plastics of such materials is also reported in the literature (1,57,86). In contrast with lyotropic polymers, high molecular weight rod-like polymers cannot be subjected to large extensional or shear flows without chain breakage, and only relatively low molecular weight thermotropic polymers are processible from the melts (46). Therefore, most thermotropic polymers currently known cannot be prepared and extruded into fibers at a sufficiently high molecular weight to achieve a high level of mechanical strength as aromatic polyamide fibers (Kevlar).

Aromatic polyamides such as poly (1,4-benzamide (PHB) and poly (p-phenylene terephthalamide (PPTA) exist in solution preferentially in highly extended chain conformations (14). This is reflected in very high values (1.7) of the exponent a in the Mark-Houwink relationship ($[\eta] = K M^a$ where K and a are constants and M is the molecular weight),as well as in high values of chain persistence length (300-400 Å) (14). Above a critical concentration of polymer in solution, these polymers exhibit lyotropic mesophases that are the key factor in the formation of ultrahigh modulus, ultrahigh strength

materials. The spinning of anisotropic solutions into fibers can lead to products of nearly perfect orientation without subsequent stretching of the extruded and solidified filaments. These results suggest that the lyotropic mesophases consist of highly oriented polymer chains. It should also be noted that the degree of orientation achievable by spinning of the lyotropic dopes can exceed that of fully drawn melt-spun fibers from flexible polymers such as polyester or nylons (47). Strength and modulus of fibers produced from anisotropic solution can be very high (3.0-3.5) GPA and 600-1000 GPA, respectively (46,47). This implies a large degree of structural perfection in addition to nearly perfect orientation. Kevlar-type aromatic fibers at the present time, represent the most important technological development based on the chemistry and physics of liquid crystalline high molecular weight polymers (47).

Spinning of fibers from nematic dopes and their properties of such fibers have been reviewed extensively in literature. Since the appearance of the reviews by Schaefgen et al. (159) and White and Fellers (193) some new relevant findings appeared in the scientific or patent literature. Totally aromatic rigid-rod polymers have also been reported by Wolfe and his co-workers (199). These consist of aromatic and hetrocyclic units. The presence of such aromatic and aromatic hetrocyclic

units assures excellent thermal and thermo-oxidative stability, which is important in aerospace applications (199). The elastic modulus of these polymers such as poly (p-phenylene-benzobisthiazde) PBT can reach as high as 250 GPA, with twice the modulus of Kevlar 49 (11). However, a strength of 2.4 GPA and elongation to break of 1.5 percent appears inferior to Kevlar.

Another important development is the spinning of cholesteric dopes of cellulose in aqueous solution of a cyclic amine oxide, such as N-methylmorpholine N-oxide, to yield fibers with strengths of the order of 1 GPA (213). Oriented cellulose films and fibers from a mesophase system were reported later by Chanzy and Peguy (43). They emphasized that cellulose mesophases provide access to new ways of orienting cellulose. This finding has some importance as it may open the way to highly oriented cellulose fibers with modulus close to the theoretical value.

Cellulose derivatives from liquid crystalline solutions also are reported in literature (29,132). The wet spun solution of cellulose triacetate(CTA) and mixture of trifluorocetic acid/methylene chloride into fibers gave strength of 3.5 g/den (132).

Mechanical properties of Kevlar films have been reported by Flood et al. (63). The modulus of the films were found in ranges of 0.2-8.3 GPA. The uniaxially

oriented films showed tensile strength of order 0.28 GPA in the machine direction and about 0.0075 GPA in the transverse direction. The biaxially oriented films showed tensile strengths in the machine and transverse directions of 0.05 GPA.

Another important factor improving mechanical properties of lyotropic materials is the annealing process. Annealing Kevlar fibers under tension at temperatures of 300-500°C is known to create a marked increase in modulus and tensile strength (112). Typical modulus, tensile strength and percent elongation values for Kevlar fibers, however, are reported to be 83, 3.6 GPA and 4.4 percent, respectively.

In the case of thermotropic, aromatic polyesters which form mesophases first were melt spun into fibers by Tennessee Eastman and DuPont investigators(100,106). In attempting to enhance the mechanical and physical properties of the amorphous polyethylene terephthalate, Jackson and co-workers (88,89,120) prepared a compositional series of copolyesters of polyethylene terephthalate and p-acetoxybenzoic acid (PHBt). They reported that the melts of the copolyesters of polyethylene terephthalate with p-acet-oxybenzoic acid contents greater than 30 mole percent (PHBt) were liquid crystalline and the copolyesters could be injected molded into high-modulus ($\simeq$ 12GPA) specimens. The maximum mechanical performance

were observed (flexural modulus 17.2 GPA and tensile strength 107 MPA) with the copolyester of PET and 60 percent PHBA and improved remarkably as the thickness of the specimen was reduced from 0.5 to 0.1 inch.

However, the injection-molded specimen of the copolyester of PET and 80 mole percent in PHBA by Zachariades and Logan (208) exhibited lower mechanical performance although a higher performance was expected assuming a random distribution of the PET and PHBA units in the copolyester increased from 60 to 80 mole percent. These lower values of modulus and tensile strength obtained by Zachariades et al. (208) in their oriented fibers and films were explained to be due to the heterogeneous structure developed at temperature below 329°C. They found that the mechanical performance of the oriented specimens (films and fibers) were dependent on their structure. The considerable increase in the tensile strength and the four times and eight times increase in the modulus of the films and fibers were obtained above 329°C which they believe to be due to the chain continuity in their morphologies and the higher shear conditions in the fiber drawing process.

Acierno et al. (1) studied the influence of operating conditions and draw ratio on the mechanical properties of two samples of PET/PHB containing 30 and 60 mol percents p-oxybenzoate. These polymer melts were extruded at

various temperatures ranging from 225-285 ^{o}C into air at room temperature. The spun filaments were taken up at various take-up velocities between 10 and 300 m/min. As-spun filaments were then subjected to additional annealing or drawing treatments. They found that modulus increases with draw ratio but decreases with increasing extrusion temperature. The highest modulus obtained was about 32 GPA. This is well within the ultrahigh modulus range (46). It was also found the modulus increased by annealing. Their values of modulus and strength for samples with 60 mol percent p-oxybenzoate were higher than values reported for the same material by Tennessee Eastman investigators (88,106). A possible explanation of this discrepancy may be due to the fact that these fibers have a greater orientation than of the injection-molded samples, which is particularly effective the lower processing temperatures.

F. Diffusion and Permeation Behavior of Polymer Films

The diffusive transport of gases and vapors in polymer solids is of practical interest since polymer membrances play an important role in many technical biological processes.

The first definitive description of the mechanism of permeation of small molecules through polymer films is reported by Graham (82) in 1866. The process was

described as the condensation and solution of gas at one surface followed by diffusion through, in the form of a liquid, and evaporation to the gaseous state at the other surface. The observation was also made that those gases penetrate most readily which are most easily condensable and most soluble in water or other liquids.A correlation was also made between the solubility of the gas in rubber and its rate of passage through the film. The non-porous nature of the rubber and its similarity to a liquid rather than to a solid were emphasized and the effect of increasing temperature was correctly discussed as causing an increase in the softness or liquid nature of the rubber leading to a greater rate of penetration, even though the solubility of the gas was considered to be reduced by increasing temperature due to the reduced ease of condensation. A reduction in the solubility of carbon dioxide in rubber when the latter was vulcanized was noted. Also the value of rubber membranes for the separation of gases was stressed and quantitatively demonstrated.

A few years later, in 1879, Wroblewski described that the solubility of gases in rubber obeyed Henry's law (the solubility is proportional to the partial pressure of the gas). Then he applied Fick's linear diffusion law as for free gases and liquids and first combined these two simple relationships to formulate the well-known

permeability equation

$$J = D_{\circ} S_{\circ} \frac{P_1 - P_2}{L} \qquad (79)$$

Where J is the amount of gas passing though unit area per sec, D is the diffusion constant, S is the solubility coefficient and P_1 and P_2 the partial pressures of the permeating gas at the two sides of the membrane of thickness L. The product D.S. is termed the permeability constant. As a rule, S.D. and P are functions of local concentration of permeation or of the gas pressure in equilibrium with the local concentration. In the case of liquid permeation, one usually introduces a partition coefficient as the ratio between the concentration of the permeation in the membrane and in the free liquid outside the membrance (82).

However it is important to note that detailed studies into the mechanism of the diffusion of small penetrant molecules in high polymers are simplier with gases than with water vapor or organic vapor. The vapors are complicated in that their solubility is not directly proportional to the pressure (ie., Henry's Law is not obeyed). Furthermore, the diffusion constants are often highly dependent on the concentration of penetrant in the polymer. The situation is much less complicated with the gases since Henry's Law is obeyed and the diffusion constants are independent of concentration.

For the reasons indicated above gases are preferred for studies into the mechanism of sorption and diffusion and on the effects of polymer structure and morphology and other features. It should also be stressed, that studies into the diffusion and sorption of vapors are of great interest and yield additional data of value concerning the effects of polymer-penetrant interaction on the transport process (49).

When the diffusant component has a molecular size much smaller than the monomer unit of a given polymer and the thermodynamic interaction between the two component is very weak, a limited rotational oscillation of only one or two monomer units would be sufficient to give a cross-section for the diffusant molecule to jump thermally from one position to a neighboring one. The diffusion of simple gases, such as hydrogen, argon, nitrogen, and carbon disulphide, in ordinary polymer substances and of water in hydrophobic media usually involves such a molecular mechanism. Molecules comparable with, or larger than, the monomer unit of a polymer require for their diffusion a co-operative movement by the micro-Brownian motion of several monomer units. Such substances include most organic vapors, which are either swelling agents or solvents for ordinary polymers. Many features of their diffusion reflect the micro-Brownian motion of long-chain molecules and thus are unique to

polymer systems. Recent work has demonstrated that sorption and permeation, which are typical diffusion controlled processes, of organic vapors in polymer solids exhibit different features for different polymers (170).

Most of the work on diffusion and permeation reported in the literature have dealt with gaseous substances and water vapor in polymer solids. Published diffusion and permeation data on organic vapors are very limited and mainly concerned with glassy polymers (114).

The effect of orientation on the transport properties of films have been reported by various investigators (16,85,87,115,137,186). The permeabilities of both crystalline and non-crystalline polymers have been shown to decrease with increasing orientation. Among those which exhibit this behavior are polyethylene (87, 116) polypropylene (85,87) polyvinyl chloride (82,87) polycarbonate (87) and polyethylene terephthalate (85, 87,186).

Although the permeability decrease for polyethylene was shown to depend upon the method of orientation (87), it has not been firmly established whether or not diffusivity always decreases proportionately with the degree of orientation (87). However, there are evidences that the mode of orientation such as uniaxial versus biaxial affects the relationships between transport parameters and orientation (82,148).

Brady, Jabarin, and Miller (82) investigated the

effects of temperature, stretch rate, and degree of biaxial orientation on the transport properties of poly (vinyl chloride) including oxygen permeability, diffisivity and solubility, and water vapor permeability. They reported that permeability decreases with increasing orientation, but exhibits a minimum as a function of stretch temperature and stretch rate. Although diffusivity decreases with increased orientation, little change in diffusivity was observed with stretch temperature. They (182) found an increase in molecular "order" with annealing temperature and time using x-ray diffraction and thermal techniques. They suggested that microstructural changes caused by annealing plays a strong role in determining the final permeability level.

Recently Paulos and Thomas (137) in their studies of blown high density polyethylene (HDPE) films investigated the effect of orientation on the structure and transport properties of produced films. They reported that uniaxial orientation has a marked effect upon the film permeability characteristics. Upon orienting the film to a draw ratio of 10X created 90 percent reduction in water vapor transmission. Extruded bubble orientation and post orientation temperature were also found to be effective upon water vapor transmission. Increasing the extrusion draw down ratio from 1.7 to 2.4 resulted in a 40 percent decrease in water vapor transmission. Furthermore,

over a 50 percent reduction in water vapor transmission was observed when the post orientation process was conducted at 100°C instead of 127°C due to a higher degree of sample orientation retained at lower temperature.

Other important factor effecting permeation and diffusion in polymer is the degree of crystallinity. Peterlin (141) carried out extensive studies of the dependence of diffusive transport on morphology of crystalline polymers. He noted that crystalline polymers with more or less regular alternation of extremely thin crystalline and amorphous layers demand a substantial modification of the description of transport properties. Most of the transport takes place through the amorphous layers while the crystals are practically impermeable. The elastic tensile deformation enhanced sorption and diffusion by reducing the density of the amorphous component. He added that, the high anisotropy of diffusion and the drastic reduction of sorption and diffusion of fibrous material are the consequence of the microfibrillar morphology with the large fraction of highly aligned and closely packed taut tie molecules which eliminate many sorption sites, enormously reduce the diffusivity and increase its concentration dependence. Also the transport properties are extremely sensitive to any change of chain arrangement which yields a change in fractional free volume in the amorphous region. Annealing lets the crystals

grow in their thickness, removes crystal defects, sharpened the boundaries between crystalline and amorphous component, relaxes the taut tie molecules and results in a drastic decrease in permeability and sorption.

The influence of drawing on the transport properties of gases and vapors in polymers have been studied by other investigators (137,194,204). Williams et al. (194) have shown that drastic decreases in transport behavior do not always accompany drawing. In fact, the extent of decrease in the transport behavior is mainly dependent on the medium in which the material is drawn. Under certain drawing conditons, the rate of diffusion can be actually increased. This increase in transport behavior can be very substantial, often several orders of magnitude higher than the undrawn materials. In the case of cold drawing, plastic deformation was found to reduce the number of sorption sites and increase the activation energy of diffusion, but it does not change the energy conditions at the sorption sites. These changes in the sorption and transport properties were considered as being a direct consequence of the denser packing and ordering of the tie molecules in the amorphous regions brought about by the cold drawing process. Similar effects have been noted by other researchers (50,180) using different penetrant-polymer systems.

Gas permeability of deformed polyethylene films are

reported by Yasuda et al. (204) and Paulos and Thomas (137). Yasuda et al. concluded that the transport properties of low-density polyethylene film under strain and after drawing or rolling demonstrate the basic difference between elastic and plastic deformation. In elastic deformation, the sorption, diffusion, and permeability increase with strain. This is due to the increase of fractional free volume as a consequence of the increase of specific volume of the film under tensile strain. Their results indicate that leveling off of diffusivity and permeability with increasing strain and the subsequent drop below the values of unstrained material can be interpreted as a result of the recoverable plastic strain. The continuing increase in sorption excludes the interpretation in terms of reduced fractional free volume which would yield a simultaneous decrease of sorption and diffusion.

Transport properties of cellulose acetates cast films are reported by Lonsdale, Merten and Riley (109). They measured the gross transport properties in two types of experiments, one involving normal osmosis, the other reverse osmosis. Diffusion and distribution coefficients of water and sodium chloride have been measured. They found that the diffusion coefficient of water varies from 5.7 to 10^{-6} to 1.3 x 10^{-6} cm^2/sec. and the diffusion coefficient of salt varies from 2.9 x 10^{-8} to 3.9 x 10^{-11}

as the acetyl content is increased from 33.6 to 43.2 wt percent. They also studied the effects of the degree of crystallinity on the water sorption of cellulose acetate. Moreover, water vapor sorption by amylose and cellulose acetates are also investigated by Baernes, Skaar and Luner (27). They prepared three different cast films from cellulose diacetate, amylose diacetate, and cellulose triacetate. Heating cellulose acetate at 70° C for 4 min. was shown to have little effect on sorption but increasing the acetyl content (CTA) reduced both the hydrated, or surface-bound, water and the water of solution. Amylose acetate sorbed less of both hydrated water and water of solution, and heating at 120°C for 30 min. reduced the water of solution considerably. This was attributed to a higher degree of ordering crystallinity, resulting in a decreased availability of sorption sites and surface area in the amylose polymers.

CHAPTER III

EXPERIMENTAL METHODS AND PROCEDURES

A. Materials

Polymers

The polymers used in this study are cellulose triacetate type RB-95 supplied by the Celanese Fibers Company and Kevlar® 29 quarter-inch staple fiber provided by E.I.DuPont de Nemours.

A powdered form of CTA type RB-95 with the degree of substitution (DS) 2.92 was selected since it dissolves more easier than other types such as KB-175. The viscosity of RB-195 in 91 percent weight methylene chloride, 9 percent methanol is reported by the manufacturers of this polymer to be 116 cps.

DuPont Kevlar 29 which has been identified by various investigators as being (p-phenylene terephthalamide) has been abbreviated in this study as PPTA. PPTA was washed with Fisher Scientifics purified carbon tetrachloride to remove surface treatments.

Solvents and Non-Solvents

Fisher reagent grade 96 percent sulfuric acid and fuming sulfuric acid with 30 percent excess SO_3 were

mixed in order to obtain 100 percent sulfuric acid. Dichloroacetic acid purified was supplied by Fisher Scientific, and 95-97 percent formic acid was from Aldrich Chemical Company.

Non-solvents were used for coagulation of the polymer dopes in wet extrusion experiments. Both the coagulants, isopropanol and methanol, were industrial grades from Fisher Scientific Company, water (H_2O) was added to methanol to obtain desirable coagulant concentration of MeOH- H_2O.

The silicone oil used in the procedure of degassing the polymer solutions was Dow Corning 200 with the viscosity of 100 centistoke. Sears 10W-40 "weight" hydro-carbon mineral oil with viscosity of 170 centipoise was used for the mandrel process experiment.

B. Preparation of Solutions

PPTA-H_2SO_4 Solutions

Solvent History. In order to prepare a solution of PPTA/H_2SO_4 a solvent of 100 percent sulfuric acid must first be prepared. This was done by adding fuming sulfuric acid to 96 percent concentrated H_2SO_4. This procedure is as follows;

1. About 150 ml of distilled water is placed in a 400 ml breaker. This beaker was stirred using a stir

bar and a magnetic stirrer.

2. Four to five drops of phenolphthalein indicator is introduced into the beaker while the stirrer is turned on.
3. A 5 ml glass syringe fitted with a #18 needle is used to draw 3 ml of concentrated sulfuric acid.
4. This needle was removed and replaced by a Teflon^{R} stopcock fitted with a #23 needle.
5. The syringe, stopcock, and the needle assembly were then weighted.
6. About one ml of concentrated sulfuric acid (96 percent) is added from the syringe into the beaker while stirring.
7. After delivering of the acid into the beaker, the needle, stopcock, syringe, and syringe assembly were weighted.
8. The acid-water solution is titrated using 0.5N NaOH.
9. In order to obtain proper results three titrations were usually necessary.
10. The following equation was used to calculate percent concentration,

$$\text{Percent } H_2SO_4 = \frac{(\text{ml base})\ (N)\ (4.9039)}{\text{weight of sample}} \qquad (80)$$

After determination of the sulfuric acid

concentration, the appropriate amount of fuming sulfuric acid was added to bring the concentration to 100 percent. This was done in approximately 300 ml quantities allowing 10 minutes between each mixing for the bottle to cool.

Preparation of PPTA fiber. Kevlar® 29 fibers have an oily coating which must be removed prior to contact with sulfuric acid. This is to prevent any reaction with H_2SO_4 which may result in a degradation of the polymer solution. This procedure is as follows;

1. The fibers were placed in a 2000 ml beaker
2. Carbon tetrachloride was added to the beaker under a ventilated hood
3. This was allowed to sit for about thirty minutes and then agitated by hand using rubber gloves.
4. After squeezing the fibers and remove them from the beaker they were placed in fresh carbon tetrachloride and step 3 was repeated.
5. Upon completion of step 4, the fibers were placed under the ventitated hood covered by paper towels and left for twenty four hours to dry.

Mixing. For preparation of PPTA/H_2SO_4 the dry fibers are placed in 800 ml jar. Usually 123 grams of Kevlar fibers is mixed with 600 grams (330 ml) of 100 percent H_2SO_4 in order to make a 17 percent concentration PPTA/H_2SO_4 solution. Concentrations are determined by weight percent. All the mixing takes place within a dry box

made of poly (vinyl chloride), PVC, and poly (methyl methacrylate), PMMA, filled with nitrogen to avoid absorption of moisture. The photograph of the dry box is shown in Figure III-1.

The mixer is ½ horsepower, General Electric AC motor, contained within the dry box. The mixing procedure for preparing Kevlar-sulfuric acid solutions was carried out as follows;

1. 800 ml jar was first weighted with its Teflon^{R} lid
2. About 375 ml of 100 percent sulfuric acid was introduced into the jar and weighted
3. The amount of PPTA needed for 17 percent concentration was determined and weighted
4. The 800 ml jar contained of 100 percent H_2SO_4, the PPTA wrapped in aluminum foil, two osterizer eight ounce jars with stainless steel blades and caps, one 1000 ml Erylynmeyer flask with stopper, and two Fisher Scientific scoopulas with their handles wrapped with electrical tape were placed into the dry box. The dry box then was filled with nitrogen.
5. The PPTA was added into the jar by hand using the scoopula until all the fibers were placed into the jar. Stirring was first done by hand until approximately homogenuous solution is achieved. The solution begin to heat up as it is stirred.

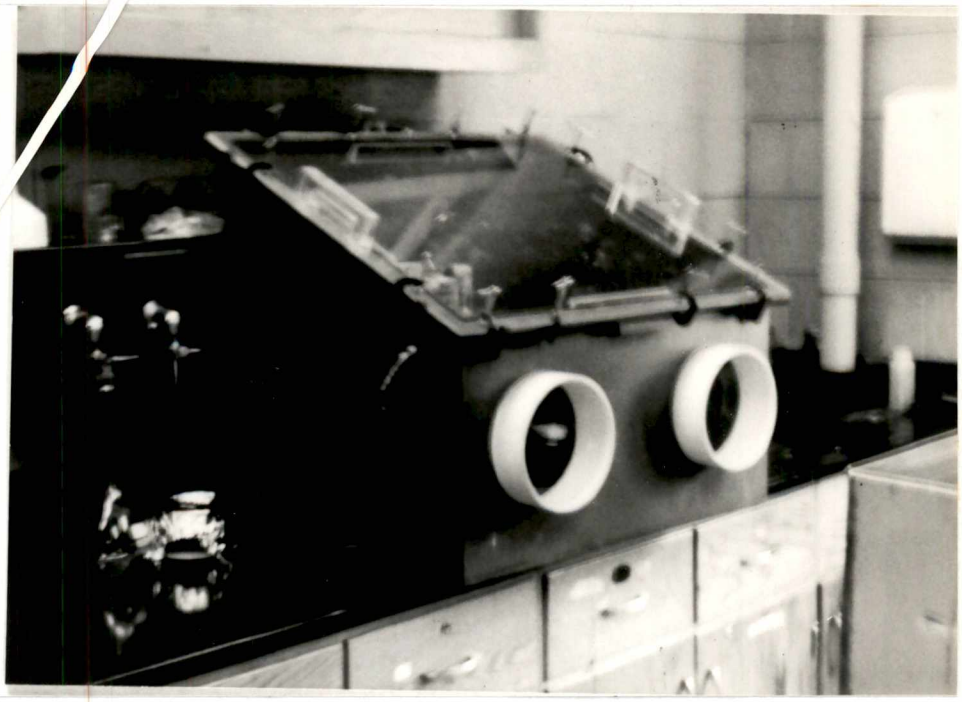


Figure III. 1. Dry box used for preparation of PPTA/H_2SO_4 solutions.

6. Upon completion of step 5, about two thirds of the polymer solution was placed into the eight ounce stirring jar. The stirring jar was then attached to the blender for further mixing of the solution. This mixing was carried out periodically for about 2 to 3 minutes. Between each period the solution was stirred by hand in order to obtain totally homogeneous solutions in which no PPTA can be seen.
7. The remaining polymer-solvent mixture from the 800 ml jar was mixed with about one-third of the newly mixed solution in the remaining stirring jar using the same procedure as step 6.
8. In the last step, the contents of both stirring jars were blended and poured into the 1000 ml flask. The lid was secured on the flask and sealed with Teflon^{R} tape.

Degassing. To produce films without flaws due to air bubbles, the solution must be thoroughly degassed. This was accomplished by applying a vacuum to a fluid PPTA-solution. The flask containing the polymer solution was placed into the silicone oil bath which was heated using a Corning magnetic stirrer-hot plate, model number PC-351. The nitrogen was bled into the flask to prevent water contamination and to control the solution at the desired level. The vacuum pump was used from

Duo-seal and contains a 1/5 horsepower motor. Complete removing of the bubbles usually takes 15-24 hours.

Cellulose Triacetate Solutions

Solvent history. A number of investigators (132, 136,215) have listed several solvents in which CTA forms liquid crystalline solutions. Prominent amongst these are halogenated organic acids. A mixture of dichloracidic acid and formic acid was found recently by Omatete et al. (216) to give liquid crystalline solutions of this polymer. In addition this also had suitable processing characteristics such as viscosity at reasonable temperature (60°C to ambient) and easily coagulated from the polymer solution. Though a mixture of DCA and FA (2:1 by weight) was used.

Mixing. Solutions were formed by taking a measured mass of CTA and adding a measured mass of solvent. Thus the percent concentration are Kg of polymer per 100 Kg of solution. This is different from percent concentration given as gram of polymer per 100 ml of solvent.

The CTA powder form first is dried in the oven at 50°C for twenty four hours. The amount of CTA polymer and DCA/FA (by mass ratio 2:1) for the desired concentration were weighted to be mixed. As an example, a typical 30 percent solution concentration usually

contains about 450 grams of CTA, 700 grams dichloroacetic acid, and 350 grams of formic acid. These quantities are then mixed using a Ross Planetary mixer model 130 LDM. The photograph of the mixer is shown in Figure III-2. This mixer could produce solution from 0.5 Kg to over 5 Kg. The two rotating blades and inside chamber are made of stainless steel. With a proper seal it allows mixing under vacuum, thus degassing the solution simultaneously. This method of degassing was not used as it led to excessive loss of the solvent. By circulating coolant through its double wall, one can control the temperature of the mixing chamber. All the solutions were made at room temperature. Solution concentrations up to 30 percent or more can easily be produced in less than one hour using this mixer.

Degassing. CTA solutions were degassed in a vacuum oven by drawing continuous vacuum on the solution and raising the temperature up to about 50°C. Usually about 1.5 Kg solution is poured into a flat 2-liter crystallization dish and placed on the piece of flat wood in the vacuum oven. The wood is used in order to eliminate contact between the dish and the hot bottom plate of the oven. The polymer solution then swells rapidly under vacuum to a desired level and then put under pressure to break the air bubbles. This was frequently repeated about

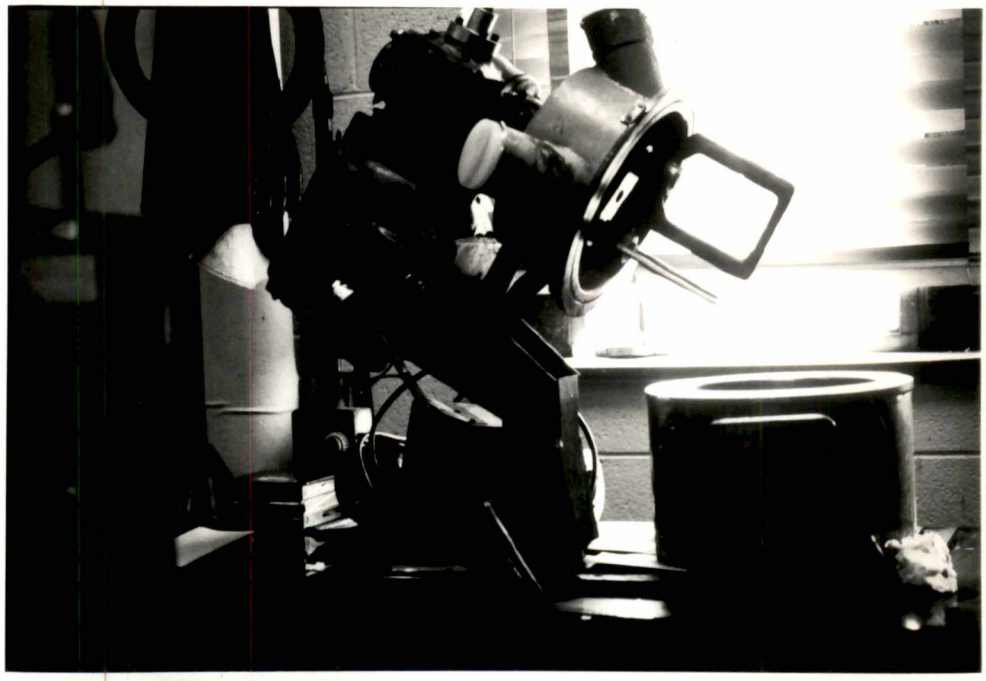


Figure III. 2. Ross planetary mixer.

five times. The solution was then raised to the highest level in its container without overflowing and the vacuum cut off. This was left for about twenty four hours to collapse under its own weight. The temperature of the oven was left at ambient (26°C) during the degassing procedure.

C. Film Processing

Kevlar® Film Extrusion Process

Apparatus. The film extrusion apparatus is shown in Figure III-3. This equipment set up may be divided into three parts;

1. The polymer dope delivery system
2. The die and mandrel
3. The coagulation bath

The polymer dope delivery system initially consisted of a stainless steel reservior into which the polymer solution is poured. The piston is made from stainless steel and Teflon®. The Teflon® provides a seal against the reservior wall to prevent oil leakage into the polymer solution. The extrusion pump is made by Zenith laboratories. It involves a ¼ horse power low speed General Electric motor which operates a gear pump used to transfer the oil from the oil reservior placed above the motor (see Figure III-3a). Changing the motor speed allows one to control the extrution rates.

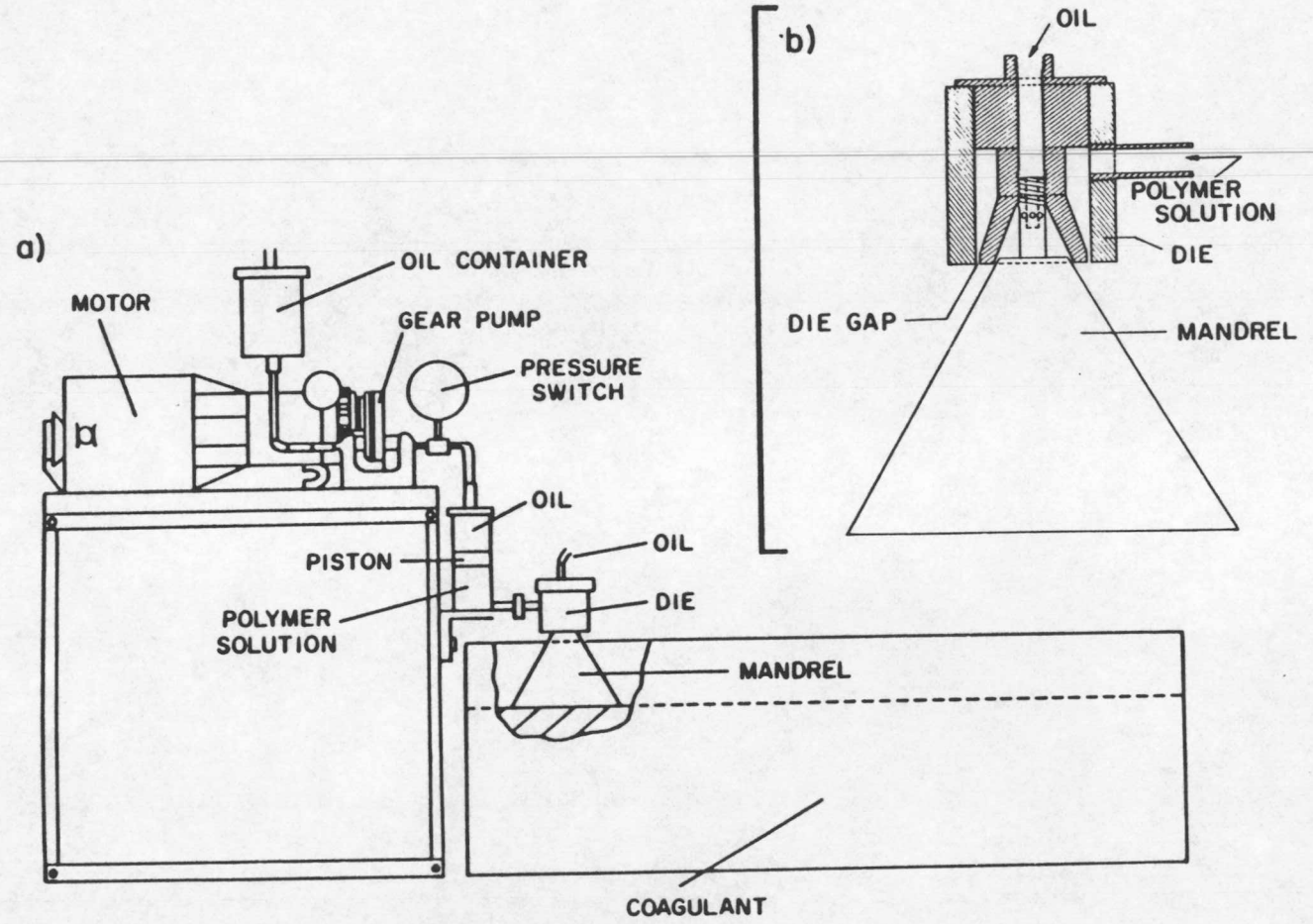


Figure III. 3. Mandrel process for producing biaxially oriented PPTA film.
a. Overview of the process
b. Cutaway view of the annular die and mandrel.

The die is made of type 304 stainless steel and was designed by Aoki et al. (13). The schematic of this die is shown in Figure III-3b. The mandrel is made of poly (vinyl chloride), PVC, to prevent corrosion. The dimensions of die, mandrel, and reservior are presented in Table III-1.

Heating of the reservior and die was carried out using specially fitted band heaters made by Hot Watt of 120 volt 200 Watt, and 120 volt 120 Watt respectively. These heating bands are connected to two Athena temperature controllers with a range of 30°C to 300°C. The thermocouples were iron-constant Teflon^{R} coated.

The coagulaion bath was a 20 gallon (76 liter) capacity rectangular stainless steel tank. This bath is 50 in (1.26m) long, 8 in (0.2m) wide and 12 in (0.305 m) deep. The take-up rollers are also made from stainless steel. They are detachable from the coagulation container. These rollers assist drawing the film without ripping it.

In the mandrel process, the oil is pumped through a 2000 ml sepratory funnel suspended above the die and mandrel over the surface of the mandrel. A valve is used to control the oil flow rate from the sepratory funnel (see Figure III-3).

Processing operation. After the polymer solution is degassed, preparation for film processing is as follows:

1. The polymer solution must be checked via cross

TABLE III.1. DIMENSIONS OF RESERVOIR, DIE AND MANDREL

Reservior	Dimensions	Die (nm)		Mandrel	
Width	20. cm	Radius	34.83	Initial Radius	16.5 mm
Length	126 cm	Annular Radius	25.4	Final Radius	80 mm
Height	30.3cm	Height	80	Height	112 mm
Volume	7.62 $x10^4$ml	Gap	0.03	Angle from Vertical	30°

polarized microscopy for anisotropy

2. The polymer reservior system and the annular die are carefully cleaned and connected. This is critical and all the passages in the die and reservior must be clear of any solid polymer or dust, in order to reduce any blockage of the polymer solution. This also allows for a good seal between the piston and reservior wall.
3. Wire mesh screen used as a filter is placed in plates between the reservior and die
4. Specially fitted heating bands are placed on the reservior and die and connected to Athena controllers
5. Iron-constantan thermocouples are connected to the reservior and die and the desired operation temperature is set on the controllers.
6. The bottom of the die around the gap is usually coated with 10W-40 weight oil to prevent the film from adhering to the die as it emerges from it
7. This set-up is left for about 30-60 minutes so that the operation temperature reaches a steady state
8. Upon reaching the desired temperature, the polymer solution is now removed from the oil bath and poured into the reservior while tilted to minimize air trapped by the solution. About four centimeters should be left in the top of the reservior to allow for insertion of the piston

9. If a biaxial film is to be made, the mandrel is placed into the bottom of the die leaving a gap of 0.4 cm between the die and the top of the mandrel.
10. The coagulation bath is filled with the desired coagulant and the adjustment of the coagulant level to die entrance is made.
11. The draw rollers are connected into the coagulation container in a proper position
12. Both the pump reservior and the separatory funnel are filled with the proper oil. The separatory funnel is stoppered and connected into a nitrogen tank and the stopper is held down by electrical tape.
13. After the solution within the reservior and annular die reached the temperature set on the controllers, an additional five minutes of heating is given to assure that the system is in steady state temperature.
14. The pump is set on the proper extrusion rate and the stopcock is opened to the sepratory funnel allowing the oil to flow over the mandrel. The oil flow rate can be controlled through nitrogen pressure.
15. The solution is extruded through the die and over the lubricated mandrel into the coagulation bath. When the film begins to emerge over the mandrel

surface, the flow rate may be reduced after coverage is obtained.

16. The film is taken-up by hand around the take-up rollers in the coagulation bath.

17. The film exiting the coagulation bath is transfered into a holding tank of water. After several days; the film is cut open, flattened, and dried in aluminum frames for twenty four hours.

For uniaxial film, the operation is the same except the polymer solution is extruded directly into the coagulation bath without using the mandrel.

As the run ends, the apparatus beginning with the die, the reservior, and other connecting parts were cleaned immediately in order to minimize possible corrosion or pitting by the sulfuric acid.

CTA Film Extrusion Process

Equipment. The film extrusion apparatus used in processing of PPTA/H_2SO_4 solutions has undergone several modifications (216). This new system was used to produce CTA films. The schematic representation of this equipment is shown in Figure III-4. In this set up, a hydraulic Dayton model 4Z191 Piston system is used in order to push another piston made from stainless steel surrounded by a Teflon^R seal down into the polymer reservior which was

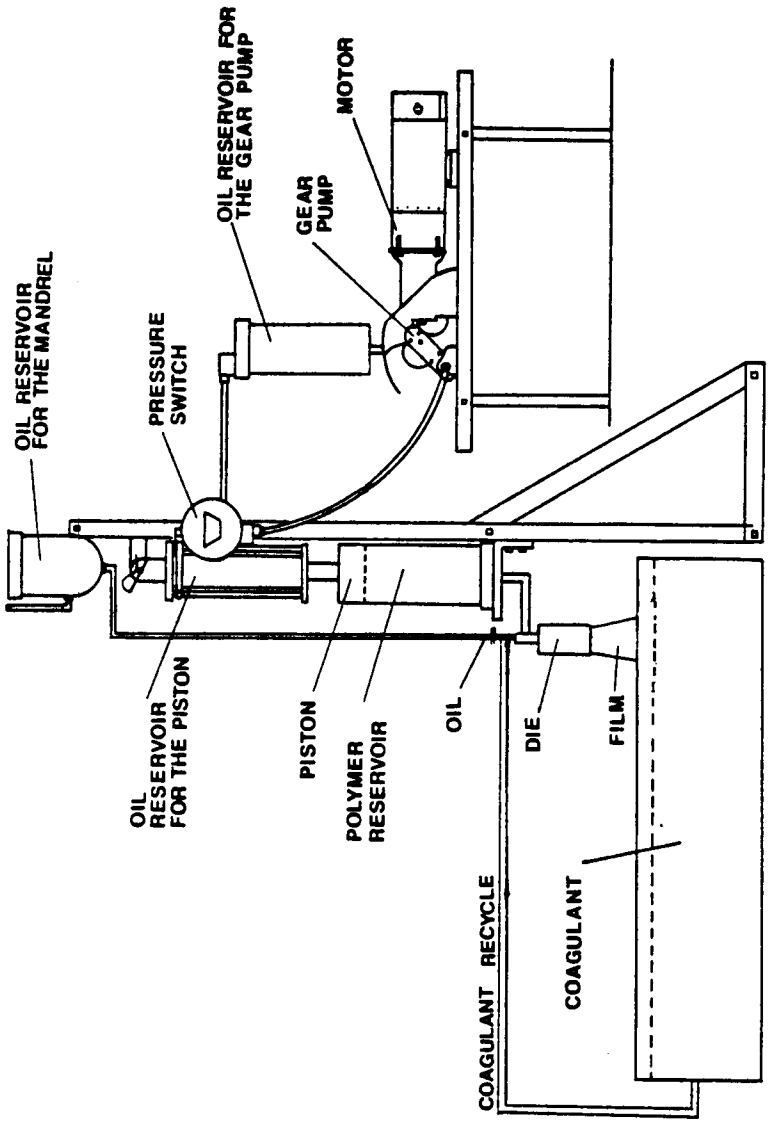


Figure III.4. Wet film extrusion of set-up with coagulant recycle.

nearly twice the capacity (1.3 liter) of the first reservior. In this case, only hydraulic fluid is pumped through the gear pump via a B and B motor type 18 GCT-40 with horse power of 1/3 in a closed system. By flipping a valve, the direction of the piston in the polymer solution reservior could be reversed. Other features are a reservior to deliver lubricating oil to the mandrel, and an automatic pressure controlled shut-off on the hydraulic system. All the parts that come in contact with the polymer solution were made of stainless steel.

The original die (see Figure III-3) with 5.08 cm in diameter, 0.3 mm annular gap, and made of stainless steel, recieved the polymer from the side. It was felt this design produced nonuniform film thickness (13); thus a new die of the same annular dimensions with polymer solution entering from the top and other features ensuring adequate backpressure was designed by Flood et al. (63). This is shown in Figure III-5. This new die does seem to produce film with better uniformity. However, since this die was also made of type 304 stainless steel and it was found in this study that dichloroacitic acid is corrosive to the material, a new die with the same design and dimensions were made from stainless steel type 316. This selection was based on

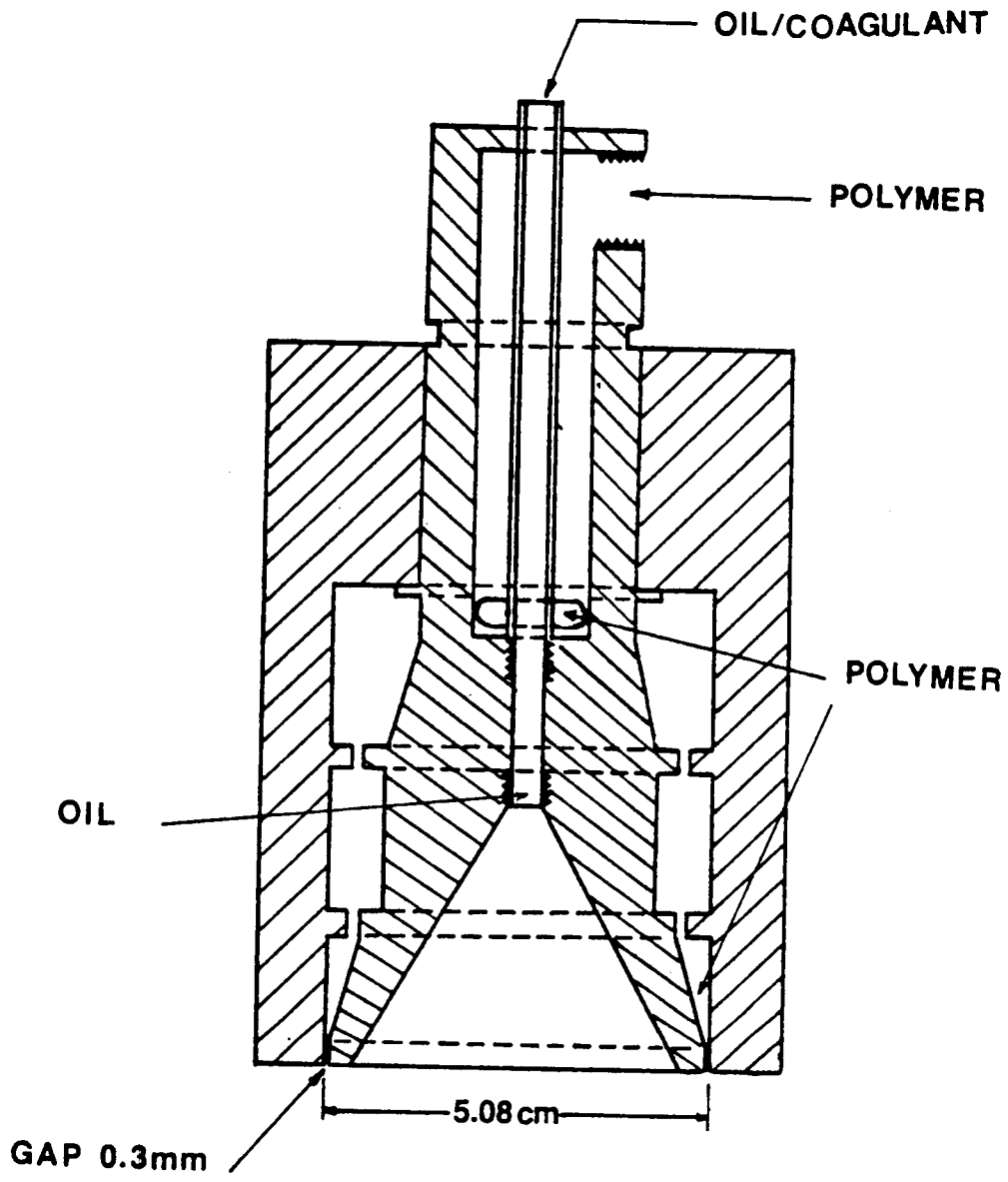


Figure III. 5. Current die design.

experimental corrosion resistance tests to DCA/FA.

A 40 gallon (151 liter) capacity Aminco refrigeration bath with heating and cooling coils and a thermostat for temperature control made by American Instrument Co. was used. This bath contains a pump for recycling the coagulant, not only for mixing thoroughly but also it was used for blowing-up the film to impart biaxial orientation. Take-up rollers were made of stainless steel and may be fitted to this coagulation bath as desired.

This new film extrusion apparatus has been so designed that the die level above the coagulant may be varied with a hand operated 1½ ton hydraulic jack. This is needed for adjusting the air gap between the die and the coagulant for the various types of film production.

Heating of the die and reservior including temperature controllers and thermocouples were similar to those described for PPTA/H_2SO_4 extrusion apparatus.

However, several problems existed in the production of biaxialy oriented CTA films using the recycling coagulant system, that is the coagulant is recycled from the top of the die into the film emerging from it. The first problem was due to the long distance from the die inner hole to the coagulant level in the bath. The fluid was creating a lot of bubbles which lead to breakage of the films. Second, a high blow-up ratio was impossible and third, the coagulation rate of CTA films was too slow.

With regard to these problems the recirculating process was modified. A tube was designed and connected to the die inner hole in such a way that the coagulant spread equally around the bottom of the tube against the inner side of the film. By adjusting a baffle plate at the bottom of the tube, the flow rate can be controlled. This allows one to produce films with various blow-up ratios. Higher blow-up ratios create a decrease in film thickness which leads to a faster coagulation rate of CTA films. This tube is shown in Figure III-6 and III-7.

Processing operation. The processing operation for CTA films are somewhat similar to those of Kevlar films explained earlier. About 1.5 Kg of polymer solution is mixed in the Ross Planetary mixer, poured into a 2-liter crystallization dish and degassed in the vacuum oven. After mixing and degassing the solution, the film extrusion apparatus is set up. The polymer reservior system, the die and the circular tube for biaxial film production are carefully cleaned and connected for operation (see step 1 through 8 on page 158) The bath is filled with isoproponal. Dry ice is added to the coagulant in order to cool it from room temperature to Ca. zero degree centigrade. The refrigeration system is then used to maintain it at that temperature. This was because usually 40-50 hours were taken for the refrigeration

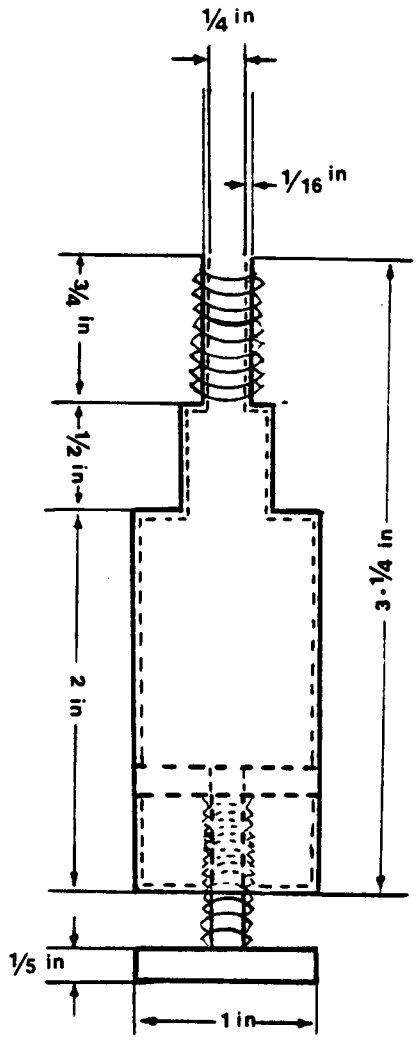


Figure III.6. Circular tube for blowing CTA films.

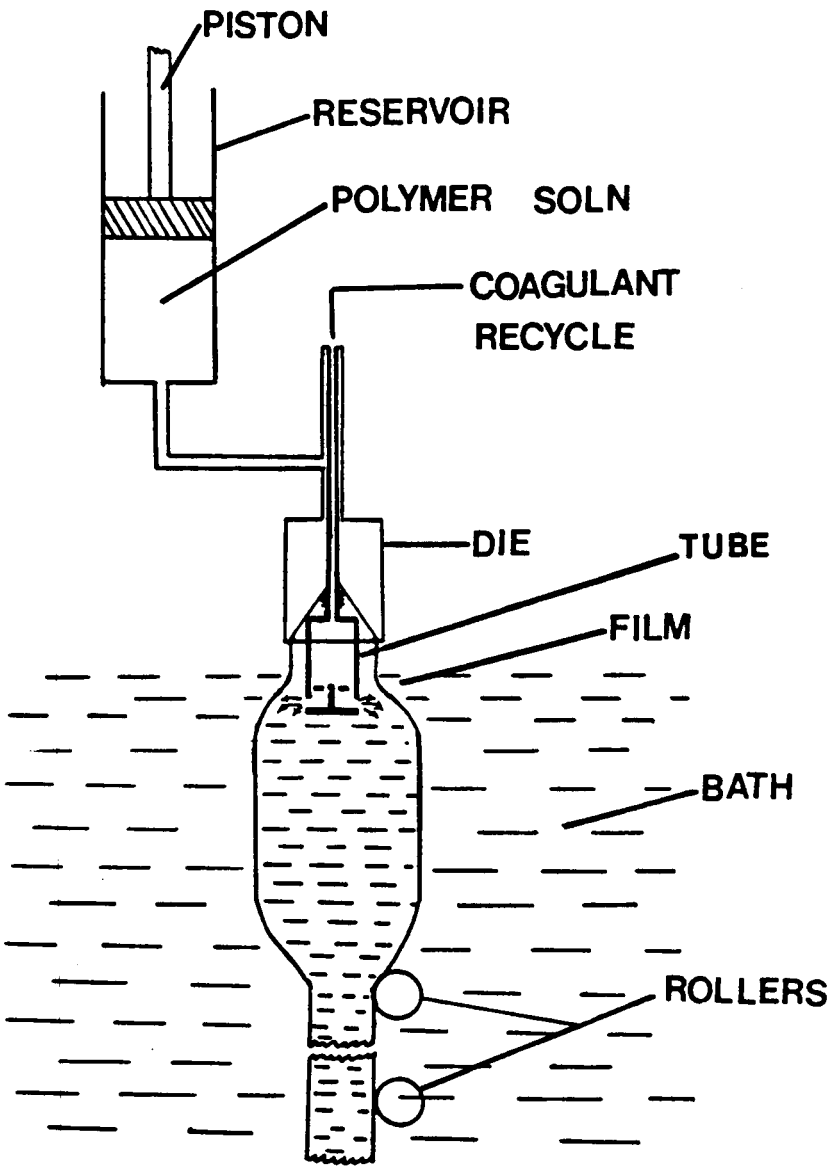


Figure III. 7. Schematic of coagulant blow-up film extrusion.

system to cool the coagulation from room temperature ($26^{o}C$) to about zero degree of centigrade.

After repeating steps 1 through 8 on page 158, and the solution reached steady state temperature, the film can be extruded via a piston connected to the hydraulic system into the annular die. The desired speed is set on the controller of the motor driving the gear pump. For biaxial film production, the circular tube is screwed onto the die inner hole and the flow rate of the coagulant is determined. There is usually an air gap between the die and the coagulant level in the bath but there is not any air gap between the tube opening and coagulant level. The tube is placed inside the coagulant in the bath. The coagulant is recycled from the top of the die into the tube. As the film is pulled through the coagulant and under the first take-up roller its area is constrained, and depending on the adjusted coagulant flow rate varing blow-up ratios can be put in the film (see Figure III-7).

The rest of the operation including the production of uniaxial films are the same as described earlier for Kevlar.

D. Film Characterization

Scanning Electron Microscopy (SEM)

An AMR model number 900 high resolution scanning electron microscope made by Advanced Metals Research Corporation was used. The principal components of this instrument are given in Figure III-8. The films were examined along fracture edges formed parallel and normal to the machine direction and also normal to the film surface. The film samples to be sued for fractured edge photomicrographs were mounted in slotted sample holders with epoxy glue. To obtain photomicrographs from the sample surface, the films were glued flat onto the sample holder surface. The uniaxially oriented films were nicked with a razer blade and peeled to investigate the internal structure of the films. This was done by mounting the samples horizontally on aluminum sample holders over double-sided adhesive tape as shown in Figure III-9. After the samples were mounted (on mounting stools), they were sputter coated with gold-palladium in a vacuum chanber. The coating of metal on the polymer films proved to be extremely important to obtain the higher magnification micrographs without charging in the electron beam.

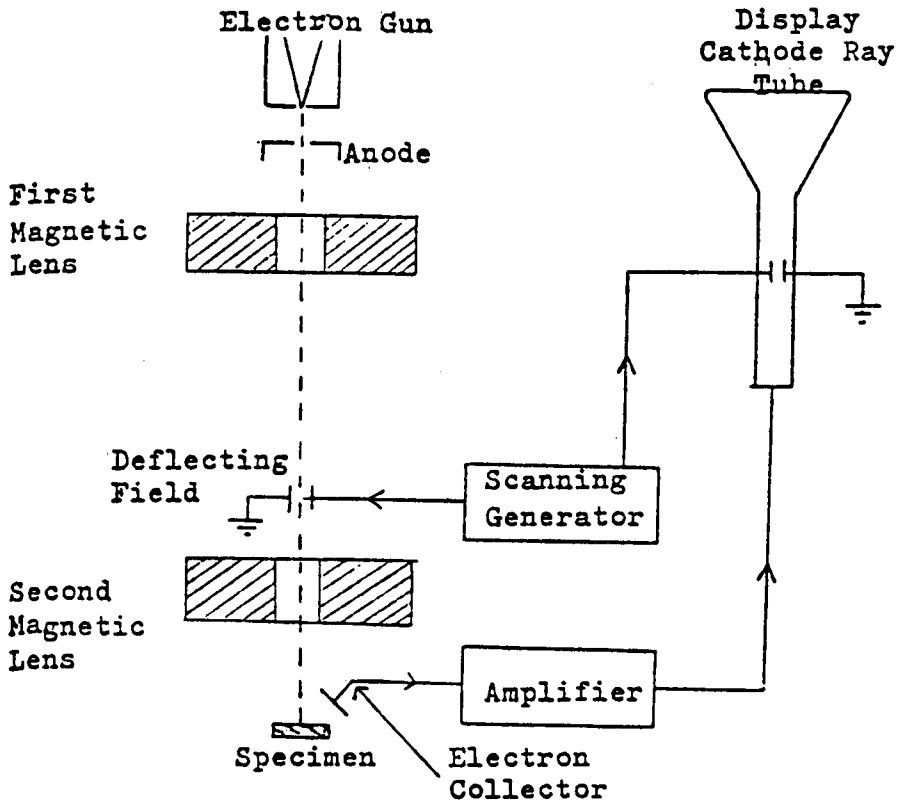


Figure III.8. Principle of the scanning electron microscope.

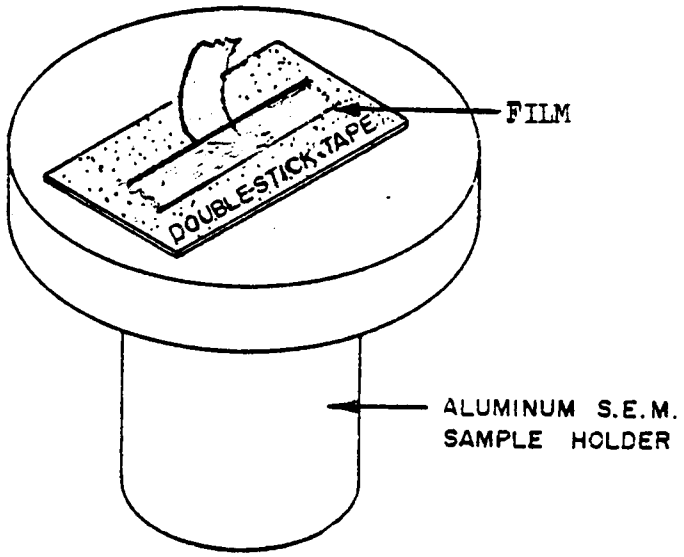


Figure III.9. SEM sample mounting technique.

Mass Density

The densities of the films were determined using density gradient columns. Three columns were constructed from isotropyl alcohol and distilled water and from sodium bromide and distilled water. The density of Kevlar film sample 1 was determined using the first column (isoproponal-H_2O), while the latter columns were used for the rest of the samples. The construction of these columns were according to a technique described by Tung et al. (217) and Wiley (218). In this technique a linear column is made by continuous mixing of a heavy and a light solution. Two solutions, a more dense one (A) and a less dense one (B), are kept in equal volume communicating vessels while a steady stream of the heavy liquid is continuously drawn to fill the column. The pressure differential caused by the depletion of solution (A) causes fluid to flow from the liquid (B) to the heavy solution (A) container. If the more dense side is kept well mixed, as the density gradient column is being filled, a linear gradient will result as a consequence of the linear variation of the density in vessel (A) with time. All the film samples were added into the column at room temperature ($26^{o}C$) for approximately twenty four hours to reach their equilibrium values.

The experimental details and calculations are shown in appendix A.

Differential Scanning Calorimetry (DSC)

A model DSC-2 Perkin Elemer Differential Scanning Calorimeter was used to investigate the transiton temperature of one CTA film. This was first done for CTA sample number seven (30 percent concentration, blow-up 3.3X) to select an annealing temperature. However, as the study progressed the need to measure the heat of fusion (ΔH) of the CTA samples arose. This was carried out at the Celanese Fibers Company- Charolette, North Carolina using a DuPont model 1090 Differential Scanning Calorimeter. The sample weights were in the ranges 5.02-5.08 mg and the scan rate was 10 degree per minute. Thus, the heat of fusion of the samples may be obtained from the measurement of the area under the curves using the following relationship,

$$\Delta H \text{ (calories)} = \frac{\text{Heat of fusion of standard} \times \text{Weight of standard} \times \text{Sample peak area}}{\text{Standard fusion peak area}} \quad (81)$$

Qualitative Small Angle X-Ray Scattering (SAXS)

Qualitative small angle x-ray patterns were obtained using a Rigaku General Electric Rotating anode x-ray

generator and a modified Kiessig camera with pinhole collimation. Patterns with a resolution of 400°A were obtained with a custom made collimator. A mechanical vacuum was used to reduce air scattering effects between the film samples and the x-ray film. The sample to film distance was 40 cm. Exposure times were varied from eighteen to twenty four hours to adjust the relative intensities for the films with varying thickness. The operating radiation settings for generator were 30 Kv and 20 ma.

Quantitative Small Angle X-Ray Scattering

The 10 meter SAXS facility of the National Center for Small Angle Scattering Research (NCSASR) at the Oak Ridge National Laboratory was used to quantitatively measure intensity profiles and integrated intensities from stacked films (two mm thickness). This allowed us to quantitatively investigate void shapes, average void sizes, and void size distribution as a function of processing condtions used.

A schematic representation of the 10 meter SAXS is shown in Figure III-10. The operation of this camers is via a computer program called SAX. Generally, SAX is activated with the input and output assignments to the LSI terminal that is directly connected to the modcomp

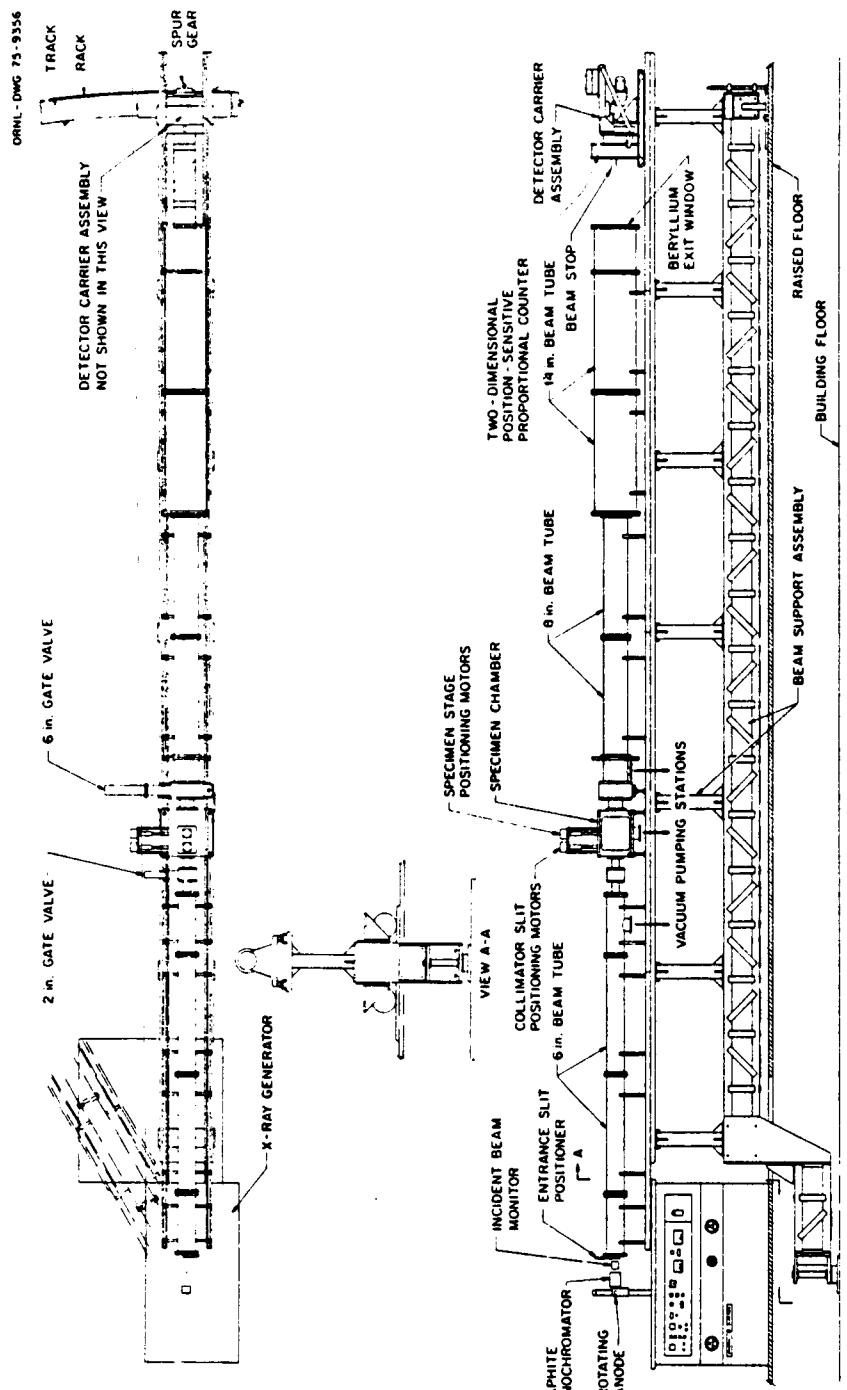


Figure III.10. Diagram of 10 meter small angle x-ray scattering.

computer. The system utilizes a Rigaku rotating anode x-ray generator, graphitic crystal monochromatization of the incident beam, pinhole collimation, and a two dimensional positon sensitive detector. The distance between the pair of pinhole collimators was 1620 mm. The Kevlar film sample to detector distance was 5000 mm giving a system resolution 4.0 mrad. This distance was 4128 mm for CTA films. The incident wave length was 1.542 Å (CuK α).

The x-ray generator voltage and current were operated at 40 Kv and 30 mA respectively. A glassy carbon was used in order to measure the sample transmission. Air scattering was reduced by evacuating the camera with a mechanical pump.

The detector area is resolved into a 64 X 64 element array. A microprocessor maps the position and intensity recorded by each element of the array into a minicomputer memory address. The data recorded in the computer memory from different samples were corrected on-line for background scattering, cosmic radiation,detector sensitivity, variation in incident beam intensity, sample transmission coefficient, and exposure time. The absolute intensity of the incident beam was established from absorption measurements made with a series of nickel foils. Fully corrected data are presented as a

two dimensional contour plot of intensity versus scattering angle.

Polarized Light Microscopy

Anisotropy of the solutions and samples of the films were examined using a Leitz-Ortholux polarizing light microscope. The sample was placed between the glass slides and viewed as the stage was rotated.

Small Angle Light Scattering (SALS)

A spectra-physics 130B helium-neon gas model 452P laser with wavelength 6328 Å was fitted onto an optical bench. A polarizer, an analyzer, a sample holder, and a polaroid film folder were also fitted onto the bench. This assembly, including a timer for adjusting the exposure time, was used to obtain SALS patterns of the films. This is shown schematically in Figure III-11. The samples were placed between glass slides and soaked in a liquid with the same refractive index as the sample. This was to prevent any surface scattering from the sample. A prepared sample was then placed between cross polarizer and analyzer. It was possible to vary the sample to film distance from 5 to 100 centimeters. The sample to detector distance for all the samples were kept constant. The light scattering patterns were recorded on black and white type 55 polaroid films.

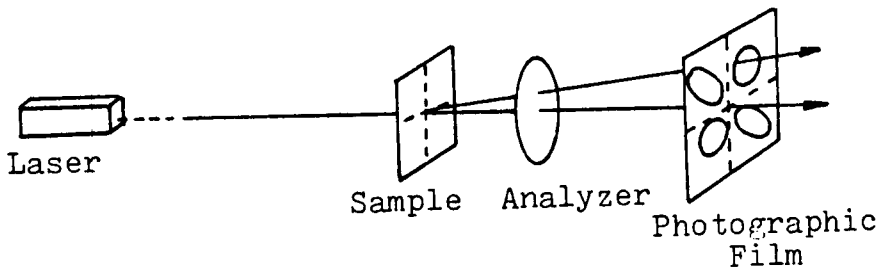


Figure III.11. Small angle light scattering.

Wide Angle X-Ray Scattering (WAXS)

Qualitative WAXS patterns were made using a Philips Norelco X-ray Generator and a flat plate camera. The radiation used was Ni filtered CuKα of wavelength 1.542 Å and operating scatterings were 40 Kv and 15 mA.

Film samples were prepared by stacking the films together with a thickness of about 1 mm. The WAXS patterns were obtained with the x-ray beam normal to the plane of the films. This was carried out by taping the samples directly to the sample holder which was attached to the beam collimator by a rubber attachment (see Figure III-12). The sample to film distance was 3.70 centimeters and the exposure times were varied in order to obtain relatively constant intensities for samples with different thickness.

Pole Figures and Orientation Functions

Pole figures were prepared in a General Electric XRD-5 diffractometer equipped with a single crystal orienter using the method of Heffelfinger and Burton (219). The radiation was CuK α with a wavelength of 1.542 Å. The films were stacked and glued together by applying a weight to the sample to ensure proper adhesion. Then the film samples were cut to the desirable size,

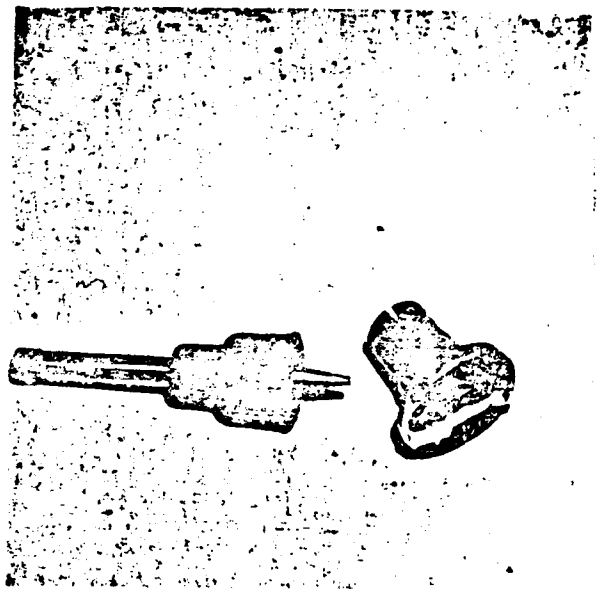


Figure III.12. Sample holder attachment for obtaining WAXS patterns.

usually between 1 and 1.5 mm^3 by a razor blade. This sample thickness selection was based on the technique described by Alexander (9) for wide angle X-ray diffraction experimental measurements. Once the sample is made, it is mounted on a polystyrene rod (see Figure III-13). Two samples are needed for each film. For one sample the polystyrene stick is glued to the machine direction face of the stacked film (Figure III-13a) and for the other sample the polystyrene rod is glued to the transverse direction face of the stacked sample (Figure III-13 b).

The pole figures for the Kevlar films were prepared for the 2.150 $\mathring{A}$ reflection corresponding to the 006 planes and the 3.935 $\mathring{A}$ reflections which represent the 200 planes. These pole figures give concentration distributions of the c and a crystallographis axes in space. An additional pole figure was also obtained from (110) plane for further orientation function measurements. These were obtained from $\langle Cos^2 \theta \rangle$ values generated from intensity data of the (110) and (200) pole figures using the methods developed by Wilchinsky (193) and White and Spruiell (192). More details of this technique and calculations are shown in Appendix B.

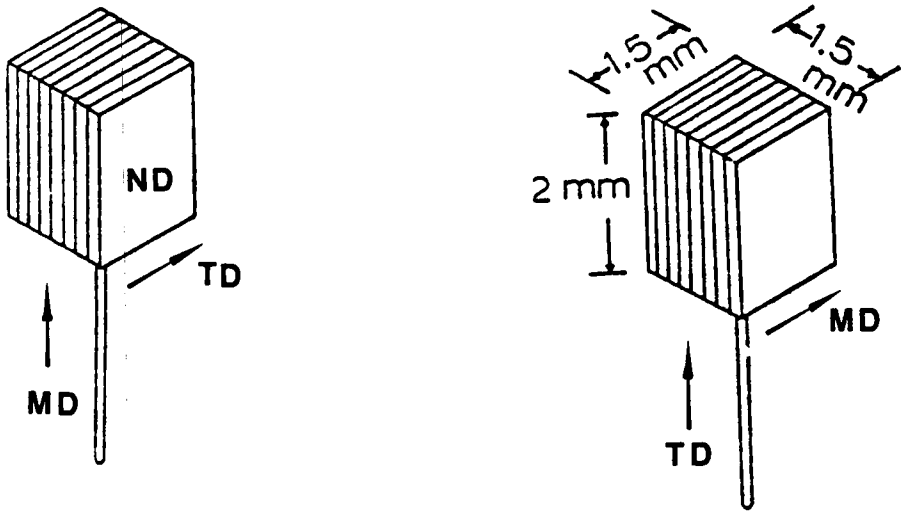


Figure III.13. Sample mounting for pole figures.

Birefringence

Birefringence measurements were made representing the difference in index of refraction between the machine and transverse directions, $\Delta n_{12} = n_1 - n_2$ and between the machine and thickness directions. $\Delta n_{13} = n_1 - n_3$. Thus $\Delta n_{23} = n_2 - n_3 = \Delta n_{13} - \Delta n_{12}$. These measurements were carried out using an optical bench instrument. This instrument is equipped with a babinet compensator and provides a means for both rotating and tilting the sample in the polarized light beam. The experimental details and calculations are presented in Appendix C.

Tensile Mechanical Property Measurements

The tensile properties of all the film samples were obtained at room temperature with a table model Instron Tensile Testing machine model number 1122. The Instron tensile test applies a force to the sample and this force is monitored as a function of time on the recorder. The film samples were cut in 2 cm by ½ cm using a razor blade and the measurements were carried out on the machine, 45 degree angle, and transverse directions. For extruded Kevlar film sample number one, the gauge length was 1 cm and the width was 1/2 cm.

A cross head speed of 2 mm/min was used while the chart speed was 200 mm/min. Instron air clamps with a clamping force of about 20 pounds were used to clamp the sample. The reported results were obtained by averaging three tests on each sample.

CHAPTER IV

STRUCTURE DEVELOPMENT IN PPTA/H_2SO_4 FILMS

The experimental procedures for producing films from PPTA/H_2SO_4 were explained in the last chapter. In this chapter processing conditions for a series of five different films and their characterization will be discussed.

A. Processing Conditions

It is possible to operate the apparatus of Figure III-3, over a wide range of concentration and temperatures. The concentrations below 8 percent were found by Flood (63) to form gels and become very inelastic, resulting in very poor spinnability (the polymer solutions were not able to be stretched or expanded under conditions of elongational flow) regardless of temperature. The higher the solution concentration, the easier the solution was to process into a film.

However, the intention in this study was to operate under conditions where in the PPTA/H_2SO_4 solutions are in the liquid crystalline form. This is important and has been proved to aid in producing higher degrees of orientation in PPTA fibers (102,103). Therefore, seventeen percent solutions were chosen because of their high degree of

processability as compared to lower concentrations and also because of the low temperatures at which they could be extruded (that is 60° to 70° centigrade) as compared to higher concentrations. A processing temperature of seventy degrees centigrade was selected in order to help reduce polymer degradation and to keep the polymer within the anisotropic region (63).

Five samples were prepared under process conditions summerized in Table IV-1. One film (sample number 1) was extruded from the die directly into the coagulation bath. Sample 2 has a relatively low drawdown ratio, while Sample 3 was high. The main objective of the uniaxial film process was to induce molecular orientation in the machine or pulling direction. No air gap was between the end of the die and the coagulant surface in producing uniaxial films. However, an attempt was made where the polymer solution was extruded through the annular opening of the die into an air gap between one and one-half inch. But the film ripped with tears in the machine direction when drawdown was applied.

Drawdown ratio was measured by dividing the initial film thickness to the final average thickness. This is a relative measurement due to the effects of coagulation, swelling or shrinking, and nonuniformity of the film. Take-up was carried out by hand. Thus, the specific take-up

TABLE IV.1. SUMMARY OF EXPERIMENTAL RUNS AND THEIR PROCESS CONDITIONS

Run No.	Coagulant	Film Type	Extrusion Rate (ml/min)	Processing Temperature (C^{o})	Percent Concentration
1	25% H_2O 75% MeOH	Extruded/no drawdown	85	70	17
2	25% H_2O 75% MeOH	Extruded/moderately drawdown	85	70	17
3	25% H_2O 75% MeOH	Extruded/highly drawdown	85	70	17
4	25% H_2O 75% MeOH	Mandrel Processed B.R.*=3.3X	85	70	17
5	25% H_2O 75% MeOH	Mandrel Processed B.R.*=3.3X/ annealed	85	70	17

B.R.*=Blow-up ratio

velocities were difficult to determine. The extrusion rate was constant for all the films.

The fourth film (sample number 4) was prepared using the mandrel in order to induce molecular orientation in both the machine and transverse directions. In this case, oil was extruded through the center of the die onto the conically shaped mandrel (see Figure III-3, page157) to give a relatively frictionless surface for the polymer film to be drawn over. This also produces an elongational flow rather than shear flow in which a higher degree of orientation is expected (63). A fifth film (sample number 5) was prepared by annealing sample 4 under tension at 350°C for 30 seconds. The short time was chosen in order to prevent degradation of the polymer film.

A number of investigators (13,63,102,103) have listed several coagulants for PPTA/H_2SO_4 solutions. Some of these are water, ethanol, methanol, and ethylene glycol. A mixture of methanol-water (75 percent MeOH-25 percent H_2O) was used as coagulant for processing of both uniaxial and biaxial films.

Take-up for mandrel processed film was also accomplished by hand. If the take-up rate was lower than the extrusion rate, film buckling resulted at the mandrel base. Consequently, the film would adhere to the mandrel. Due to this buckling effect, the drawdown ratio can be

controlled. Attempts were made to use a take-up roll in order to obtain a constant drawdown ratio, but the quantity of solution available for each run (about 300 to 400 ml) was not enough to achieve a steady state condition.

B. Void Characterization

Scanning Electron Microscopy

The scanning electron micrographs of surfaces and cross sections of films 1-5 are shown in Figure IV-1 -IV-5. Cross sections are cut parallel and perpendicular to the machine direction, so one is looking through the edge view and the end view (machine direction) of the films. Figure IV-1 exhibits SEM photomicrographs for surface (IV-1a), end view (IV-1b), and edge view (IV-1c) of extruded or undrawn film sample 1. Surface markings indicating flow lines in the extruson direction can be seen from a view normal to the film plane (Figure IV-1a). Complex void structures are present in both cross sections of this film. There appears to be a skin like structure on the outer boundaries of the film surface. The voids start from the outer skin and proceed toward the center of these cross-sections. Fibrillar structure can also be seen in these cross sections. The fibers have diameters in the order of 5-10 μ and are perpendicular to the film machine direction. At the center of the film, large holes

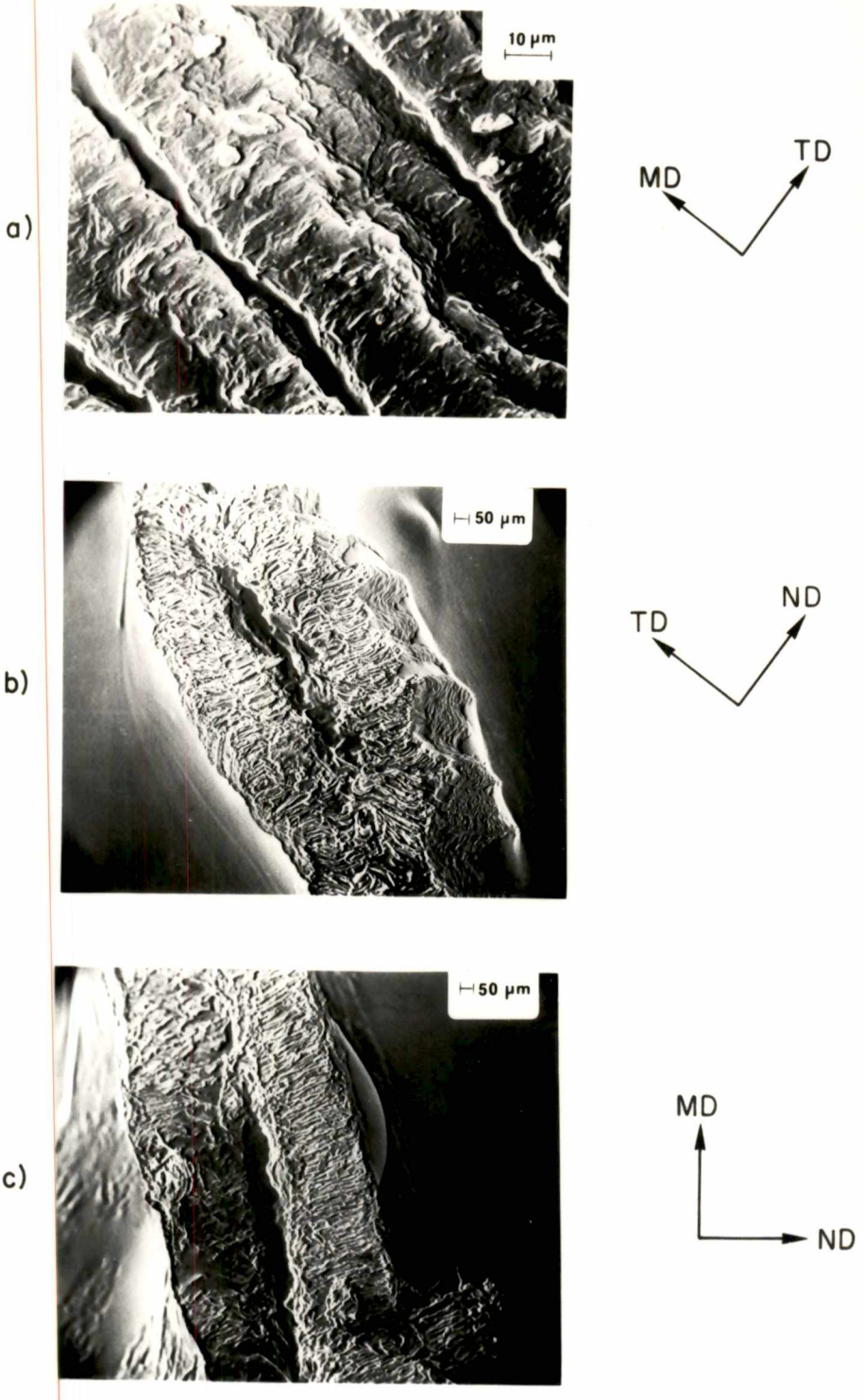


Figure IV. 1. SEM photomicrographs for cross-sections and surface of Sample 1)Extruded film.

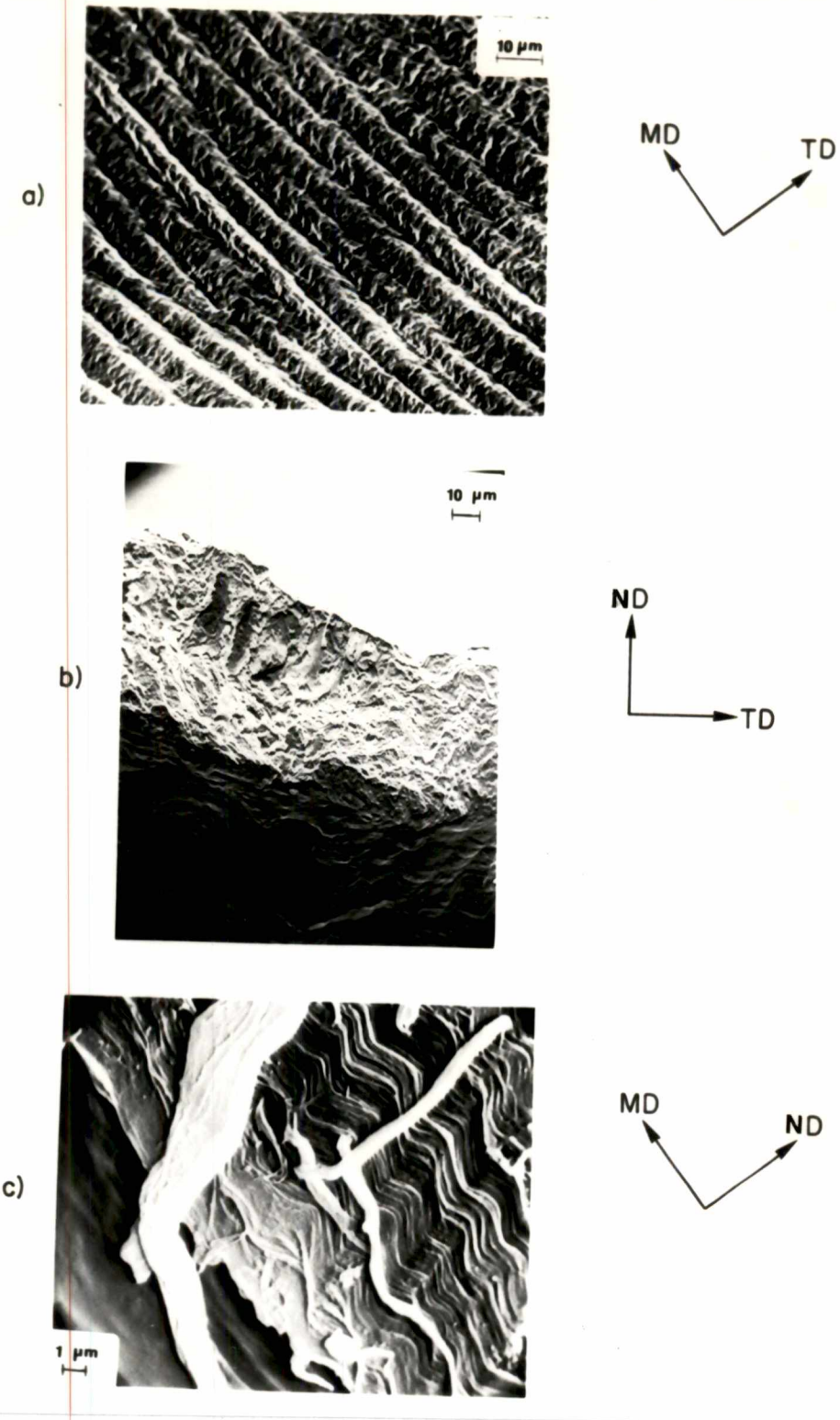


Figure IV. 2. SEM photomicrographs for cross-sections and surface of Sample 2)Uniaxial low drawdown film.

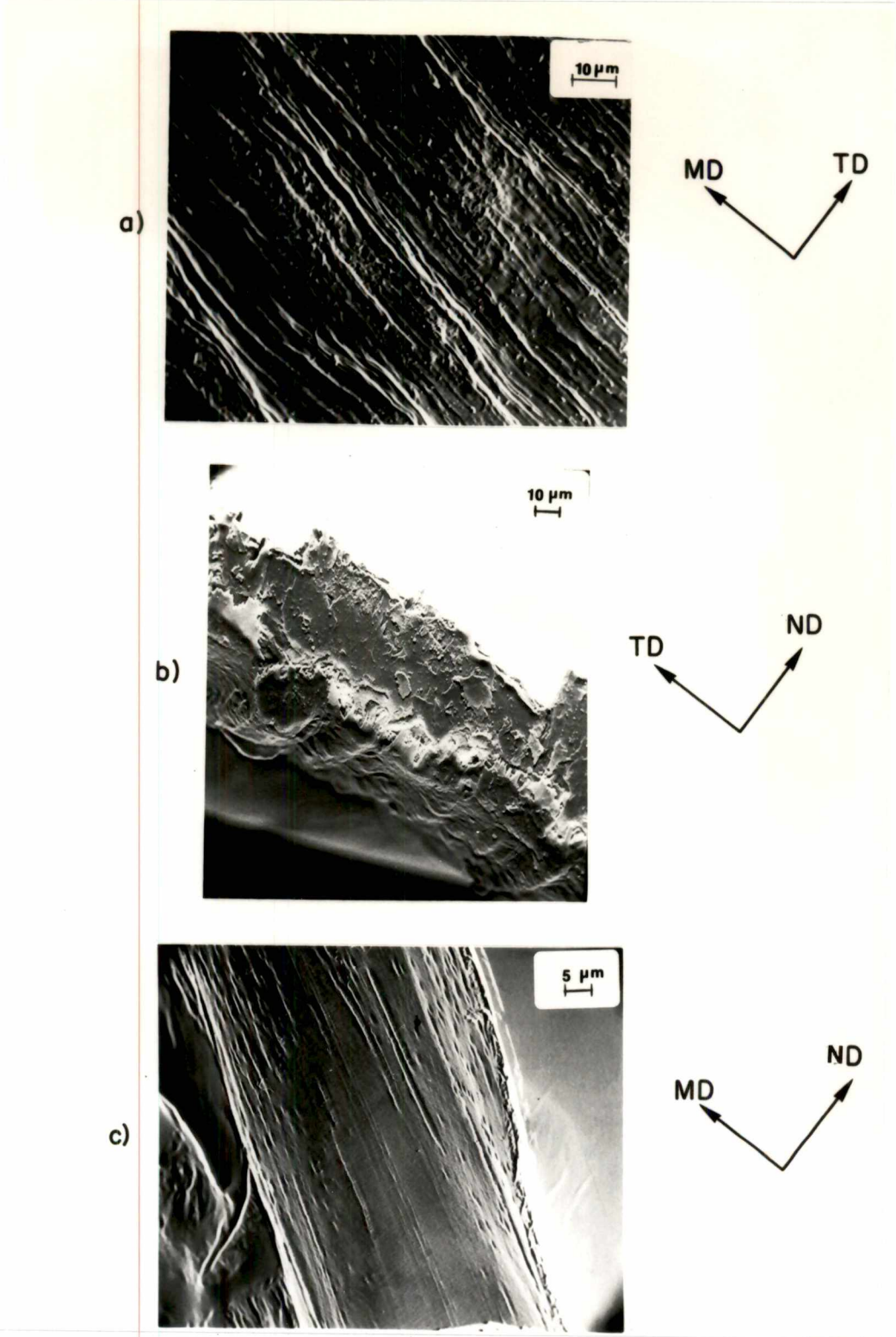


Figure IV. 3. SEM photomicrographs for cross-sections and surface of Sample 3)Uniaxial high drawdown film.

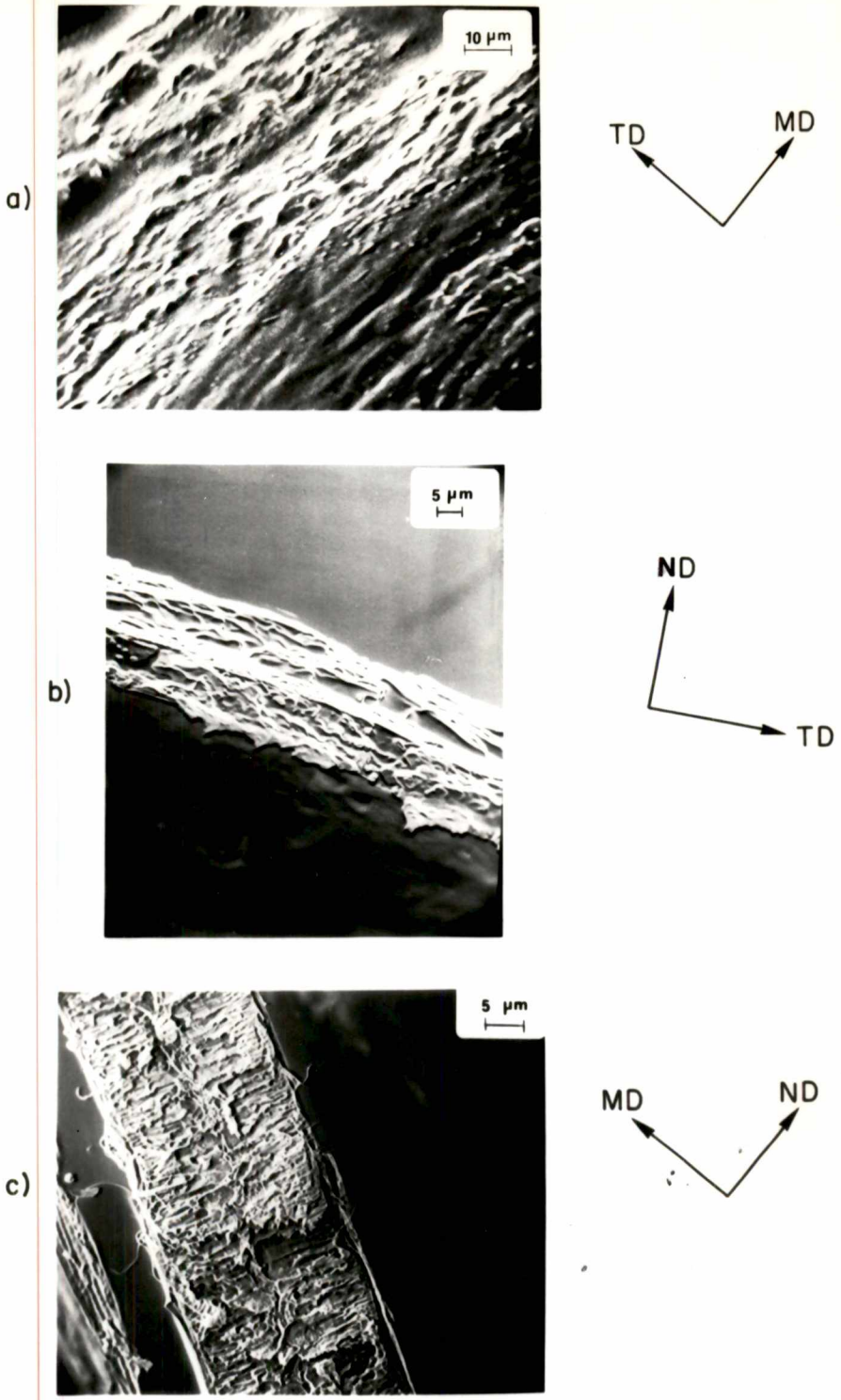


Figure IV. 4. SEM photomicrographs for cross-sections and surface of Sample 4)Mandrel processed film.

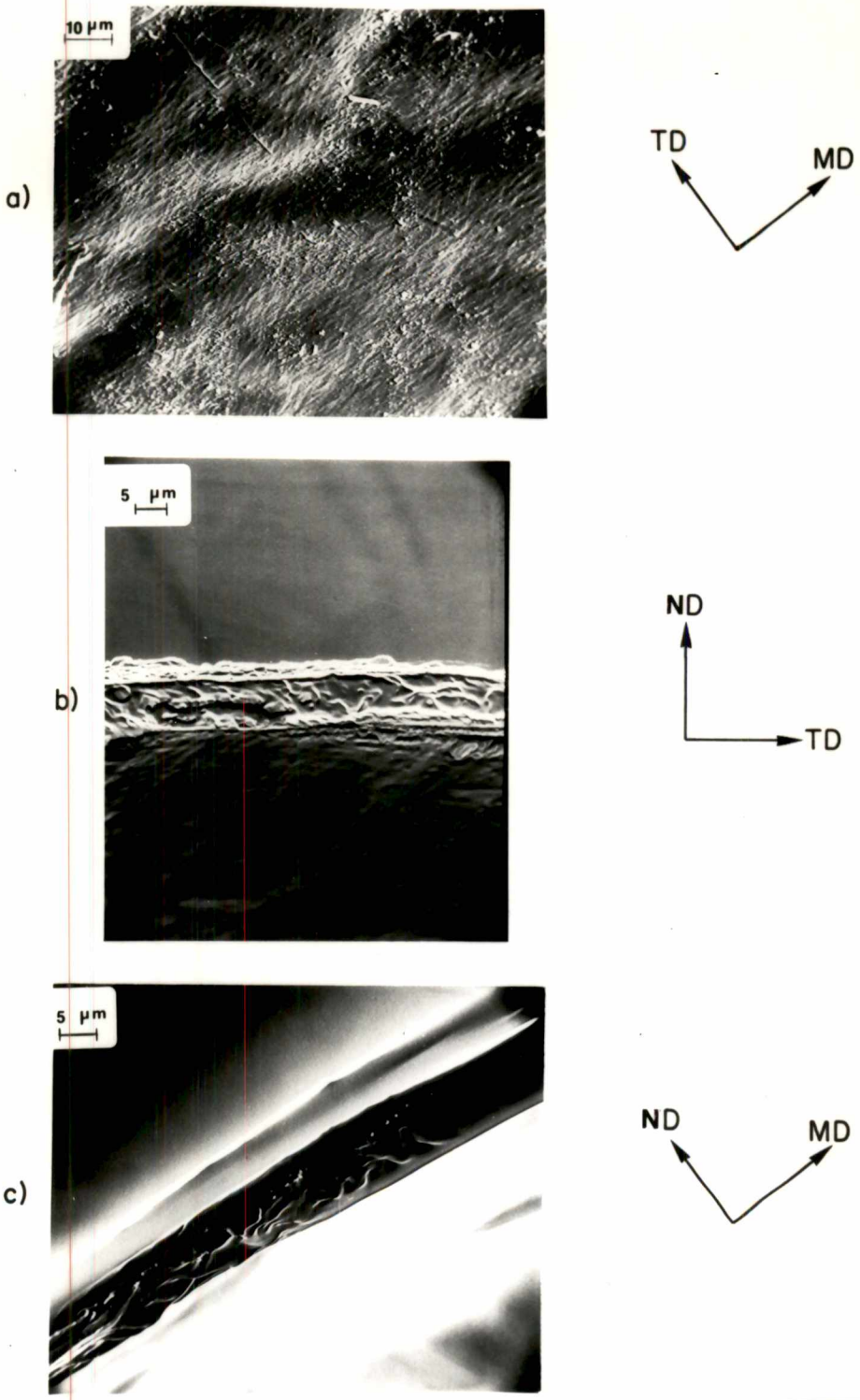


Figure IV. 5. SEM photomicrographs for cross-sections and surface of Sample 5)Annealed mandrel film.

are seen. These holes are elongated and perpendicular to the extrusion direction. The film can easily be split apart at these holes and pulled into two separate sections.

SEM patterns for cross-sections and surface of sample 2, low drawdown uniaxial film, reveal different features than those of thick extruded film(see Figure IV-2). Wrinkles are also present on the surface of this film, while the cross-sections exhibit very few voids compared to undrawn sample No. 1. Skin like structure was observed and no distinct voids at the center of the cross sections were seen. It appears from a comparison of Figure IV-1 through Figure IV-3 that as the drawdown ratio increases, the voids become smaller. The fibrillar structures are still found slightly in uniaxially stretched film (sample 2), but they do not make the aligned structure any more. In highly uniaxial drawdown film 3, these fibrillar structures are merely observed (see Figure IV-3). It is noteworthy that the microstructure seen in the cross section becomes more smooth and less defective with increasing drawdown ratio. The cross-sections of highly uniaxial film are however smoother than both film 1 and 2, and the voids are not visible in this film. The surface marking are much smaller and this film easily fibrillate in the machine direction.

Figures IV-4 and IV-5 give the SEM results for biaxially expanded film 4 and annealed sample 5, respectively. A view normal to the film surface of sample 4 exhibits a relatively smooth surface as compared to the wrinkled surface of undrawn and uniaxially drawn films. The surface markings are absent and typical cross sectional views of this film are also shown in Figure IV-4.

Annealing effects can be seen from the SEM results of sample 5. Both cross-sections and surface of this film appear to become smoother after annealing (compare Figure IV-4 with Figure IV-5).

Density

Densities and average thickness of film samples are listed in Table IV-2. Sample 1 has a density in gram/cm^3 of 0.88 while samples 2 and 3 show higher densities of 1.25 and 1.33 respectively. This increase of densities from 0.88 to 1.33 apparently results from the drawdown occuring during the processing of these films. The thickness of these films also decreases from 0.99mm to 0.043 mm as the drawdown ratio increases. As the theoretical crystal density of PPTA is 1.48, the density of pure solid partially crystalline polymer should still be 1.4. The differences in densities appear to be due to the existance of voids within the samples. It is reasonable

TABLE IV.2. DENSITIES AND AVERAGE THICKNESS FOR PREPARED FILMS

Sample No.	Method of Preparation	Thickness (mm)	Density ($grams/cm^3$)
1	Extrusion/Coagulation	0.990	0.88
2	Extrusion/Moderate Uniaxial Drawdown/ Coagulation	0.058	1.254
3	Extrusion/High Uniaxial Drawdown/ Coagulation	0.043	1.329
4	Extrusion/Flow over Mandrel/Coagulation	0.027	1.250
5	Extrusion/Flow over Mandrel/Coagulation Annealed	0.027	1.308

to consider sample 3 with its higher density contains less voids compared to sample 2 and also sample 2 has less voids than sample 1. This is consistant qualitatively with the results observed in SEM photomicrographs. In highly uniaxial drawn film 3, one hardly observed the trace of the fibrillar structures seen in film 1 and 2. The smooth cross-sectional views may suggest that the density of the film is much higher than that of film 1 and 2.

The density of mandrel processed film (sample 4) is 1.25 g/cc and lower than the highly uniaxial stretched film 3. However, an increase of density is obtained for the mandrel film after the annealing process (compare sample 5 to 4).

Void fraction was estimated using the density data. A two phase model was applied for this measurement. The amorphous density may be neglected due to the nature of molecular rigidity of PPTA. Though, if one assumes that the discrepancy between the experimentally evaluated density and the crystalline solid density (ρ solid= ρ crystal = 1.48g/cc) is due to the presence of voids, the volume fraction of voids, ϕ , can readily be derived using the following expression,

$$\phi = 1 - \frac{\rho}{\rho_o} \qquad (82)$$

Where ρ is the experimentally observed sample density and ρ_o is the crystalline density. The above expression was used to estimate void fractions of PPTA films and the results are listed in Table IV-3. This table exhibits void fraction of 0.405 (40 percent) for extruded sample 1. This decreases for low drawdown uniaxial sample 2 to 0.32 (32 percent) and 0.102 (10 percent) for highly drawn uniaxial film 3. A decrease of void fraction can also be seen after annealing process (compare results of sample 4 to sample 5).

Qualitative Small Angle X-Ray Scattering

Figure IV-6 contains small angle x-ray patterns for Kevlar films where the x-ray beam is normal to the plane of the film. The SAXS pattern for extruded film (sample 1) exhibits the greatest scattering intensity. The scattering is isotropic (uniform in all directions). The scattering in film 2 (uniaxial low drawdown film) is more concentrated in the equatorial direction. This intense diffuse equatorial scattering is accentuated in film 3. The origin of this diffuse equatorial scattering would seem to be the presents of microvoids (9,71,171,172) elongated in the stretching direction of the film.

For film 4, the mandrel processed film, the diffuse

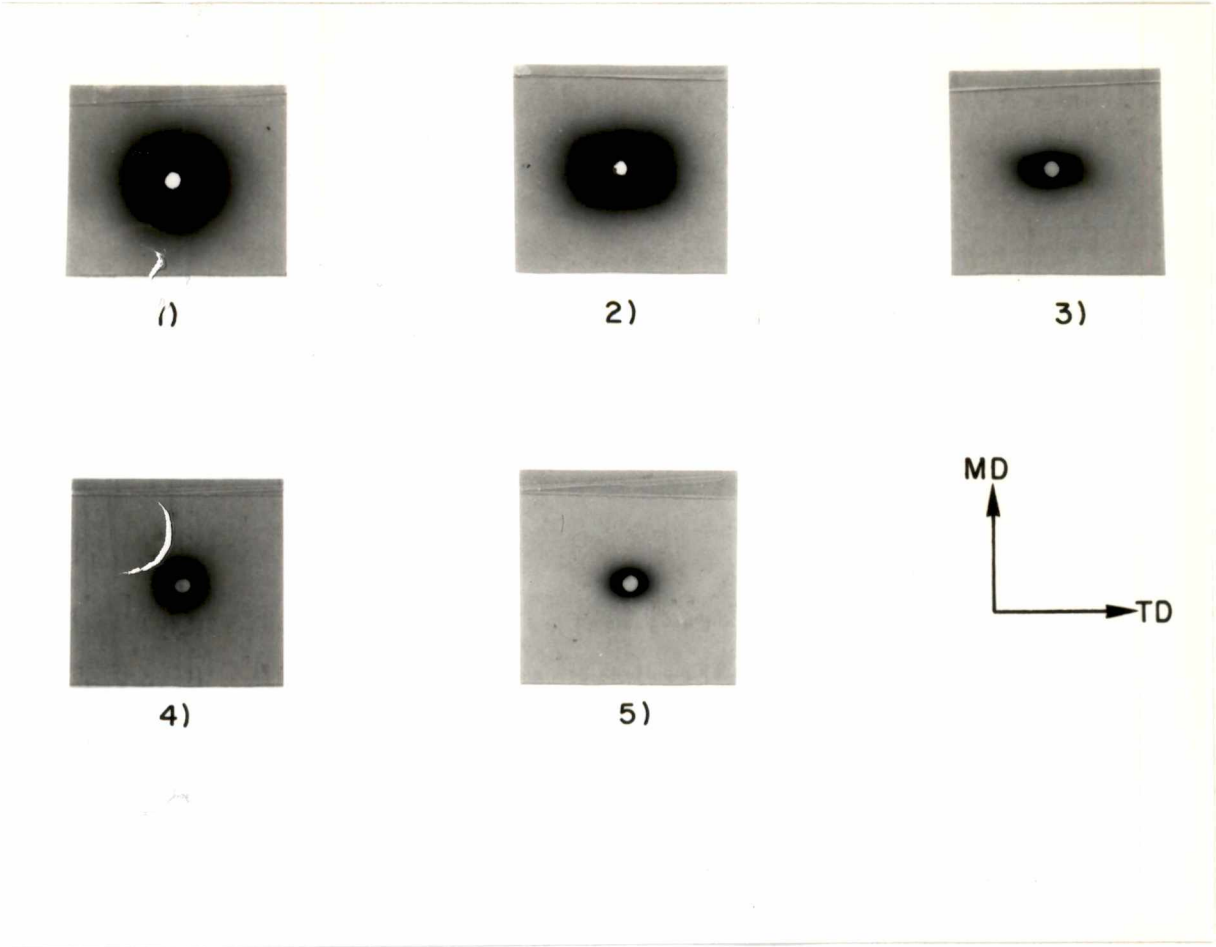


Figure IV. 6. SAXS qualitative film patterns of
1. Extruded
2. Uniaxial low drawdown
3. Uniaxial high drawdown
4. Mandrel processed
5. Annealed mandrel film

scattering intensity decreases as it is shown in Figure IV-6 for sample 5 (annealed at 350°C for 30 seconds).

The diffuse scattering intensity for various films may be ordered as follows;

$$1 > 2 > 3 \simeq 4 > 5$$

Quantitative Small Angle X-Ray Scattering

Based on preliminary qualitative measurements, the samples were quantitatively studied for further understanding of the interaction of processing variables on microvoid formation using the 10 meter small angle x-ray facility at the NCSASR located in the Oak Ridge National Laboratory in Oak Ridge, Tennessee.

Figures IV-7 through IV-11 show contour plots for films 1-5, respectively. Figures IV-7, 9, and 10 contain contour plots for the cases where the x-ray beam is parallel to the ND, TD, and MD of the films. The results where the beam is parallel to the ND are similar to those obtained from qualitative film patterns. All three contour plots for sample 1, the extruded film, are almost isotropic and indicate the voids in this film do not have preferred direction but are randomly oriented (see Figure IV-7). This is reasonable, because the film sample was prepared by free extrusion of the dope into the coagulation bath.

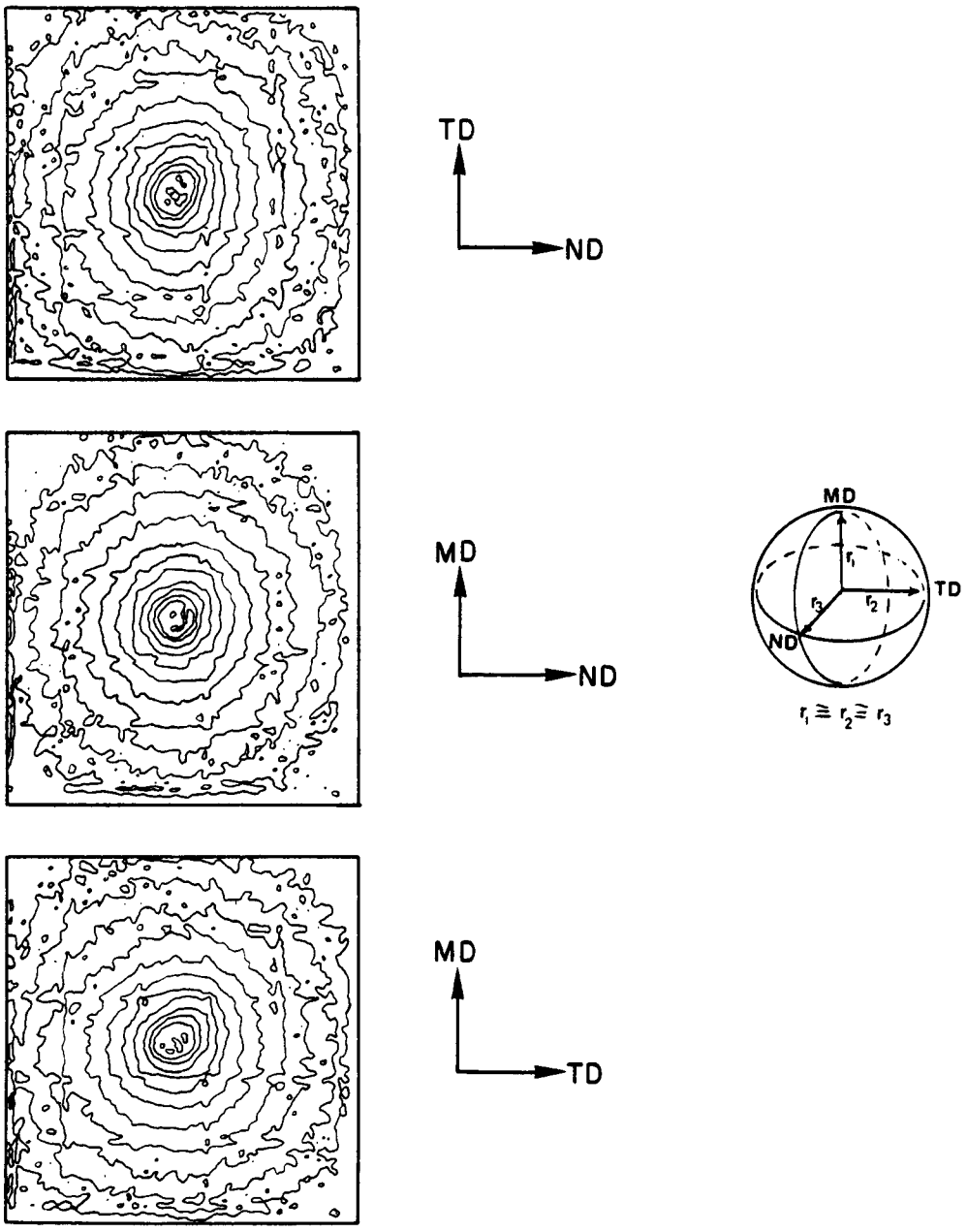


Figure IV. 7. SAXS intensity contour plot for three directions relative to Sample 1) Extruded Film.

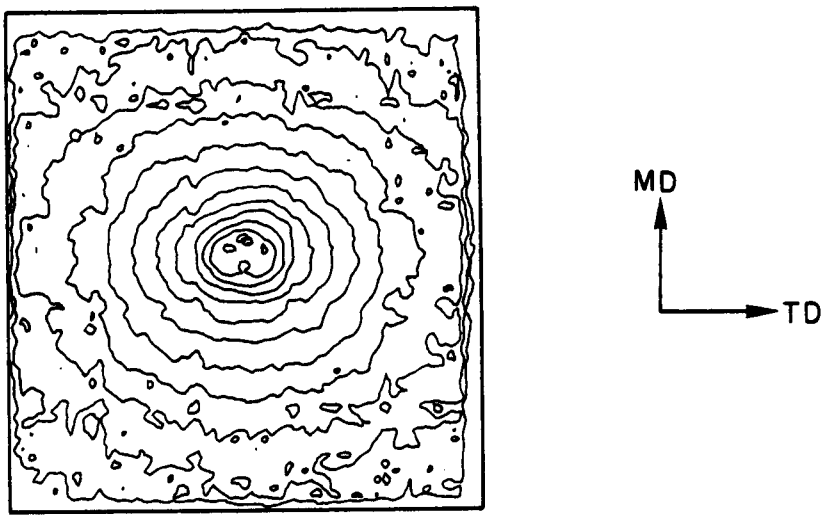


Figure IV. 8. SAXS intensity contour plot for the beam normal to the extrusion plane of Sample 2)Uniaxial low drawdown film.

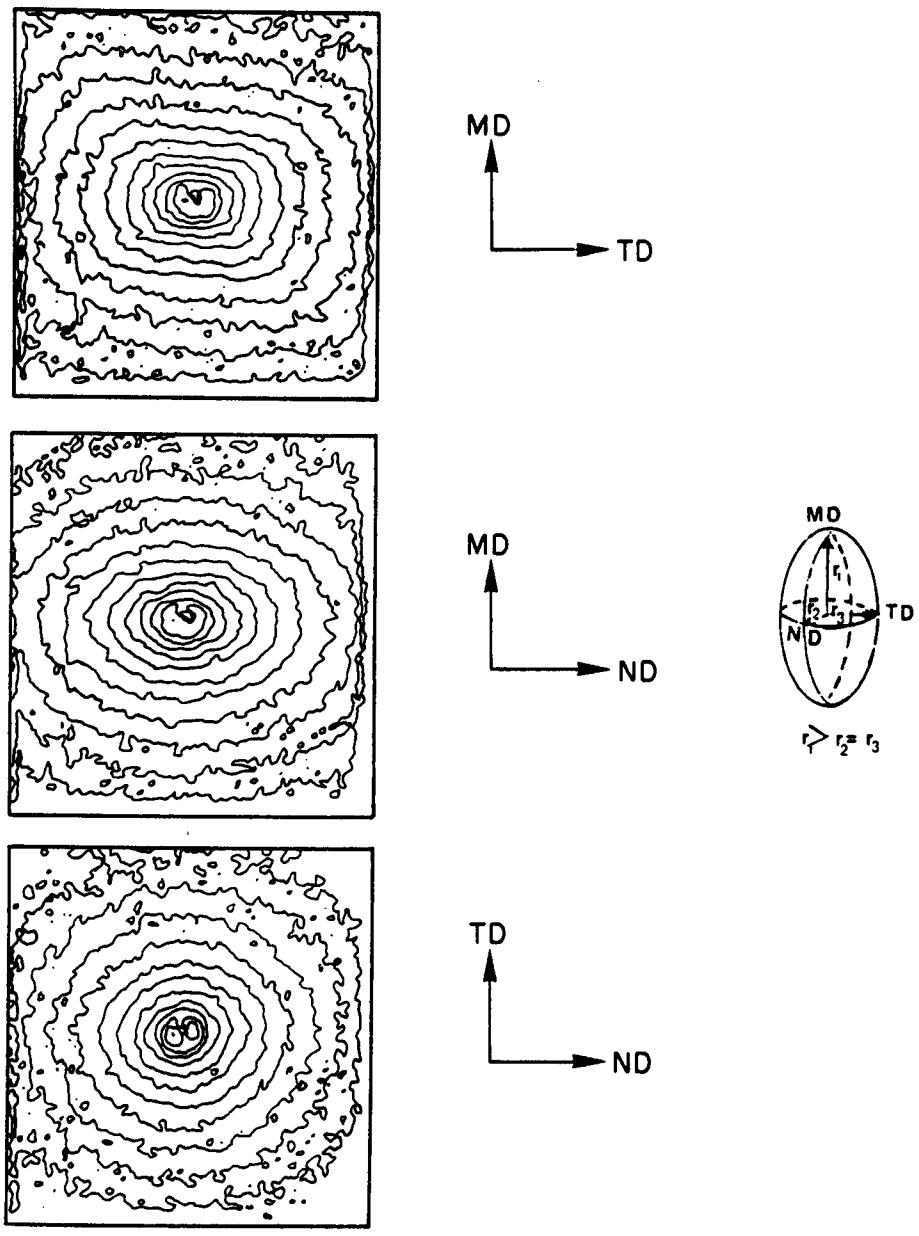


Figure IV. 9. SAXS intensity contour plots for three directions relative to Sample 3)uniaxial high drawdown film.

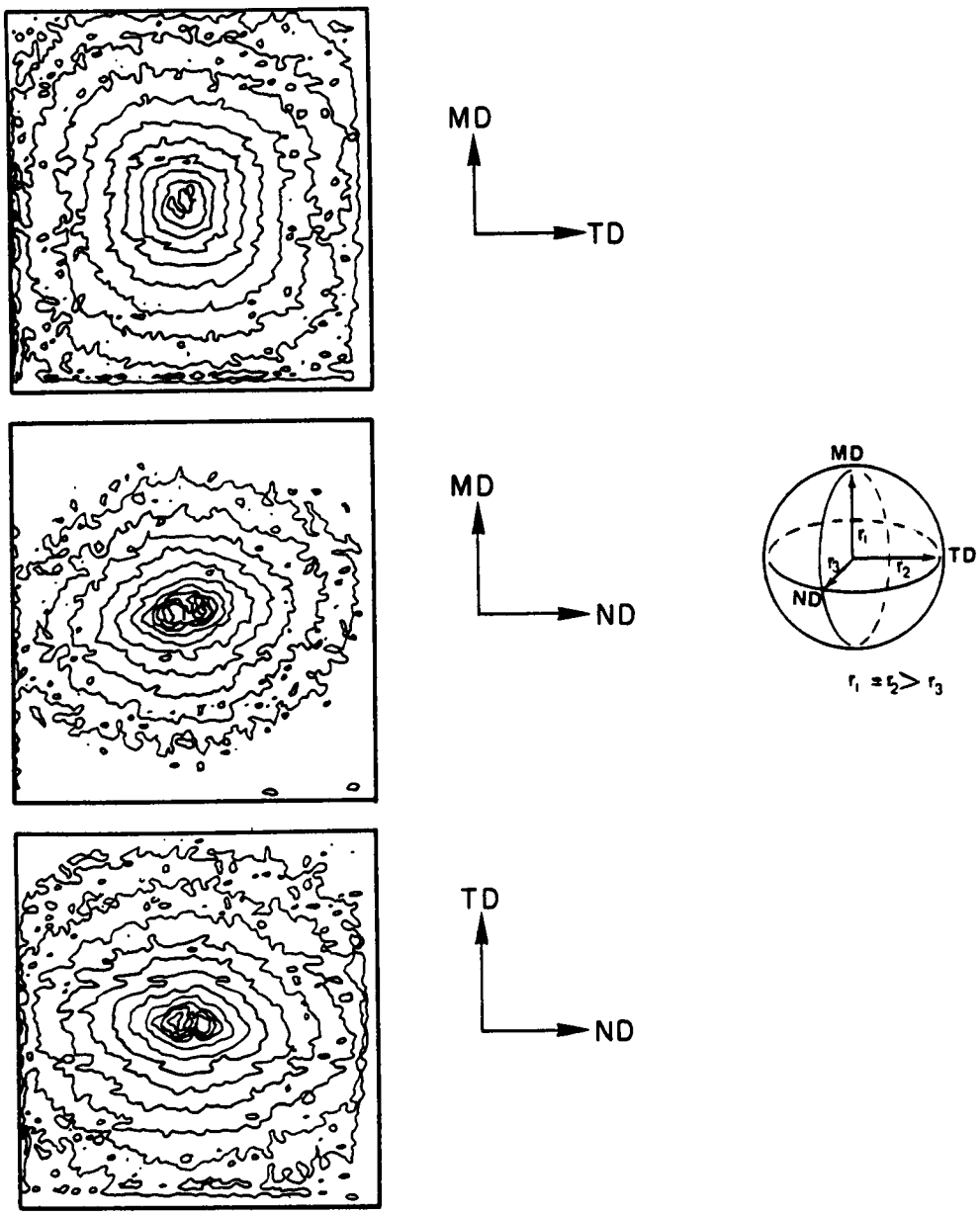


Figure IV.10. SAXS intensity contour plots for three directions relative to Sample 4)mandrel processed film.

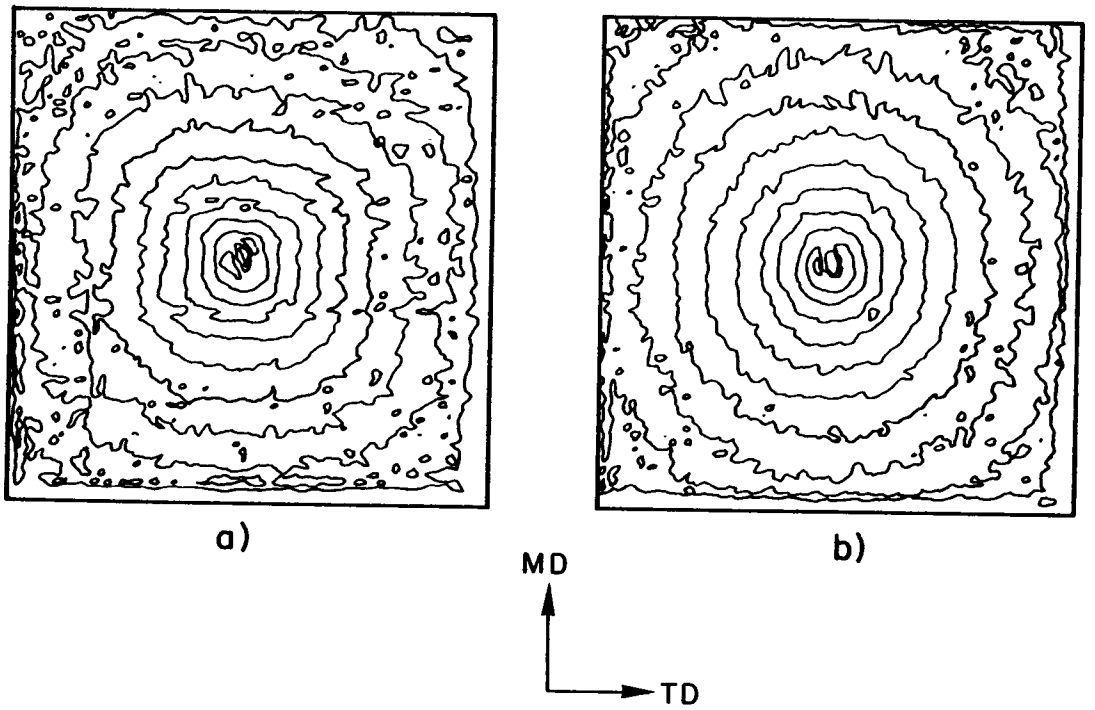


Figure IV.11. SAXS intensity contour plots normal to the extrusion plane for Sample 4)Mandrel processed and Sample 5) Annealed mandrel films.

A typical void shape for the extruded sample may be drawn as shown in Figure IV-7.

In Figure IV-8, the contour plot for sample 2, where the x-ray beam is parallel to the ND is shown. The scattered intensity is concentrated in the equatorial direction indicating the voids are not spherical in shape. This anisotropy of the diffuse scattering is more pronounced in Figure IV-9 for highly drawndown uniaxial film 3. Anisotropic contour plots are obtained for both cases where the beam is parallel to the ND and where the beam is parallel to TD of the stacked films. On the other hand, an isotropic pattern is obtained where the beam is parallel to MD of stacked films (machine direction). These contour plots indicate the voids are prolate-ellipsoid in shape and are elongated in the machine direction of the uniaxially drawn films. This is also drawn in Figure IV-9.

In biaxially stretched film the voids are expanded in the plane of the MD-TD (or compressed in the ND) as seen in Figure IV-10. The contour plots for this film parallel to TD and MD, and isotropic where the beam is parallel to ND of the film. These patterns indicate oblate-ellipsoid shaped voids for sample 4. An example of these voids is also drawn in Figure IV-10. A comparison of the contour

plots where the x-ray beam is parallel to the ND is shown in Figure IV-11 for mandrel processed film (IV-11a) and after annealing (IV-11b). Both of these are isotropic and qualitatively a decrease of intensity cannot be seen as a function of annealing process (unlike results obtained from qualitative SAXS film patterns); however, quantitative measurement of void sizes exhibits a substantial decrease in void size after the sample was annealed (see Table IV-3, p. 202).

Determination of void size and void size distribution. In order to determine the approximate average dimensions of the voids, we used Guinier analysis and the method of Debye and Bueche. These analyses were applied to intensity profiles taken along the equatorial and meridional directions through the center streak scattering. For isotropic patterns this was applied to the average intensity around the center streak scattering.

Following Guinier (9,70,71) we may represent the angular distribution of scattered x-ray by the Gaussian formula,

$$I(S) = I(0) \exp\left(\frac{16\pi^2 \sin^2\theta}{3\lambda^2} R^2\right) \qquad (83)$$

(see Chapter II, page 86 to 89). This distribution is expected to be valid at very small angle (70) and is based on presuming a dilute system of randomly oriented particles.

Figures IV-12 through IV-15 give Guinier plots, where tangents to the first few intensity points at very small angles are drawn. These plots are log I (θ) as a function of K^2 (scattering vector) for different spatial directions of samples 1-4. The void sizes so determined from these plots are listed in Table IV-4.

The undrawn or extruded sample exhibits average void dimensions which are approximately the same in all directions of the film. These have longer dimensions in the machine direction when the beam is parallel to ND of the film, and also when the beam is parallel to the TD for uniaxial film sample 3, indicating a shape change as a function of drawdown ratio. A decrease in void size can be seen after the annealing process. This is clear from the values obtained for annealed film (compare sample 4 to 5 in Table IV-4).

When there is a distribution of particle sizes the scattering at small angles can be represented as (91)

$$I(\theta) = I(0) \int_0^\infty R^3 W(R) e^{-K^2R^2/3} dR \qquad (84)$$

Where W (R) is a particle size-distribution function. One may estimate following Jellinek et al. (91), as a series of particles of different discreet sizes as

TABLE IV·4. VOID SIZES DETERMINED BY GUINIER PLOTS

Sample No.	Beam Direction	Void Size (nm) MD	TD	ND
1	Normal to film	21.5	21.8	
	Normal to edge	24.2		24.2
	Normal to end		20.7	22.0
2	Normal to film	26.0	26.0	
3	Normal to film	26.3	24.0	
	Normal to edge	22.9		18.3
	Normal to end		23.3	21.2
4	Normal to film	22.7	22.7	
	Normal to edge	33.5		28.4
	Normal to end		28.5	
5	Normal to film	18.9	18.9	

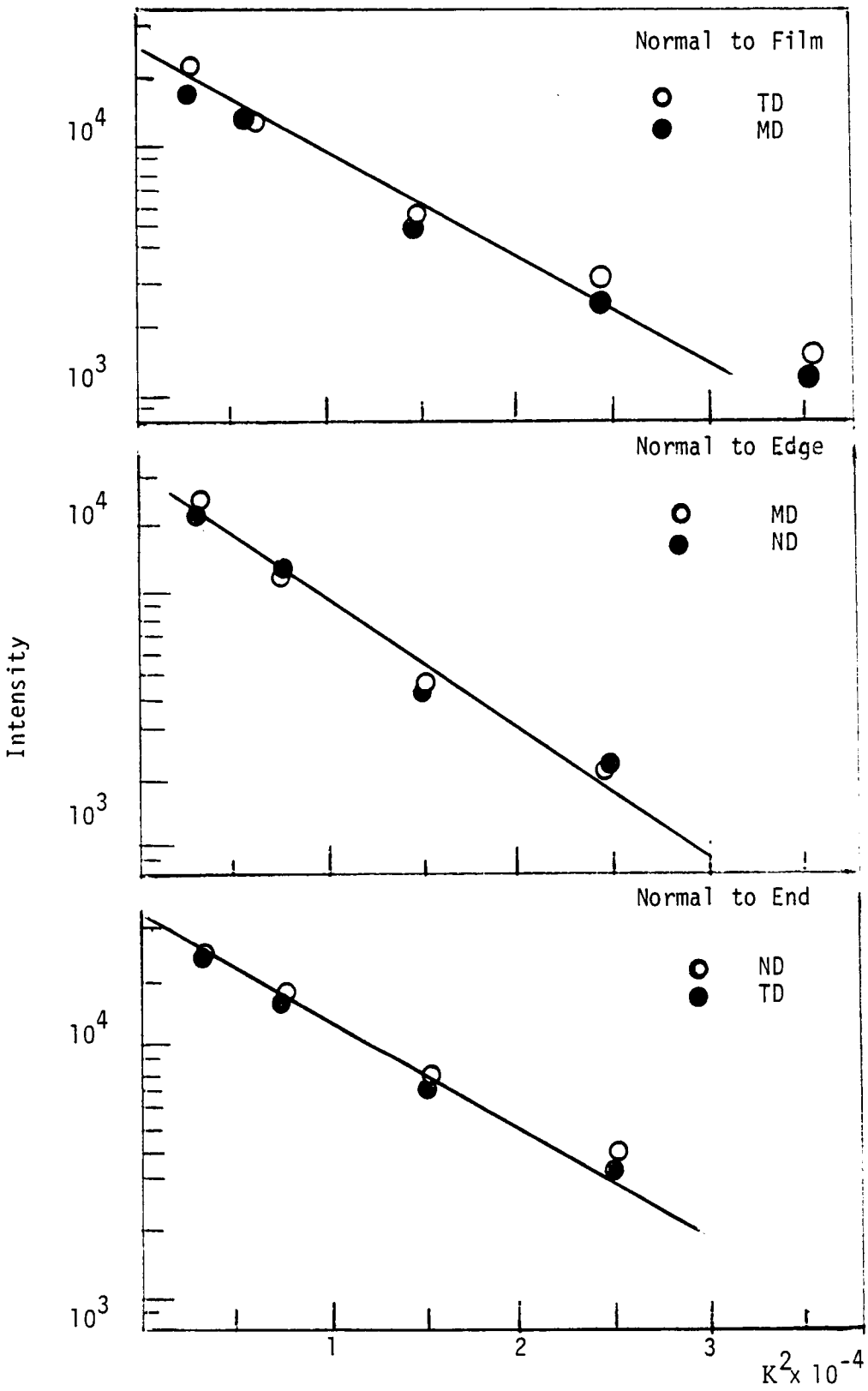


Figure IV.12. Guinier plots for Sample 1)Undrawn film.

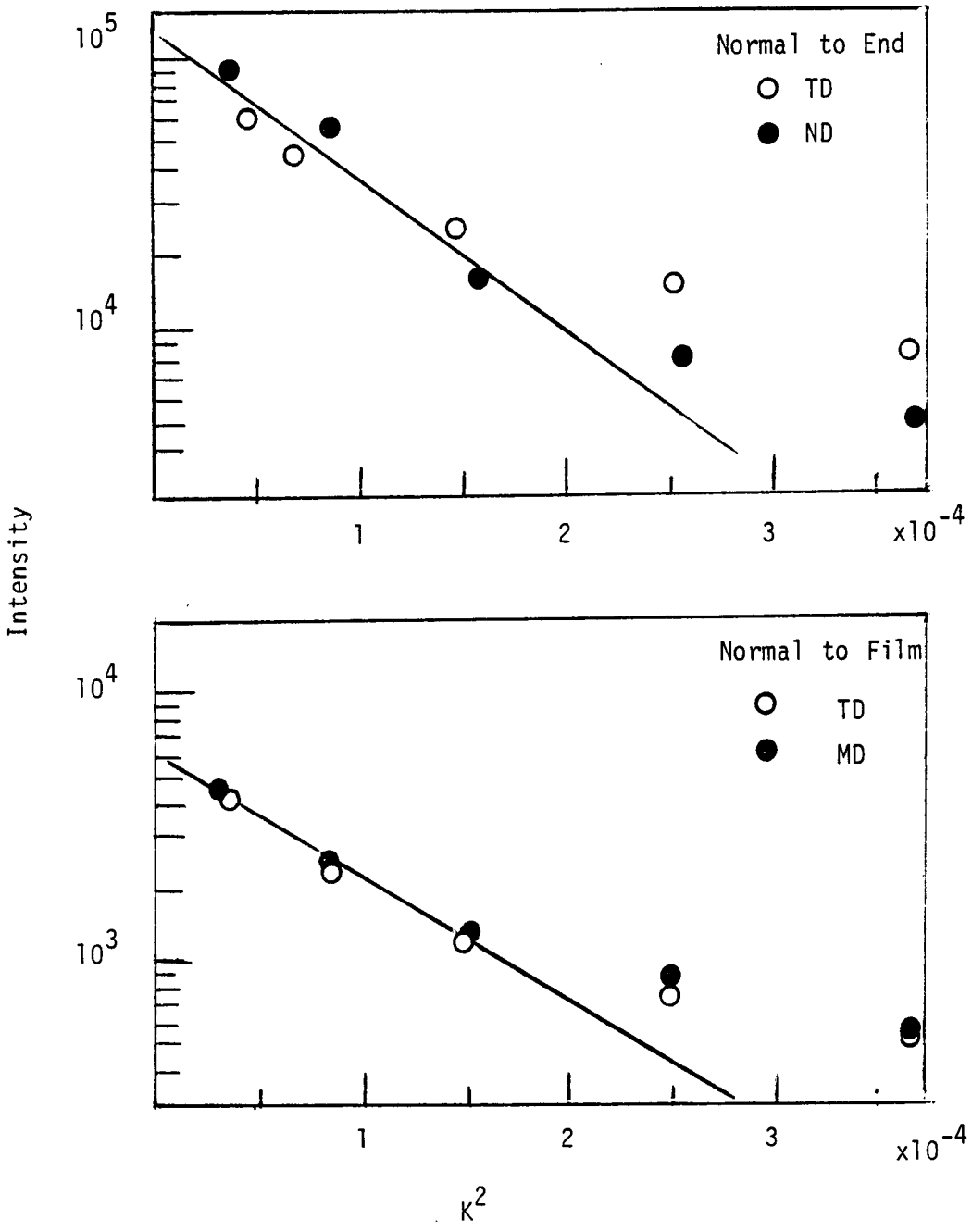


Figure IV.13. Guinier plots for Sample 2)Uniaxial low drawdown film.

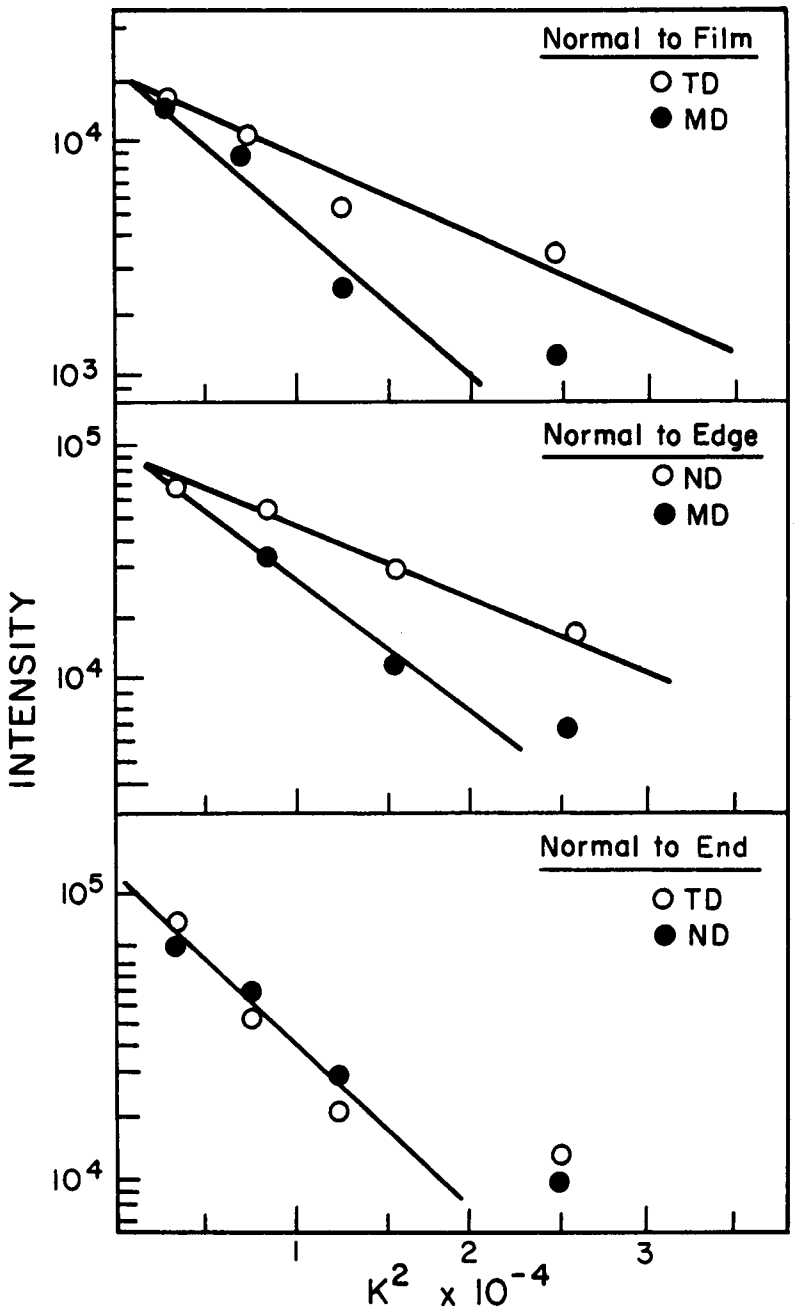


Figure IV.14. Guinier plots for Sample 3)Uniaxial high drawdown film.

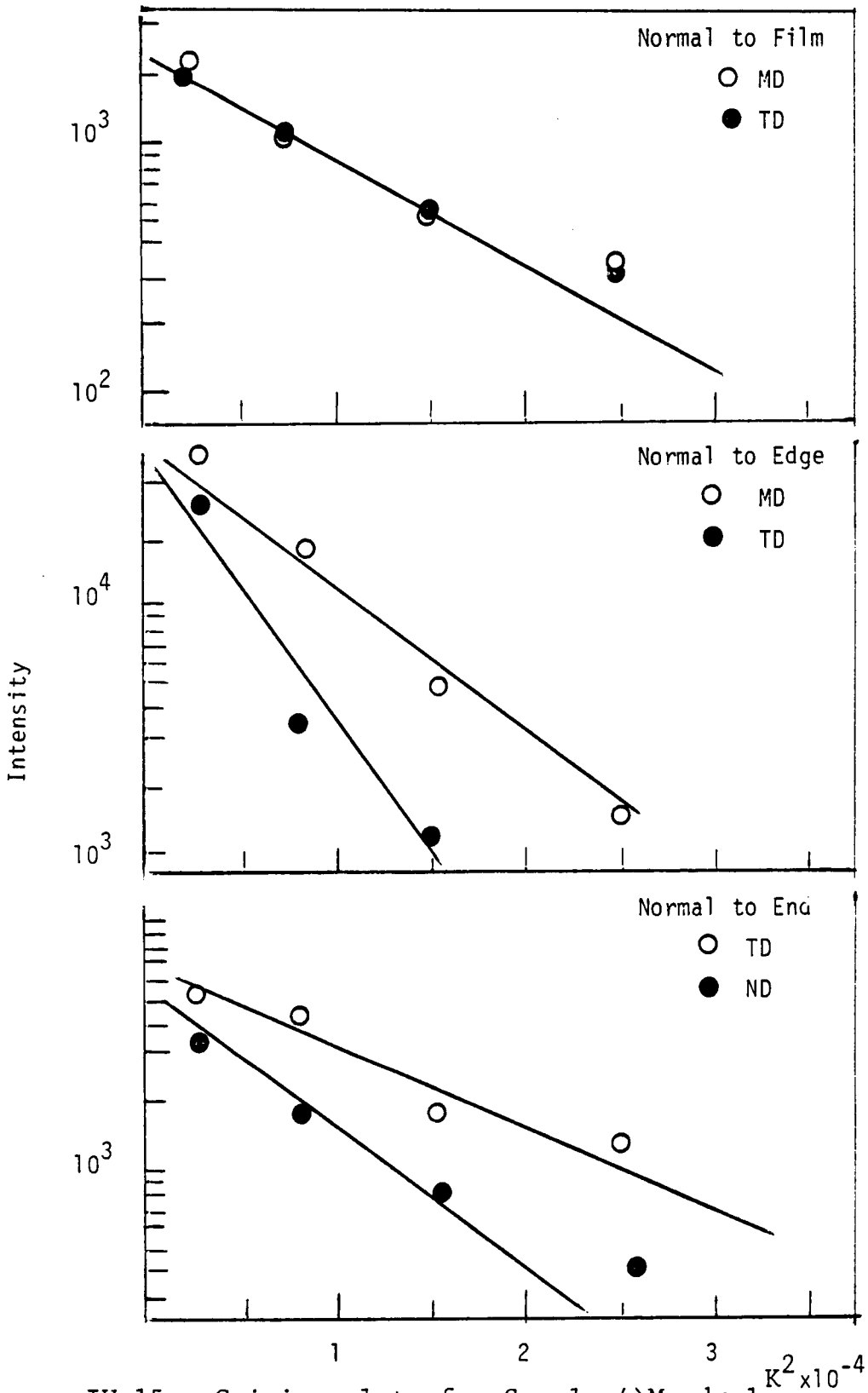


Figure IV.15. Guinier plots for Sample 4)Mandrel processed film.

$$I(\theta) = I(0) \sum A_i e^{-K^2 R_i^2/3} \qquad (85)$$

Considering first the smallest group of particles or voids of size R_1, one may evaluate their size from a tangent to the $I(\theta)$ $-K^2$ curve at very small K. The next particle group is obtained from repeating the plot using,

$$\frac{I(\theta)}{I(0)} - A_1 e^{-K^2 R_1^2/3} \qquad \text{versus } K^2$$

The quantities R_i and A_i give void sizes and relative quantities of voids, (ie., void fraction). Due to the reciprocity between the dimensions of inhomogeneity and the angular extent of the small angle scattering the tangent at the highest scattering angle of the plot of log $I(\theta)$ versus K^2 gives the size of the smallest group of particles. The intercept of $K^2 = 0$ is proportional to A_i. Typical plots of this technique for films 3 are shown in Figure IV-16 to IV-18, and the results for sample 1,3, and 4 are presented in Table IV-5. It seems from this table that the percentage of the smallest voids (of about 5.1-5.6 nm) presented in any directions of the extruded film are much higher (49-89 percent) than the largest voids (of about 19.5-25 nm) with 6.3-34 percent. This general trend can also be seen for both uniaxial drawn and biaxially expanded film 3 and 4. But the percentage values for smallest voids seems to decrease as drawdown ratio increases, while these values for

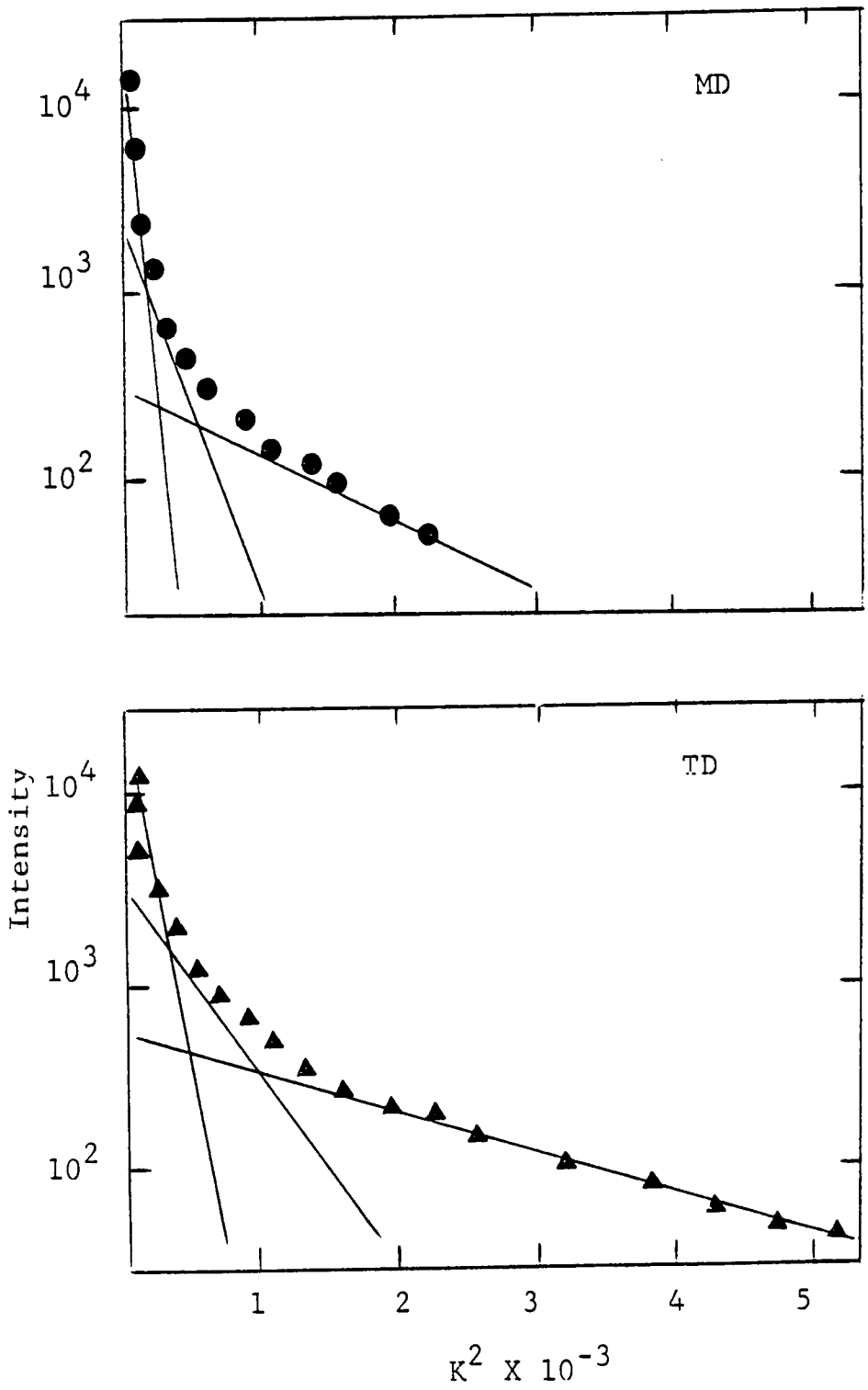


Figure IV.16. Jellinek-Solmon-Funkuchen plots of through view for film 3.

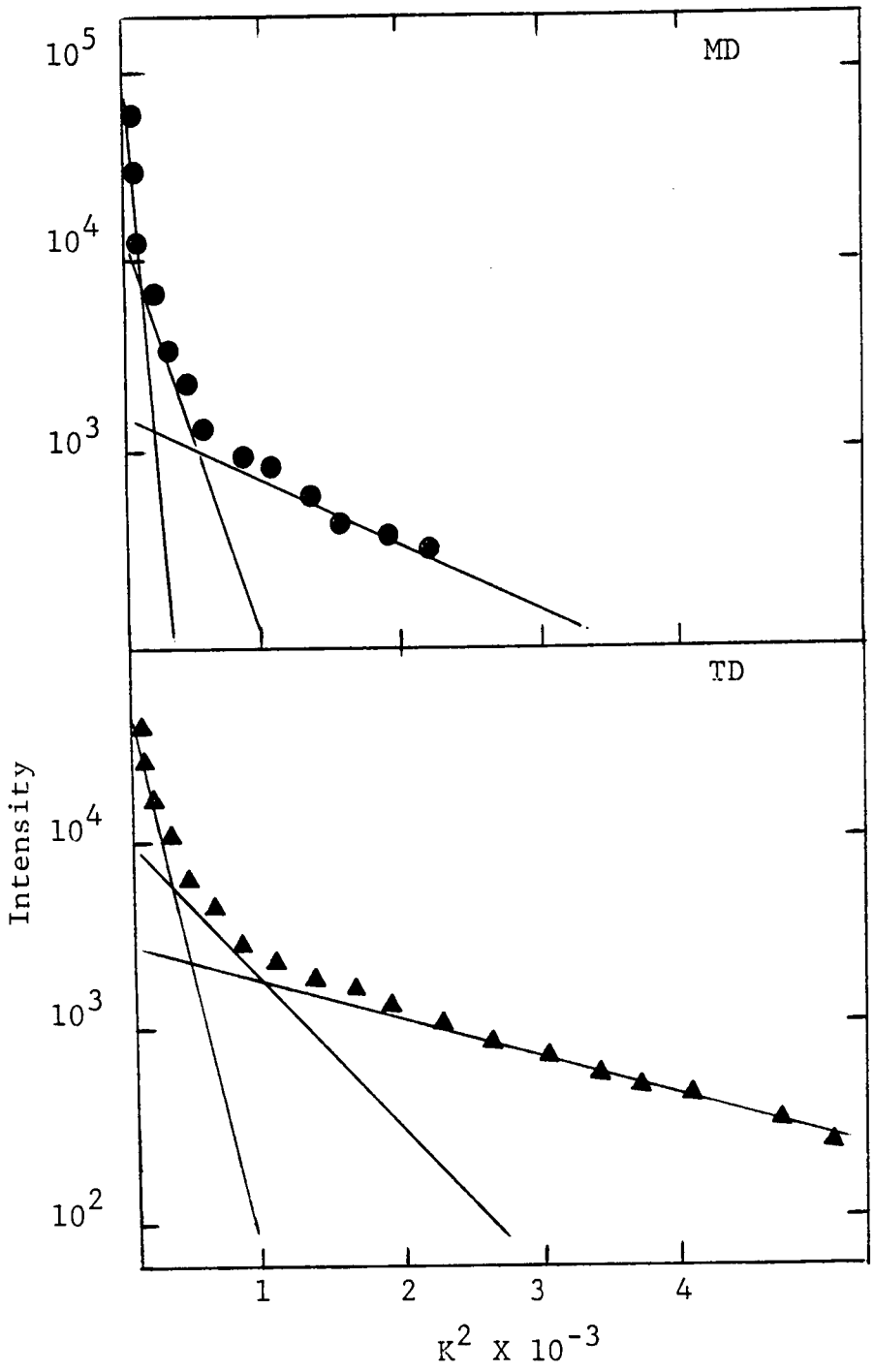


Figure IV.17. Jellinek-Solmon-Funkuchen plots of edge view for film 3.

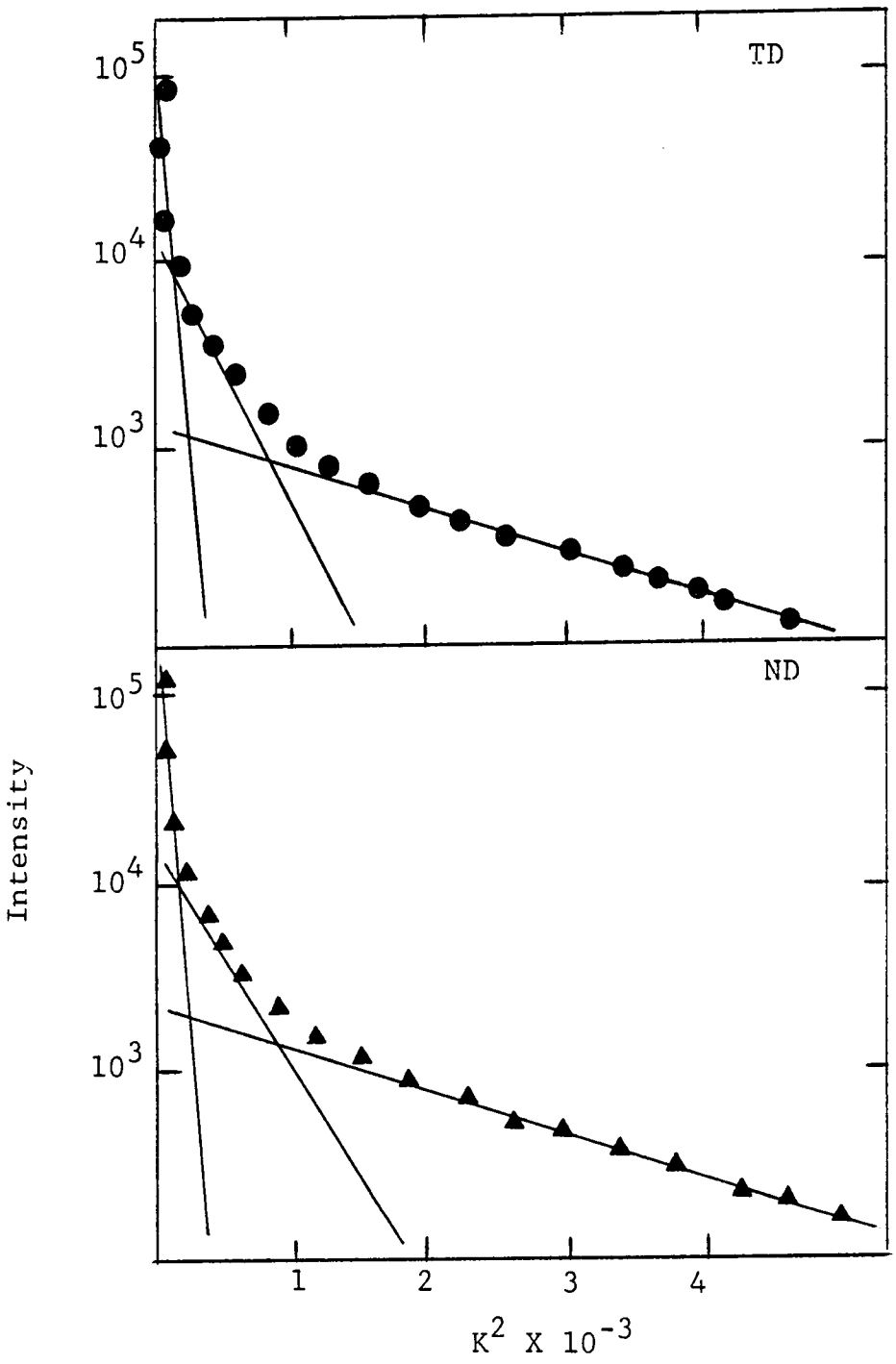


Figure IV.18. Jellinek-Solmon-Funkuchen plots of end view for film 3.

TABLE IV.5. VOID SIZE DISTRIBUTION BASED ON METHOD OF JELLINEK et al.

Sample No.	Beam Direction	Void size, R(A) and void fraction, f(%) MD R(nm)	MD f(%)	TD R(nm)	TD f(%)	ND R(nm)	ND f(%)	Void fraction ϕ
1	Normal to film	5.1	89.0	5.1	89			0.405
		10.5	4.4	10.5	4.4			
		22.8	6.3	22.8	6.3			
	Normal to edge	5.6	50.5			5.6	50.5	
		12.1	25			12.1	25	
		25.0	25			25.0	25	
	Normal to end			5.3	49	5.3	49	
				9.8	17	9.8	17	
				19.5	34	19.5	34	
3	Normal to film	6.1	48	5.0	54			0.102
		14.7	25	10.7	24			
		28.4	28	23.1	22			
	Normal to edge	6.3	53			4.7	53	
		14.6	23			9.3	27	
		28.0	23			18.1	20	
	Normal to end			5.1	49	5.1	53	
				12.1	29	11.3	27	
				29.2	22	26.6	20	
4	Normal to film	5.0	58	4.9	60			0.115
		10.6	29	11.3	29			
		23.0	13	25.2	11			
	Normal to edge	5.2	51			4.6	48	
		12.9	24			10.1	27	
		33.5	25			28.4	25	
	Normal to end			4.8	55	4.7	62	
				10.8	32	9.7	24	
				28.6	13	22.0	14	

largest voids increase with increasing drawdown ratio (compare values of sample 1 to those of sample 3 in Table IV-5).

Void sizes were also estimated using the Debye-Bueche (52,221) method. These authors developed a theory of scattering by voids of random size and shape. They pressume an exponential correlation function of form

$$\gamma(r) = e^{-r/a} \tag{86}$$

Where "a" is called correlation length. This leads to an angular intensity distribution of form

$$I(\theta) \simeq V\eta^2 W. \frac{8\pi a^3}{(1+ K^2 S^2 a^2)^2} \tag{87}$$

Therefore, plots of $(I)^{-\frac{1}{2}}$ against K^2 should yield a straight line. The value of "a" can be obtained from the slope intercept ratio and relates to R_d, the average pore diameter (see Chapter II, page 90 for details). Typical plots of this technique for film 1 are presented in Figure IV-19 to IV-21 and the results of void sizes computed from this method are summerized in Table IV-6. The values obtained by this procedure are much smaller than those determined by the method of Guinier. This will be explained and discussed in a later section of this chapter.

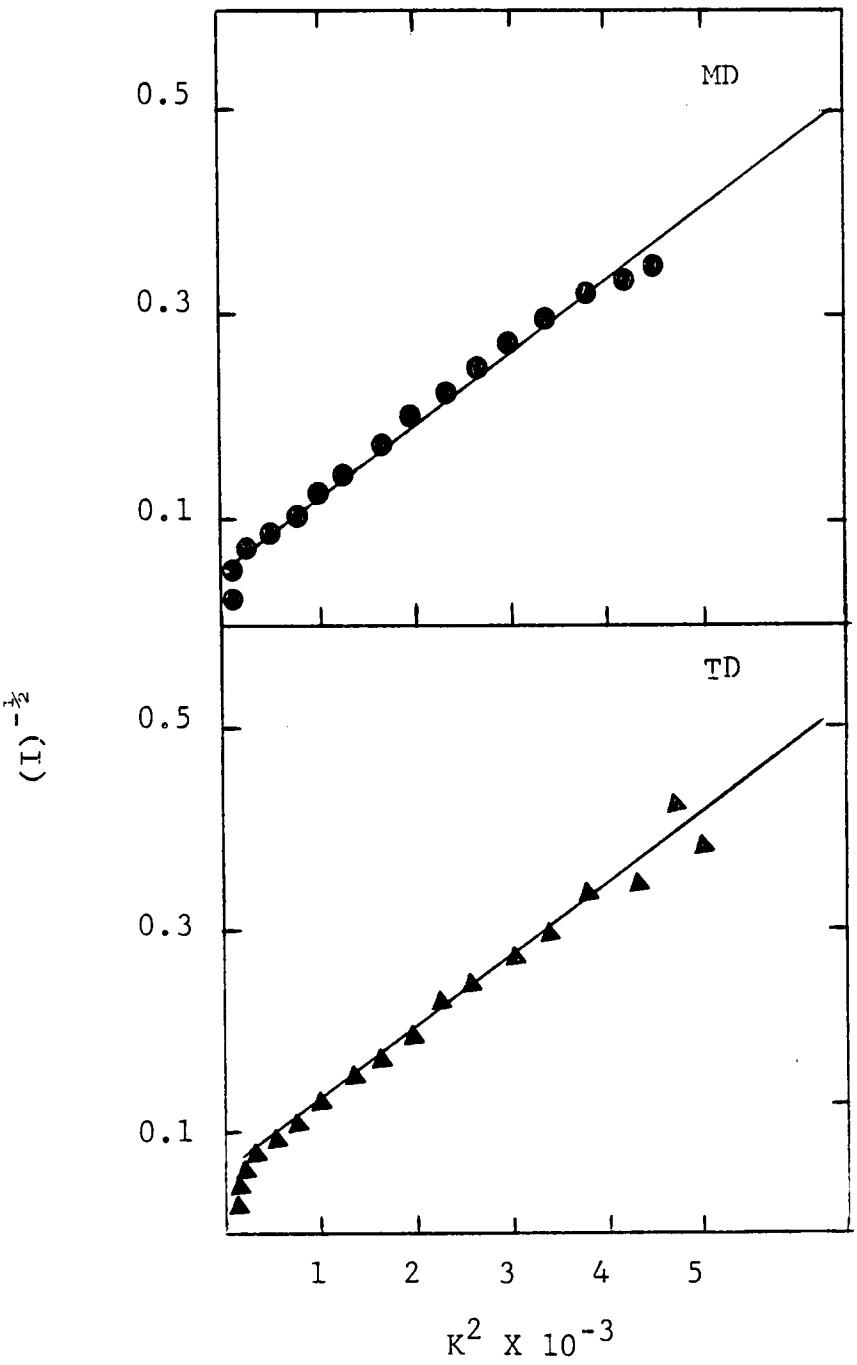


Figure IV.19. Debye-Bueche plots of through view for Sample 1)undrawn film.

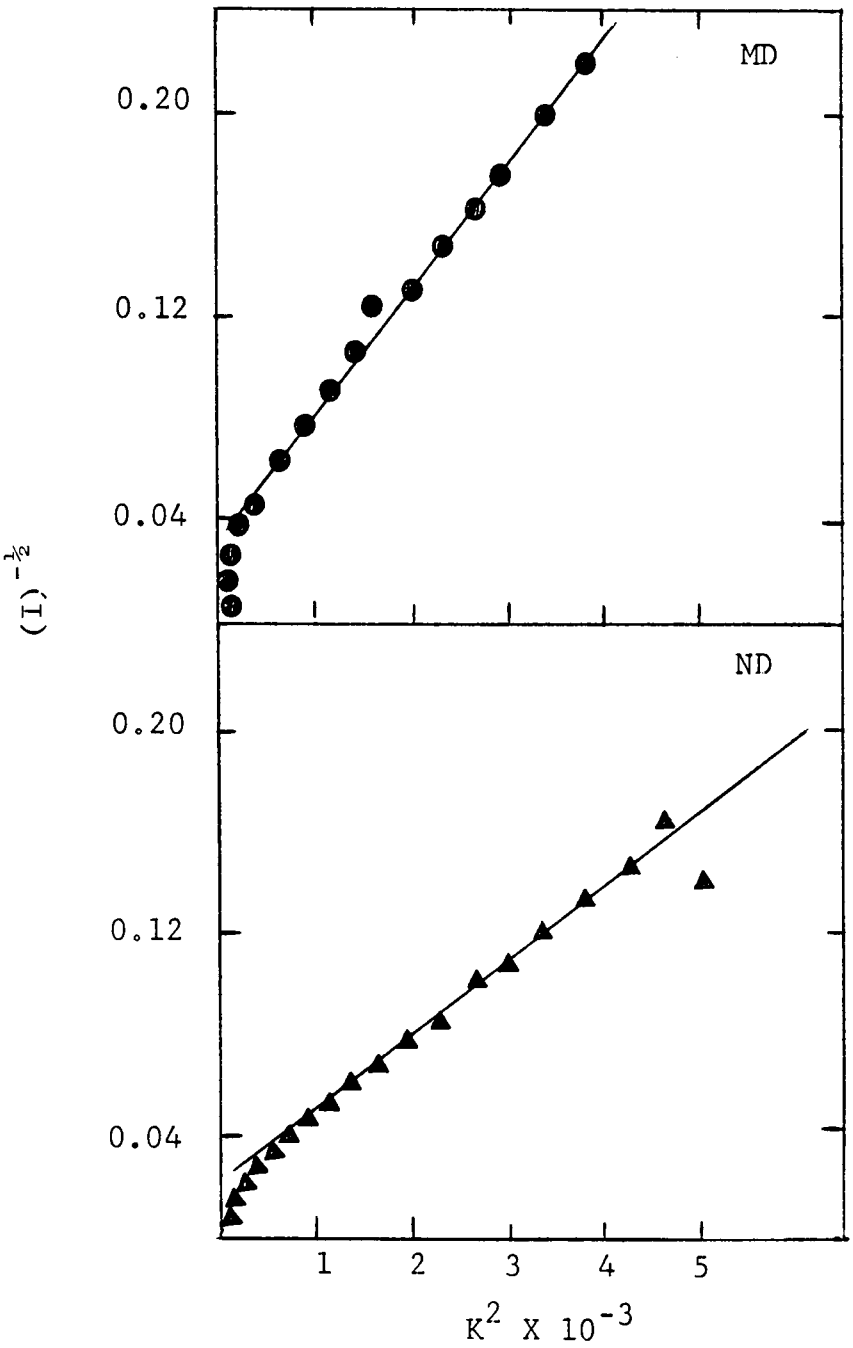


Figure IV.20. Debye-Bueche plots of edge view for film one.

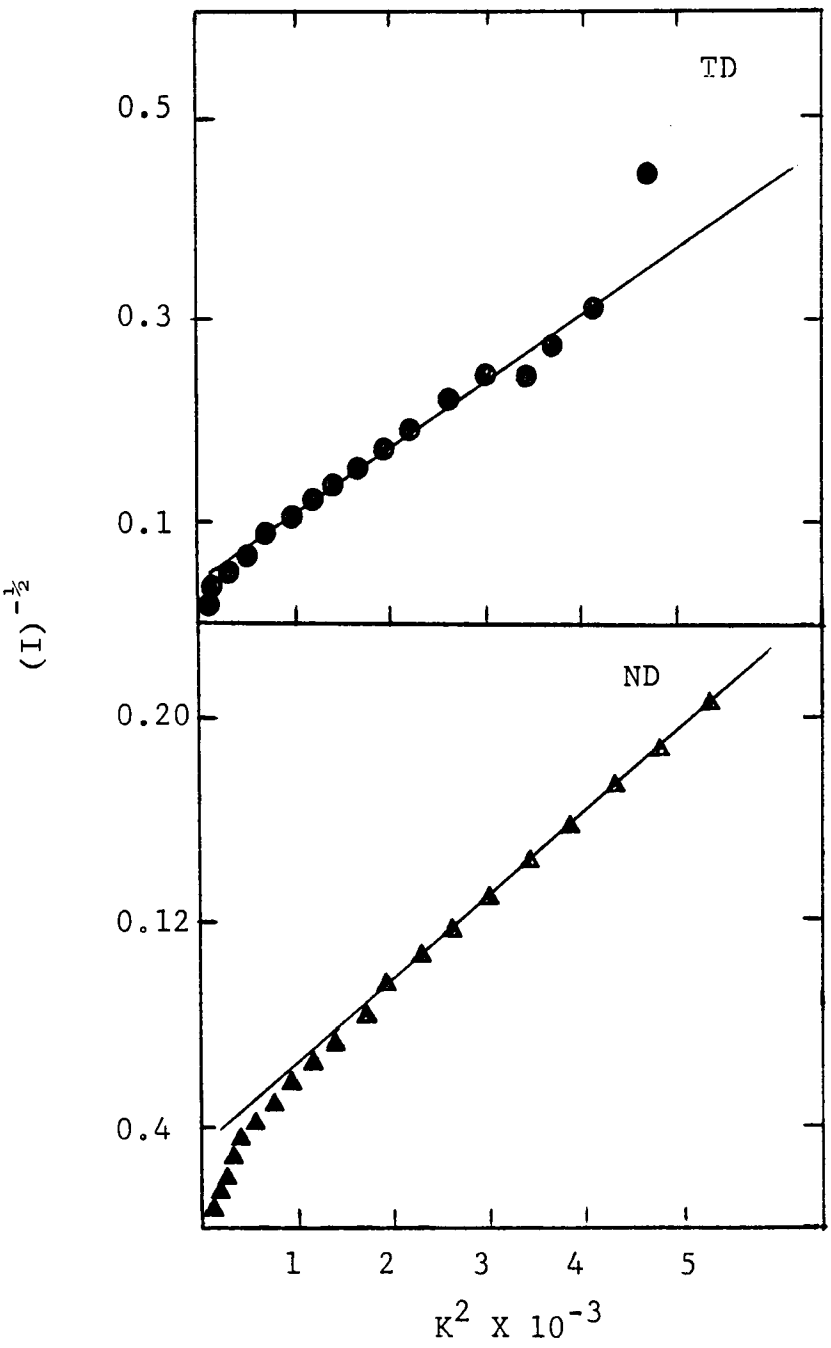


Figure IV.21. Debye-Bueche plots of end view for film one.

TABLE IV.6. SUMMARY OF VOID SIZE DETERMINED BY DEBYE et al. TECHNIQUE

Sample No.	Direction	Correlation Distance, nm	Density* (g/cc)	Void Fraction `φ'	Average Size, nm
1	MD-TD	5.01			12.11
	MD-ND	3.74	0.88	0.405	9.43
	TD-ND	4.40			11.10
3	MD	4.95			8.27
	TD	4.18			6.97
	MD	4.66	1.329	0.102	7.77
	ND	4.22			7.04
	TD	4.08			6.81
	ND	3.90			6.51
4	MD	3.43			6.10
	TD	3.43			6.10
	MD	4.08	1.250	0.155	7.25
	ND	3.37			5.99
	TD	4.07			7.22
	ND	3.00			5.33
5	MD	3.73			6.32
	TD	3.81	1.308	0.116	6.46

* $\rho_{solid} = \rho_{crystal} = 1.48$ g/cc employed two phase model

C. Molecular Orientation

Qualitative Wide Angle X-Ray Scattering

Figure IV-22 presents WAXS film patterns for Kevlar film samples 1-5. These patterns were taken with the x-ray beam normal to the plane of the PPTA films. The machine direction is vertical and the transverse direction is horizontal. The five rings from the inner to outer reflection are (110), (200), (211), (004) and (006) as shown in Figure IV-22. The (006) reflections indicate orientations of the c-axis in the machine direction for sample 1 through sample 3. The degree of orientation, as determined by the length of the arcs, does not appear to be very high for extruded sample 1. The (006) reflections however, exhibit little orientation in this film, and increasingly large uniaxial orientations in the machine direction in film 2 and 3 respectively.

The mandrel processed film 4 and annealed sample 5 show no orientation in the plane of the film. Sharper reflection rings are present for sample 5 indicating higher crystallinity brought about by annealing.

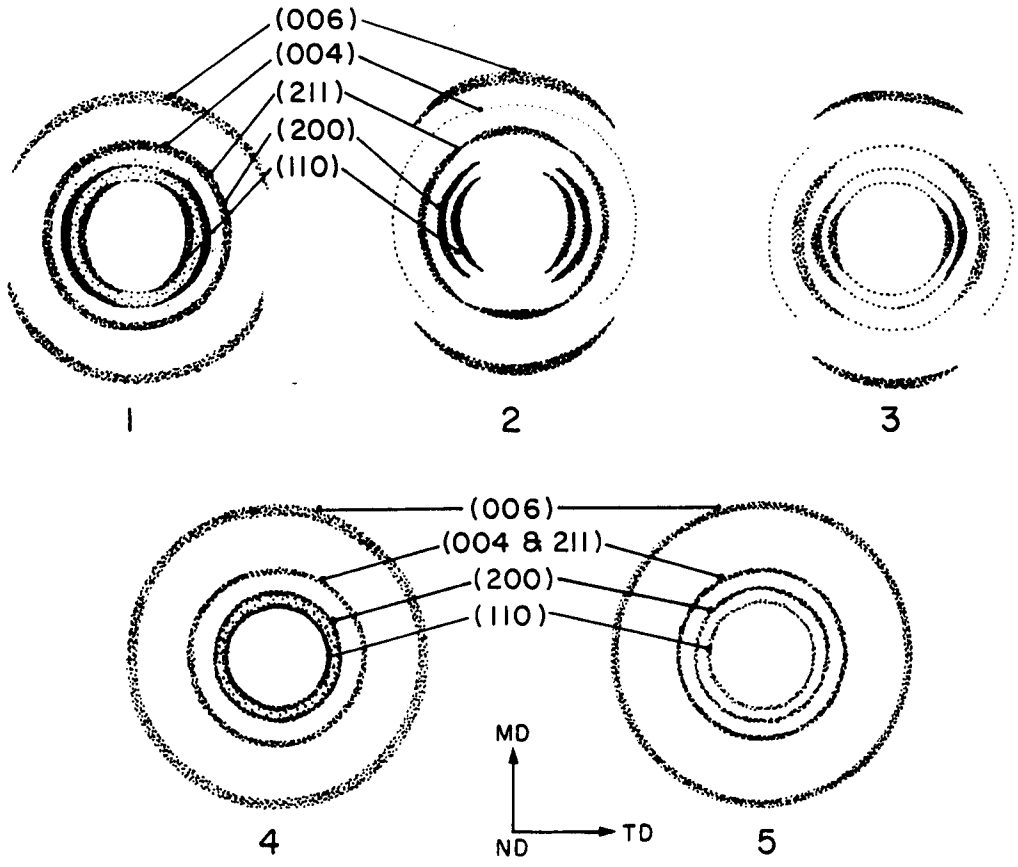


Figure IV.22. Schematic of typical WAXS patterns taken normal to the extrusion plane of;
1. Extruded
2. Uniaxial low drawdown
3. Uniaxial high drawdown
4. Mandrel processed
5. Annealed mandrel film

Pole Figures and Orientation Functions

Specimens for pole figures were prepared following the procedure described in Chapter III. Results are shown in Figures IV-23 to IV-27. Figure IV-23 exhibits pole figures for the (200) and (006) reflections for extruded sample 1. The (006) poles represent the orientation of the c-axis, while (200) poles are equivalent to orientation of the a-axis. This figure shows the existance of uniaxial orientation in the machine direction. The C-axis shows some orientation in the machine direction, while the a-axis orientation exhibits a symmetric orientation about this axis. Pole figures for film 2 and 3 are presented in Figure IV-24 and IV-25. These figures exhibit the influence of drawdown on orientation. The c-axis orientations are in the machine direction for both low drawdown uniaxial film 2 and highly drawdown film 3, but the orientation levels are higher for film 3. The a-axis of these films is almost perpendicular to the machine direction but concentrated in the normal direction, especially for sample 2. The highly drawn sample 3 exhibits a more uniaxial fiber type orientation.

Biaxially drawn films 4 and 5 exhibit orientation of the (006) poles,which represent c-axis being approximately equally distributed between the machine

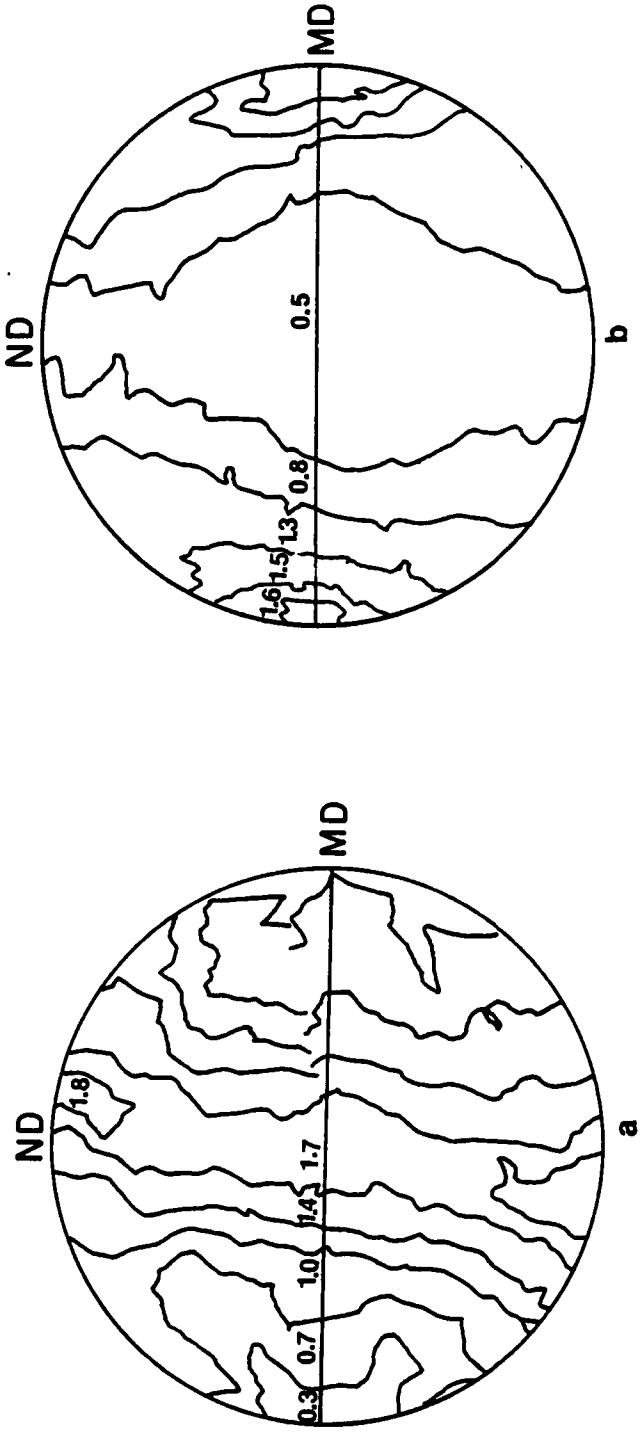


Figure IV.23. Pole figures for extruded PPTA film
a. 200 Reflection
b. 006 Reflection

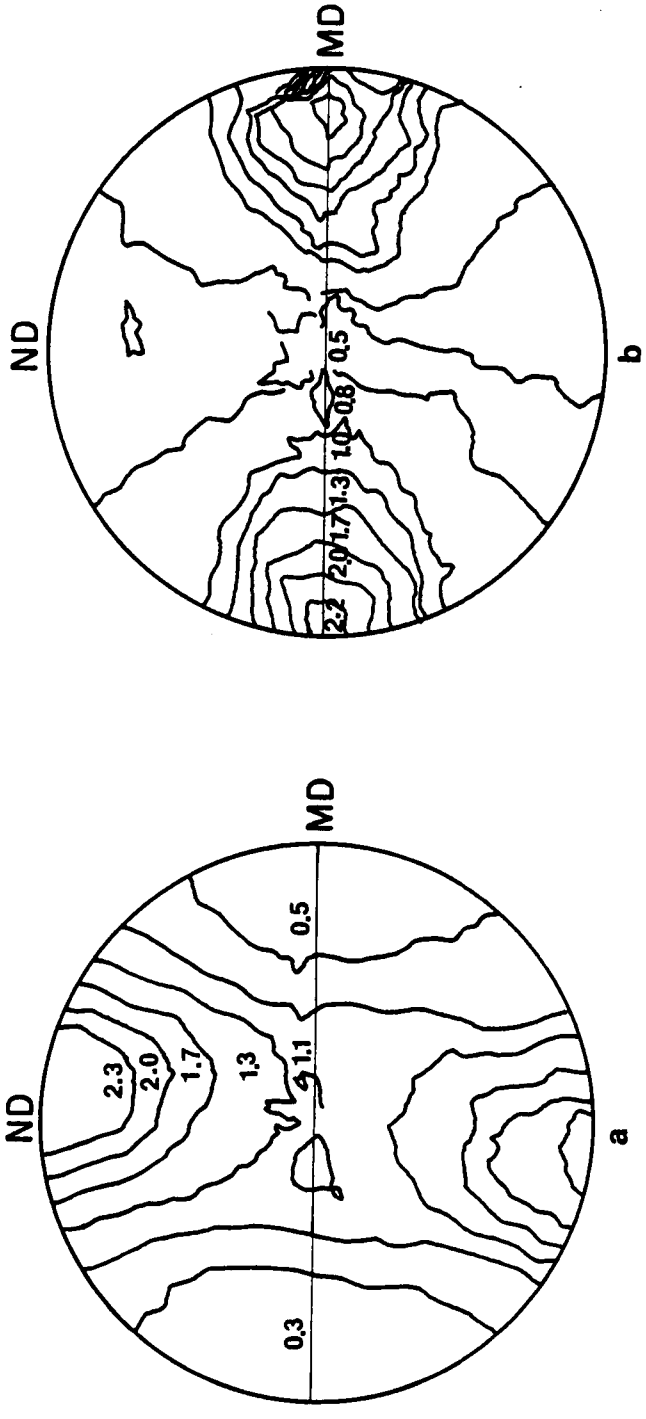


Figure IV.24. Pole figures for uniaxially low drawdown PPTA film
a. 200 Reflection
b. 006 Reflection

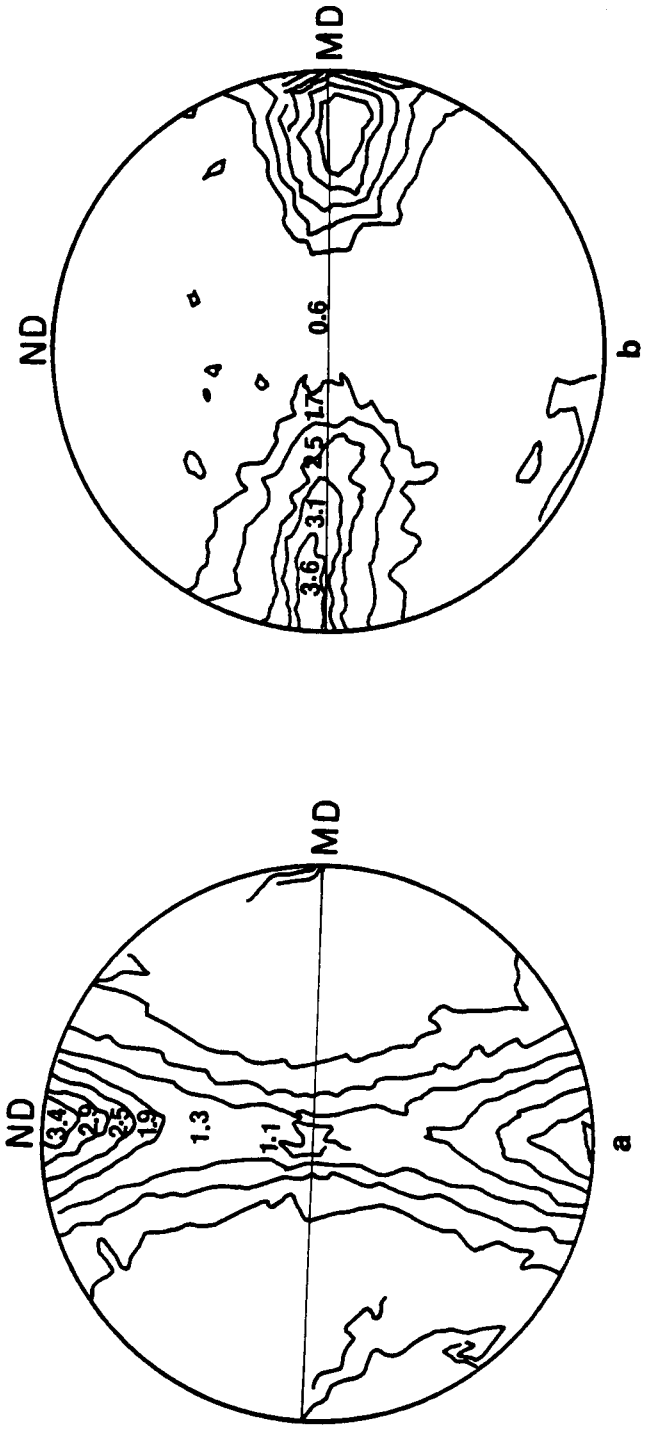


Figure IV.25. Pole figure for uniaxially high drawdown PPTA film
a. 200 Reflection
b. 006 Reflection

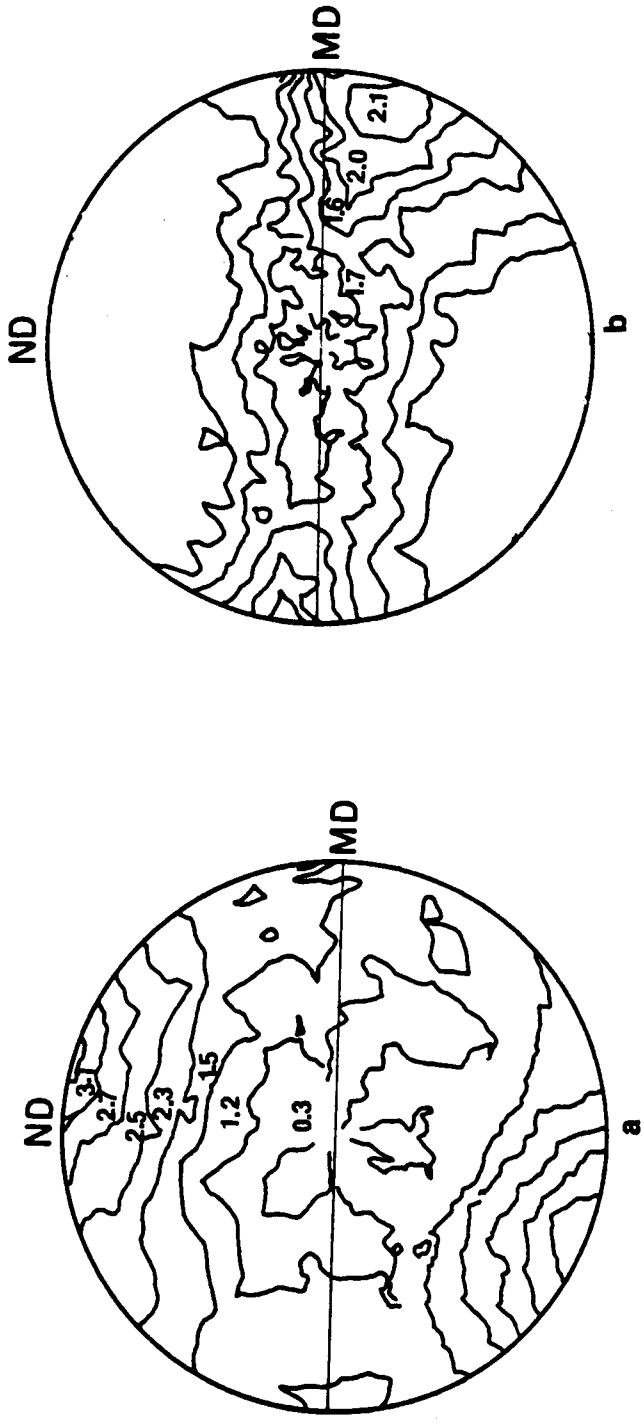


Figure IV.26. Pole figures for mandrel PPTA film
a. 200 Reflection
b. 006 Reflection

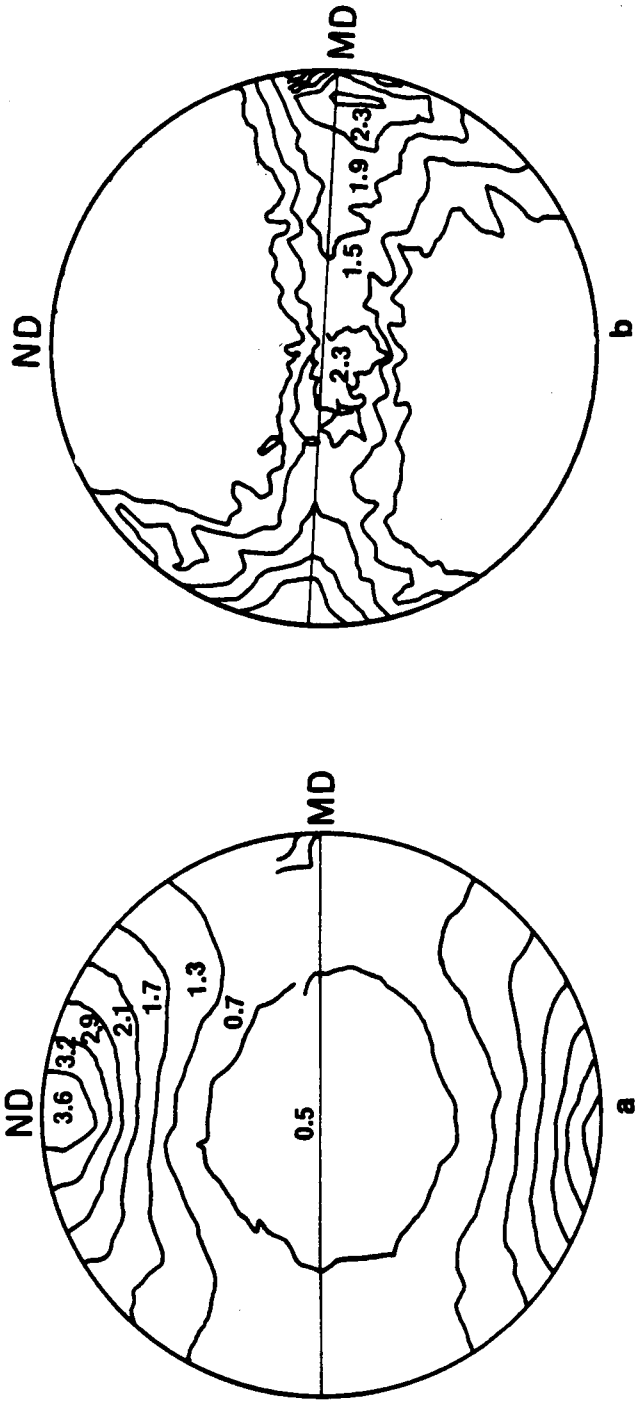


Figure IV.27. Pole figures for annealed mandrel PPTA film
a. 200 Reflection
b. 006 Reflection

direction and the transverse direction. The a-axis represented by the (200) pole is concentrated in the thickness (normal direction) direction of these samples (see Figure IV-26 and IV-27). The influence of the annealing process on the orientation of PPTA film can be seen from the pole figures for film 5 with an enhanced biaxial orientation.

Biaxial orientation factors were determined from the pole figures using the procedure described in previous chapter. Table IV-7 gives the results for the a-, b-, and c-axis crystalline orientation functions of the PPTA unit cell relative to reference directions 1 (MD) and 2(TD). These values are also plotted on the orientation triangle in Figure IV-28.

The extruded or undrawn film has f_{1c}^{B} of 0.24 and f_{2c}^{B} of 0.15. This indicates orientation of the c-axis mainly in the machine direction. The low drawdown film 2 and highly drawn film 3 without the mandrel have higher uniaxial orientation with f_{1c}^{B} of 0.32, 0.5 and f_{2c}^{B} of 0.17, 0.23 respectively.

The orientation functions for the a-axis of samples 1-3 indicate f_{1a}^{B} values that are larger or more negative than f_{2a}^{B} values. These are -0.15, -0.21, -0.29 for f_{1a}^{B} and -0.08, -0.08, -0.012 for f_{2a}^{B} of samples 1,2, and 3 respectively. The b-axis orientation factors for these

TABLE IV.7. BIAXIAL ORIENTATION FACTORS FOR PPTA FILMS

No.	f^B_{1a}	f^B_{1b}	f^B_{1c}	f^B_{2a}	f^B_{2b}	f^B_{2c}
1	-0.15	-0.09	0.24	-0.08	-0.07	0.15
2	-0.21	-0.11	0.32	-0.08	-0.08	0.17
3	-0.29	-0.21	0.50	-0.12	-0.11	0.23
4	-0.20	-0.12	0.32	-0.20	-0.13	0.34
5	-0.23	-0.18	0.41	-0.30	-0.12	0.43

films indicate the same type of orientation as that of a-axis. Values for the b-axis orientation functions are slightly lower than those for a-axis orientation factors (see Table IV-7). However in both cases the resulting points are situated near the line indicating orientation perpendicular to the machine direction (see Figure IV-28).

The film pulled down over the lubricated mandrel exhibits c-axis orientation function of $f_{1c}^{B} = 0.32$ and $f_{2c}^{B} = 0.34$. These points falling on the biaxial line in Figure IV-28 indicate nearly equal biaxial orientation of the c-axis in the machine and transverse direction. Annealed biaxial sample five gives biaxial orientation factors for the c-axis higher than those of sample four. These are $f_{1c}^{B} = 0.41$ and $f_{2c}^{B} = 0.43$.

The a-axis orientation factors for biaxial films 4 and 5 are situated along the biaxial line in the third quandrant of the orientation triangle, see Figure IV-28. This means that the a-axis in preferentially pointed normal to the film plane. The values for the b-axis orientation functions are considerably lower than those for a-axis orientation functions of both film 4 and 5 (see Table IV-7). This implies that the b-axis is more isotropically oriented as compared to the a- and c-axis.

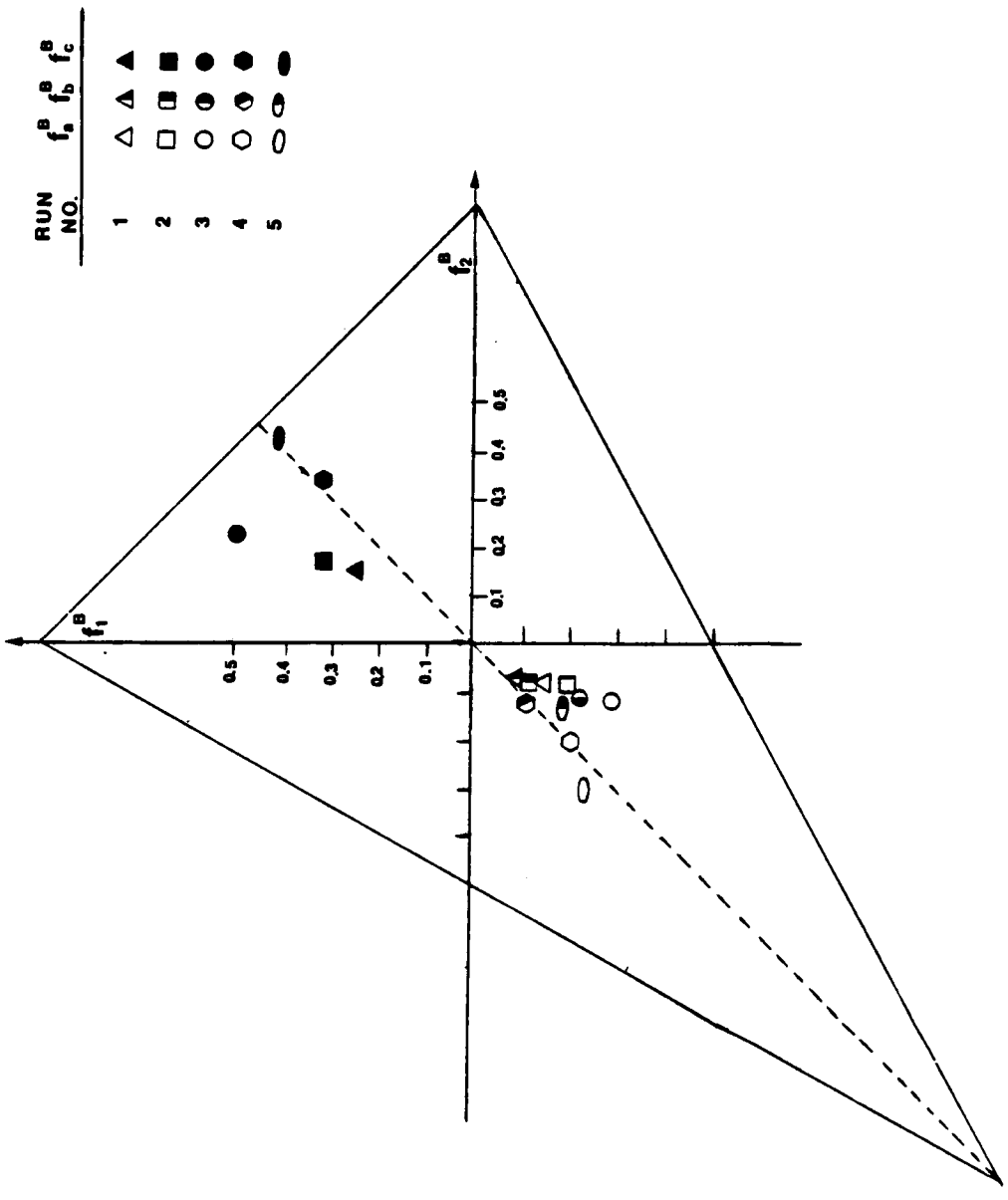


Figure IV.28. Orientation triangle for PPTA films.

D. Discussion

The main emphasis of this research work was to study the effects of void structure and orientation on the mechanical properties of films produced under various processing condition. In this section, the structural development of PPTA films will be discussed and their mechanical properties will be explained and compared to those of CTA films separately in a later chapter.

The SEM photomicrographs of all PPTA films in general reveal similar results to those obtained by Flood, White and Fellers (63). SEM photomicrographs for the cross-sectional views of sample 1 (Figure IV-1) exhibit extensive voiding at the center of the film which are elongated and perpendicular to the machine direction. These large holes in the center of the film cross-sections, and finger like void structure seen on the outer boundaries of the film edges are similar to the void structure identified by Hancock et al. (73) for wet spun Nomex^{R} fibers. However, as the drawdown ratio increases these voids become smaller (compare Figure IV-2 to Figure IV-3), and disappear for highly drawdown uniaxial film 3 (see Figure IV-3). Furthermore, in the cross-

section of sample 1, one also can easily find fibrillar structure which developed perpendicular to the film. These are still found in low drawdown film 2 but they do not make the aligned structure in this film. In highly drawn uniaxial film 3, the fibrillar structure is merely observed and the cross-sections of this film are solid, which is very similar to the cross section of Flood et al. uniaxial Kevlar film and Hancock et al. Kevlar fibers. It is also important to note that the micro-structure seen in the cross section becomes more smooth and less defective with increasing drawdown ratio. These results are qualitatively in a good agreement with density data. The density of highly drawn uniaxial film 3 reached to 1.329 (grams/cm^3), which is greater than the density of low drawdown film 2. Likewise, the density of uniaxial low drawdown film 2 is greater than that of undrawn film 1.

The biaxially expanded film 4 exhibits SEM photo-micrographs indicating a very smooth surface as compared to the wrinkled surface of undrawn and uniaxially drawn films. The cross-section of this film was expected to be solid due to the thickness of this film (0.27 mm). However, voids and fibrillar structure can be seen from the SEM patterns for this sample (Figure IV-4). The density of this sample was 1.250 significantly lower than

that of highly drawn uniaxial film 3, with a solid like cross sectional structure. After annealing this mandrel processed film, the surface and cross-sections became relatively smoother and less defective. This led to a significant increase of density from 1.250 to 1.308 (see Table IV-2).

It is also important to note that, as shown in Table IV-2, drawing the film results in an increase of density and decrease of film thickness. This abrupt change in density and thickness especially at the higher drawdown ratio (for film 3) was coupled with the macroscopic observation that the undrawn film was converted from a very opaque to a yellowish type color. The dark opaque structure observed in extruded film is attributed to structural elements greater than the wavelength of light being produced during the processing of this film. This is presumably due to the extensive voiding, seen in SEM patterns of this film. The voids were not visible in the SEM photomicrographs of highly drawn uniaxial film 3. However, the existance of small voids is easily authenticated from SAXS patterns, Figure IV-6 and Figure IV-9.

A very intensive continuous isotropic scattering, Figure IV-6, for sample 1 indicates the existance of a very irregular distribution of large electron density

variation in the film cross section. This diffuse SAXS has often been interpreted as due to the presence of voids (9), and was recently substantiated by a correlation of volume fraction of microvoids computed from the SAXS technique with microvoid fraction estimated from a combination of crystallinity (DSC technique) and density measurements for polypropylene fibers (35). However, it is apparent from SAXS patterns in Figure IV-6, that the diffuse scattering intensity decreases with increasing draw ratio. The scattering in film 2 is more concentrated in the equatorial direction and this is accentuated in film 3. This decrease in intensity of scattering indicates a decrease of voids as a function of drawdown ratio. Furthermore, the change of scattering from the isotropic pattern of extruded film 1 to equatorial scattering in uniaxial films 2 and 3 indicates a change in void dimensions. The SAXS film pattern for biaxial film 4 reveals a uniform scattered intensity around the beam stop.

Annealing of this sample resulted in a decrease of scattered intensity which is consistent with the results obtained from SEM and density measurements. In the present study selected samples were quantitatively analyzied in order to measure void sizes and void size distribution of the films, as shown in Figure IV-7 through Figure

IV-11 and Table IV-4. All three patterns for extruded sample 1 are almost isotropic, indicating the voids are approximately spherical in shape having a dimensional range from 21.5 to 24.2 nm. This is reasonable, because the film sample was prepared by free extrusion of polymer solution into a coagulant. Uniaxial highly drawn film 3 exhibit SAXS patterns indicating elongated voids with dimensions ranging from 18.3 to 21.2, 23.3 to 24.0, and 22.9 to 26.3 nm in the normal, transverse, and machine directions respectively. The void sizes when the beam is normal to the plane of the biaxially expanded film are 22.7 nm in both the transverse and machine direction. This is decreased to 18.9 nm after the annealing process which seems reasonably consistent with increase of density and SEM patterns observed in annealed sample 5.

It must be noted that the void sizes measured using the Debye-Bueche method were found to be much smaller than those obtained from the Guinier technique (compare Table IV-4 to Table IV-6). This can be explained from the fact, that some of the void seen in SEM photomicrographs are very large (micron size voids) and are not detactable by small angle x-ray due to the wavelenght of the radiation (λ =1.542 Å). Therefore we can not obtain any information on the particles or voids which are larger than about 1000 Å. Furthermore, in this Debye- Bueche

analysis the average size of void was computed from the combination of correlation length (distance between the voids) and volume fraction of void (52). The volume fraction of void was also estimated using the density data (Table IV-3). However, it is very reasonable to expect that there is distribution in void sizes and the distribution is different from sample to sample. It seems to appear that some are larger and some are smaller than the SAXS range (10 - 1000 Å). In addition the Debye-Bueche plot is usually applicable at rather high scattering angles (it always deviates at very small angles, Figure IV-19 to Figure IV-21), whereas the average size of void computed from the slope of Guinier plot at very small angles.

From this view of size distribution (in SAXS range) the data were analyzed according to Jellenik,Solomon and Funkuchen.Due to reciprocity between the dimensions of inhomogeneity and the angular extent of the small angle scattering, the tangent at highest scattering angle of the plot of logarithm of scattering intensity against the square of the scattering function gives the size of smallest voids and then the intercept at zero scattering function is proportional to the fractional volume of the voids. The difference between the original plot and the tangential line is represented by the first resolved curve. This also allows us to compute the particle size

and the fraction of second smallest particle. Similarly, the second resolved curve is for the third group.

The void size measured using this technique varies from 5 to 33 nm. This procedure is in essence an expansion of Guinier analysis. Specifically the Guinier relation holds for the random particle system of which particle concentration is quite small and there exists no interaction between the particles. The PPTA films examined in the present study contain voids at least 10 percent by volume as shown in Table IV-3.

Longman and his co-worker (220) also estimated void size distribution of porous silicas for GPC experiment, using Debye and Bueche analysis. They found that the pore sizes measured by mercury porosimetry are in good agreement with those estimated through Debye-Bueche method.

Consequently, the SAXS results are consistant with those observed and estimated from SEM and density data.

Individual structural parameters such as a,b, and c-axis orientation function Figure IV-23, IV-28 and Table IV-7, showed that the c-axis is mainly pointed in the machine direction, while the a-, and b-axis rotate about the c-axis. The orientation functions, WAXS pattern and pole figures all demonstrate the same type of orientation in extruded film 1 which is a fiber type texture, without the high degree of orientation. These

observations are in good agreement with the mechanical property results described in Chapter VI and presented in Table VI-1 and Figure VI-1 for this specimen.

It is noteworthy that this film was just extruded and no drawdown was applied on it. The degree of orientation is relatively high considering the extrusion condition. This may be attributed to the easily oriented nature of the liquid crystalline solutions.

Furthermore Shimamura et al. (162) in their extruded hydroxypropylcellulose (HPC), which was considered to be a thermotropic liquid crystal, found skin-core type structure. This undrawn filament exhibited a higher degree of orientation in the outer skin than the material inside the skin (core). This was believed to be achieved during the flow through the reservior and die. A similar situation may be attributed to the extruded film 1 in the present work.

The WAXS patterns, pole figures and orientation functions for both low and high drawdown uniaxial films indicate the same type of orientation as observed for undrawn or extruded except that orientation is enhanced in these films. The c-axis orientations are in the machine direction for both films 2 and 3, but orientation levels are higher for film 3. The a-axis of these films is almost perpendicular to the machine direction. Film 3 exhibits a more uniaxial fiber orientation as a

consequence of increase in drawdown ratio; see Figure IV-24, IV-25 and Table IV-7.

For biaxial mandrel processed film, there is also consistant agreement among WAXS pattern, pole figure, and orientation factors. All three methods indicate biaxial orientation of the c-axis in the machine and transverse directions. The a-axis appears to be oriented normal to the film plane. WAXS pattern, pole figures, and orientation functions for sample 5 show the influence of heat treatment on orientation. The results of these structural parameters for this sample are indicative of an enhanced biaxial orientation see Figure IV-28 , IV-27 and Table IV-7.

However, in general the undrawn or extruded film exhibits poor mechanical properties as compared to those of uniaxially drawn films (see Chapter VI, Table VI- 1 and Figure VI- 1 through VI- 7). This can be attributed to the low level of orientation and existance of extensive voiding in this film. The uniaxially drawn films 2 and 3 showed higher levels of orientation compared to the extruded film. The cross-sectional views of these films, expecially uniaxial highly drawn film 3, together with their higher density values may suggest that the machine direction tensile strength of these samples are much higher than that of the extruded film. It should be noted that the films 3 and 5 with the least voids and

having higher orientation factors were the strongest among other processed films. The mechanical properties of each individual film will be further discussed and compared to those described by other investigators for PPTA films and Fibers (13,63,102) in Chapter VI and Chapter VII.

CHAPTER V

STRUCTURE DEVELOPMENT OF CTA FILMS

Since experimental procedures for producing CTA films were discussed in Chapter III, it now becomes important to explain the processing conditions in which certain parameters play important roles and have to be considered. A series of ten films including a commercial cast CTA film supplied by Celanese Fibers Company have been characterized and are discussed in this chapter.

A. Processing Conditions

In order to produce CTA films from both isotropic and anisotropic solutions, the solvent and coagulation selections must be carefully considered. It is found that cellulose triacetate yields better defined structures in the anisotropic phase. The extent of structure developed is dependent upon long range order or crystallinity of the polymer. The structure in the anisotropic phase is also dependent upon the quality of the solvent. Better solvents tend to yield better defined structure (29).

Moreover, the solvent and coagulation selections are not independent for the coagulant must extract the solvent from the polymer solution. This also influences the

structure of the final polymer product (63,76,101).

Various researchers (29,115,136) have listed several suitable solvents in which CTA forms liquid crystalline solutions. Furthermore Omatete (216) found that various coagulants can be used in processing of CTA films. Isopropanol was the most suitable coagulant for solutions of CTA in dichloroacitic acid (DCA), but the coagulation rate for this system was too slow in a continuous film extrusion process. It was found that this coagulant did not extract the solvent fast enough to permit orienting the uniaxial film by stretching, or freeze in the orientation imparted on the film extruded over the mandrel. The film would adhere together during take-up. The most adequate coagulant was found to be methanol cooled $5^{o}C$.

In the present study, a mixture of DCA/FA with the mass ratio 2:1 was chosen as a solvent and the coagulant was isopropanol cooled to about zero degree centigrade. Since the coagulation rate is relatively slow for CTA/ DAC/FA in cold isopropanol, deformation and coagulations are simultaneously possible. This is very important due to the fact that the molecular orientation is strongly related to the stress applied to the polymer solution.

Solution concentrations ranging from 23 to 30 percent were prepared using procedures described in Chapter III. A series of eight films were processed

using apparatus in Figure III-4, under process conditions given in Table V-1.

One film (sample No.1) was extruded from the 23 percent conentration (isotropic solution) using the recycle process with blow-up ratio of 2.0 into the coagulation bath. In this case, the cold isopropanol is pumped into the film as it exits the die before it passes into the coagulant bath. The coagulant process commences immediately inside of the film and on both sides as the film enters the coagulation bath. The film is constrained as it is passed under the first roller in the bath and this results in a blow-up of the film between the die exit and this roller (see Figure III-7, page 169). Furthermore, as the coagulant is pumped into the film and blows it up, it becomes thinner and coagulation speeds up.

The blow-up ratio, however depends on the coagulant flow rate and the coagulation rate. It is determined by dividing the final film diameter to the initial diameter of the film as it emerges from the die. This is a relative measurement due to the effects of coagulation and possible shrinkage that may occur during this measurement.

The film extrusion rate was constant for all the films. This was obtained by calibrating the controller setting against the piston displacement. The volume displaced is then converted to the length of film extrusion per unit time. The piston moved against air

TABLE V.1. SUMMARY OF CTA FILMS PREPARED IN THIS STUDY

Sample No.	Percent Conc.	Method of Preparation	Processing Temp.(C^o)	Extrusion Rate (m/min)	Coagulant and Coagulant Temp.(C^o)
1	23	Extrusion/Recy.Proc. B.R.=2/coagulation	40	2.0	Isopropanol at 0 C^o
2	25	Extrusion/moderate drawdown/coagulation	40	2.0	Isopropanol at 0 C^o
3	25	Extrusion/Recy.Proc. B.R.=2.5/coagulation	40	2.0	Isopropanol at 0 C^o
4	28	Extrusion/moderate drawdown/coagulation	40	2.0	Isopropanol at 0 C^o
5	28	Extrusion/Recy.Proc. B.R.=3.0/coagulation	40	2.0	Isopropanol at 0 C^o
6	30	Extrusion/moderate drawdown/coagulation	40	2.0	Isopropanol at o C^o
7	30	Extrusion/Recy.Proc. B.R.=3.3/coagulation	40	2.0	Isopropanol at 0 C^o
8	30	Extrusion/Recy.Proc. B.R.=3.3/coag./ann.	40	2.0	Isopropanol at 0 C^o
9	-	CFC (Casting)	40	2.0	Isopropanol at 0 C^o
10	-	CFC (MeOH treated)	40	2.0	Isopropanol at 0 C^o

zero pressure. It is assumed that since this is a gear pump, pushing against the polymer solution would not decrease the rate of piston displacement. The extrusion rate calibration plot, which exhibits the linear relation between extrusion rate and controller setting is shown in Figure V.1. The extrusion rate was 2 meters per minute for all the films.

A processing temperature of forty degrees centigrade was chosen in order to help reduce polymer degradation and take-up for all uniaxial and biaxial films was carried out by hand. The specific take-up velocities were difficult to determine.

Samples 2,4, and 6 were produced from 25,28 and 30 percent concentrations respectively by uniaxially drawing the extrudate down into the coagulation bath. These uniaxially drawn films were prepared in similar manner to those of uniaxial drawdown Kevlar films described in Chapter IV. Samples number 3,5, and 7 were extruded from the solution concentrations of 25,28 and 30 percent concentration with blow-up ratios of 2.5, 3.0, 3.3 respectively into the coagulation bath. Sample number 8 was prepared by annealing sample number 7 (30 percent concentration) under tension at 275 ^{o}C for 30 seconds. The short time again was chosen in order to prevent degradation of the polymer film.

An additional sample number 9 in Table V-1 was

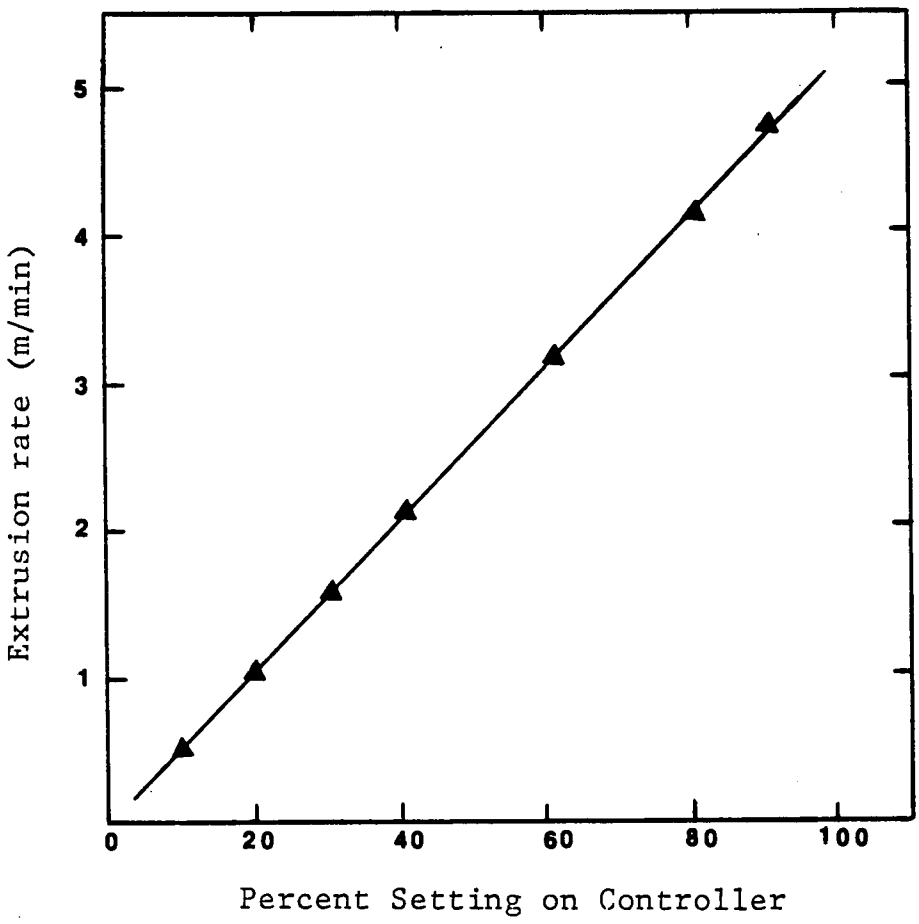


Figure V.1. Extrusion rate calibration.

supplied by Celanese Fibers Company (CFC). This film was cast and contained 15 percent triphenyl phosphite as an additive. The additive was removed by soaking this film in methanol for about forty eight hours. This is denoted as sample number 10 in Table V-1.

B. Void Characterization

Scanning Electron Microscopy

The scanning electron micrographs of both uniaxial and biaxial films were taken to investigate some morphological features of the films. The uniaxially drawn films were forceably split (peeled) after nicking with a razor blade, in order to investigate their internal structure. An attempt was made to peel the biaxially expanded films, but they did not peel due to the biaxial orientation developed in them. The microstructure, as determined by SEM, will be compared with the data obtained by small angle x-ray diffraction and density measurements in the later sections of this chapter.

SEM photomicrographs of surfaces and cross-sections of films 1-10 are shown in Figures V-2 through V-11. The SEM patterns of the "peeled" uniaxially drawn films are also included in Figures V-3, V-5 and V-7. The cross-sectional views of isotropic biaxially expanded film 1 exhibit voids on the order of 5 to 30

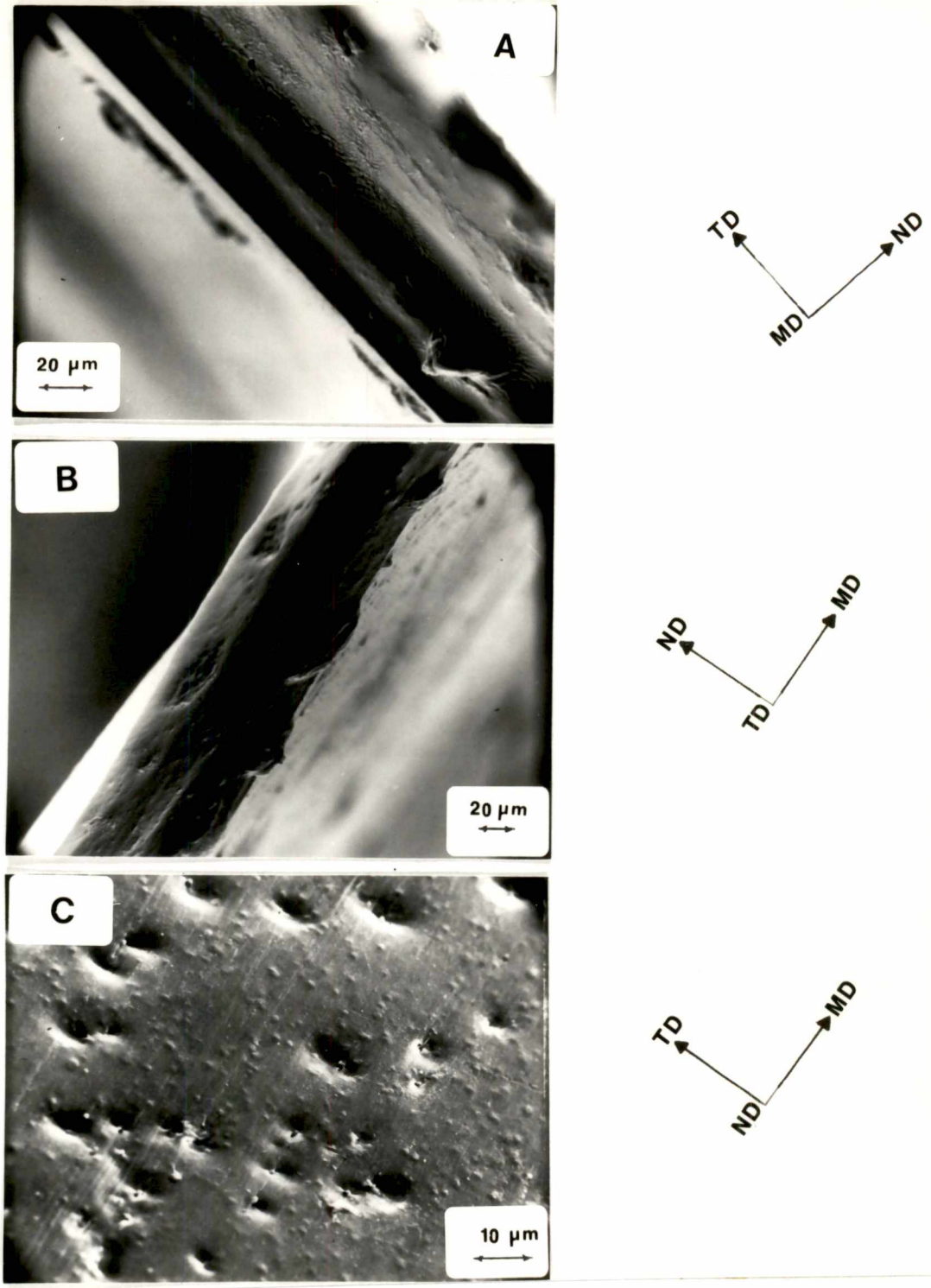


Figure V. 2. SEM photomicrographs for Sample 1;
a)End view b)Edge view c)Surface

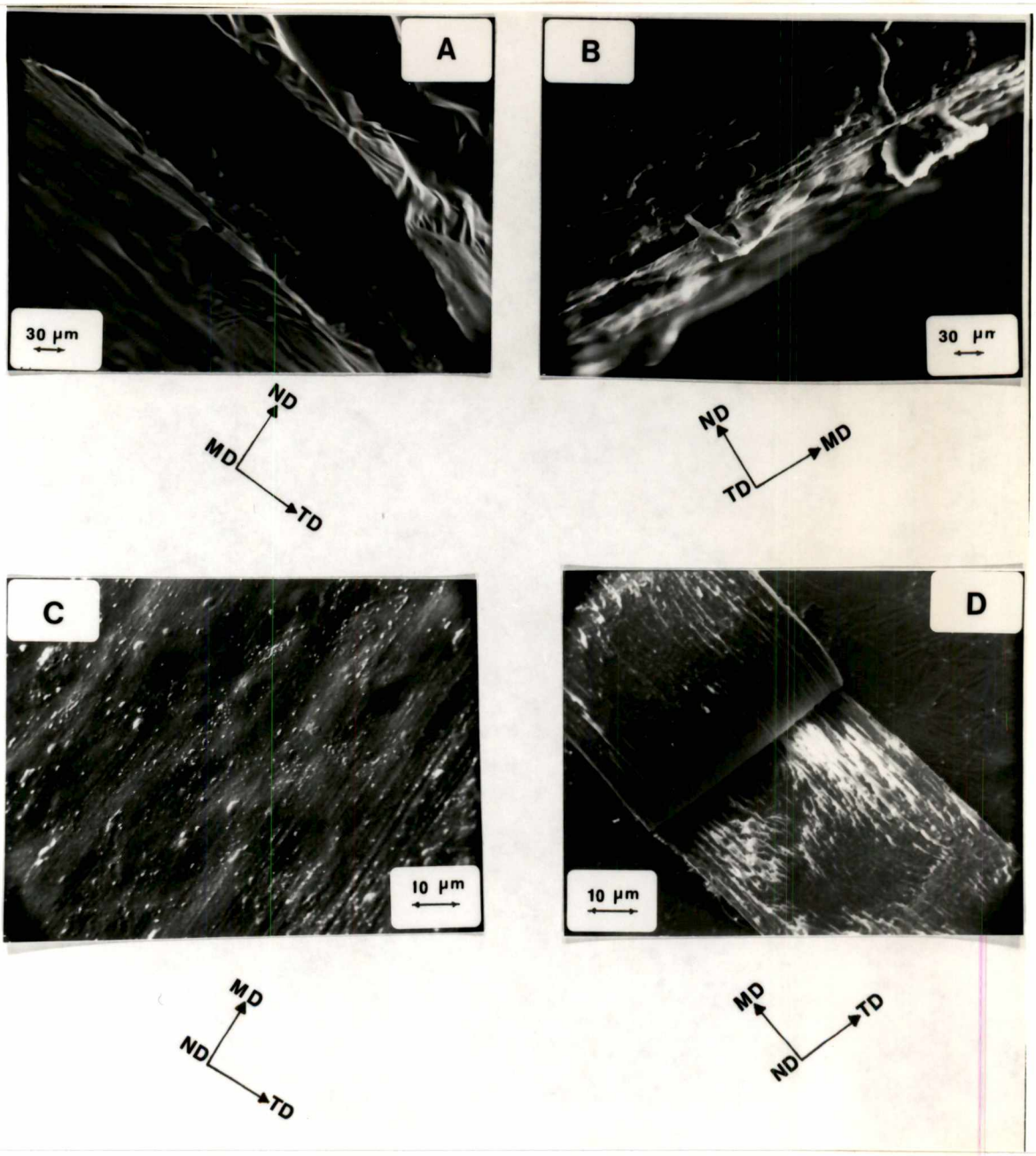


Figure V. 3. SEM photomicrographs for Sample 2;
a)End view b)Edge view c)Surface d)Peeled

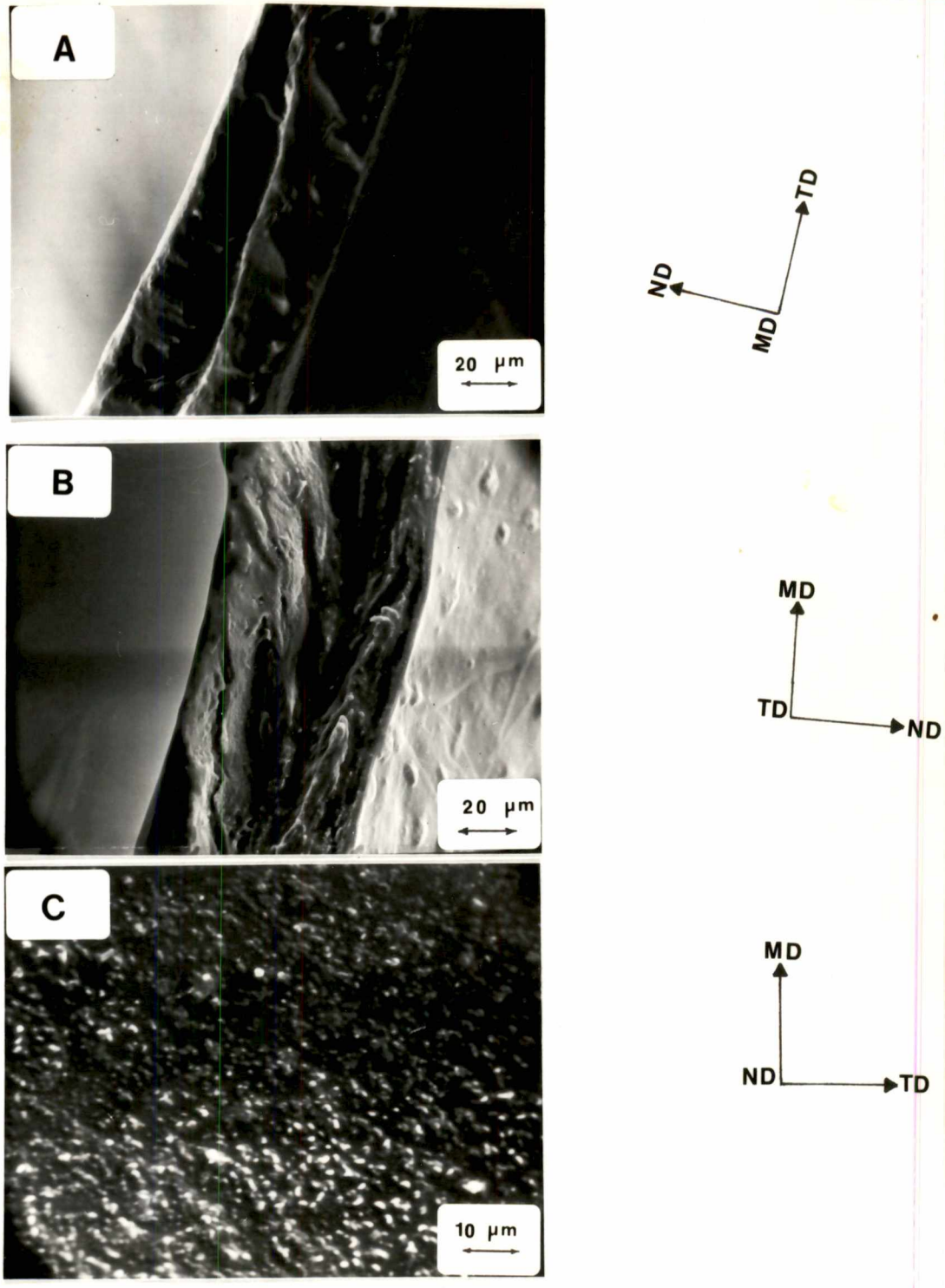


Figure V. 4. SEM photomicrographs for Sample 3;
a)End view b)Edge view c)Surface

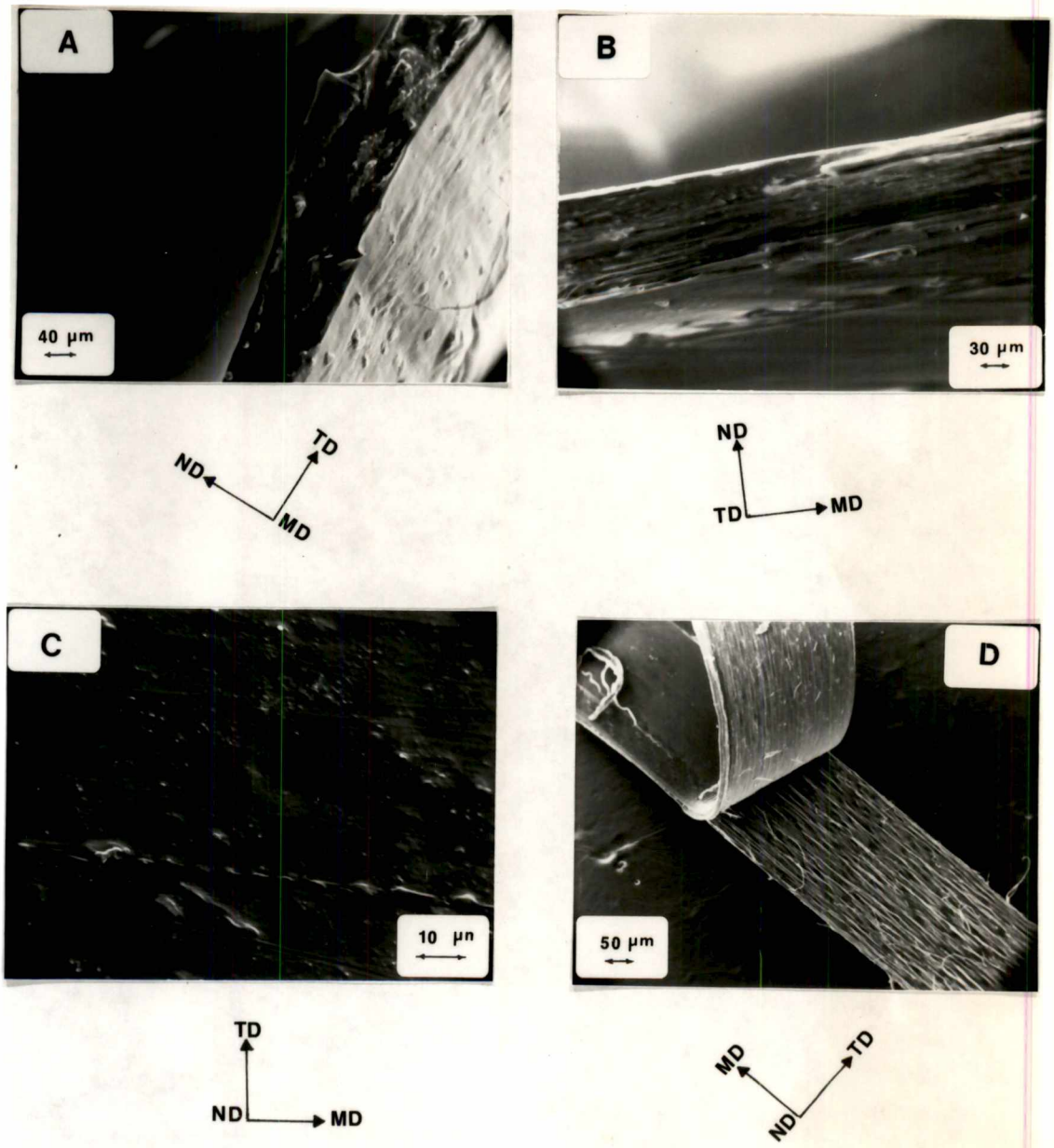


Figure V. 5. SEM photomicrographs for Sample 4;
a)End view b)Edge view c)Surface d)Peeled

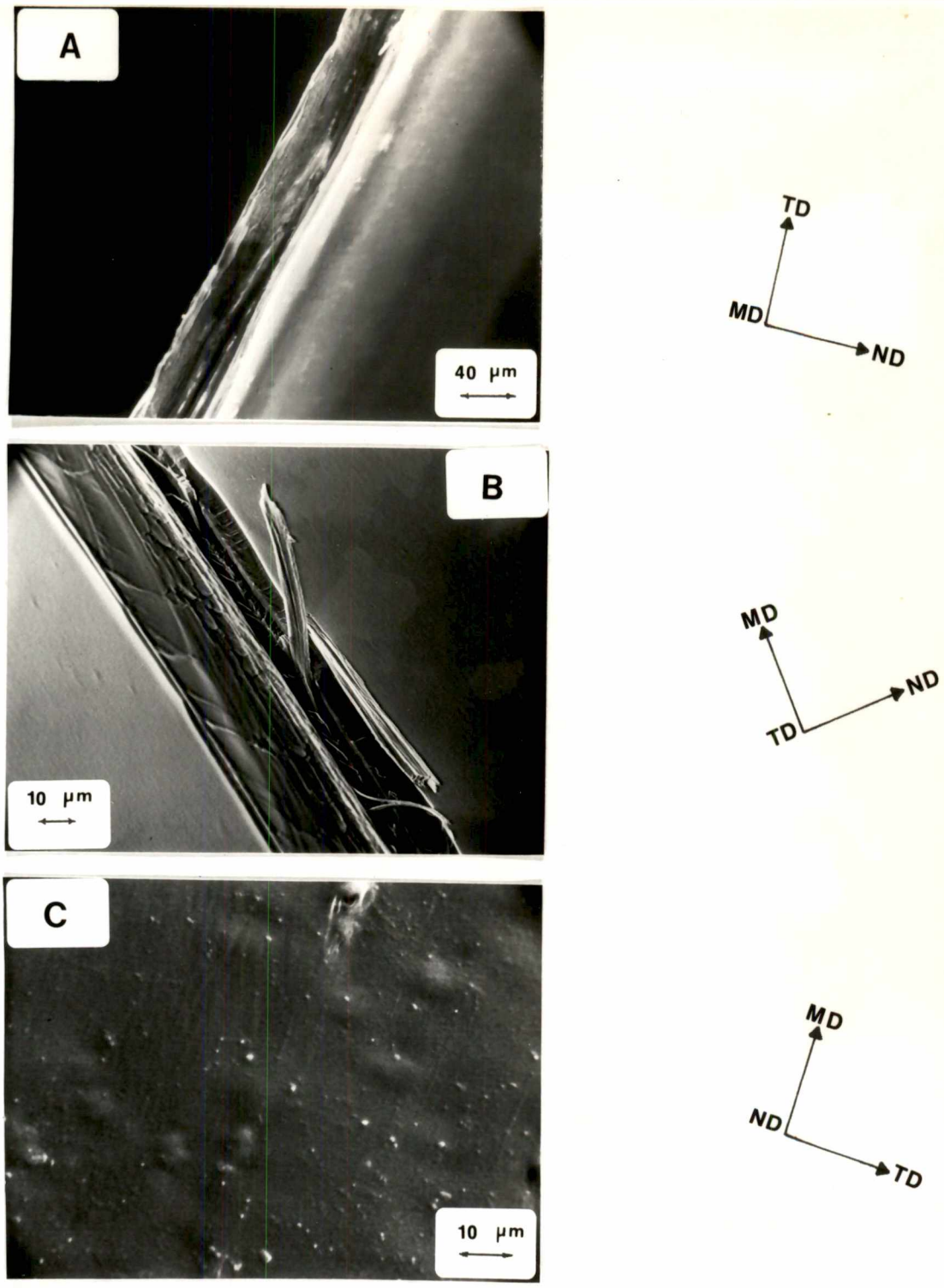


Figure V. 6. SEM photomicrographs for Sample 5;
a)End view b)Edge view c)Surface

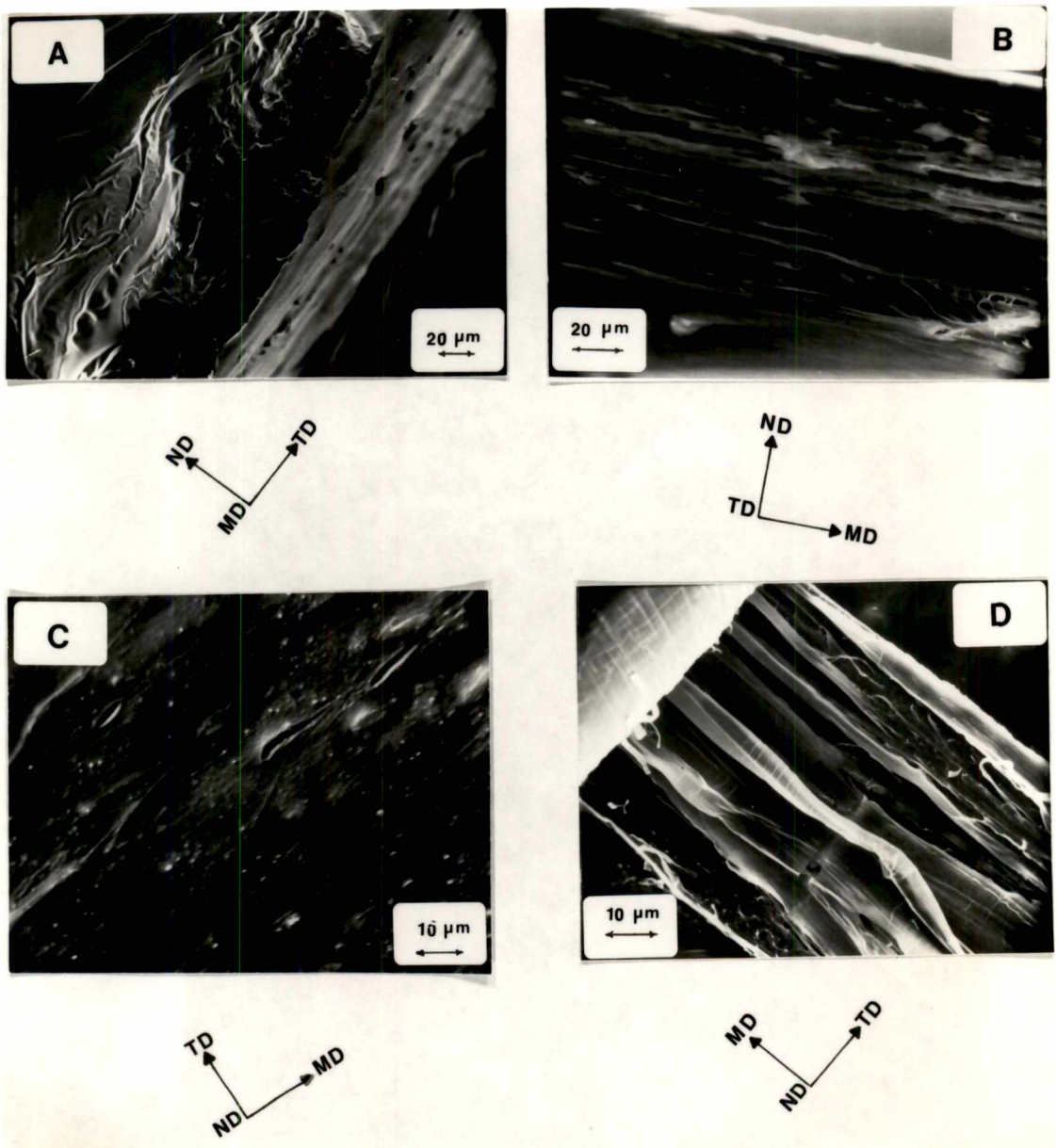


Figure V. 7. SEM photomicrographs for Sample 6; a)End view b)Edge view c)Surface d)Peeled

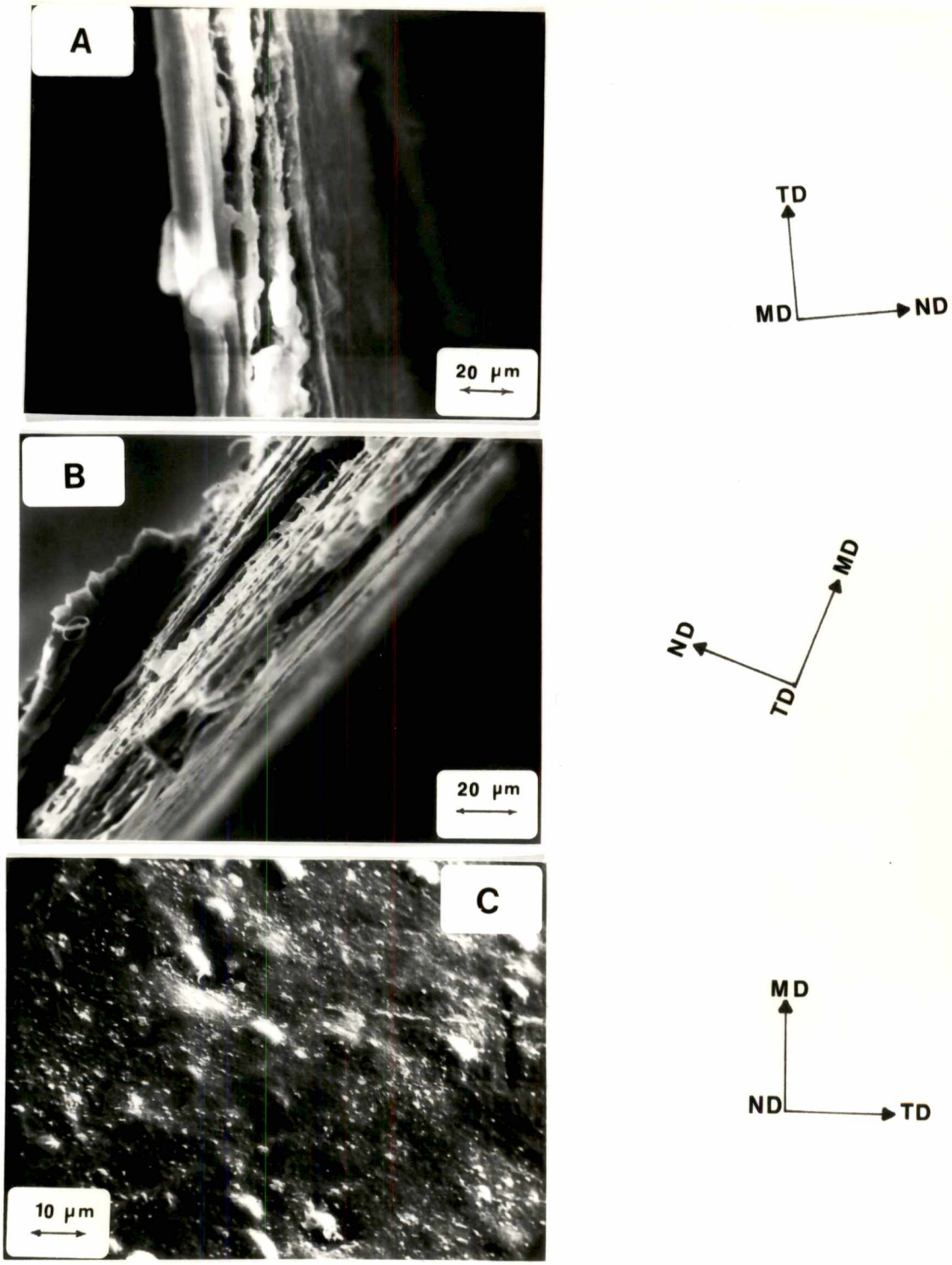


Figure V. 8. SEM photomicrographs for Sample 7;
a)End view b)Edge view c)Surface

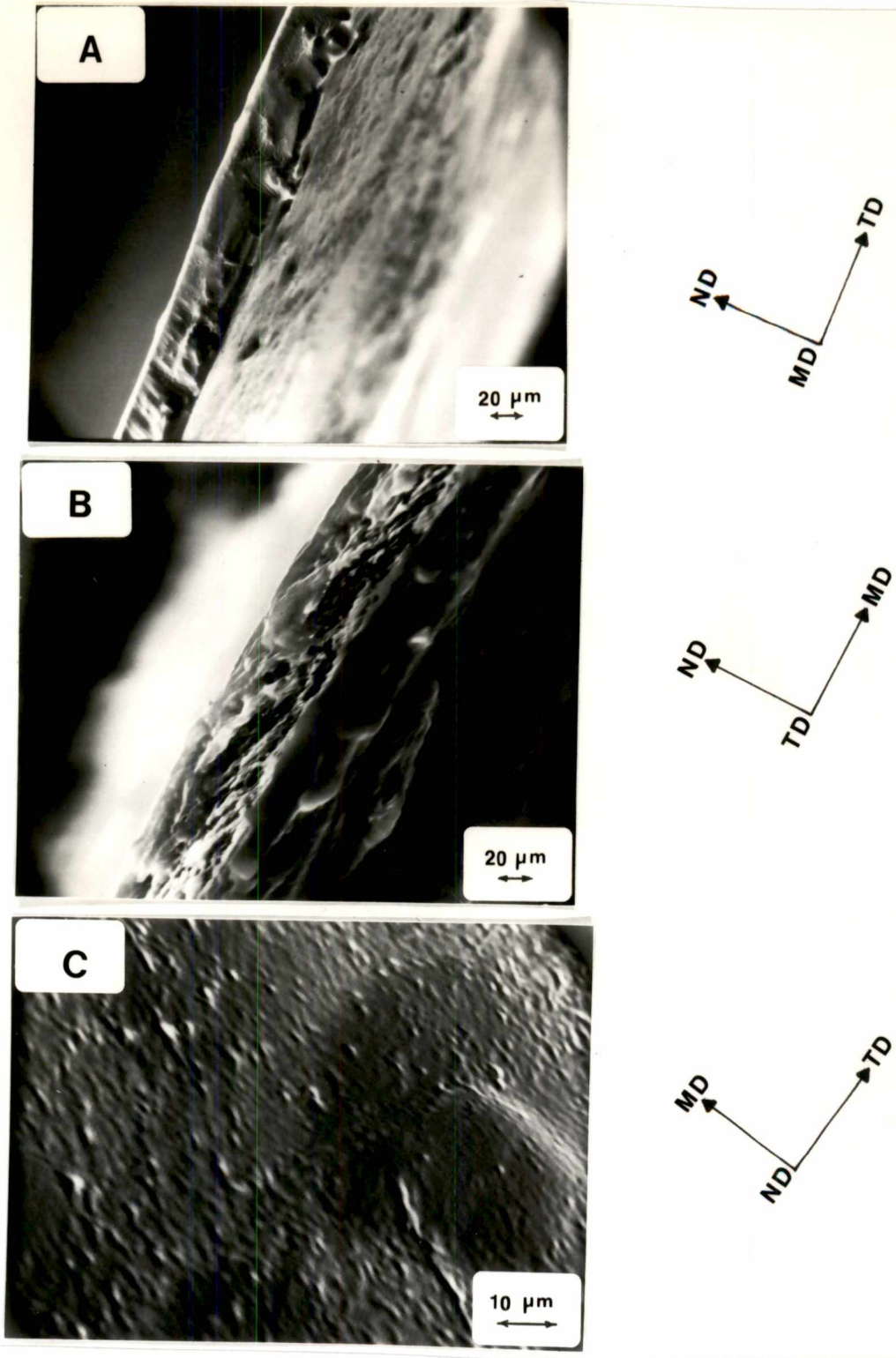


Figure V. 9. SEM photomicrographs for Sample 8;
a)End view b)Edge view c)Surface

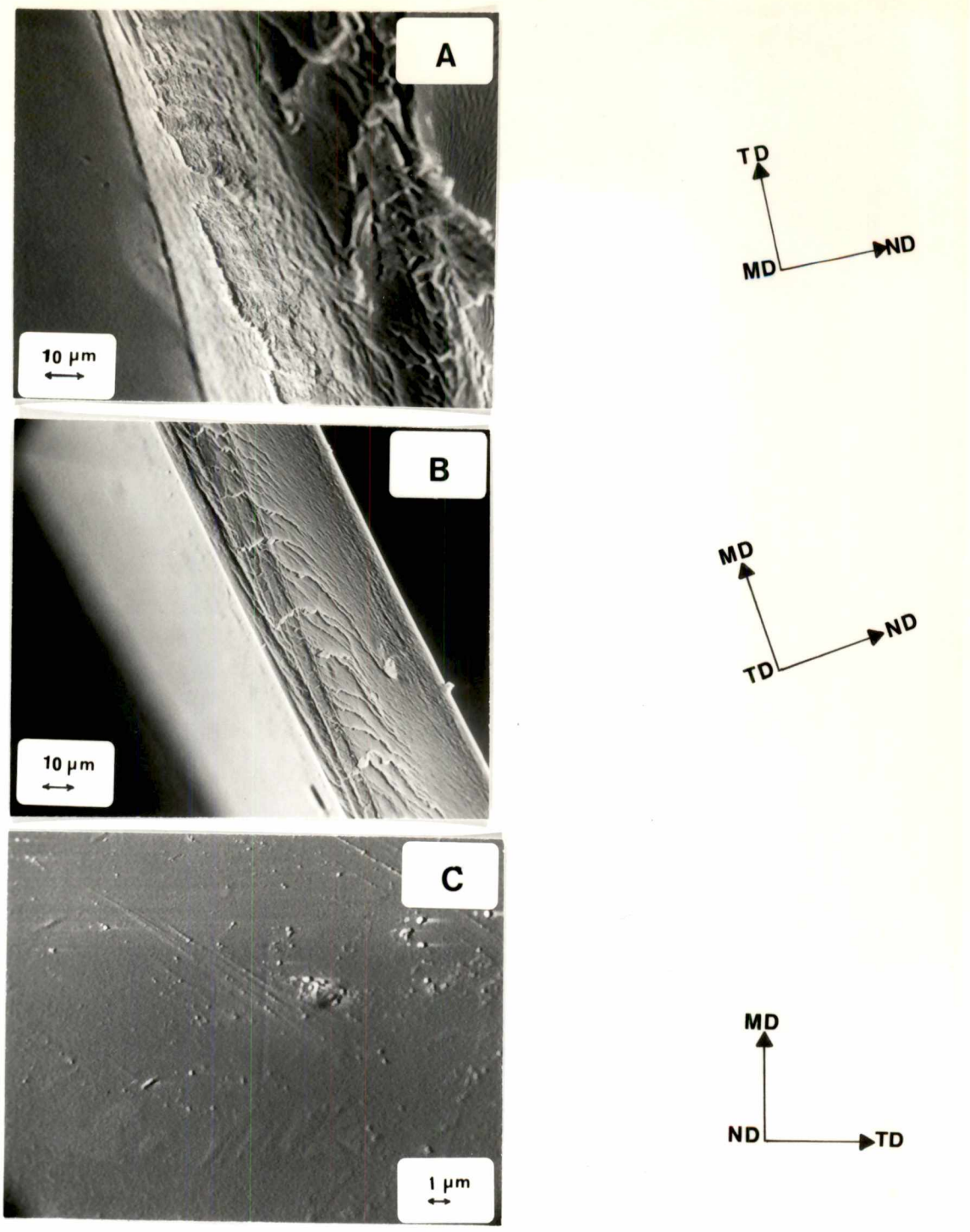


Figure V.10. SEM photomicrographs for Sample 9;
a)End view b)Edge view c)Surface

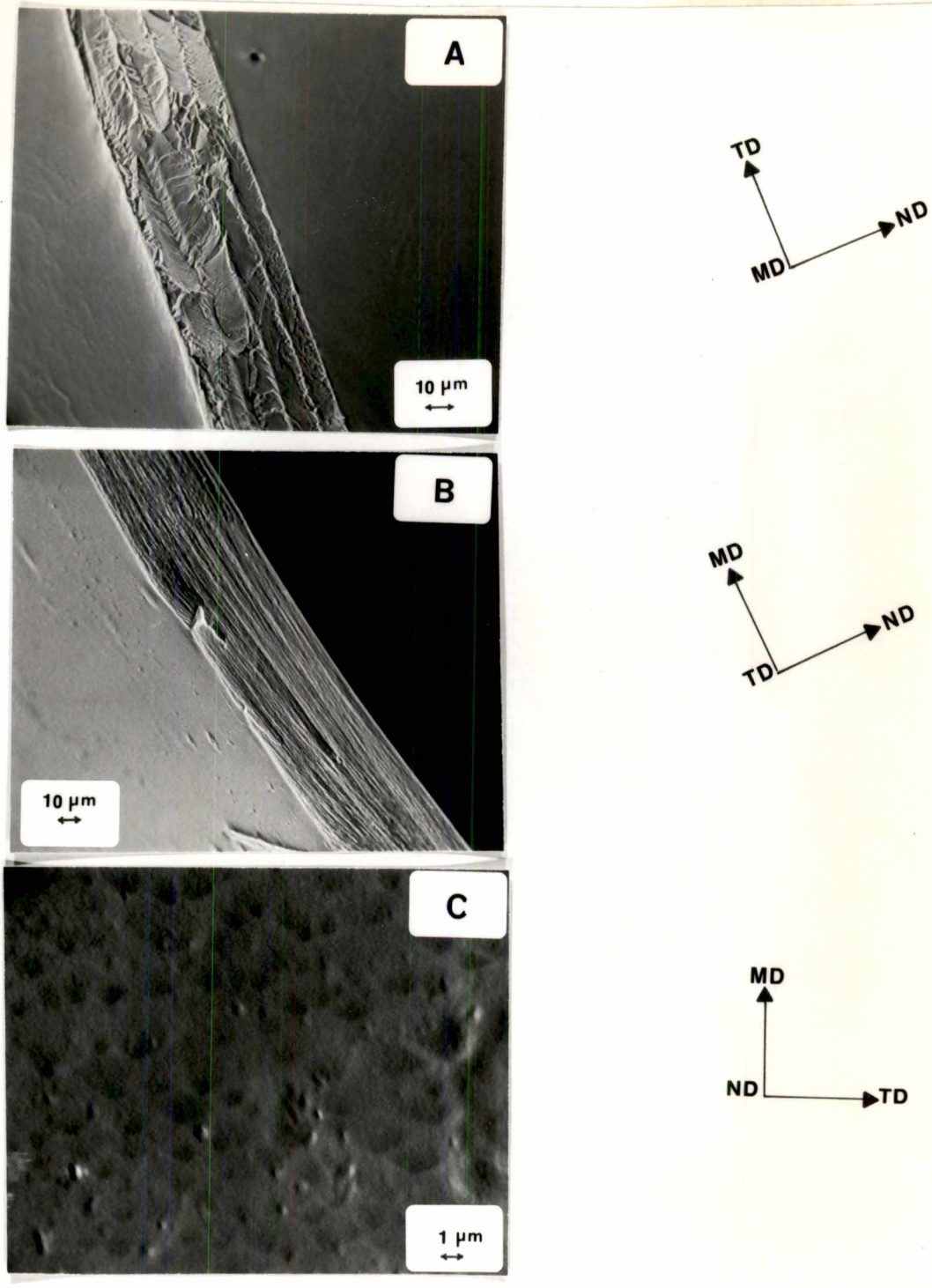


Figure V.11. SEM photomicrographs for Sample 10; a)End view b)Edge view c)Surface

μ which are distributed within this films. Smaller sized craters on the order of 5 to 10 μ can also be seen from the SEM pattern of surface of this film (see Figure V-2). Anisotropic biaxial film 3 exhibits a rough surface containing small particles on the order of 1 to 5 μ. These are not present in biaxial film 5 produced from 28 percent concentration (compare figures V-4C to V-6C). The cross-sections of this film are not as smooth as film 1, and some cracks are present parallel to the machine direction (see Figure V-4B). It seems as the solution concentration increases the voids become bigger and more complex. This can easily be seen from SEM photomicrographs of Figure V-6 and V-8 for sample 5 and 7 respectively. The surface of biaxial film 5 is very smooth compared to that of film 7. The microstructure seen in the cross sectional view of biaxial film 7 is rough and more defective compared to biaxial sample 5. This may be related to their densities and how the coagulation is influenced by the dope concentration.

The annealing effects can be seen in SEM photomicrographs of sample 8. Both cross-sections of these films are smoother and less defective compared to the original unannealed sample 7. The SEM pattern of Figure V-9C, for heat treated sample 8 also indicates the surface of this film become smoother after the annealing process (compare Figure V-8c to V-9c).

In addition to the surface and cross-sections of uniaxial films, the internal structure of these films were also investigated. These results are shown in Figure V-3, V-5, and V-7. Surface marking indicating flow lines are seen in the extrusion direction of all three films. The cross-sectional views of film 2 are smooth and the internal structure of the peeled sample of this film (Figure V-3d) is also smooth with no or very little existance of the fibrillar structure. Fibrillar structures are more pronounced and are elongated in the machine direction for film 4 (see Figure V-5d). Elongational voids can easily be seen in the cross-sectional views of this film which are parallel to the machine direction (Figure V-5b). However, the surface of this film seems to be smoother than the other uniaxially drawn films.

Extensive voiding and fibrillation can be seen from SEM photomicrographs of uniaxial film 6 produced from 30 percent concentration (Figure V-7). The peeled view of this film exhibits a ribbon-like fibrillar structure with voids elongating along the machine direction (Figure V-7D). However, it is also apparent from the "peeled" and cross-sectional views of these uniaxially drawn films that as the solution concentration increases the voids become bigger and more complex as was also observed from the cross-sections biaxially oriented films.

The commercial cast film 9 shows a very smooth surface and solid-like cross-sections (Figure V-10). A rough surface can be seen after the extraction of the additive from this film; see Figure V-11. This surface view exhibits voids on order of about 1μ created as a consequence of the methanol treatment. The cross-sectional views for this MeOH treated film 10, seems to be slightly different compared to untreated sample 9.

Density

Table V-2 shows the average thickness and densities for samples 1 through 10. The densities range from 1.257 to 1.302 g/cm^3. It is apparent from this table that as the solution concentration of the sample increases the density decreases. A significant change of the density can be observed by comparison of isotropic sample 1 and anisotropic sample 7. Samples 2,3,4 and 5 showed very little change of density as a result of the various conditions. However, a substantial increase in density is observed as a function of the annealing process. The heat treated film 8 exhibits a density of 1.301 g/cm^3. The density of this film before annealing was 1.257 g/cm^3 (see sample 7). A slight decrease in density is also seen for methanol treated sample 10 (compare the

TABLE V.2. AVERAGE THICKNESS AND DENSITIES FOR CTA FILMS

Sample No.	Solution Conc.(wt%)	Method of Preparation	Average Thickness (mm)	Density (g/cm^3)
1	23	Extrusion/Recy.Proc. B.R.=2/coagulation	0.11	1.297
2	25	Extrusion/moderate drawdown/coagulation	0.19	1.291
3	25	Extrusion/Recy.Proc. B.R.=2.5/coagulation	0.07	1.292
4	28	Extrusion/moderate drawdown/coagulation	0.13	1.291
5	28	Extrusion/Recy.Proc. B.R.=3.0/coagulation	0.04	1.293
6	30	Extrusion/moderate drawdown/coagulation	0.12	1.277
7	30	Extrusion/Recy.Proc. B.R.=3.3/coagulation	0.04	1.257
8	30	Extrusion/Recy.Proc. B.R.=3.3/coag./ann.	0.04	1.301
9	-	CFC (Casting)	0.05	1.302
10	-	CFC (MeOH treated)	0.05	1.301

result for sample 10 to that of untreated CFC casted film 9).

In the present study, an attempt was made to estimate the volume fraction of the voids using the mass density data. If one assumes that the difference between the crystalline density of the films and the density values is due to the presence of voids within the samples, the volume fraction of voids " ϕ " can easily be derived as follows;

$$\phi = 1 - \frac{\rho}{\rho_c} X_c - \frac{\rho}{\rho_a} (1-X_c) \qquad (88)$$

Where ρ is the experimentally observed sample density, ρ_c is the crystalline density, ρ_a the amorphous density, and X_c is the crystallinity determined by the Differential Scanning Calorimetry (DSC) technique.

However, since CTA films produced in this study showed higher experimental values of heat of fusion (Δ H) than theoretically calculated values reported for cellulose triacetate in the open literature (222, 223,224), we were unable to measure the crystallinity of the films using DSC technique. The heat of fusion obtained for the films will be explained and discusses in the next section of this chapter.

Small Angle X-Ray Scattering - Quantitative

SAXS intensity contour plots for the cases where the beam is parallel to the ND, TD, and MD of the films are shown in Figures V-12 through V-20.

Figures V-12, V-14, V-16, and V-19 show the contour plots for the biaxially stretched film samples 1, 3, 5, 7 and 8, respectively. The contour plots, where the beam is parallel to the ND are isotropic, while they are anisotropic when the beam is parallel to both the MD and TD of the films. These indicate the voids in these films are expanded in the plane of MD-TD or compressed in ND as it is drawn in Figure V-18. It seems from these contour plots that the greatest scattering intensity is from the biaxially expanded film 7 produced from 30 percent solution concentration (Figure V-18). The isotropic sample 1 exhibits the least scattering (Figure V-12). These contours also indicate that the scattered intensity increases as the solution concentration increases. This can be attributed to the higher concentration of the solution used to form sample 7 (Figure V-18) coagulates leaving more voids than sample 5 (Figure V-16) likewise, sample 5 has more voids than sample 3 (Figure V-14), and sample 3 has more voids than isotropic film 1 (Figure V-12).

Sample 8 (Figure V-19), the annealed film, also shows a reduction in the scattering intensity compared to sample

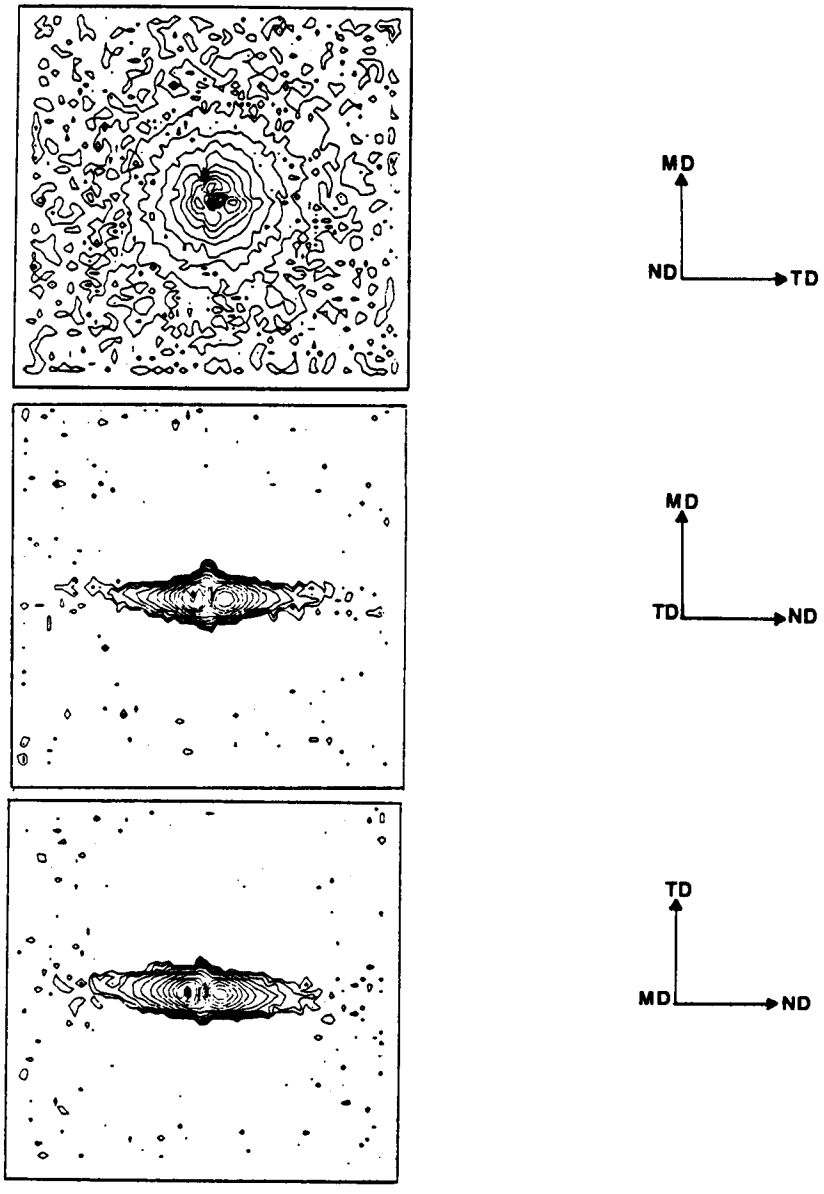


Figure V.12. SAXS intensity contour plots for three directions relative to Sample 1.

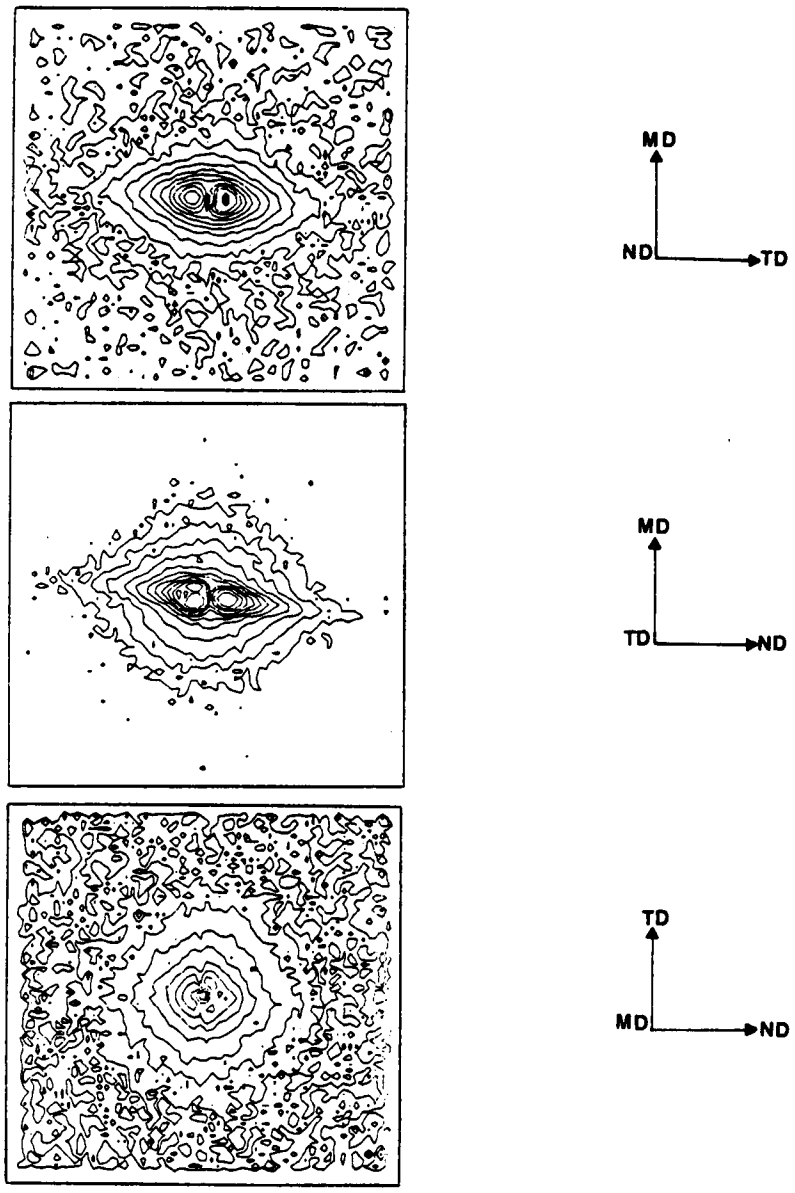


Figure V.13. SAXS intensity contour plots for three directions relative to Sample 2.

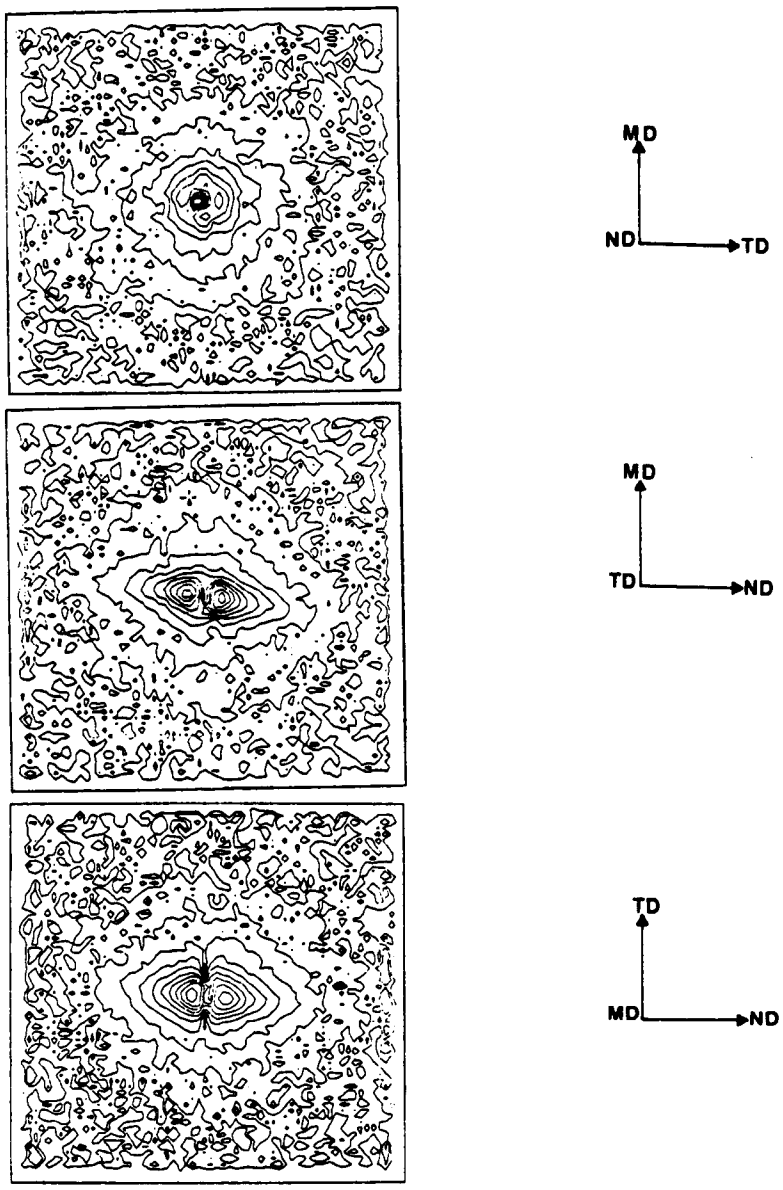


Figure V.14. SAXS intensity contour plots for three directions relative to Sample 3.

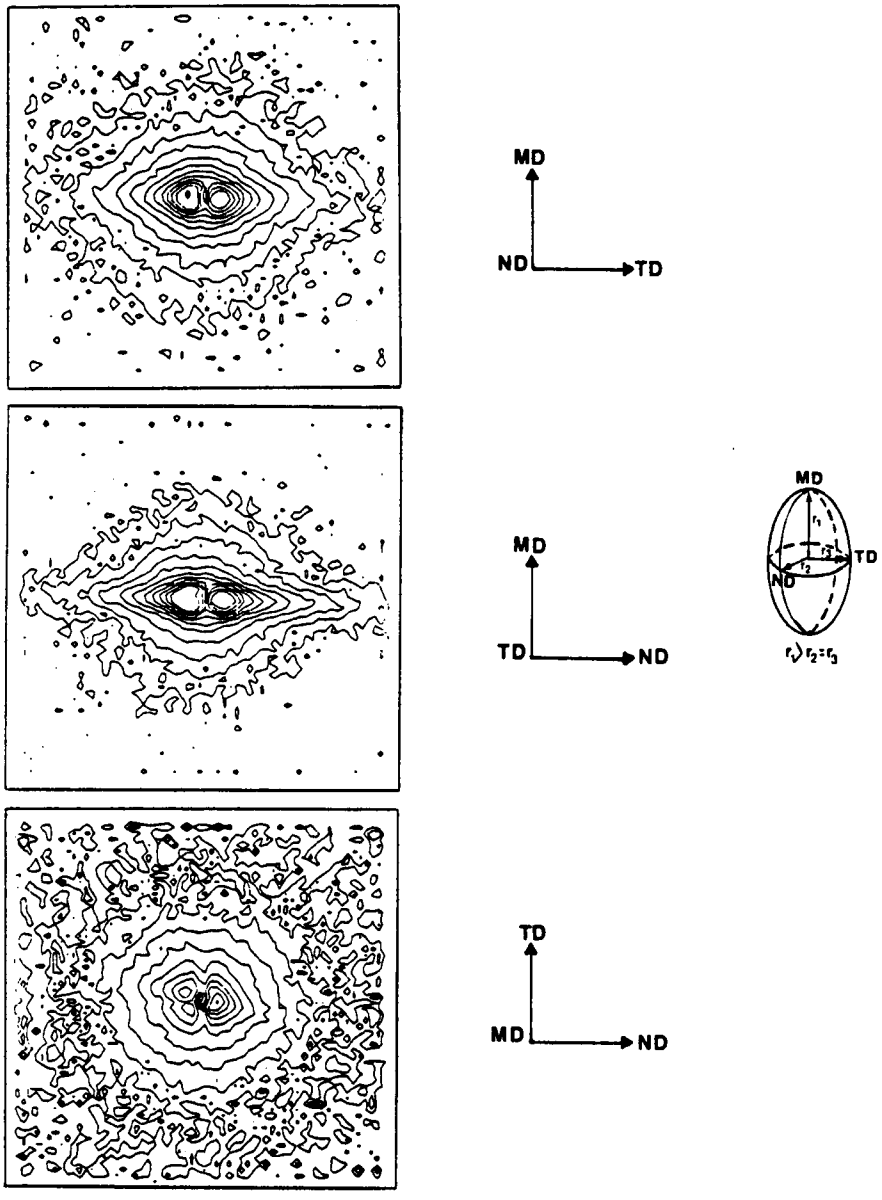


Figure V.15. SAXS intensity contour plots for three directions relative to Sample 4.

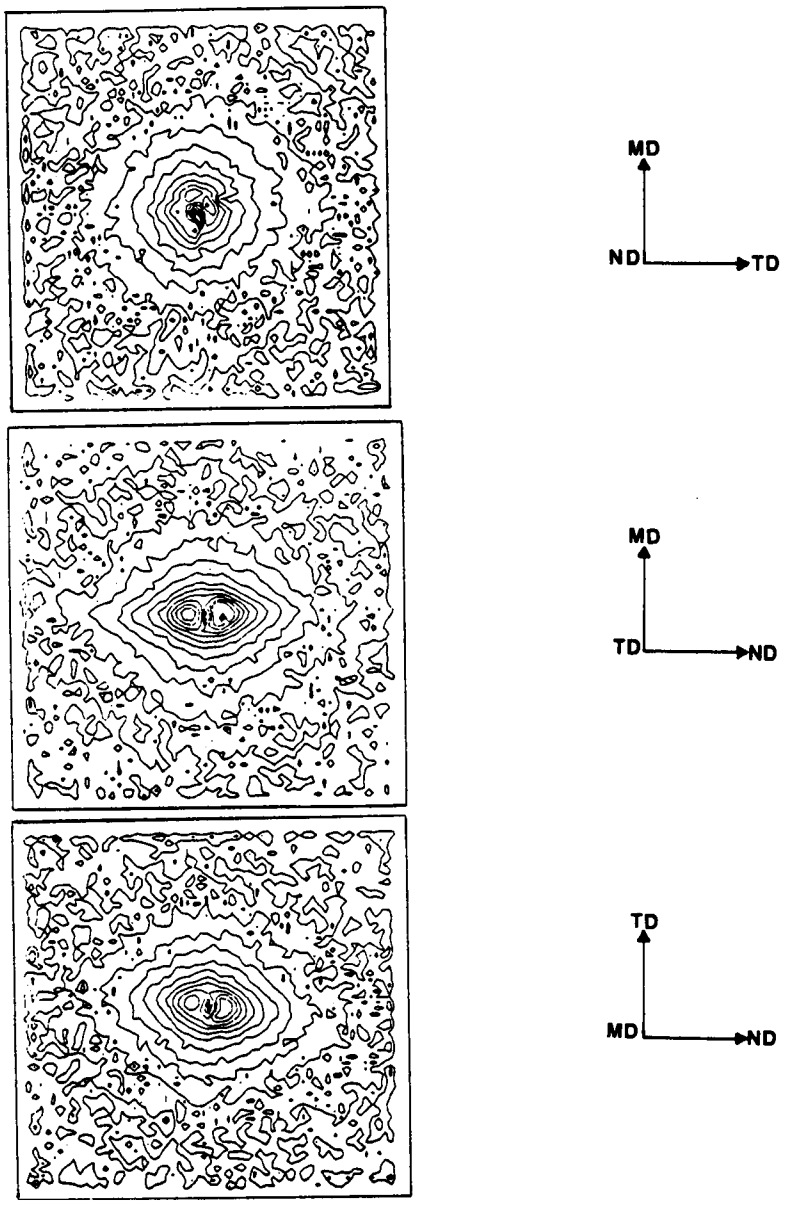


Figure V.16. SAXS intensity contour plots for three directions relative to Sample 5.

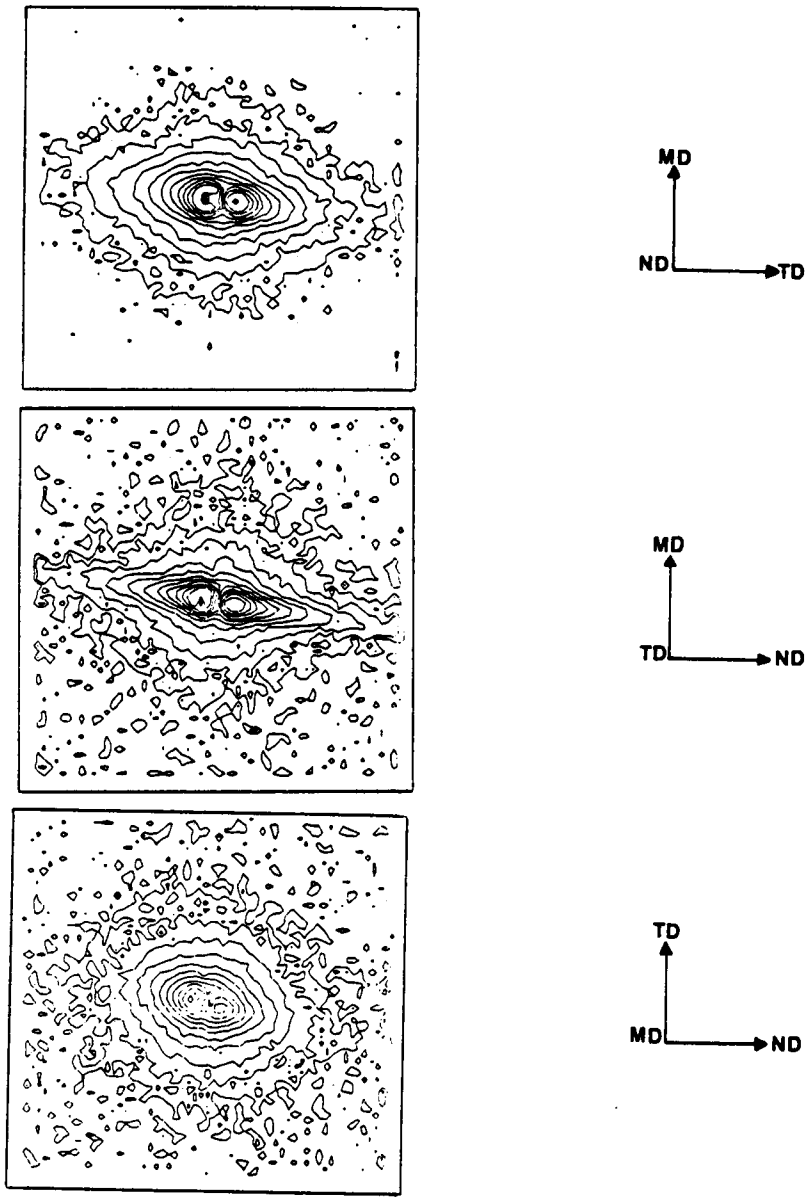


Figure V.17. SAXS intensity contour plots for three directions relative to Sample 6.

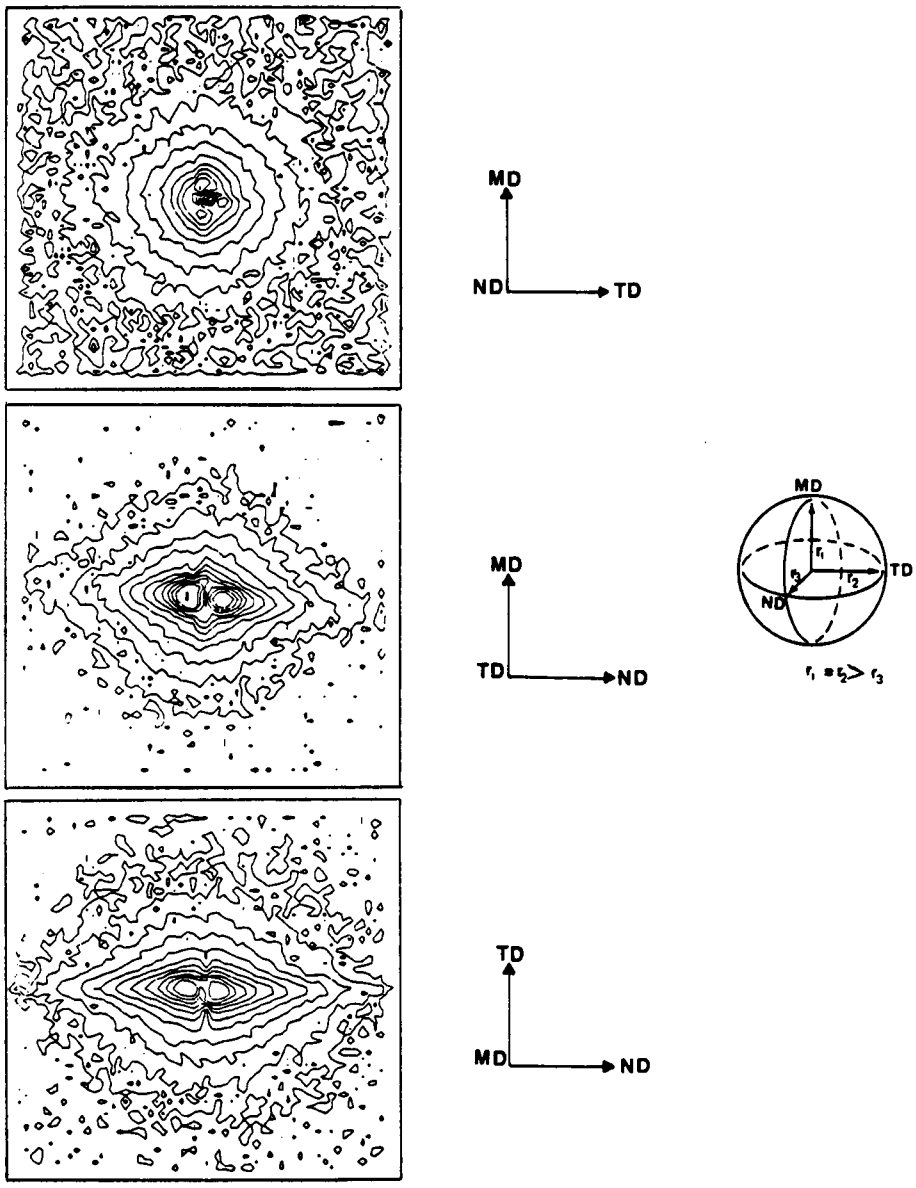


Figure V.18. SAXS intensity contour plots for three directions relative to Sample 7.

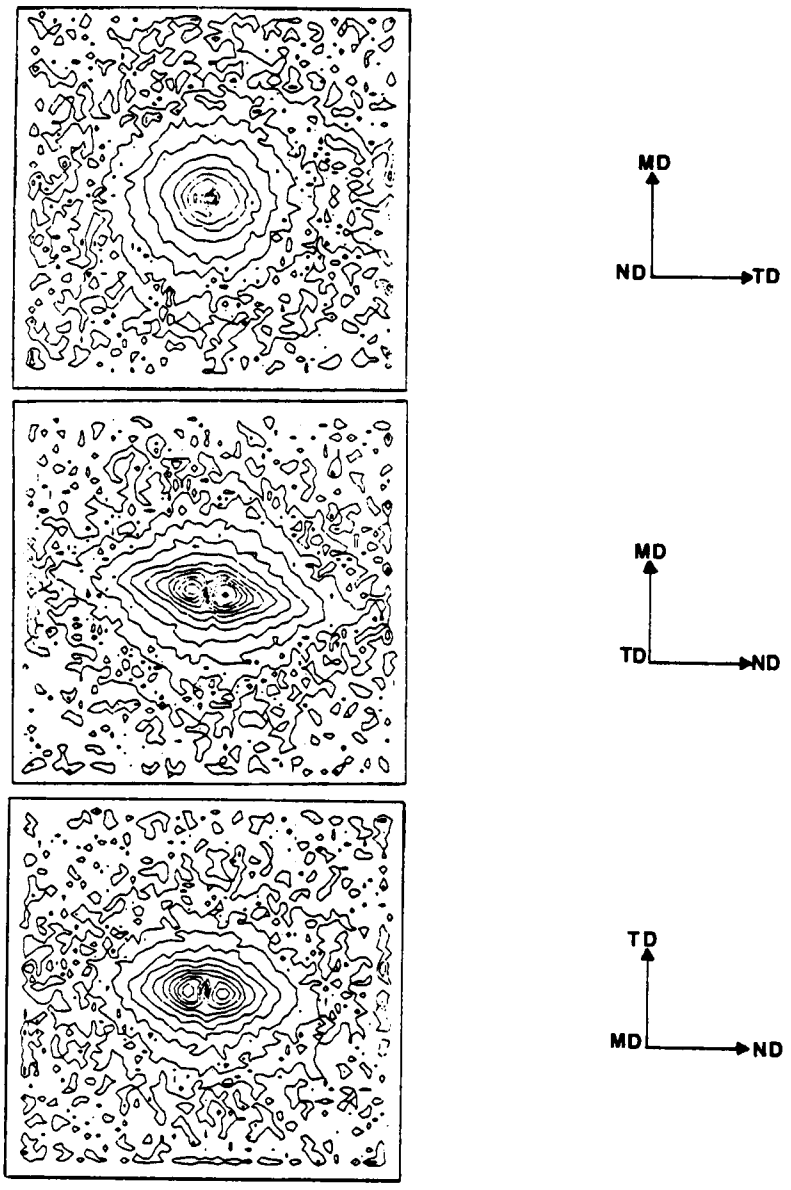


Figure V.19. SAXS intensity contour plots for three directions relative to Sample 8.

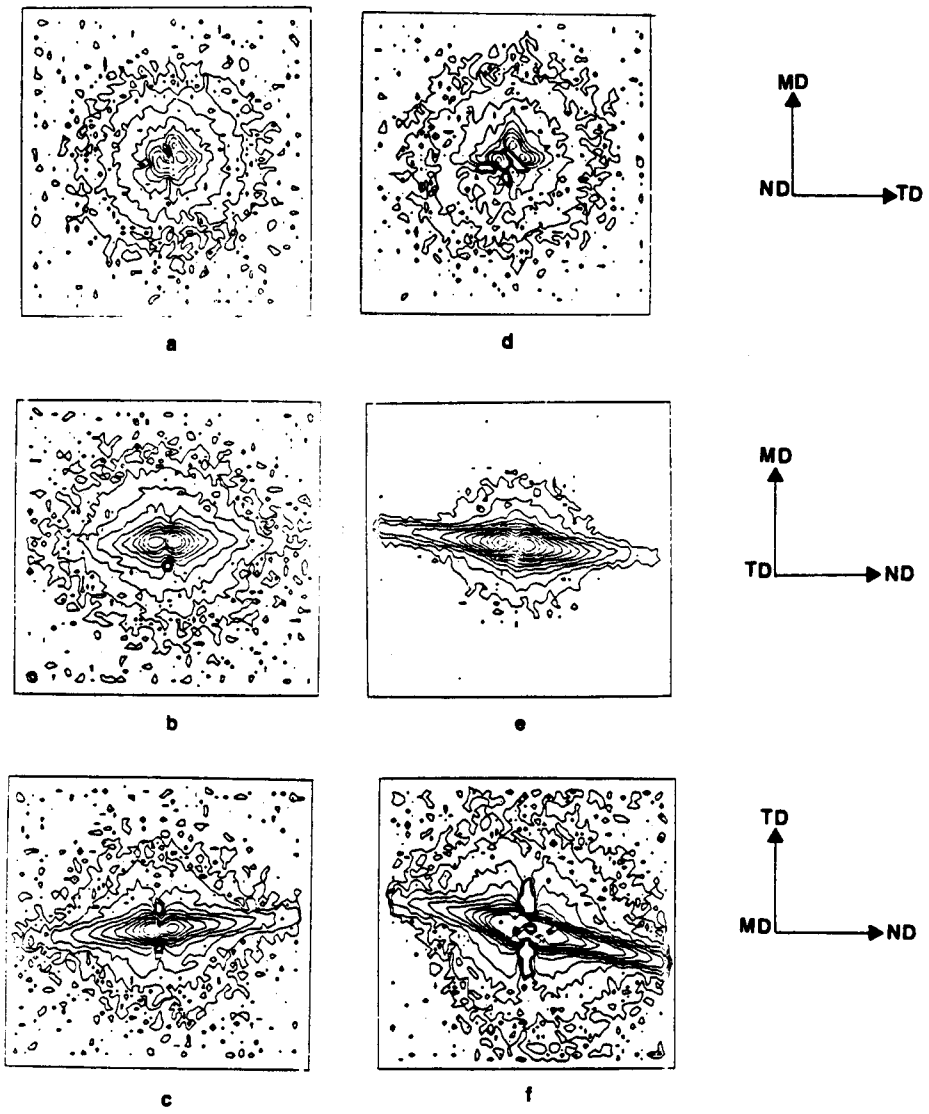


Figure V.20. SAXS intensity contour plots for three directions relative to Sample 9 (a,b,c) and Sample 10 (d,e,f).

7 (Figure V-18) which is the original sample (unannealed).

The contour plots of uniaxial films are presented in Figures V-13, V-15, and V-17. The patterns obtained based on a beam parallel to the TD and to the ND of the film show that the scattered intensity is more concentrated in the equatorial direction. But the contour plots where the beam is parallel to the MD of the films indicate the scattering is most likely uniform in this plane. Consequently, these contour plots correspond to prolate ellipsoid shaped voids elongated in the machine direction as it is also drawn in Figure V-15. Furthermore, the scattered intensity for uniaxially drawn films also increases intensity for uniaxially drawn films also increases as solution concentration increases (compare Figure V-13 to V-15 and V-17).

Both cast film 9 and methanol treated film 10 exhibit contour plots which are qualitatively similar. These are shown in Figure V-20. The patterns on the left side of this figure (a, b, and c) are for sample 9 and the contour plots on the right side (d, e, and f) belong to methanol treated film 10. Surface reflection seems to occur where the x-ray beam is parallel to the MD and TD of stacked films of sample 10. However, an attempt was made to eliminate such surface reflection by tilting the samples greater than 15° from the x-ray beam, but the streak is still apparent for some of the samples studied. This

will also be discussed in the next section of this chapter.

Determination of void fraction from SAXS. If we presume the scattered intensity for the films is due to microvoids we may calculate the volume fraction of microvoids from quantitative SAXS data. This is computed from the invariant, Q, of the scattered intensity given by

$$Q=\int I\ (\underline{S})\ dV_s \tag{89}$$

where $\underline{S}$ is the diffraction vector dV_s is a volume element in reciprocal space. The integral is taken over the entire intensity distribution near the origin of reciprocal space, and hence Q is the total integrated intensity near the origin in reciprocal space.

Kratky and Miholic (104) have shown that the mean square electron density fluctuation in the sample is proportional to the invariant, that is

$$(\overline{\rho-\bar{\rho}})^2 = K\ Q \tag{90}$$

where;

$$K = \frac{1}{i_e N^2\ d\ a\ \lambda^3} \tag{91}$$

Here , i_e, is the Thomson scattering constant for a free electron, N is Avogadro's number, d is the specimen thickness in centimeters, a is the sample to detector distance in centimeters, and λ is the wavelength of the radiation.

However more details of this measurement are explained

in Chapter II and the computer program used for calculating the mean square fluctuation of the electron density, $\overline{(\rho-\bar{\rho})^2}$ is presented in Appendix D.

For the films containing microvoids we may also write,

$$\overline{(\rho-\bar{\rho})^2} = \rho_o^2 \phi(1-\phi) \qquad (92)$$

Where ϕ is the volume fraction of voids and ρ_o is the polymer electron density. The above expression was used to determine the volume fraction of microvoids for all the samples. The results are presented in Table V-3. These void fractions varied from 0.006 percent to 0.18 percent. Since there could be some surface reflection for some of the samples, the judgement will be based on the results obtained where the x-ray beam is normal to the plane of the films.

However, it is clear from this table that the void fraction increases as solution concentration increase. Uniaxially drawn films exhibit higher values than those of biaxially expanded samples. The CFC films 9 and 10 show the least values where anisotropic sample 6 and 7 exhibit the highest value. Both of these latter films were prepared from 30 percent solution concentrations. Sample six was extruded uniaxially through the coagulation bath while sample seven is a biaxial film. This table also shows a decrease of void fraction as a function of

TABLE V.3. VOID FRACTIONS MEASURED FROM SAXS (ϕ) INVARIANT

Sample No.	$\phi \times 10^3$ Beam Direction		
	ND	MD	TD
1	0.32	0.31	0.33
2	1.20	0.91	1.11
3	0.40	1.00	1.10
4	1.25	1.10	1.23
5	0.40	1.00	1.23
6	1.51	1.60	1.30
7	0.62	1.40	1.81
8	0.52	0.79	1.20
9	0.06	0.17	0.36
10	0.09	0.23	0.15

annealing process (compare the results of annealed film eight to that of unannealed sample seven). A slight increase in void fraction can also be observed from this table for methanol treated film ten compared to CFC untreated film nine.

Estimate of void size. In order to determine the approximate average dimensions of the voids, we used Guinier analysis and the method of Debye-Bueche. As was mentioned in a previous chapter, these analyses were applied to intensity profiles taken along the equatorial and meridional directions through the center streak scattering. For isotropic patterns these were applied to the average intensity around the center streak scattering. An example of these profiles and radial average for sample five is shown in Figures V-21 through V-23.

Guinier analysis is valid at very small angles and is based on presuming a dilute system of randomly oriented particles (see the procedures given in Chapter II, page 86). Thus, typical Guinier plots of log I ( ) versus K^2 (scattering vector) for different spatial directions of sample five are shown in Figures V-24 to V-26. The void sizes so determined are listed in Table V-4.

The mean void sizes for biaxially expanded films one, three, five, seven and eight indicate these voids

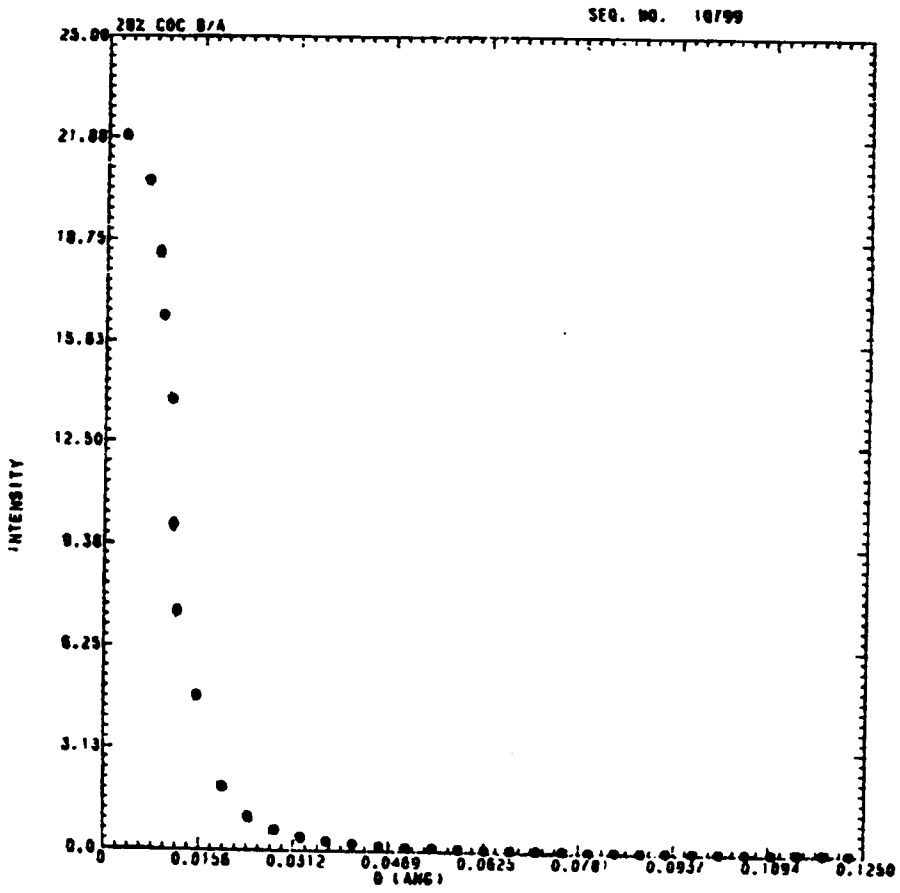


Figure V.21. Radial average of intensity versus scattering angle for Sample 5.

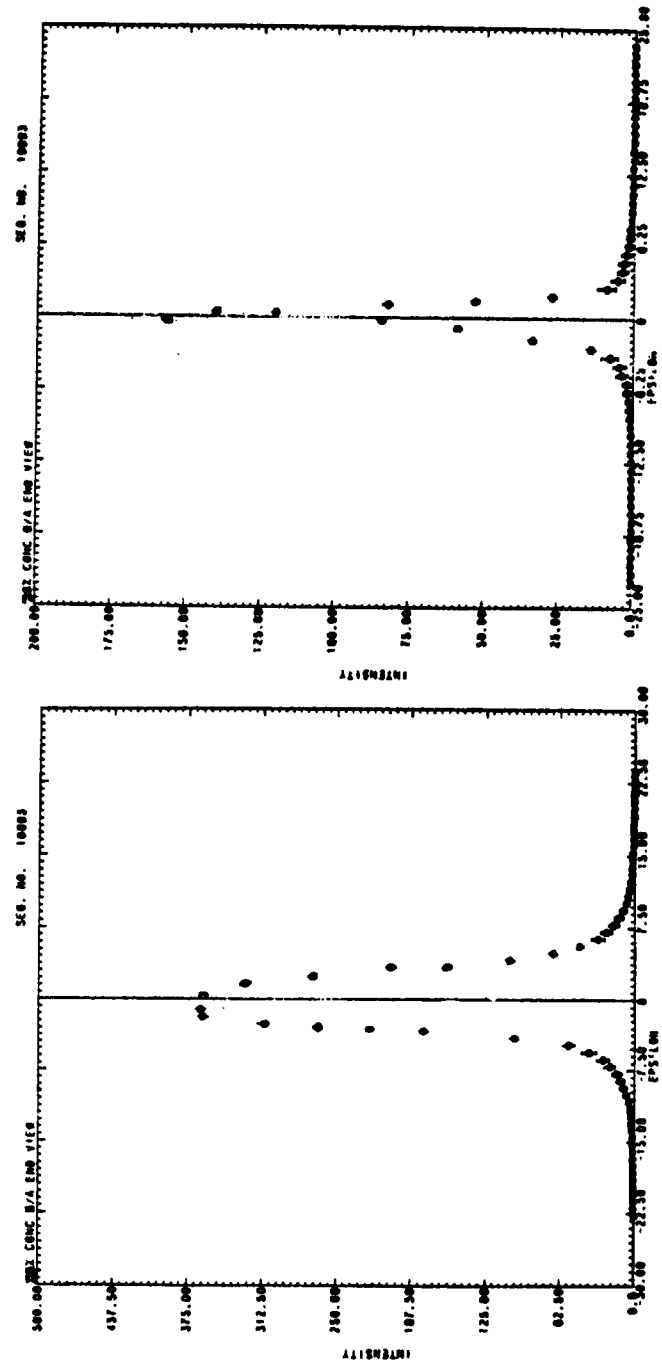


Figure V.22. Intensity versus scattering angle for end view of Sample 5.

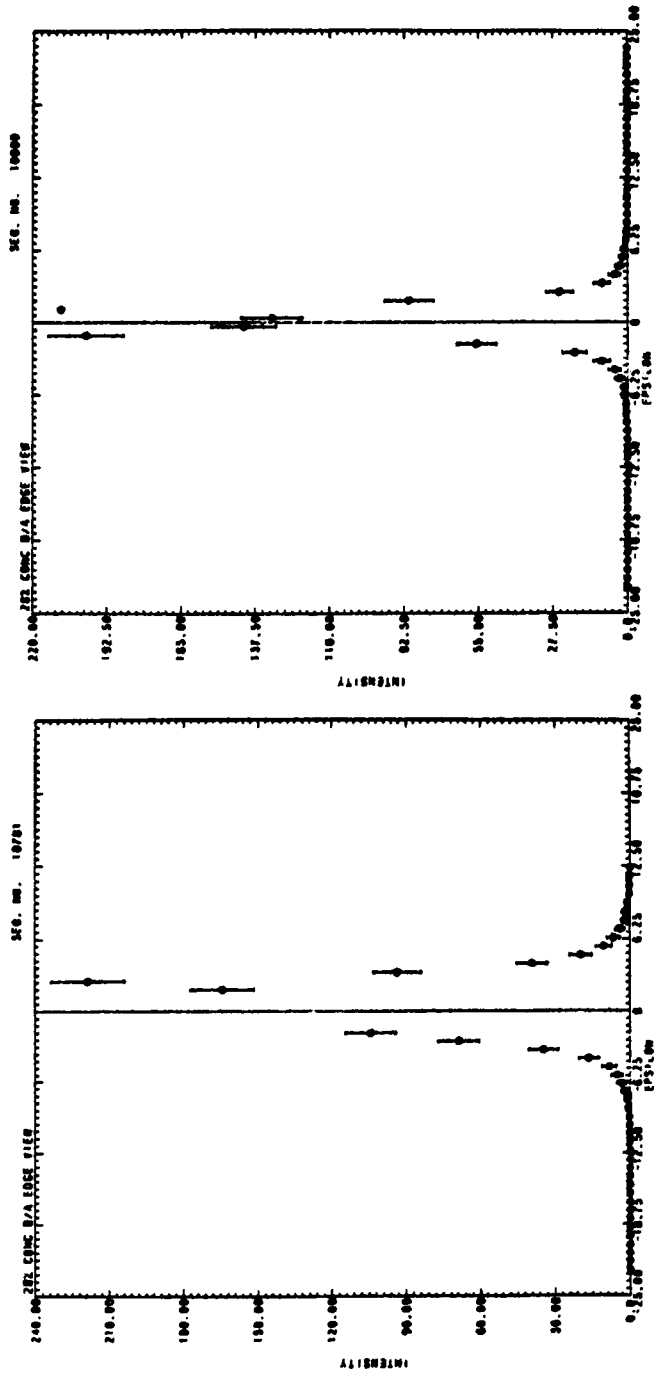


Figure V.23. Intensity versus scattering angle for edge view of Sample 5.

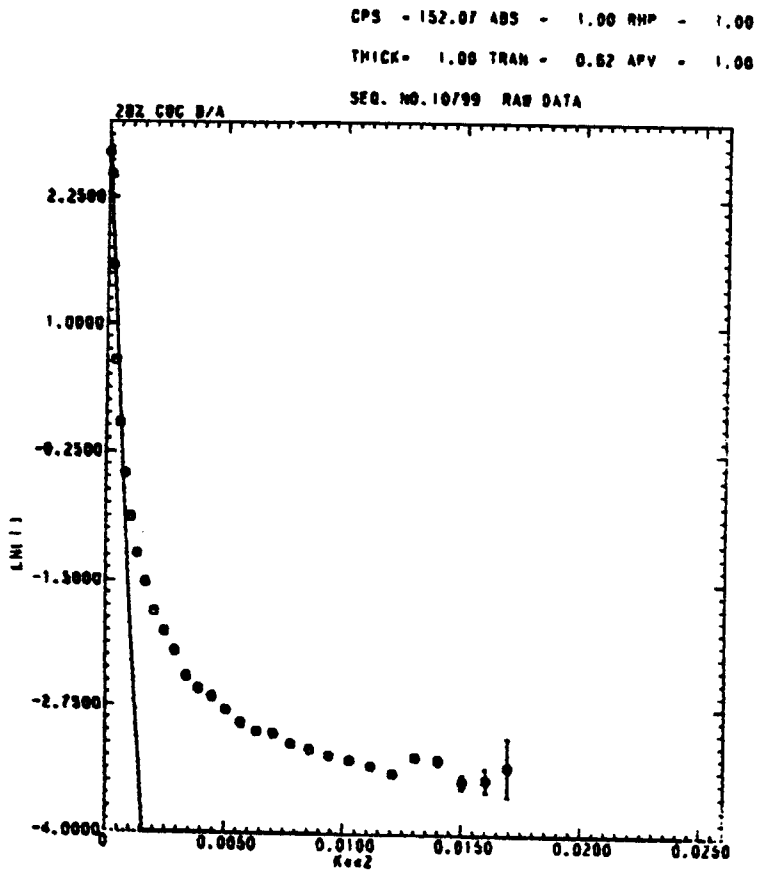


Figure V.24. Guinier plot for through view of Sample 5.

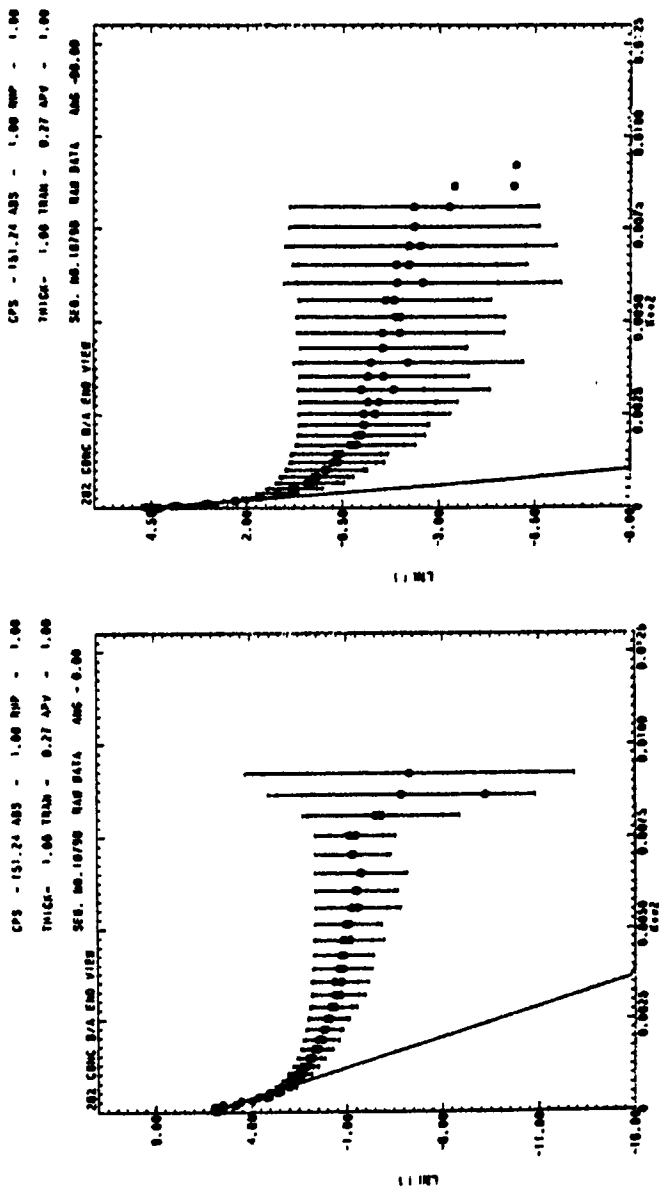


Figure V.25. Guinier plot for end view of Sample 5.

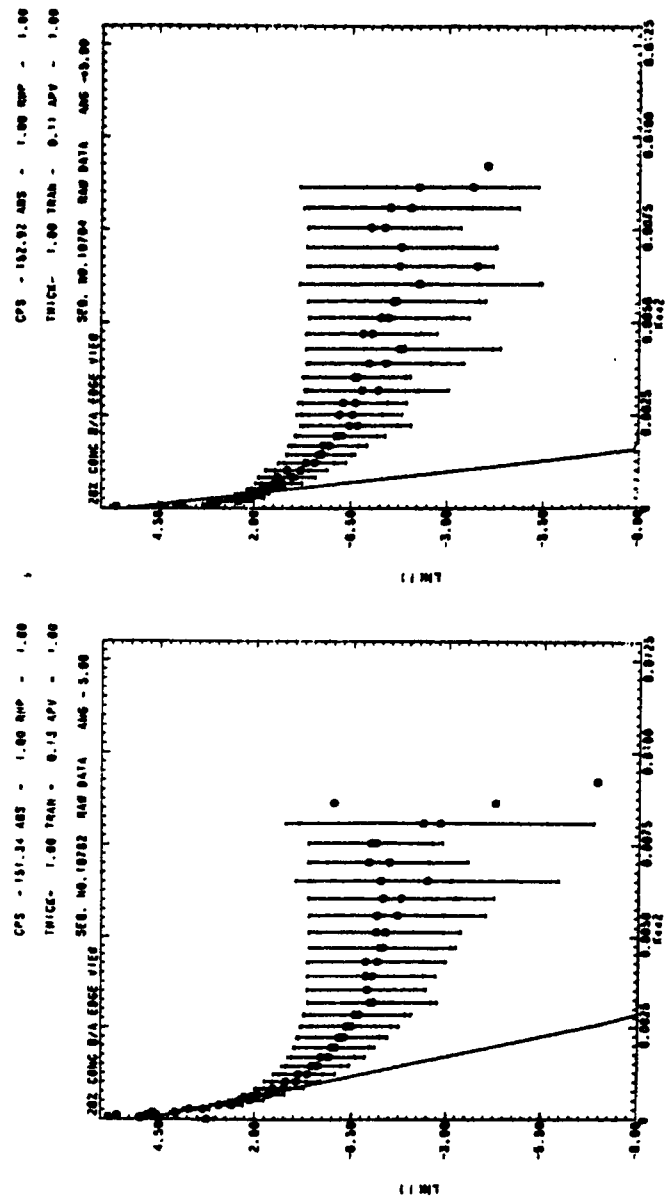


Figure V.26. Guinier plot for edge view of sample 5.

TABLE V.4. VOID DIMENSIONS DETERMINED BY GUINIER METHOD

Sample No.	Beam Direction	Ave. Void Sizes (nm) MD	TD	ND
1	Normal to film	12.67	12.67	
	Normal to edge	12.73		8.80
	Normal to end		12.61	9.21
2	Normal to film	27.67	13.60	
	Normal to edge	20.56		15.14
	Normal to end		11.81	11.81
3	Normal to film	13.30	13.30	
	Normal to edge	18.13		13.3
	Normal to end		22.76	13.74
4	Normal to film	28.27	17.35	
	Normal to edge	31.15		18.0
	Normal to end		9.74	9.74
5	Normal to film	13.96	13.96	
	Normal to edge	21.3		17.62
	Normal to end		19.16	16.66
6	Normal to film	27.3	20.4	
	Normal to edge	35.72		15.34
	Normal to end		24.2	19.7
7	Normal to film	14.21	14.21	
	Normal to edge	25.6		15.4
	Normal to end		30.12	19.05
8	Normal to film	12.65	12.65	
	Normal to edge	22.8		15.30
	Normal to end		22.75	18.90
9	Normal to film	12.69	12.69	
	Normal to edge	41.85		19.59
	Normal to end		15.29	14.04
10	Normal to film	20.58	20.58	
	Normal to edge	43.15		26.89
	Normal to end		55.9	20.54

have equal dimensions in the MD and TD where the beam is parallel to the ND of the film. They have a higher dimension in MD, lower size in ND where beam is parallel to the TD, and higher dimensions in TD, lower dimension in ND where beam is parallel to the MD of the stacked film. These dimensions indicate the voids are expanded in the plane of MD-TD or compressed in thickness of the films whereas, in the case of uniaxial films two, four, and six the void sizes show most likely equal dimensions in TD and ND where the beam is parallel to the MD, high value in MD, lower value in MD where the beam is parallel to the TD, and higher value in MD, lower value in TD where the beam is parallel to the ND of the film. Consequently these dimensions correspond to prolate-ellipsoid shaped voids elongated in the machine direction.

A decrease in void sizes can be observed as a function of annealing for sample eight (the annealed film). The void dimensions are increasing as solution concentration and blow-up ratio increase. Also CFC methanol treated film ten showed larger void sizes than untreated sample nine.

For estimation of the void sizes using the Debye-Bueche method the procedure given in Chapter II, page 90, was also used. In this method as it was described in Chapter II, the average void sizes can be obtained using a

correlation length "a" and volume fraction of voids (see Equation 69, page 91). The void volume fraction for CTA films was calculated from the SAXS invariant and used in this Debye-Bueche technique. Typical plots of this method for various spatial directions of sample 5 are shown in Figures V-27 to V-29. The results of void sizes computed are presented in Table V-5. This table indicates that the voids have similar shape as a result of the processing conditions to those obtained from Guinier analysis. However the dimensions calculated from this technique are much smaller compared to those determined from the Guinier method. But the effects of solution concentration, blow-up ratio and annealing process on the void sizes are most likely the same.

C. Molecular Orientation and Crystallinity

Birefringence

The birefringence of the CTA films was measured on an optical bench by the tilting technique as described in Chapter III. The results are presented in Table V-6. All three uniaxially drawn films two, four and six exhibit birefringence where;

$$\Delta n_{13} \simeq \Delta n_{12} > \Delta n_{23}$$

A change in the birefringence order occurs for the series of biaxially expanded films one, three, five, seven and

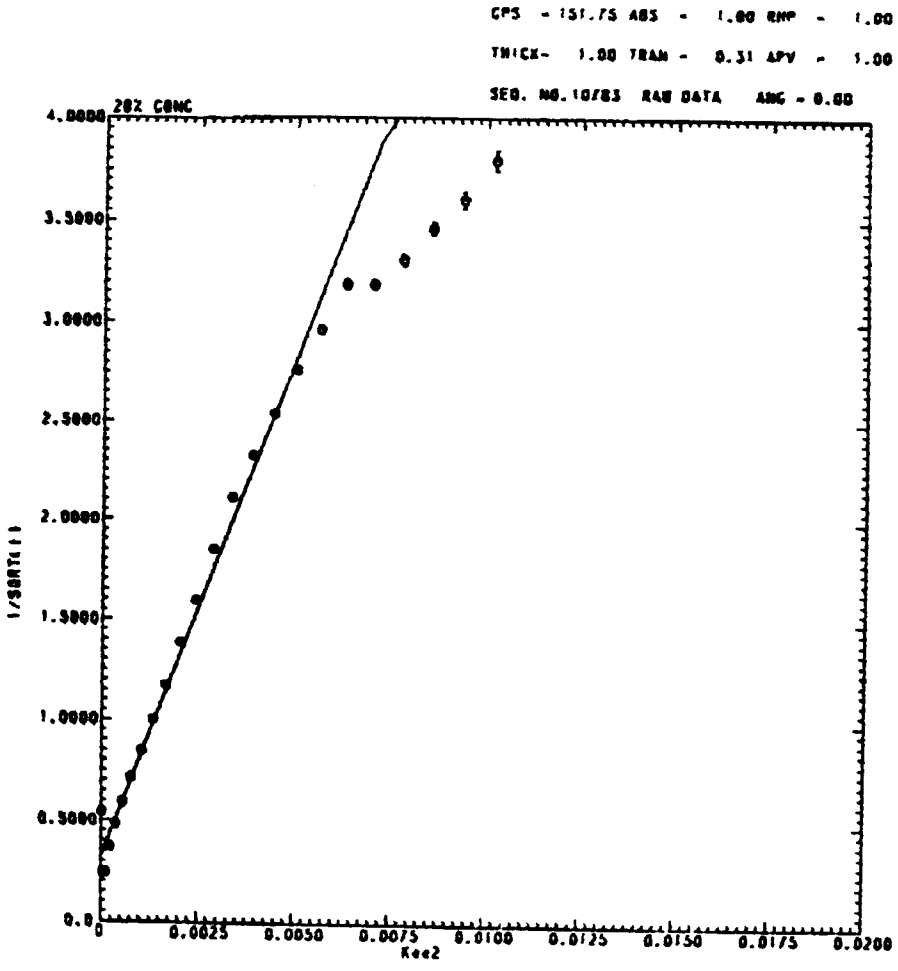


Figure V.27. Debye-Bueche plot for through view of Sample 5.

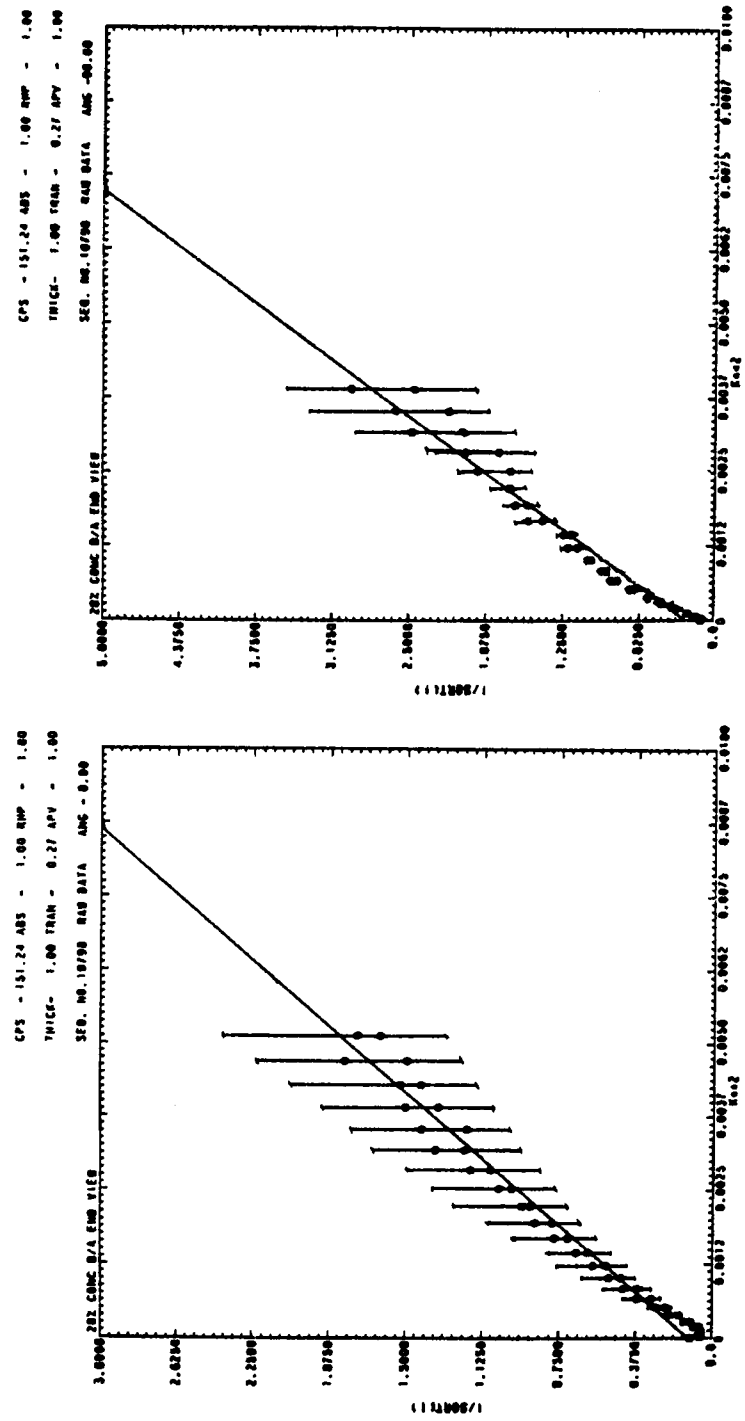


Figure V.28. Debye-Bueche plots for end view of Sample 5.

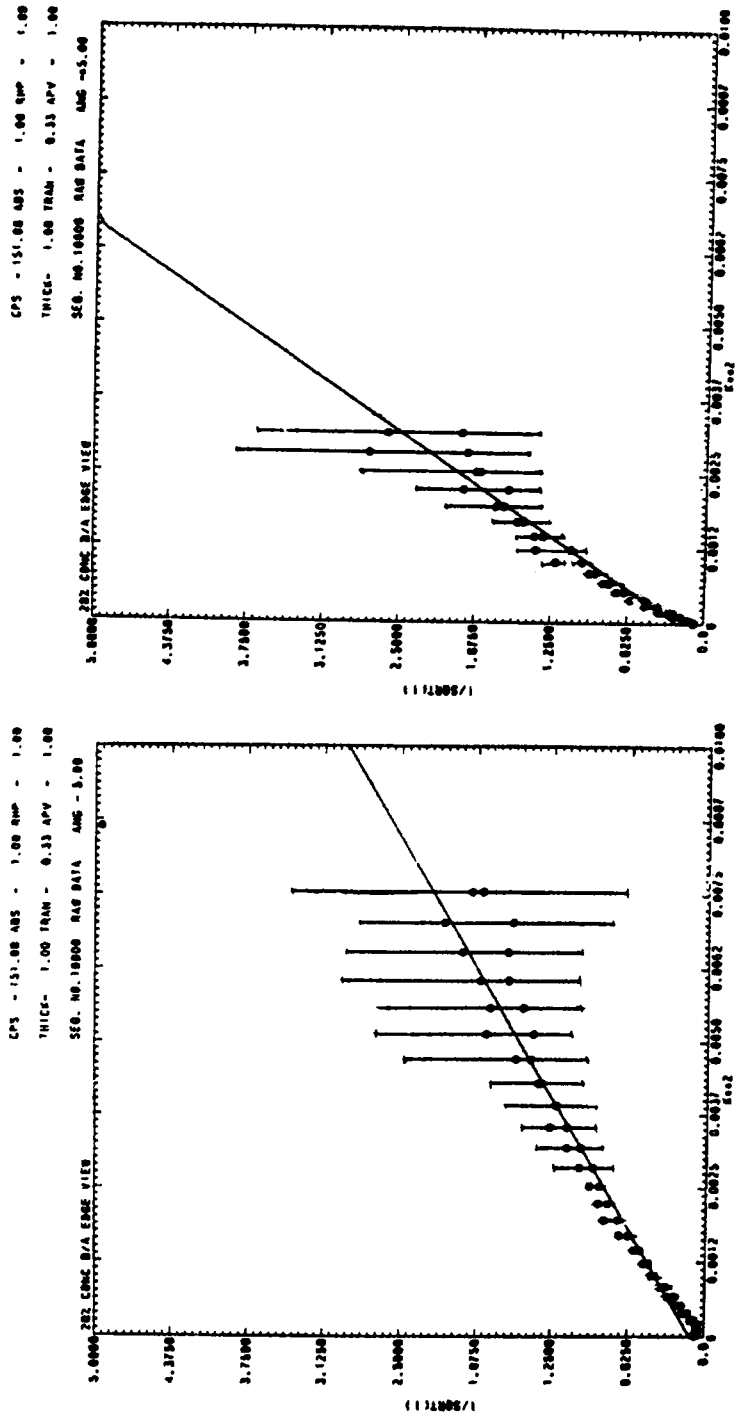


Figure V.29. Debye-Bueche plots for edge view of Sample 5.

TABLE V.5. VOID SIZES MEASURED USING DEBYE AND BUECHE TECHNIQUE

Sample No.	Beam Direction	Correlation Length (a) MD	TD	ND	Aver. Void Sizes (nm) MD	TD	ND
1	Normal to film	1.33	1.33		2.11	2.11	
	Normal to edge	1.3		0.53	2.06		0.84
	Normal to end		1.16	0.47		1.84	0.75
2	Normal to film	2.75	1.5		4.46	2.43	
	Normal to edge	2.8		1.35	4.54		2.19
	Normal to end		0.71	0.71		1.15	1.15
3	Normal to film	1.44	1.44		2.32	2.32	
	Normal to edge	1.92		0.67	3.09		1.08
	Normal to end		1.73	0.58		2.79	0.94
4	Normal to film	2.31	1.3		3.75	2.11	
	Normal to edge	2.69		0.78	4.36		1.26
	Normal to end		0.95	0.95		1.54	1.54
5	Normal to film	1.42	1.42		2.29	2.29	
	Normal to edge	1.55		0.72	2.49		1.16
	Normal to end		1.91	0.3		3.08	0.48

TABLE V.5.(continued)

Sample No.	Beam Direction	Correlation Length (a) MD	TD	ND	Aver. Void Sizes (nm) MD	TD	ND
6	Normal to film	2.4	1.4		3.92	2.28	
	Normal to edge	2.95		1.42	4.81		2.32
	Normal to end		1.04	0.95		1.70	1.55
7	Normal to film	1.59	1.59		2.64	2.64	
	Normal to edge	3.22		1.0	5.34		1.66
	Normal to end		1.83	0.96		3.04	1.59
8	Normal to film	0.96	0.96		1.54	1.54	
	Normal to edge	1.69		1.34	2.72		2.15
	Normal to end		1.32	1.02		2.12	1.64
9	Normal to film	0.78	0.78		1.11	1.11	
	Normal to edge	1.88		0.89	2.82		1.33
	Normal to end		1.23	0.42		1.84	0.64
10	Normal to film	0.87	0.87		1.21	1.21	
	Normal to edge	2.06		0.64	3.09		0.96
	Normal to end		2.08	0.66		3.12	0.99

TABLE V·6. BIREFRINGENCE OF CTA FILMS

Sample No.	Birefringence x 10^3		
	Δn_{12}	Δn_{13}	Δn_{23}
1	0.091	1.744	1.653
2	0.442	0.695	0.253
3	1.078	2.854	1.776
4	1.013	1.309	0.286
5	1.721	3.734	2.013
6	1.237	1.508	0.271
7	1.557	3.659	2.102
8	2.886	5.977	3.091
9	-	-	-
10	-	-	-

eight where $\Delta n_{13} \simeq \Delta n_{23} > \Delta n_{12}$. It is also clear that birefringence increases as the solution concentration increases. In the case of biaxial films this increase might be partially due to the fact that a higher blow-up ratio was applied for higher solution concentration (compare values for biaxial film one, three, five and seven). In general this table indicates higher values of birefringence for biaxial films compared with those of uniaxially oriented samples. A substantial increase in birefringence can also be observed as a function of annealing process (compare the results of sample seven to those of annealed sample eight in Table V-6).

The CFC commercial films nine and ten did not exhibit any birefringence.

Wide Angle X-Ray Scattering

In Figure V-30 WAXS patterns for the CTA films where the x-ray beam is normal to the plane of the films are presented. The machine direction is vertical and the transverse direction is horizontal . The WAXS pattern of sample number one (23 percent concentration) is shown in Figure V-30a. The pattern exhibits a continuous diffusion ring of uniform intensity around the beam stop. This indicates this film is isotropic with no preferred orientation on the plane of the film and no crystallinity

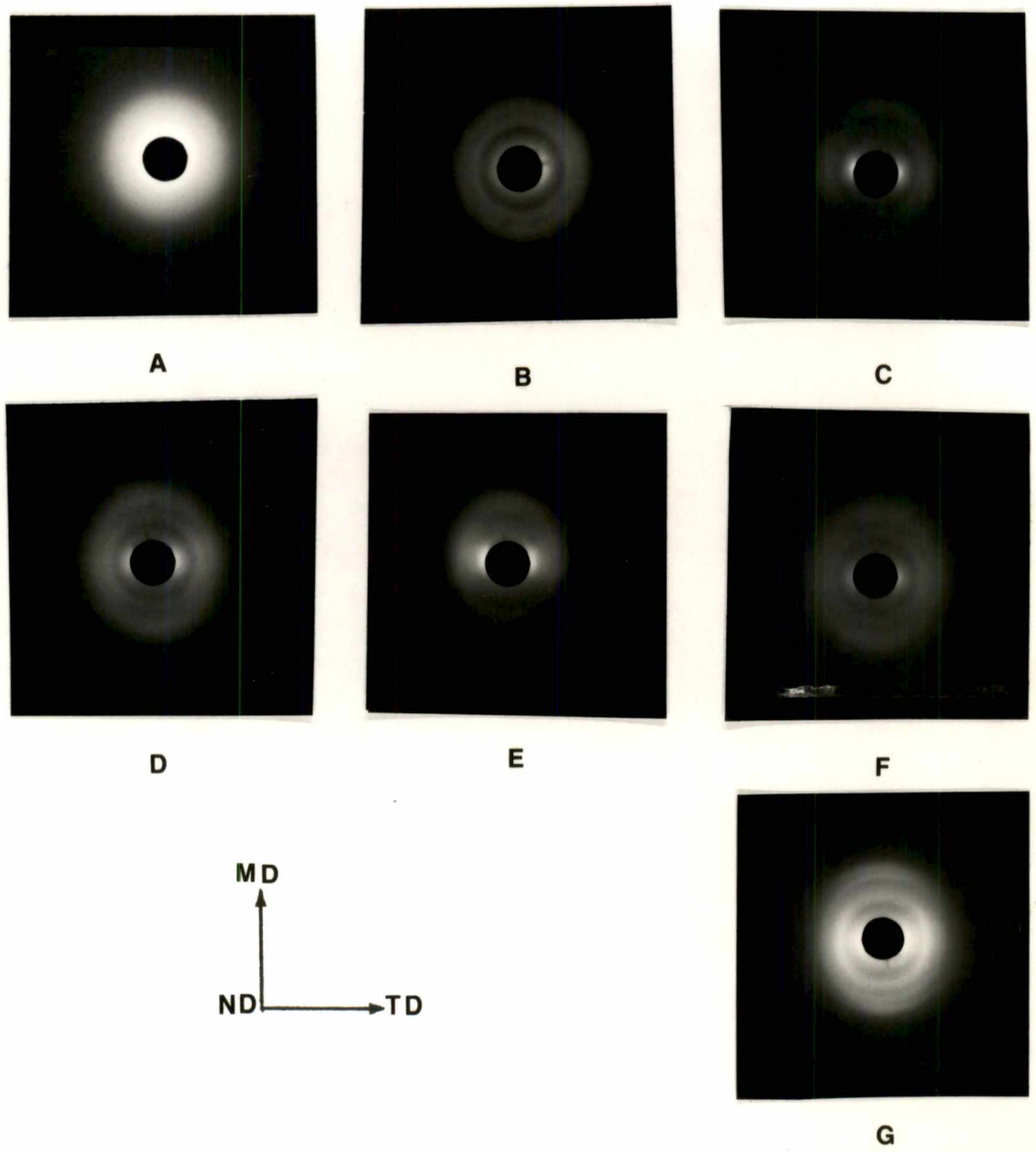


Figure V.30. WAXS patterns with the beam normal to the plane of the films, a)Sample 1, b)Sample 3, c)Sample 4, d)Sample 5, e)Sample 6 f)Sample 7, g)Sample 8

appeared in this sample. The WAXS pattern of sample 3 (25 percent concentration biaxially expanded) exhibits reflection rings indicating a well formed crystalline structure. This is shown in Figure V-30b.

In Figure V-30c to V-30g patterns for samples four, five, six, and seven and eight are shown. Qualitatively it can be seen from this figure that samples five, seven and eight are biaxially oriented while sample four and six are uniaxially oriented. This is indicated by noticable changes of the reflection rings, ie., the arc length changes. Sample eight, the anneal sample, exhibits much sharper reflection rings compared with sample seven (original sample before heat treatment). This clearly suggests an increase in crystallinity due to the annealing process.

WAXS patterns for samples nine and ten are shown in Figure V-31. Both samples exhibit low levels of crystallinity. However, the methanol treated sample exhibits weaker Debye rings which seems to be due to the extraction of the triphenyl phosphite additive.

In order to investigate more precisely the crystalline structure developed in CTA films as a consequence of various processing conditions, selected films six, seven and eight were hydrolysis. The hydrolysis consisted in treating the film samples in a stirred solution of

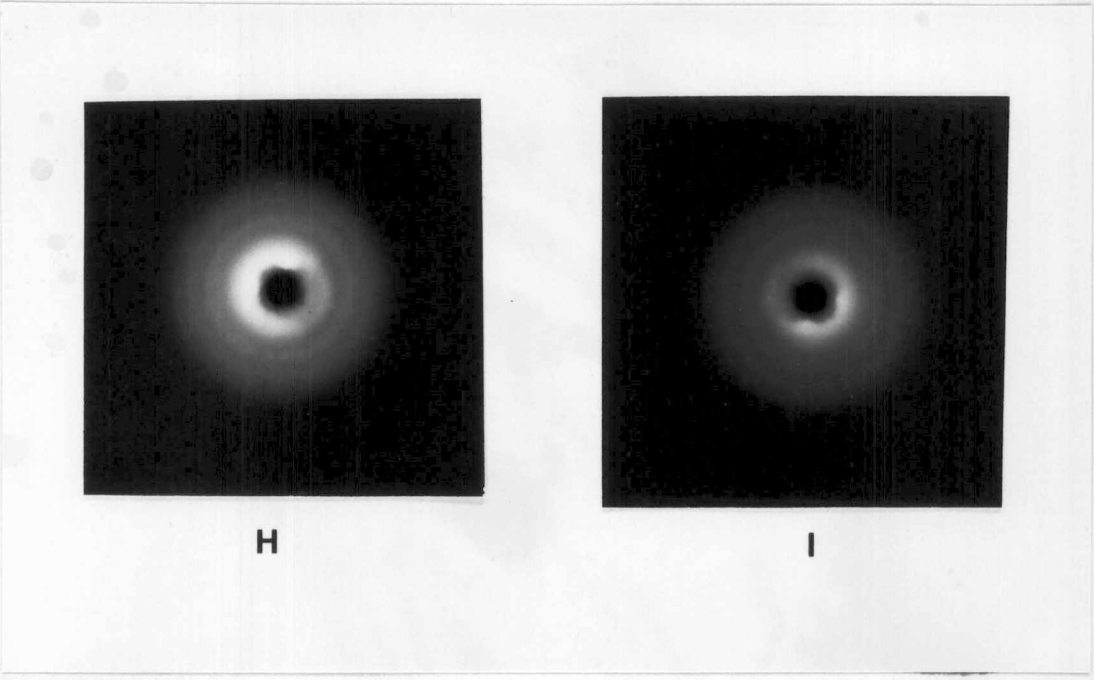


Figure V.31. WAXS patterns with the beam normal to the plane of the films for;h)Sample 9
i)Sample 10

one percent sodium hydroxide/ten percent sodium acetate for six hours at 80°C, rinsing and neutralizing with one percent acetic acid solution. The sodium acetate is used to prevent excessive swelling of the films. After hydrolysis, the samples absorbed and disintegrated in cupriethylene-diamine solution confirming the change to cellulose. The results are presented in Figure V-32 to V-34.

Figure V-32 a shows the WAXS pattern of original sample six. This pattern again shows line broadening with very short arc length in the equatorial direction. The equatorial reflections of the small angle of this pattern seems to disappear after the sample is hydrolyzed and very sharp reflection rings at higher angles are developed. These sharp reflections seem to correspond to the crystalline structure type I reported for cellulose fiber (168). However, the existance of uniaxial orientation is clearly seen from this pattern (Figure V-32b).

Biaxially expanded film seven exhibits WAXS patterns shown in Figure V-33. These patterns indicate continuous Debye rings of approximately uniform intensities around the beam stop which are sharper and more pronounced for the hydrolyzed sample (Figure V-33b). This demonstrates the existance of biaxial orientation in the film. Moreover, the expected difference between the uniaxially and biaxially oriented samples is particularaly clear in

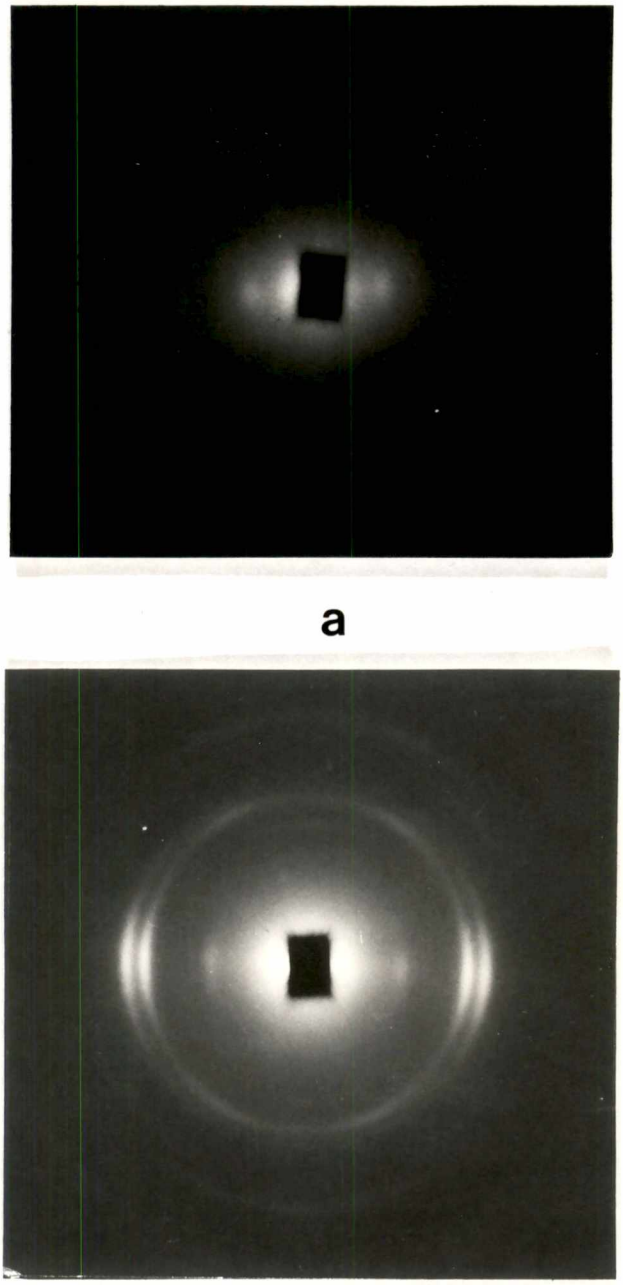


Figure V.32. WAXS patterns for Sample 6;
a)Uniaxial film, b)Hydrolyzed uniaxial film

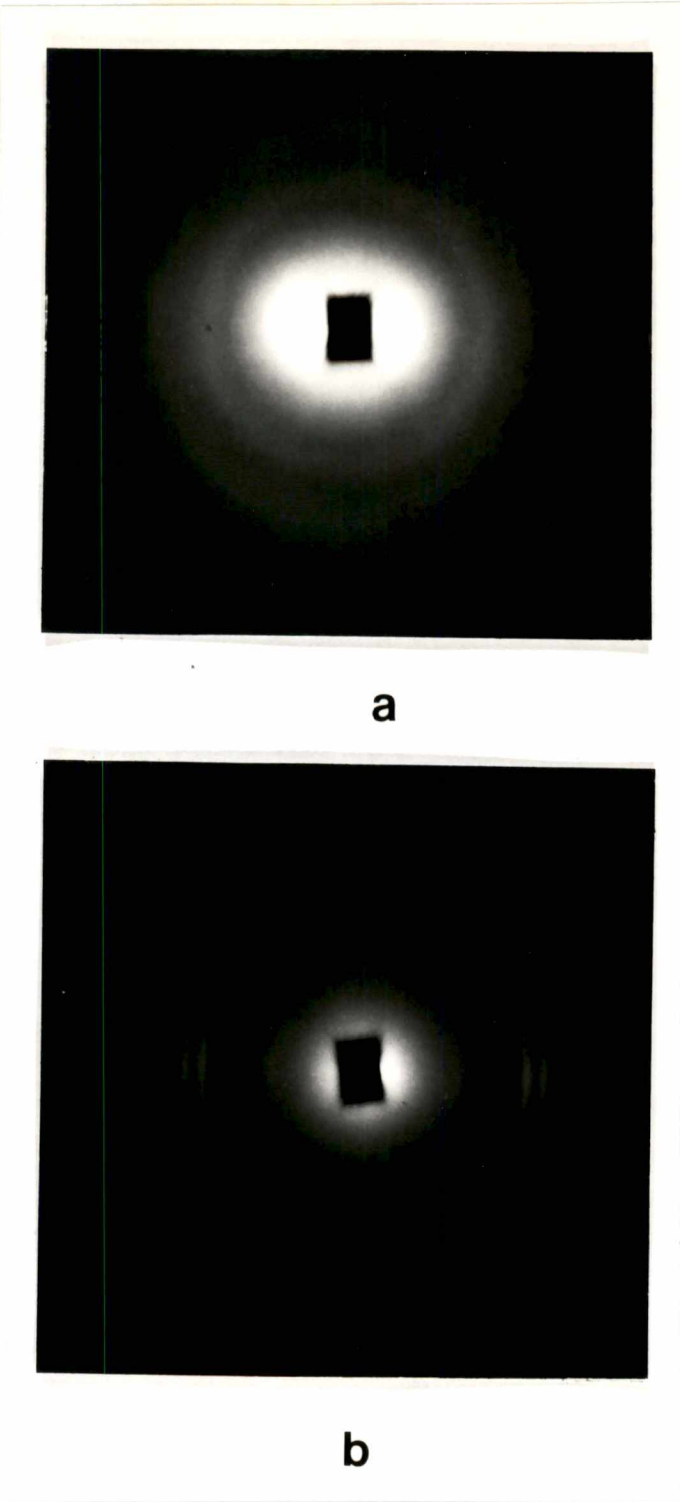


Figure V.33. WAXS patterns for Sample 7;
a)Biaxial film, b)Hydrolyzed biaxial film

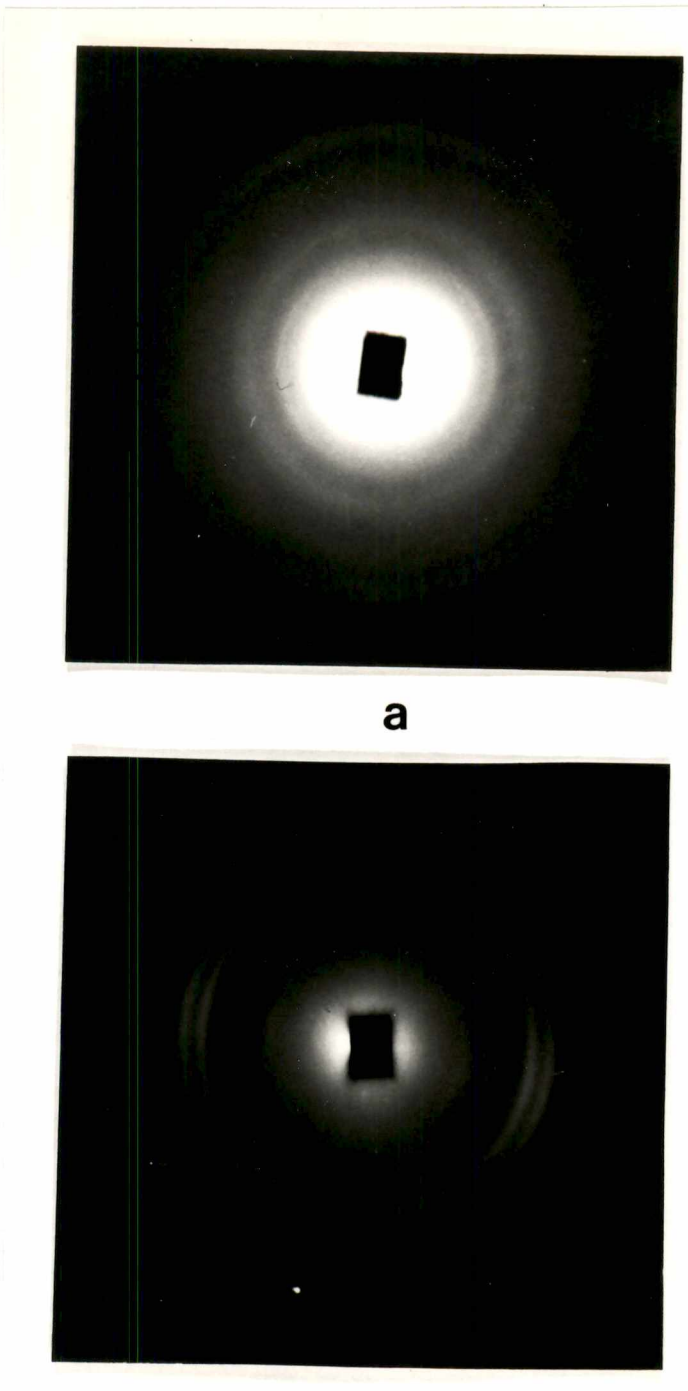


Figure V.34. WAXS patterns for Sample 8;
a)Biaxial and annealed film,
b)Hydrolyzed biaxial and annealed film

the hydrolyzed samples (compare Figure V-32b - V-33b).

More concentrated WAXS intensities are presented in the patterns of annealed sample eight in Figure V-34. The structure developing effect of the annealing treatment is most easily seen in the sharpening of the rings in the unhydrolyzed sample (compare Figure V-33 a for unannealed sample seven to Figure V-34a for sample eight after annealing).

It is important to note that the structure of CTA films, especially the original backbone configuration and spatial position, should be retained during the hydrolysis in a hetrogeneous reaction (225).

Differential Scanning Calorimetry

The DSC thermograms of CTA films are plotted in Figure V-35 through V-44. Three transitions can be seen from these plots. The first endothermic transition in the range 40-80°C is due to absorption of moisture by the film. The second transition is in the range 200-210 ^{o}C which results from the further crystallization occurring during the experiment. Finally, the third transition corresponds to melting of CTA films taking place in the range 240-300 ^{o}C. However, values for the heat of fusion of the films were determined by subtracting the area under the exothermic peak (which results

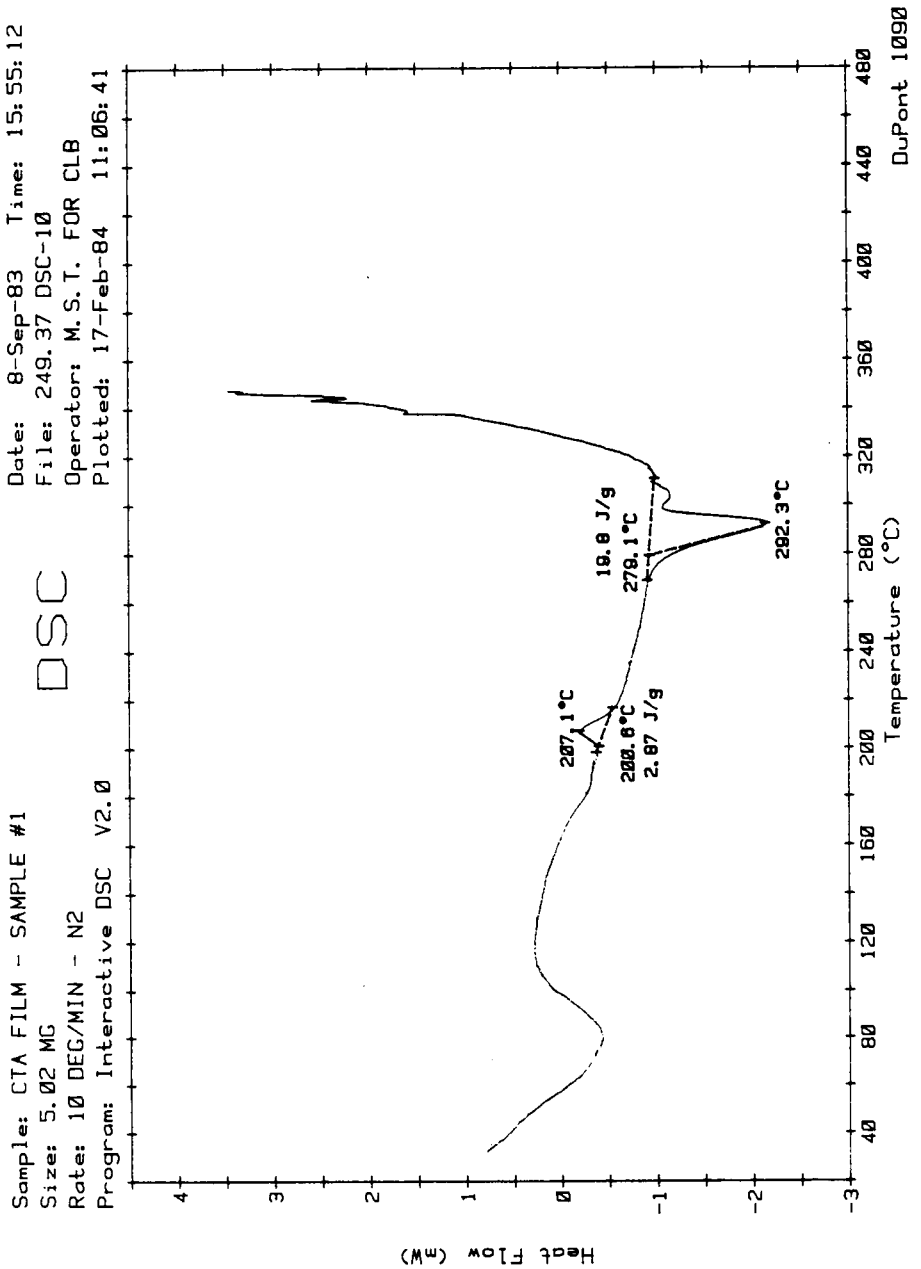


Figure V.35. DSC thermogram for film 1.

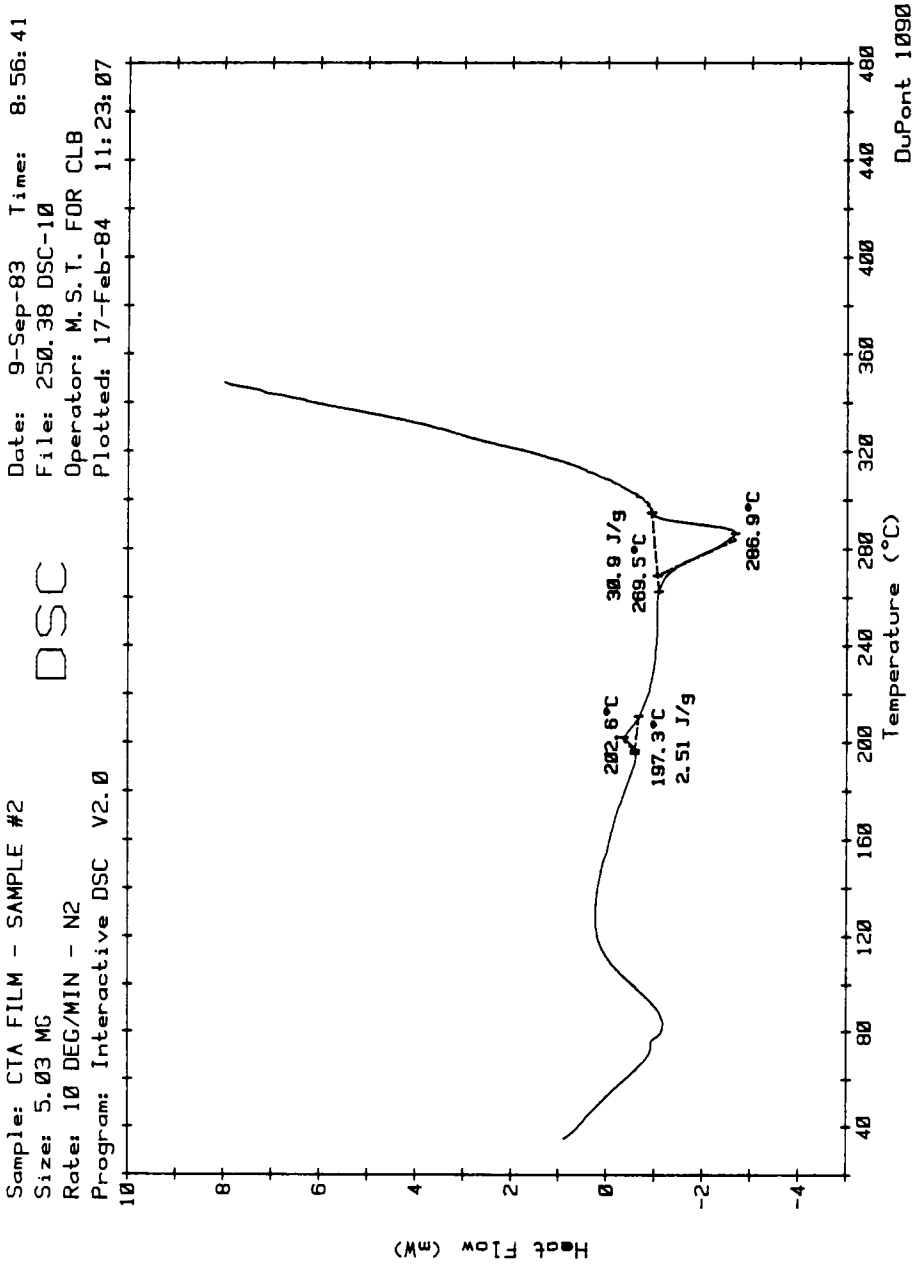


Figure V.36. DSC thermogram for film 2.

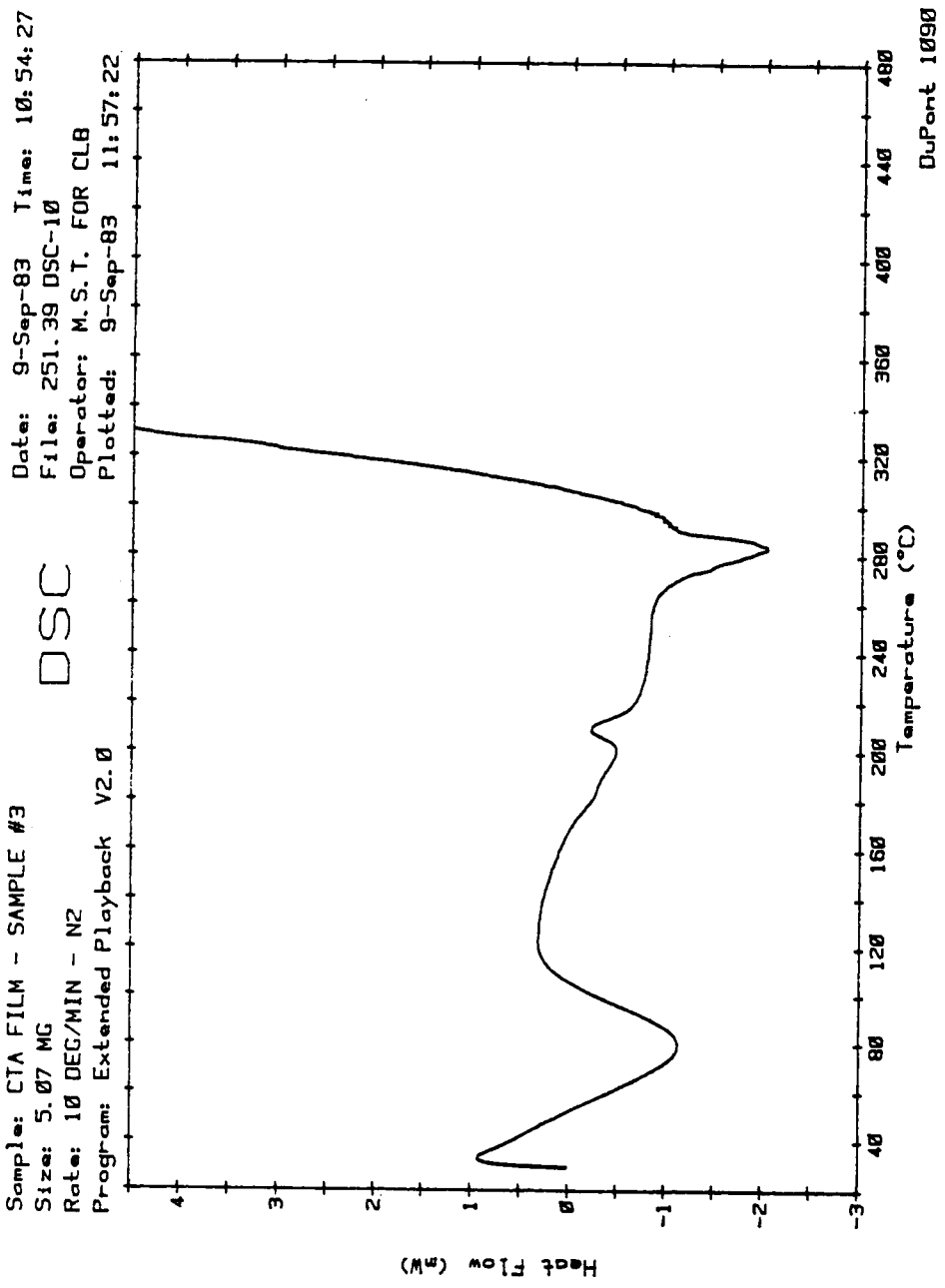


Figure V.37. DSC thermogram for film 3.

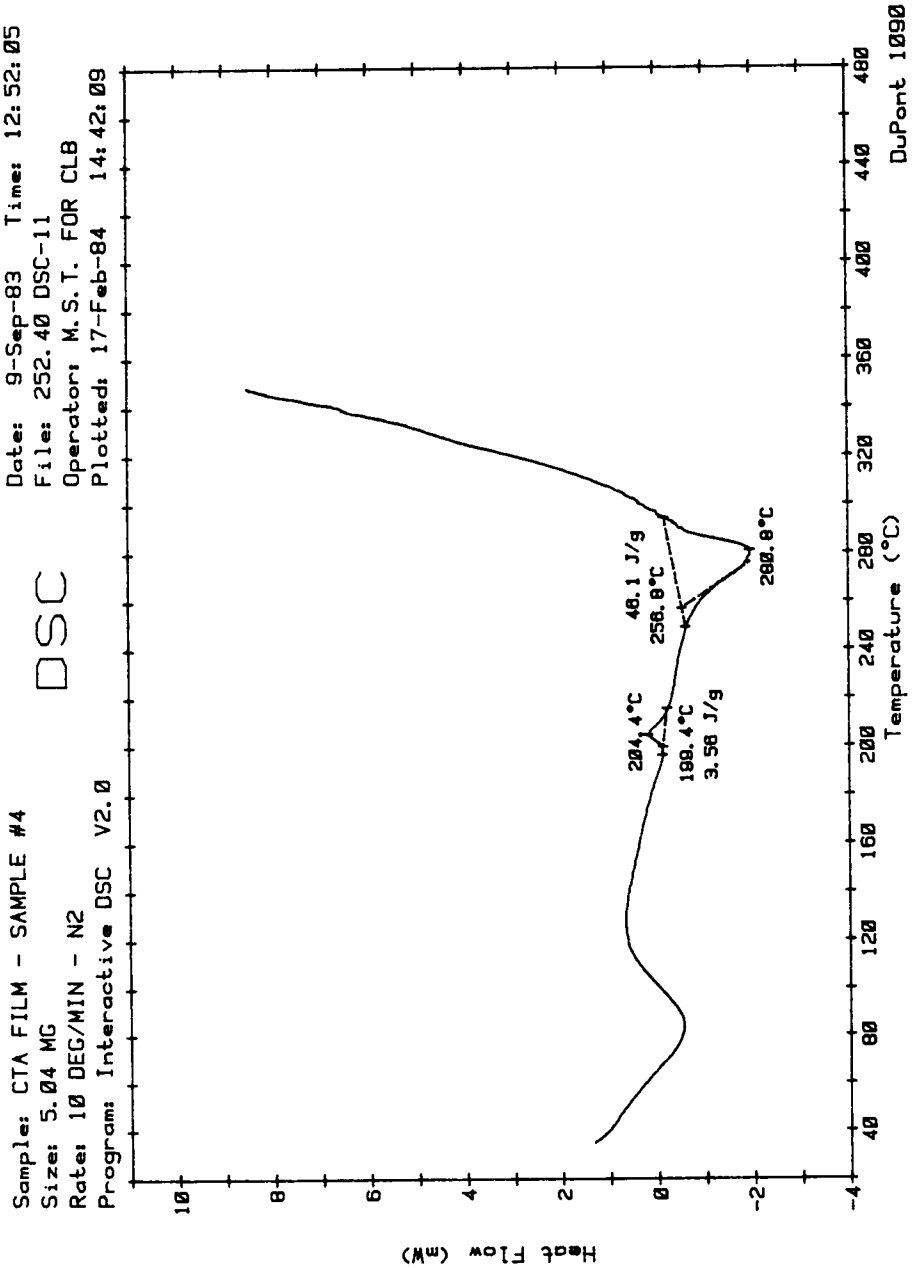


Figure V.38. DSC thermogram for film 4.

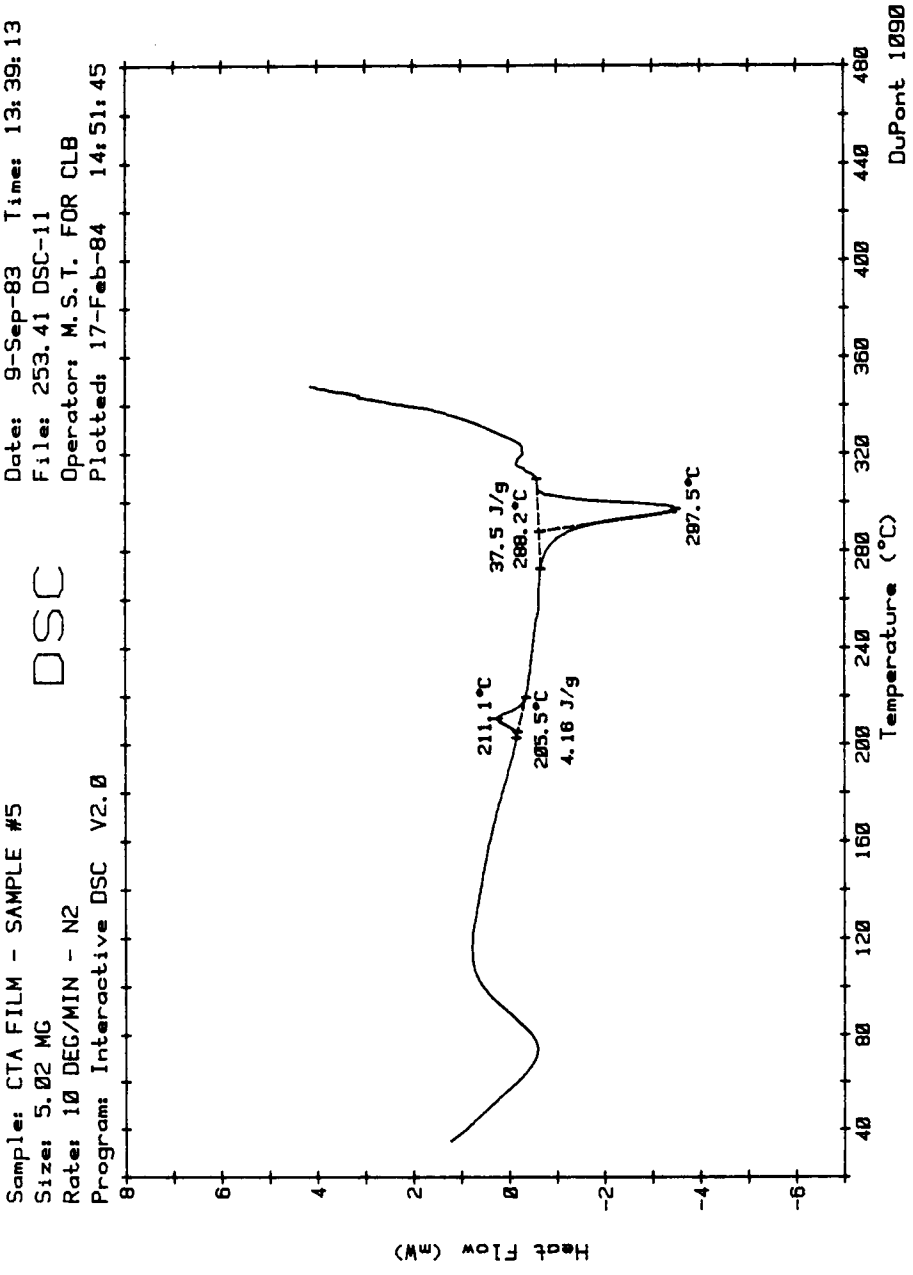


Figure V.39. DSC thermogram for film 5.

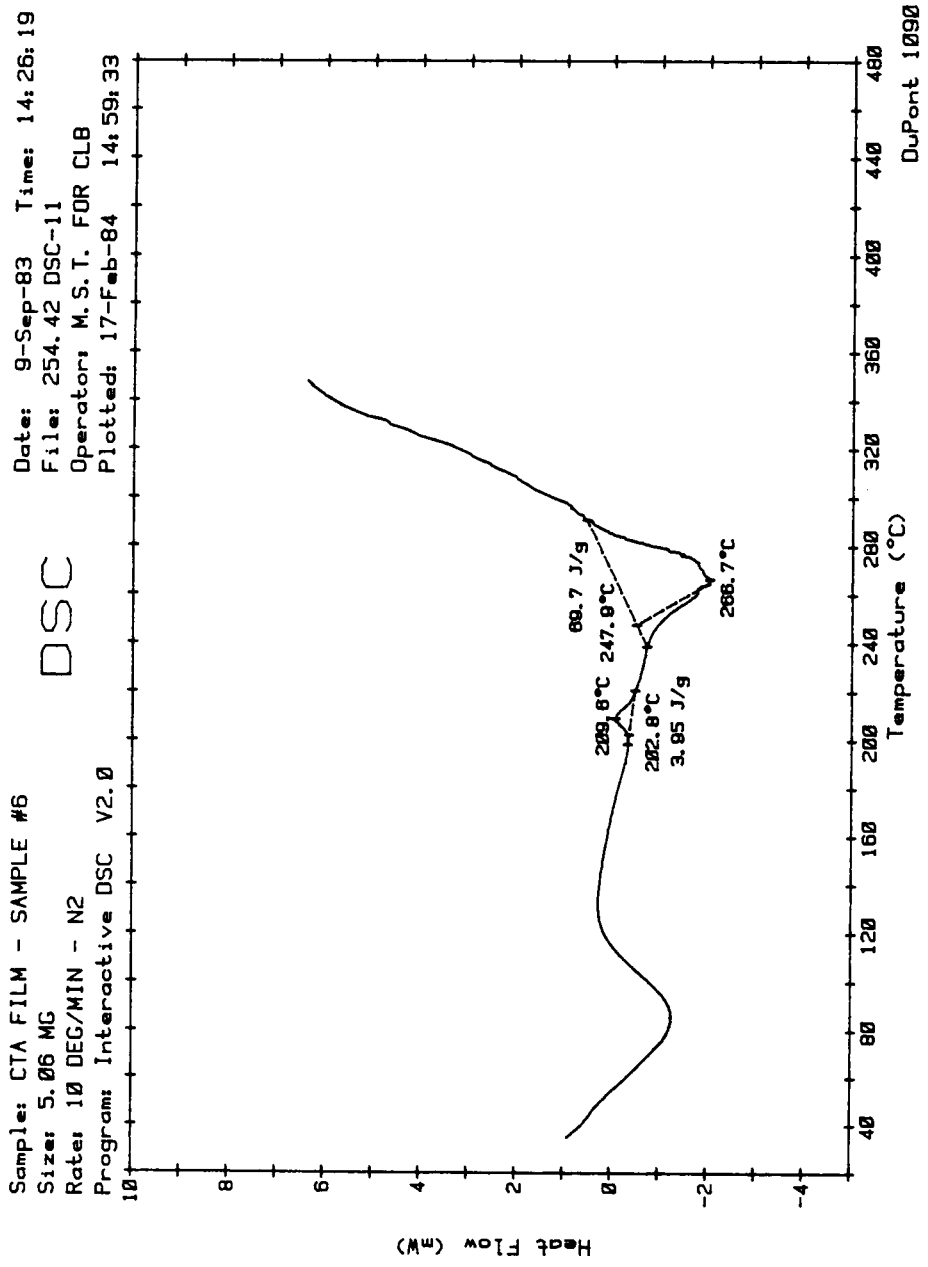


Figure V.40. DSC thermogram for film 6.

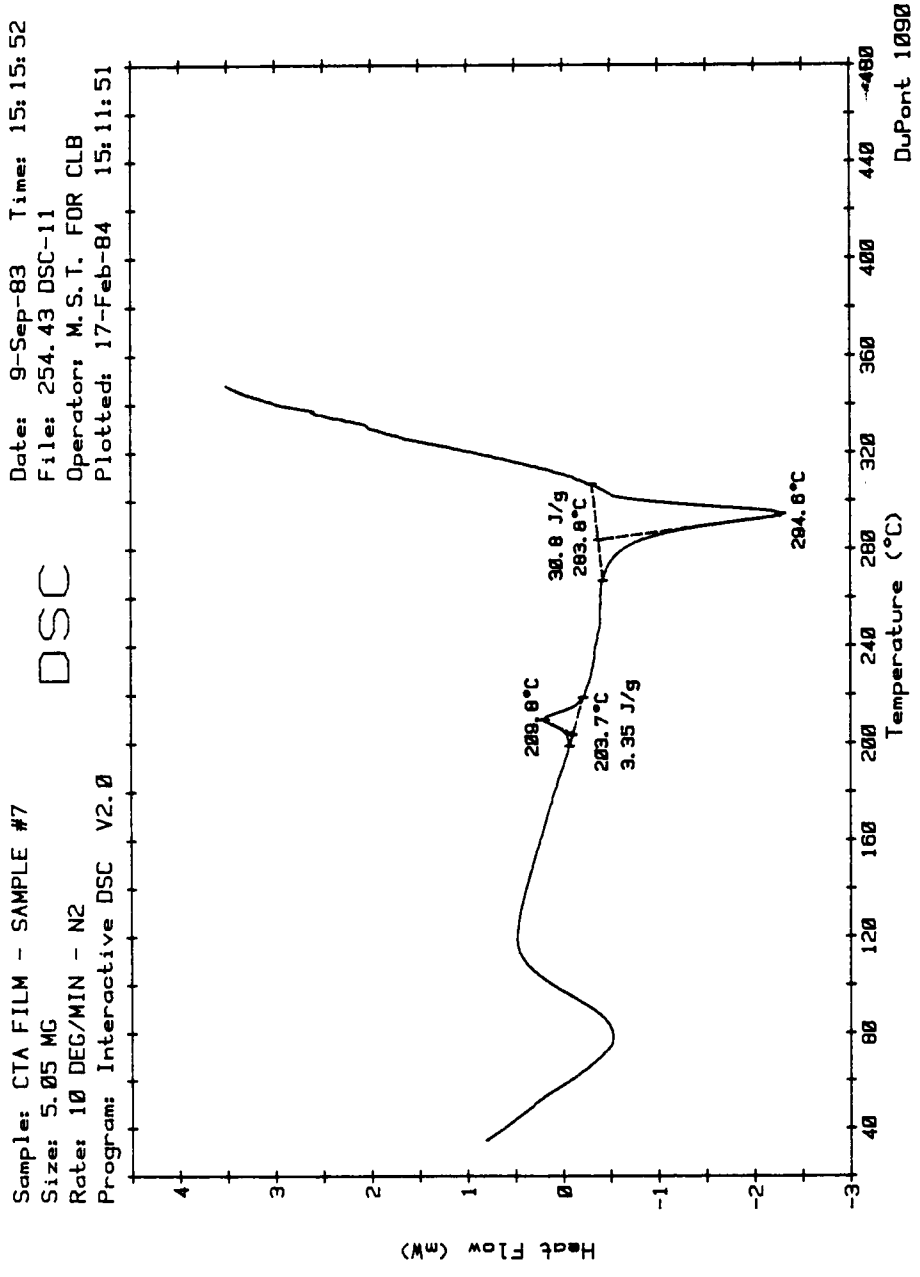


Figure V.41. DSC thermogram for film 7.

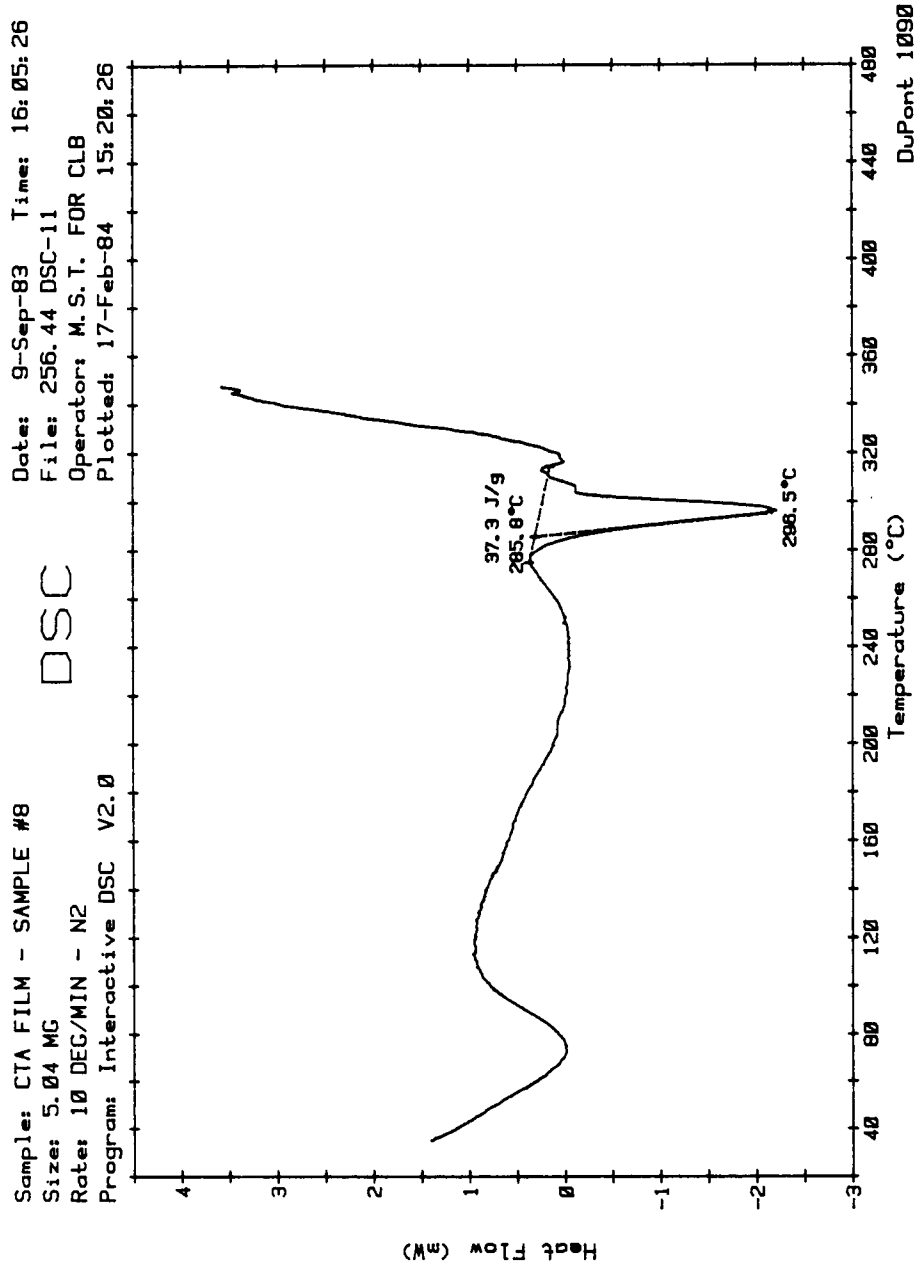


Figure V.42. DSC thermogram for film 8.

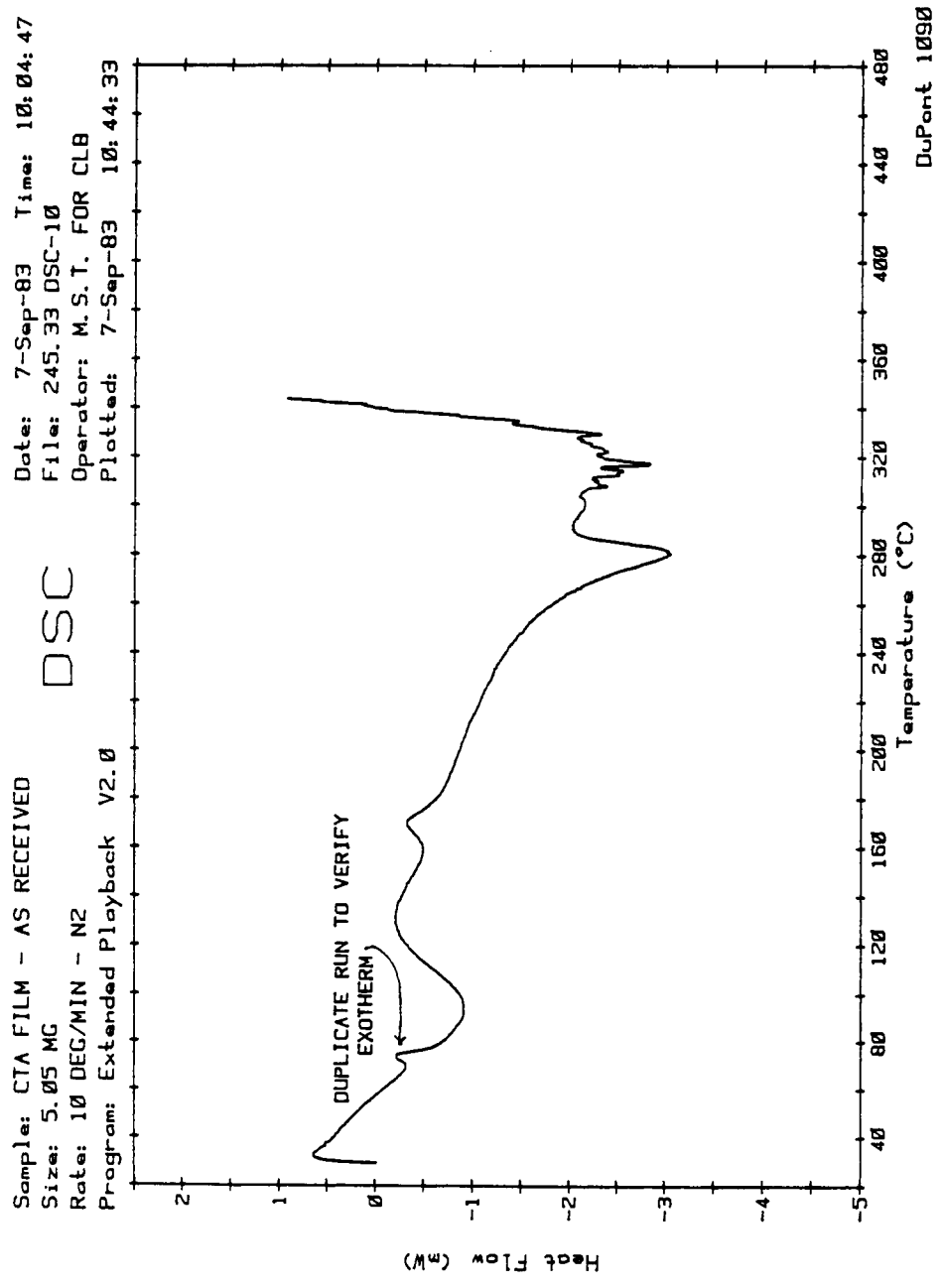


Figure V.43. DSC thermogram for film 9.

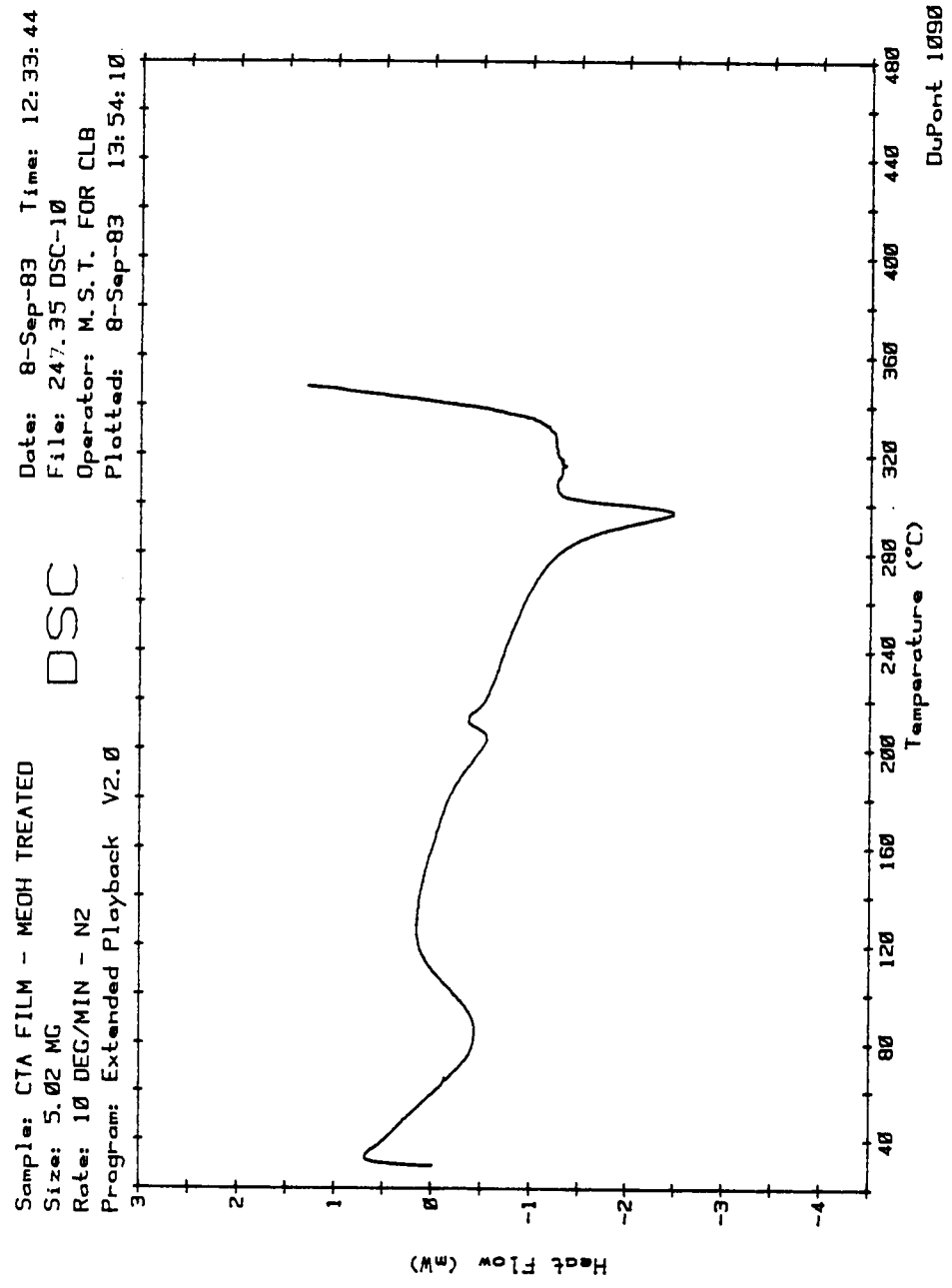


Figure V.44. DSC thermogram for film 10.

from the secondary crystallization of the samples during this experiment) from that of the endothermic peak (which corresponds to melting of CTA film). These values together with the melting temperatures for all the produced CTA films are presented in Table V-7.

Figure V-36, V-38 and V-40 show DSC scans for uniaxially drawn films two, four, and six produced from 25, 28, and 30 percent concentrations respectively. It is clear from these figures that the endothermic peaks become broader and the heat of fusion increases as the solution concentration increases (see also Table V-7). On the other hand, the melting temperature for these uniaxially drawn films decreases as the solution concentration increases. These are 286.9, 280.8 and 266.7^{o}C for films two, four, and six respectively (see Table V-7 and also figure V-36, V-38, and V-40).

The DSC traces for biaxially expanded film one, three, five, seven and eight are shown in Figure V-35, V-37, V-39, V-41 and V-42 respectively. The melting temperatures are higher and the endothermic melting peaks are fairly sharper than those of uniaxially drawn films. But the heat of fusion for a given solution concentration is higher for uniaxially drawn films (see Table V-7).

The annealing effect can be seen from comparison of Figures V-41 to V-42, where the exothermic peak is

TABLE V.7. HEAT OF FUSION AND MELTING TEMPERATURE FOR CTA FILMS

Sample No.	Film Type	Heat of Fusion ΔH (J/g)	Melting Temp. (C^{o})
1	Extrusion/Recy.Proc. B.R.=2/coagulation	16.93	292.3
2	Extrusion/moderate drawdown/coagulation	28.39	286.9
3	Extrusion/Recy.Proc. B.R.=2.5/coagulation	14.61	283.1
4	Extrusion/moderate drawdown/coagulation	42.64	280.8
5	Extrusion/Recy.Proc. B.R.=3.0/coagulation	33.34	297.5
6	Extrusion/moderate drawdown/coagulation	65.75	266.7
7	Extrusion/Recy.Proc. B.R.=3.3/coagulation	27.45	294.6
8	Extrusion/Recy.Proc. B.R.=3.3/coagulation/ annealed	37.3	296.5

is absent for sample eight. Both heat of fusion and melting point are also higher for heat treated film eight compared to origional unannealed sample seven. Another interesting feature in annealed film eight is the development of an additional endothermic peak after melting. This can be seen at about 320 ^{o}C on the Figure V-42 for this sample.

DSC thermograms for CFC films nine and ten are given in Figure V-43 and V-44. From comparison of these figures it is clear that the film nine after methanol treatment exhibits a sharper endothermic peak at about 180 ^{o}C. Two other transitions present in untreated film nine around 60 and 320 ^{o}C (Figure V-43), are absent for methanol treated sample ten.

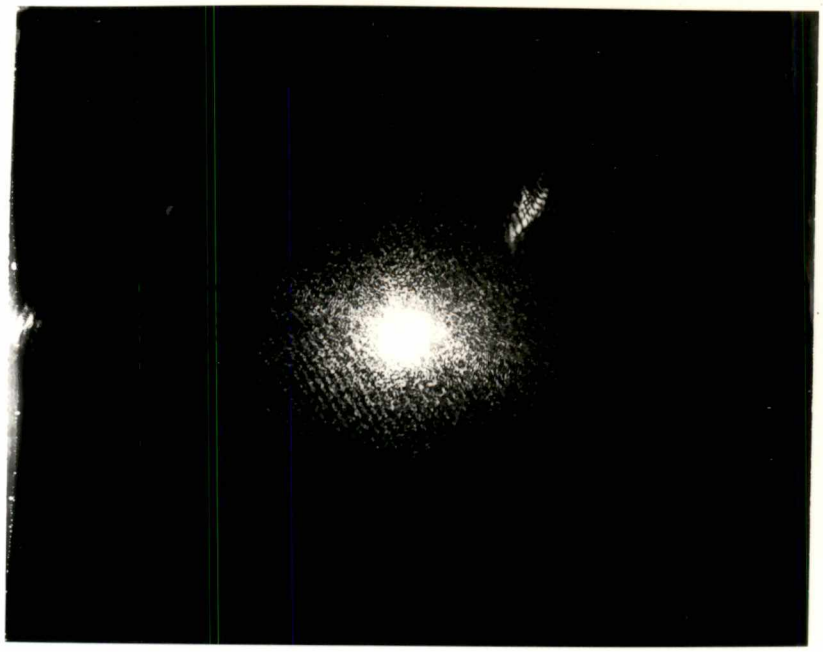
In conclusion, the existance of the voids and fibrillar structure seen in Figure V-2 through V-9 for the film one through eight suggest that calorimetry is a more useful method of determing crystallinity than density technique. However, since some of the produced film in this study showed higher experimental values of heat of fusion (Δ H) than theoretically calculated values reported for cellulose triacetate in the open literature (222,223), we were unable to measure the crystallinity of the films using the DSC technique.

D. Small Angle Light Scattering

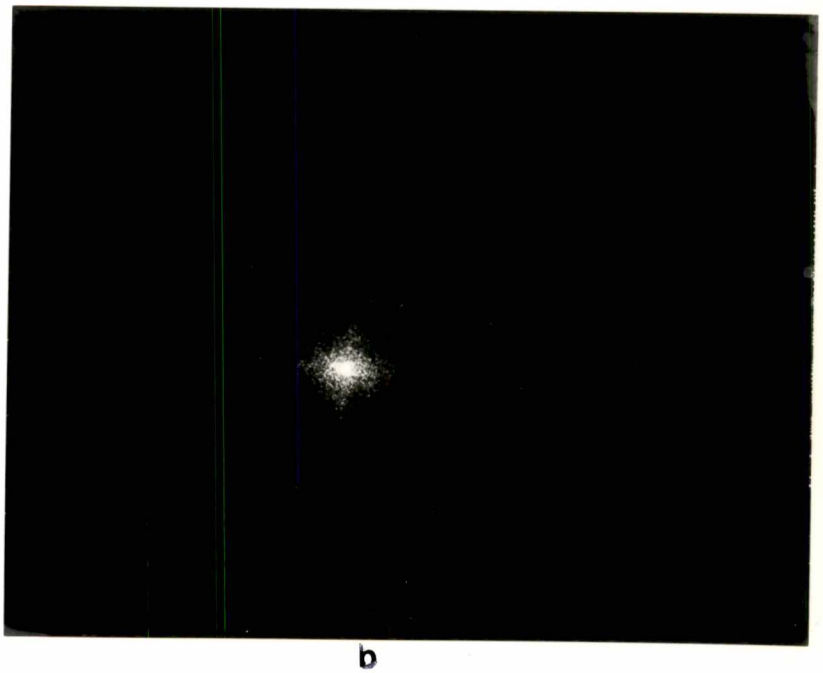
SALS patterns of the films are shown in Figure V-45 to V-52 for sample one through eight respectively. Pattern "a" in each figure is V_v and pattern "b" of each figure is H_v. The sample to film distance was kept constant at 16 cm for all the samples. The exposure time for the V_v patterns was 1/100 second and in the case of H_v due to the reduction of intensity the exposure time was increased to one second.

Figure V-45 gives SALS patterns for isotropic sample one. The H_v pattern indicates a four lobe symetric. The V_v pattern for this sample is isotropic. Anisotropic biaxially expanded films three, five, seven and eight show circular symmetrical shapes for both V_v and H_v patterns. However, there seems to be more scattering for H_v patterns of film seven and eight compared to those observed for sample three and five (see Figure V-47, V-49, V-51, and V-52).

Uniaxially drawn films, two, four, and six exhibit different scattering. The scattering intensities are concentrated in horizontal direction for both V_v and H_v patterns unlike biaxially expanded films. The H_v patterns of film two (Figure V-46) exhibits two weak horizontal lobe which are more concentrated for sample four (see

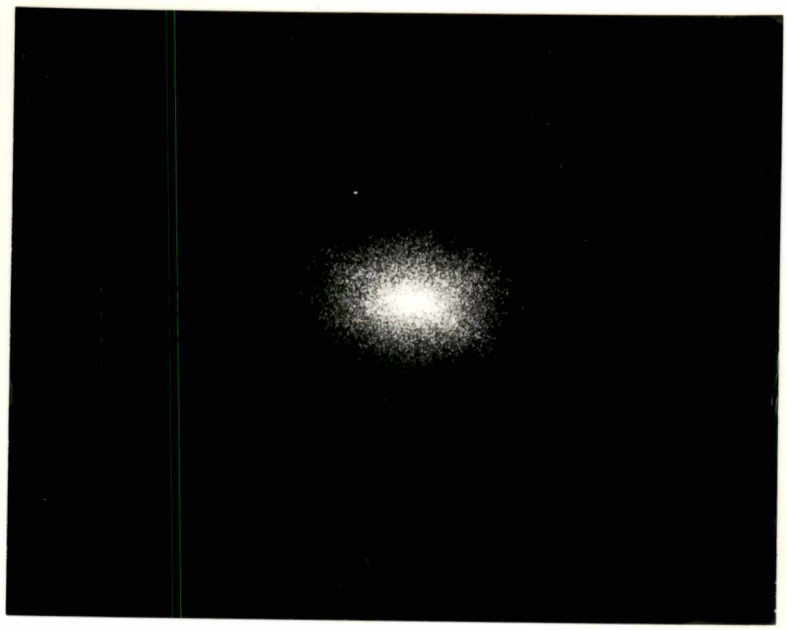


a



b

Figure V.45. SALS patterns for film 1;
a)V_V, b)H_V

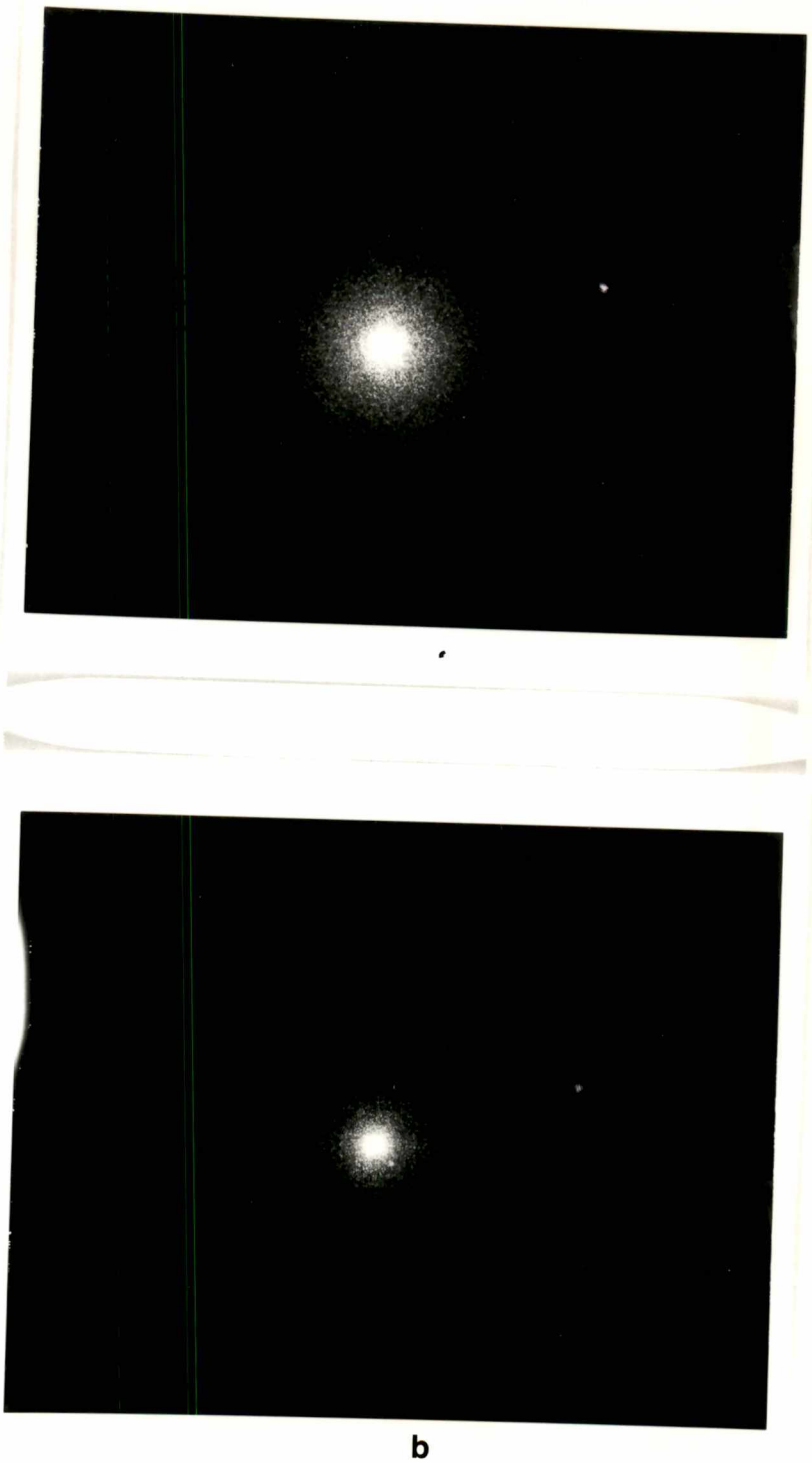


a



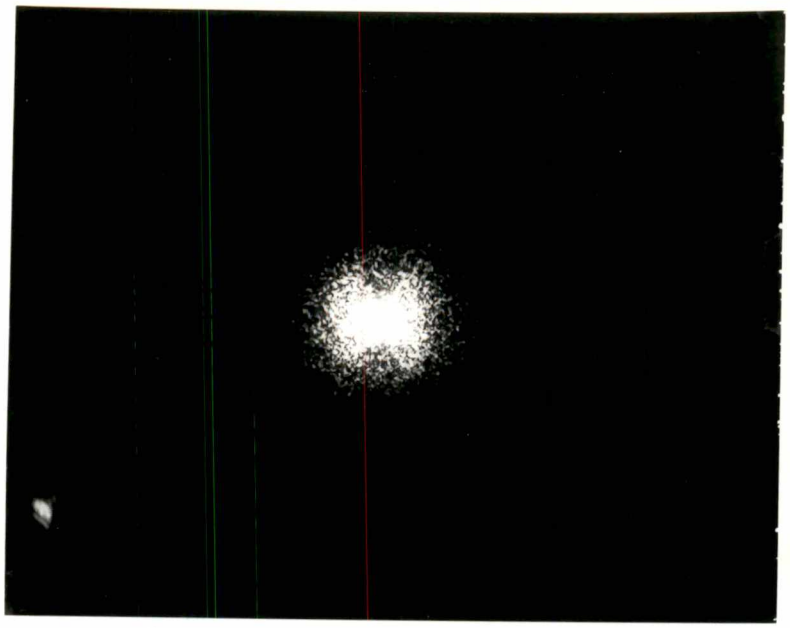
b

Figure V.46. SALS patterns for film 2;
a)V_v, b)H_v

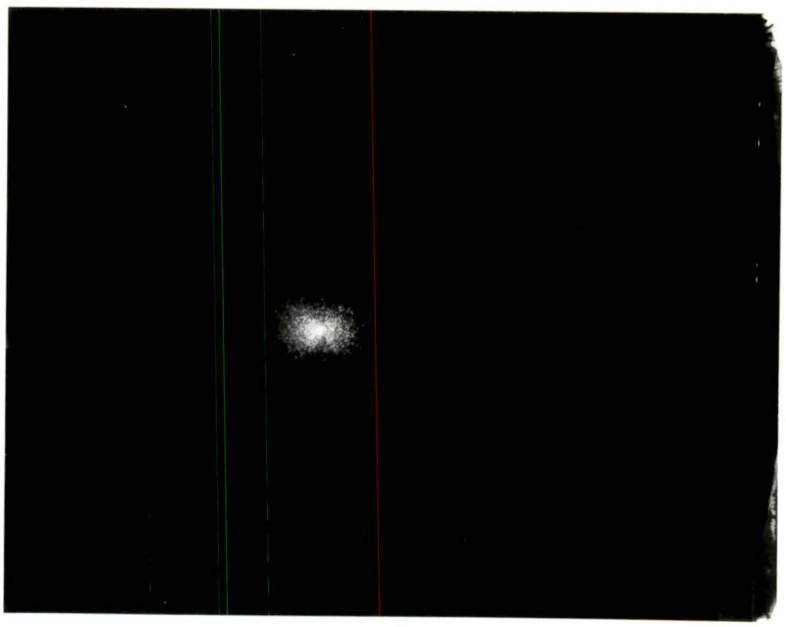


b

Figure V.47. SALS patterns for film 3;
a)V_v, b)H_v

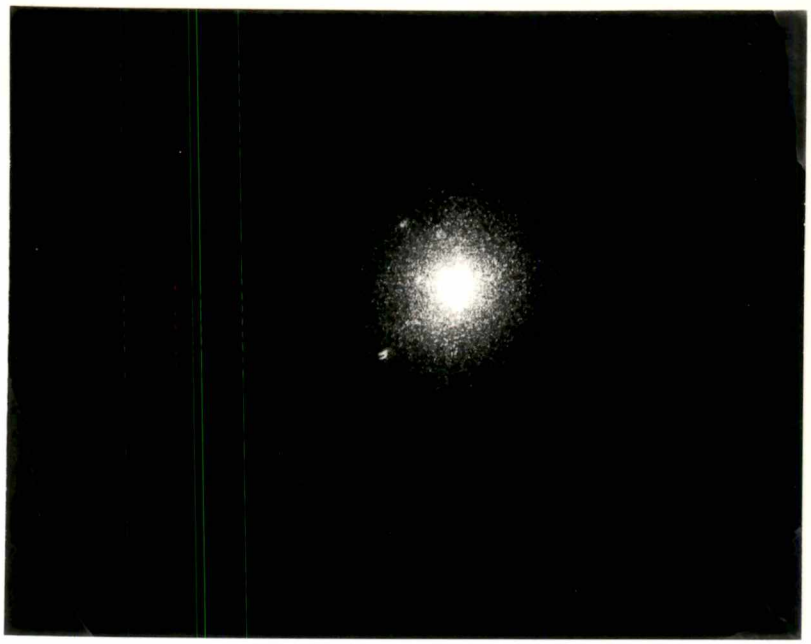


a

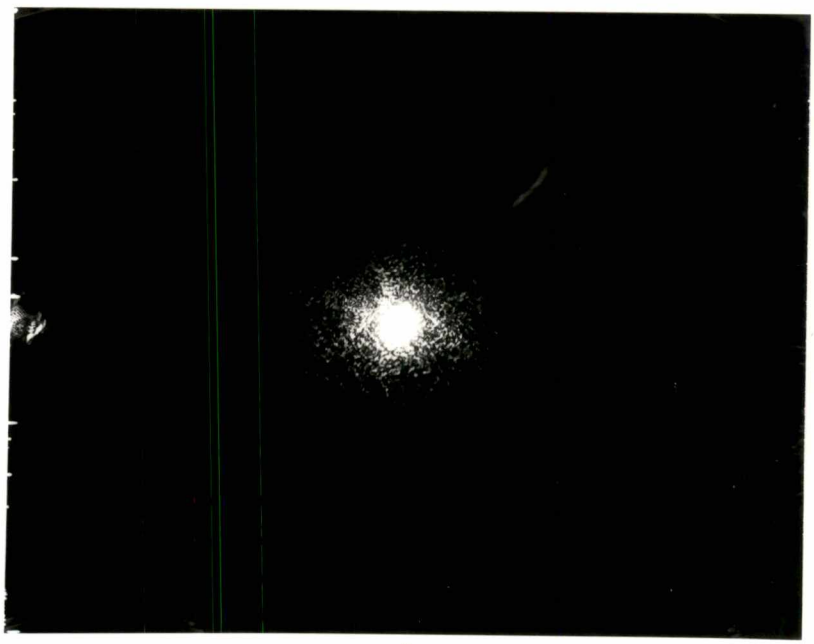


b

Figure V.48. SALS patterns for film 4;
a)V_V, b)H_V



a



b

Figure V.49. SALS patterns for film 5;
a) V_v, b) H_v

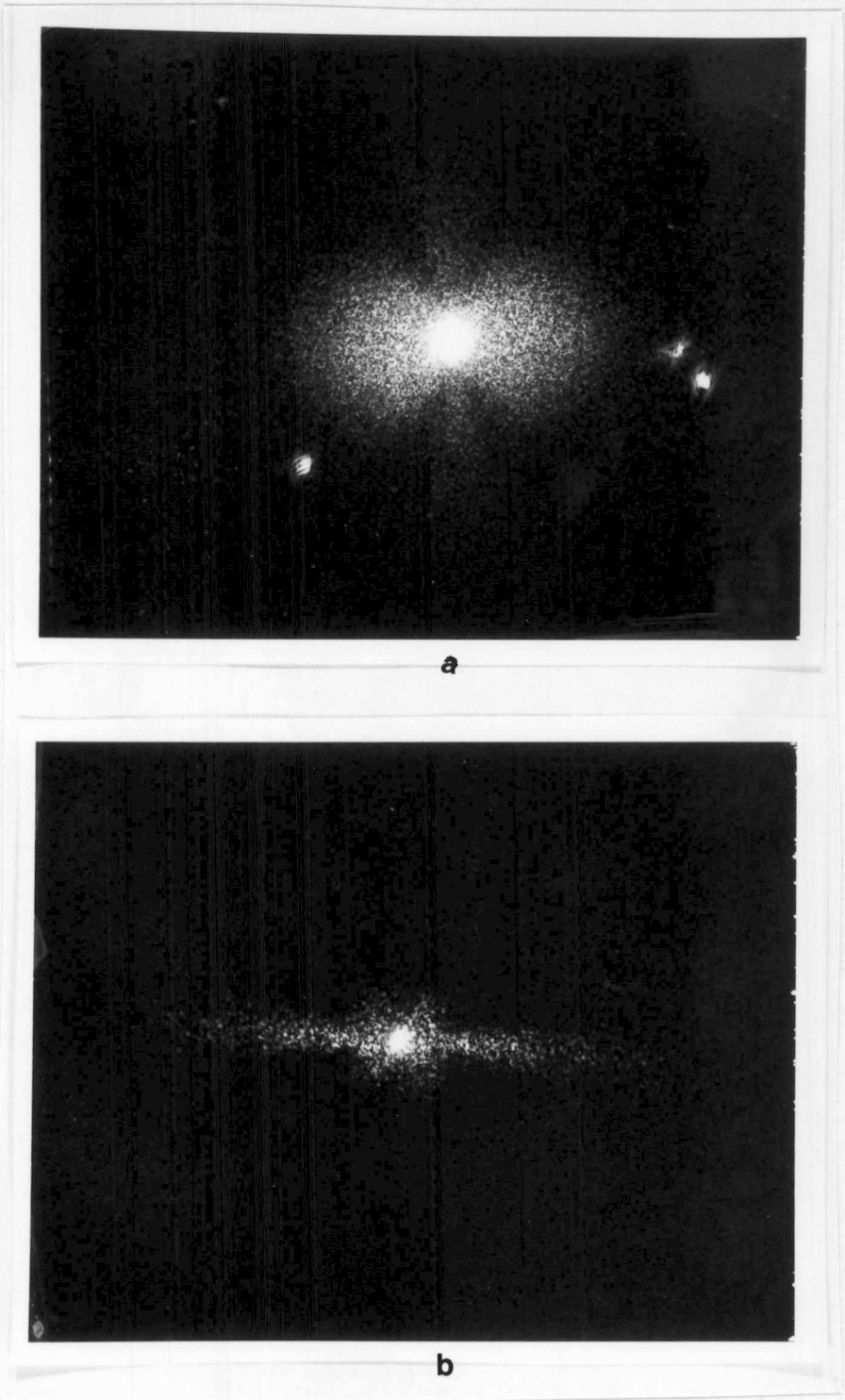
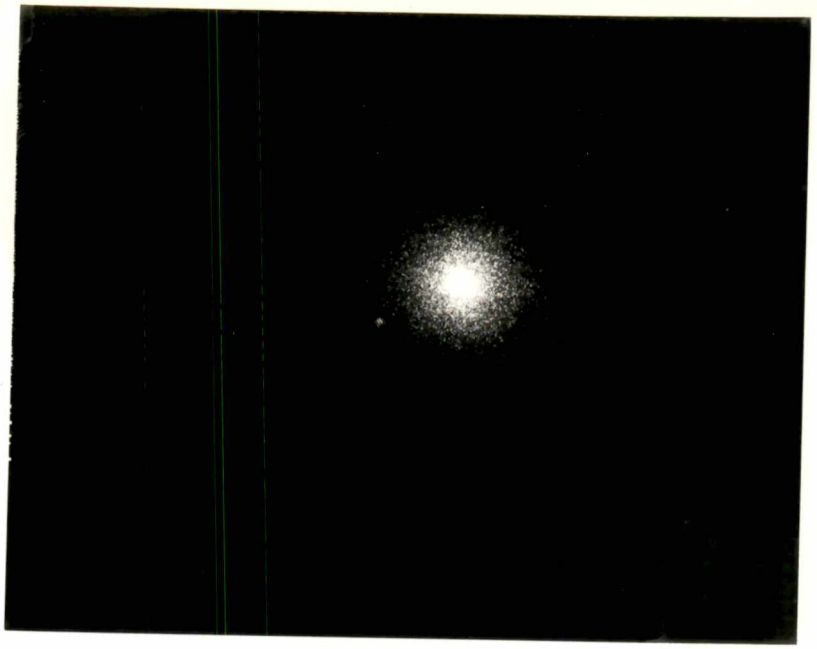
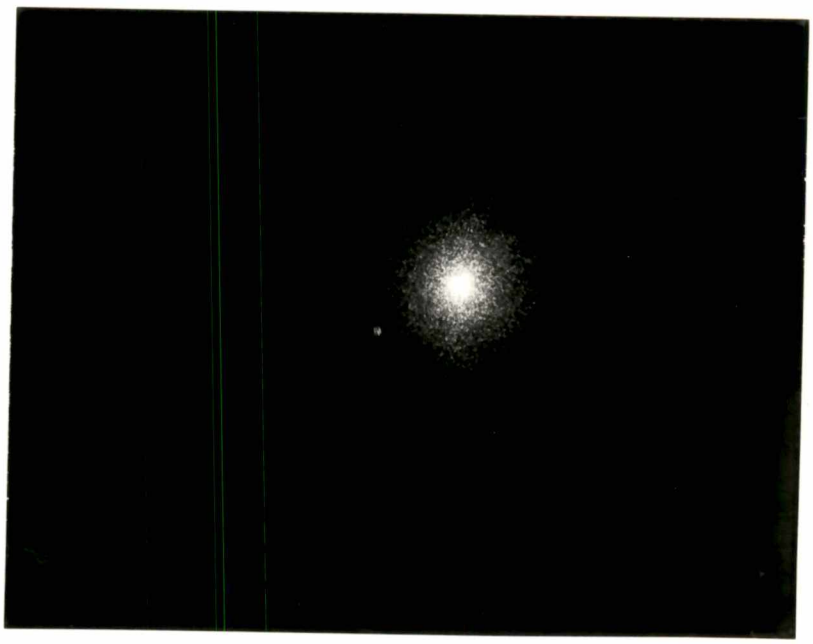


Figure V.50. SALS patterns for film 6; a)V_v, b)H_v



a

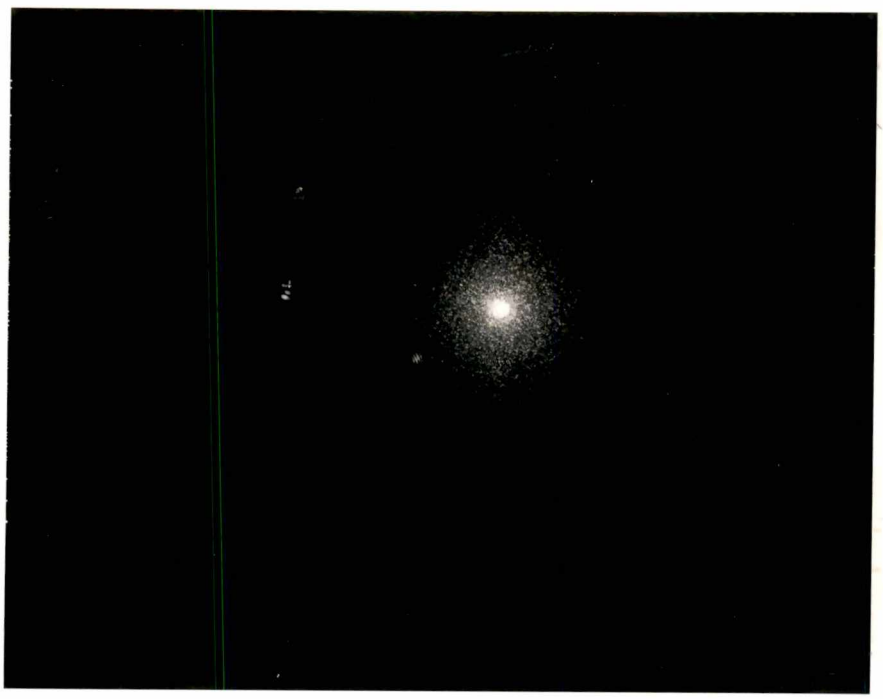


b

Figure V.51. SALS patterns for film 7;
a)V_v, b)H_v



a



b

Figure V.52. SALS patterns for film 8;
a)V_v, b)H_v

(see H_v pattern in Figure V-48) and become a long horizontal strip for sample six, the uniaxially drawn film produced from 30 percent concentration (see H_v pattern in Figure V-50). However, these SALS patterns will be compared and discussed with SALS data reported by Samuels (156), Stein (226), Hashimoto et al. (228), Hayashi et al. and recently by Liang et al (229) in the next section of this chapter.

E. Discussion

As pointed out earlier in this chapter, CTA films were produced under a wide range of processing condition. The biaxially expanded films showed better mechanical properties than that of uniaxially drawn samples. Since the coagulation rate was relatively slow for CTA/DCA/FA in cold isopropanol, the production of uniaxial highly oriented film was difficult. The extruded film was too insufficiently coagulated to support the drawdown necessary to impart substantial orientation. However, biaxially oriented films of fairly high tensile strength and modulus were prepared using a coagulant blow-up wet film extrusion process described in Chapter III. To accelerate coagulation, the coagulant was fed to the inside of the film as it was formed. Feeding the coagulant into the film not only increased the coagulation rate

sufficiently for imparting orientation, it also allowed production of films under various blow-up ratios. The blow-up ratio was controlled by varing the coagulant flow rate. In this section the structural characteristics of produced CTA films will be discussed. The mechanical properties for both CTA and PPTA films will be explained and discussed in the next chapter.

Very interesting results were observed during the investigation of the morphological features of the films. While it was expected that the uniaxially drawn films could have their surface layer easily "peeled", the biaxially expanded films were totally resistant to delamination. The SEM photomicrograph of peeled sample six produced from 30 percent solution concentration shows a ribbon-like fibrillar structure with voids-elongated along the machine direction. The cross-sectional view of this film also exhibit extensive voiding and fibrillation. The void and fibrillar structure can also be observed from the SEM patterns of uniaxially oriented film four produced from 28 percent concentration. But, they are hardly seen for uniaxial film two produced from 25 percent solution concentration. A solid-like structure can be observed from SEM patterns of this film. These observations are consistant with data obtained from density measurement (see Table V-2). However, as the solution

concentration increases, the void and fibrillation increases. Furthermore SEM patterns for biaxially expanded film also indicate as solution concentration increases the voids and they become bigger and more complex. This is clearly seen from comparison of Figure V-2 V-4, V-6 and V-8.

The microstructure seen in the cross-sectional view of biaxial film seven produced from 30 percent concentration is more defective than the other biaxially oriented films. This seems to be related to the lowest density observed for this sample and how the coagulation is influenced by the dope concentration.

The annealing effects on the structure of the film are clearly observed as expected. The SEM photomicrographs of annealed sample eight indicate a smoother surface and less defective cross-sections compared to unannealed film seven. A substantial increase of density also was found after annealing the film (see Table V-2).

Isotropic film one exhibits very few visible voids in the SEM photomicrographs and distributed within this film (see Figure V-2). The cross-sections of this film are generally smoother than other films produced from anisotropic solutions. However, the existance of small voids are easily seen from small angle x-ray contour plots obtained for this film. The diffuse scattering at a very small angle x-ray scattering often has been interpreted to be due to the presence of voids as described

in the previous chapter. However, it is apparent from Figures V-12, V-14, V-16 and V-18 that this diffuse scattering intensity increases with increasing polymer solution concentration. The least scattered intensity can be observed from the contour plot of sample one when the x-ray beam is parallel to the ND of the film in Figure V-12 and the greatest scattering can be seen from SAXS contour plot of film seven when the beam is parallel to the ND of the film. It should be noted that even though there is some surface reflection when x-ray beam is normal to the MD and TD of stacked films, sample one showed very little or no scattering while a very strong scattered intensity is presented in the contour plots of both MD and TD view of anisotropic film seven (compare Figure V-12 to V-18). Moreover, similar conditions are observed for uniaxially drawn films as a function of solution concentration. These SAXS results are generally consistent with the observations from scanning electron microscopy and density data.

The heat treated sample eight also resulted in a decrease of scattered intensity in SAXS, increase of density in density measurement, and exhibited smoother surface and cross-sections under SEM compared to original unannealed film seven.

The judgement of SAXS results in this study was based on the scattered intensity obtained for the films where the x-ray beam is parallel to the ND of the film. This was because there is some surface reflection observed for the films where the beam is parallel to the TD or MD of the stacked films. However, an attempt was made in order to eliminate such surface reflection by tilting the samples greater than about 15° from the x-ray beam. This technique may eliminate some, but surface reflections are still apparent for most of the CTA films.

Further analysis of SAXS scattering for estimation of void size and void volume fraction were achieved using various techniques described earlier in this chapter. The volume fraction of microvoids was found to increase as the solution concentration increases. Higher values were found for thicker uniaxially drawn films compared to those of the biaxially expand film (see Table V-3). A decrease in void volume fraction was observed as a function of annealing. The void size was also found to increase as solution concentration increased and decreased as a function of annealing. The void shape was found to be dependent on the processing conditions used. This was similar to the results obtained for PPTA films. However, the Debye-Bueche method revealed smaller voids compared to dimensions estimated from Guinier plots. This was explained and discussed in the previous chapter for PPTA

films, (see discussion on page 240, Chapter IV). Moreover, these techniques were applied by various authors in order to estimate particle size and particle size-distribution elsewhere (220). Smaller voids, however are reported to be obtained using Debye-Bueche technique method but there are discrepencies between the authors interpretations.

It is also important to note that an attempt was also made to estimate volume fraction of voids from a combination techniques of DSC and density measurement. This is expected to yield better information than that of invariant analysis due to the fact that the large voids are not detectable from small angle x-ray (wavelength 1.542 $\mathring{A}$). Thus the volume fraction measured from SAXS is in fact a partial measurement. However, in the DSC measurement the experimental heat of fusion for some of the samples were found to be higher than that of theoretically calculated values available in the literature (222,223). This frustrates the achievement of such an estimation. The DSC traces for uniaxially oriented films exhibit very interesting results (see Figure V-35 through V-44) which indicate very broad melting peaks for uniaxially drawn samples. While these are rather narrow and sharp for biaxially oriented films. The effect of solution concentration is particularly seen

for uniaxially oriented films. The peaks are becoming broader leading to increase of heat of fusion and decrease of melting point as a function of solution concentration. The broad peaks for uniaxial films seems to be due to the presence of paracrystallinity in these films. This can be further substantiated from the observation of line broadening in the WAXS patterns of especially produced film six from high solution concentration. The biaxially expanded films on the other hand, show WAXS patterns indicating more or less continuous Debye rings of uniform intensity which are sharper especially for annealed sample eight (see Figure V-34a). These seem to be also consistent with sharp and narrow enothermic peaks seen in the DSC thermograms of these biaxial films.

The DSC trace of annealed sample eight also exhibits a remarkable feature which is not seen for original unannealed film seven (compare Figure V-41 to V-42). The absence of the exothermic peak as a consequence of further crystallization during the DSC experiment together with a sharper WAXS pattern seen for the annealed sample eight clearly demonstrate an increase in crystallinity as a function of heat treatment. The heat of fusion of this sample increased from 27.45 to 37.3 J/g.

The uniaxially oriented films also exhibit

for uniaxially oriented films. The peaks are becoming broader leading to increase of heat of fusion and decrease of melting point as a function of solution concentration. The broad peaks for uniaxial films seems to be due to the presence of paracrystallinity in these films. This can be further substantiated from the observation of line broadening in the WAXS patterns of especially produced film six from high solution concentration. The biaxially expanded films on the other hand, show WAXS patterns indicating more or less continuous Debye rings of uniform intensity which are sharper especially for annealed sample eight (see Figure V-34a). These seem to be also consistent with sharp and narrow enothermic peaks seen in the DSC thermograms of these biaxial films.

The DSC trace of annealed sample eight also exhibits a remarkable feature which is not seen for original unannealed film seven (compare Figure V-41 to V-42). The absence of the exothermic peak as a consequence of further crystallization during the DSC experiment together with a sharper WAXS pattern seen for the annealed sample eight clearly demonstrate an increase in crystallinity as a function of heat treatment. The heat of fusion of this sample increased from 27.45 to 37.3 J/g.

The uniaxially oriented films also exhibit interesting SALS patterns. The H_v patterns of film 2 exhibits a rather weak two lobe horizontal scattering. This is concentrated and more pronounced in film four and becomes narrower for film six. Samuels (156) has studied the SALS patterns for water cast in HPC film. He explained that the undeformed film has a four lobe H_v SALS pattern and by extending the film the vertical lobes spread and eventually split in two while horizontal lobes draw out and narrow. Stein (226), Hayashi et al. (227) and Hashimoto et al. (228) have interpreted these transitons in terms of anisotropic rod-like elements. The scattering from an assembly of randomly oriented rods will give a four lobe symmetric H_v pattern. This explanation may be applied to isotropic film one, where the H_v SALS pattern of this sample is a four lobe pattern (see Figure V-45b). Moreover, the WAXS pattern of this film is also isotropic. They also added that the oriented structure domains formed by anisotropic rods will give rise to horizontal two lobe H_v pattern. This interpretation may also be applied to the uniaxially drawn films. However, the SALS patterns of uniaxially oriented films show a similar transition as described by Samuel (156).In the case of biaxially oriented films, H_v SALS patterns exhibit a circularly symmetrical shape which are similar to the patterns obtained by Liang (229)

for HPC films. These very strong scattering patterns are probably due to the crystallinity present in these films.

The WAXS patterns qualitatively exhibit development of approximately biaxial orientation in expanded films one, three, five, seven, and eight. This is particularly seen from further WAXS patterns of hydrolyzed films (see Figure V-33 and V-34). Uniaxial orientation is also clearly seen from WAXS patterns of films two, four and six. This is further substantiated after hydrolysis of uniaxial film six. In order to better understand the crystal structure and orientation development during processing of these film, an attempt was made to characterize such features using WAXS pole figures and orientation functions. It was found that the intensity of WAXS reflections were not strong enough to give sharp 2θ scans. Thus we have concluded that such an analysis would not be possible in this case. Though the orientation of the films were obtained from birefringence measurements.

Three uniaxial films exhibit birefringence where; $\Delta n_{13} \simeq \Delta n_{12} > \Delta n_{23}$. While the biaxially expanded films which showed a change in birefringence order where; $\Delta n_{13} \simeq \Delta n_{23} > \Delta n_{12}$. It is clearly seen from these observation that the film one, three, five, seven, and eight are approximately biaxially oriented as it was

qualitatively seen from WAXS patterns. The birefringence are higher for biaxially expanded films for given solution concentration compared to uniaxially drawn films. As solution concentration increases the birefringence increases also. Although all the films did not exhibit very high levels of birefringence the mechanical properties obtained for biaxially expanded film are fairly comparable with those reported elsewhere (230). This low birefringence may be related to the intrinsic birefringence of CTA film. However, Onogi, White and Fellers (127) estimated the intrinsic birefringence of hydroxypropylcellulose (HPC) as 0.038. An attempt also was made to estimate the intrinsic birefringence of CTA films following the procedures given by (127, 235), but due to lack of information available in the literature for the crystal structure and complication in chain configuration of CTA we were also unable to proceed with such an evaluation.

The commercial film from Celanese Fiber Company did not show any birefringence. Removing the plasticizers (triphenyl phosphite) from the commercial film increased the modulus, decreased the elongation alot and the tensile strength slightly. As indicated earlier, the mechanical properties will be discussed in the next chapter. However, in general, the voids resulted as a consequence of the

extraction of the triphenyl phosphite additive from the commercial film were consistent in SEM, SAXS and density measurements.

CHAPTER VI

MECHANICAL PROPERTIES OF THE FILMS

The mechanical property results are summarized in this chapter. Tensile strength, tangent modulus, and elongation to break are discussed separately for PPTA and CTA films. A general comparison including the mechanical properties of PPTA films to those of CTA films is explained in the next chapter.

A. PPTA Films

Figures VI-1,VI-2 and VI-3 give typical stress-strain curves for extruded, uniaxially drawn, and biaxially expanded films respectively. The values for tensile strength, modulus and percent elongation calculated from the stress-strain plots are presented in Table VI-1.

Figure VI-1 indicates a variation in tensile strength, tangent modulus and to some extent, elongation to break as a function of film direction for extruded sample 1. Both modulus and tensile strength are greater in the machine direction than the transverse direction. Elongation to break for this film is low indicating the brittle nature of this specimen. There is no appearance of any yield point in this stress-strain curve and this film

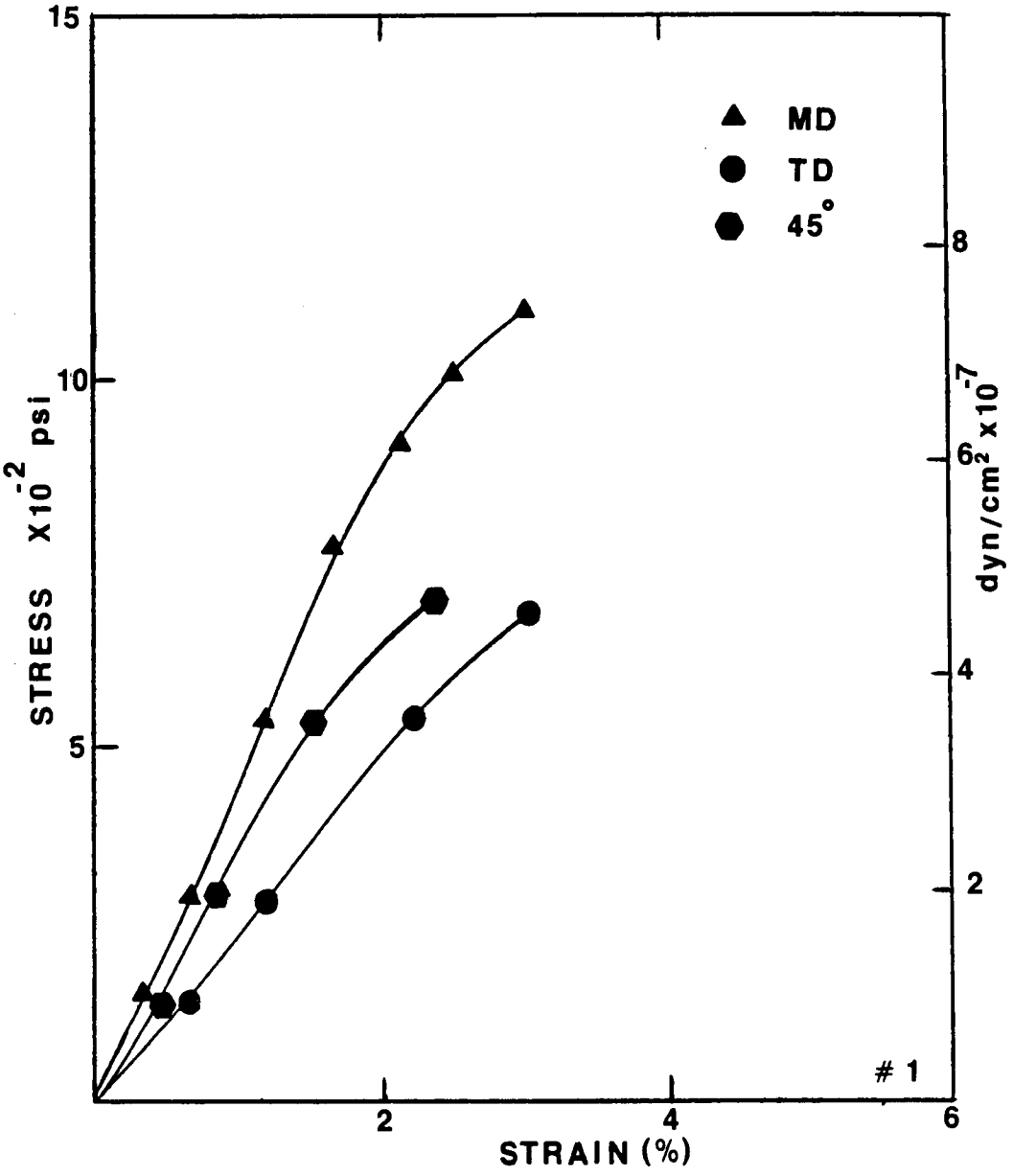


Figure VI. 1. Stress-strain curves for film 1 as a function of film direction.

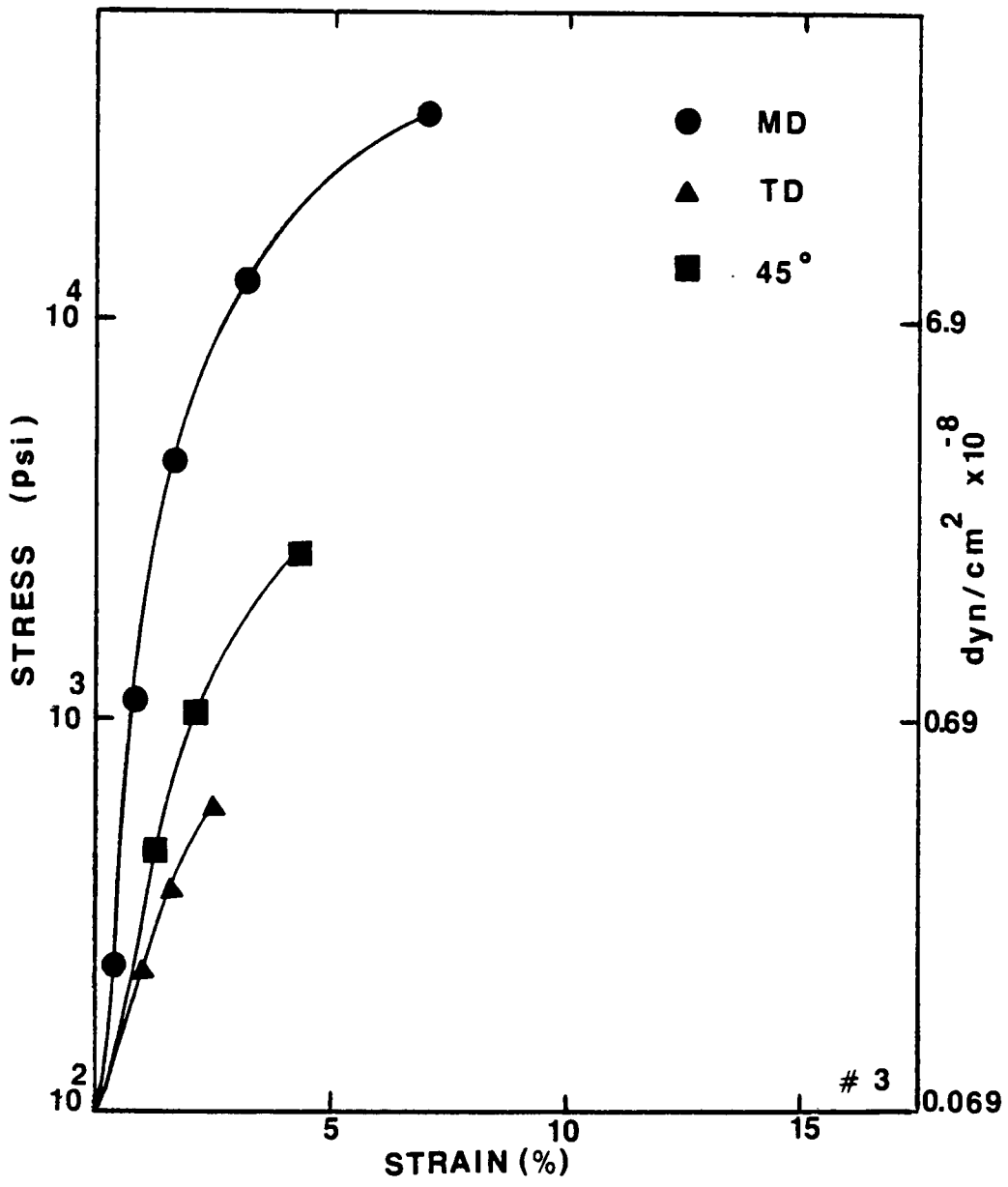


Figure VI. 2. Stress-strain curves for film 3 as a function of film direction.

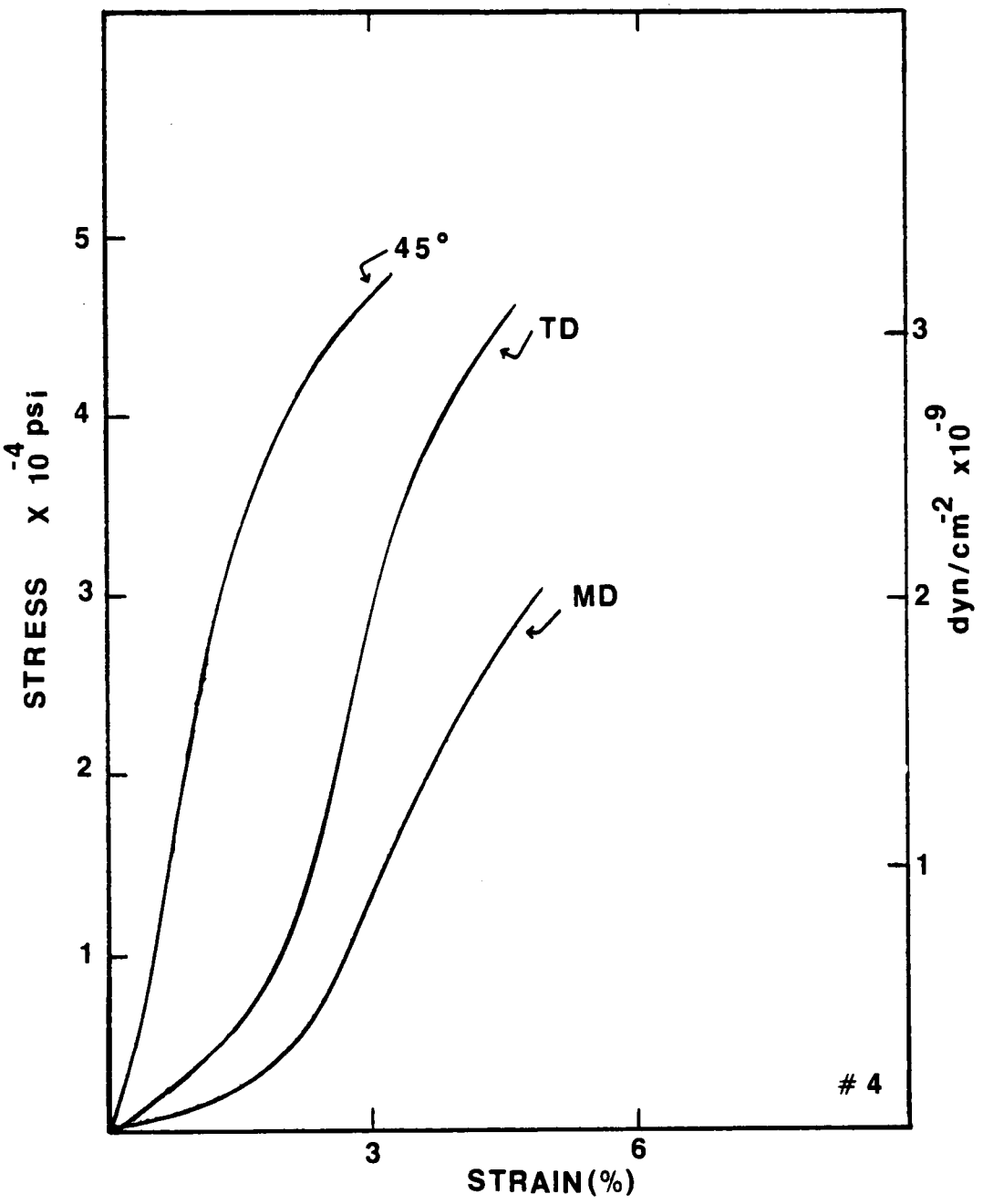


Figure VI. 3. Stress-strain curves for film 4 as a function of film direction.

TABLE VI.1. MECHANICAL PROPERTIES OF PPTA FILMS

Sample No.	Young's Modulus (dyn/cm^2)x10^{-10}			Tensile Strength (dyn/cm^2) x10^{-9}			Percent Elongation to Break		
	MD	45°	TD	MD	45°	TD	MD	45°	TD
1	0.68	0.09	0.05	0.08	0.05	0.04	3.0	2.7	3.0
2	2.0	0.93	0.67	1.4	0.12	0.06	10	3.8	7.0
3	4.5	0.40	0.08	2.3	0.18	0.04	7.0	3.2	2.0
4	1.3	3.0	2.7	2.24	3.3	3.2	4.4	3.2	4.2
5	2.3	2.3	0.98	3.8	3.9	3.7	4.0	3.3	4.0

also shows brittle fracture in all three directions.

Figure VI-2 shows stress-strain curve for uniaxially drawn film 3. It is apparent from these figures that there is a large variation in tensile strength and modulus as a function of film direction. Both tensile strength and modulus are much greater in the machine direction than the transverse direction. Percent elongation at break does not show a consistent pattern in terms of film direction. Thus it does indicate the relatively brittle nature of the film in all directions. This figure also does not show any distinct yield point and once again the brittle fracture can be observed in all three directions of the uniaxially drawn film.

Figure VI-3 is for biaxially expanded film four (mandrel processed film). It is clear from this stress-strain plot that the failures in all directions of the film are brittle fractures. The breaking strength and modulus are more or less in the same order for all three directions of the film. A remarkable increase in breaking strength and modulus are observed as a function of annealing (see Table VI-1), there is not a significant change in elongation to break.

Initial Modulus

Plots of initial modulus as a function of film direction are shown in Figure VI-4 and VI-5 for film 1-5. The modulus values may also be seen in Table VI-1. The general shape of the plots for films 1-3 is an oval, with the long axis in the machine direction. It can be seen from Figure VI-4 that as the drawdown ratio increases the machine direction elastic modulus increases. The undrawn film one exhibits modulus values of 6.8×10^9 dyn/cm^2 in the machine direction versus 5.3×10^8 dyn/cm^2 for the transverse direction. The uniaxial low drawdown film 2 has twice the modulus in the machine direction as in the transverse direction. Film 3 exhibits an order of magnitude greater machine direction initial modulus than for film 2, while the transverse direction initial modulus of this film is much smaller than that of the uniaxial low drawdown film 2 (see also Table VI-1).

Figure VI-5 gives the modulus for the mandrel processed film four and annealed film five. The general shape of these plots seems to be round as compared to oval for the uniaxial films. The machine direction tensile modulus of biaxially expanded film four is lower than that of the transverse direction. This is opposite for annealed film five, where the transverse direction

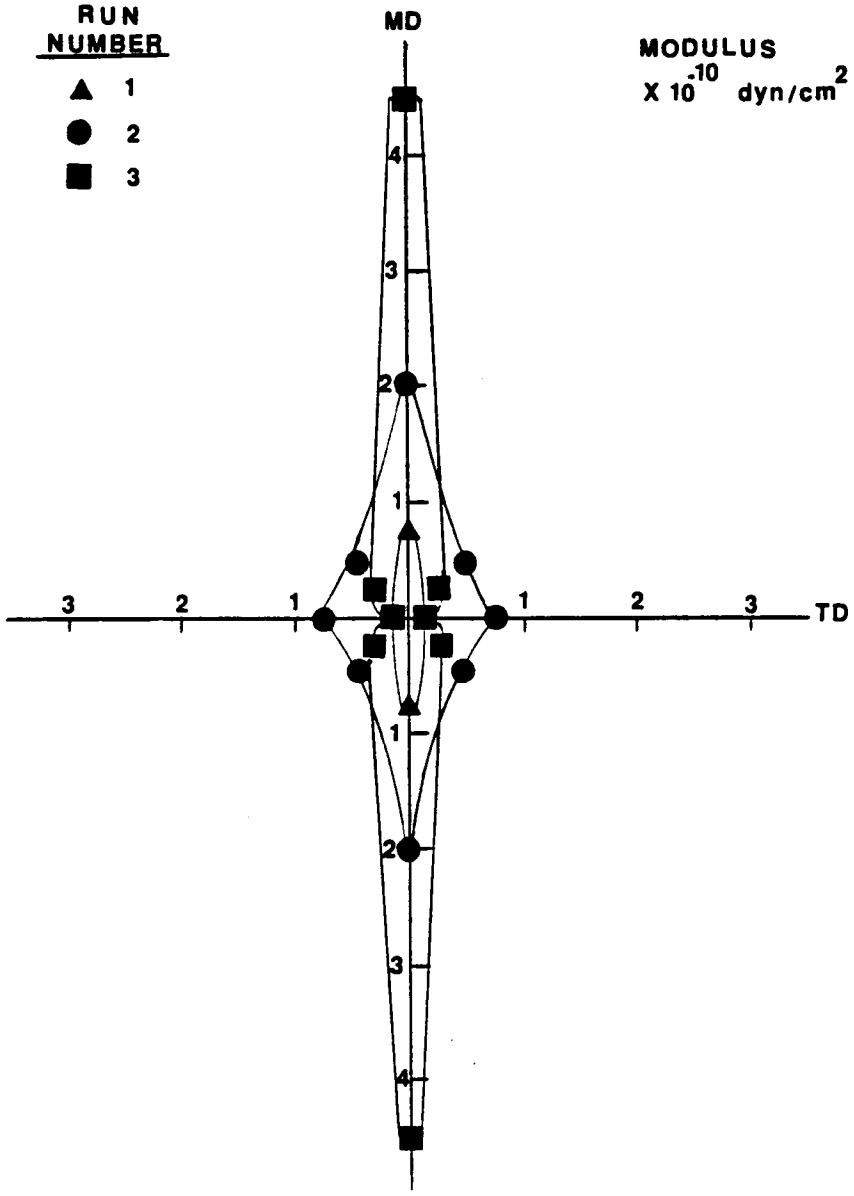


Figure VI. 4. Radial plots of modulus as a function of film direction for;
1. Extruded
2. Uniaxial low drawdown
3. Uniaxial high drawdown

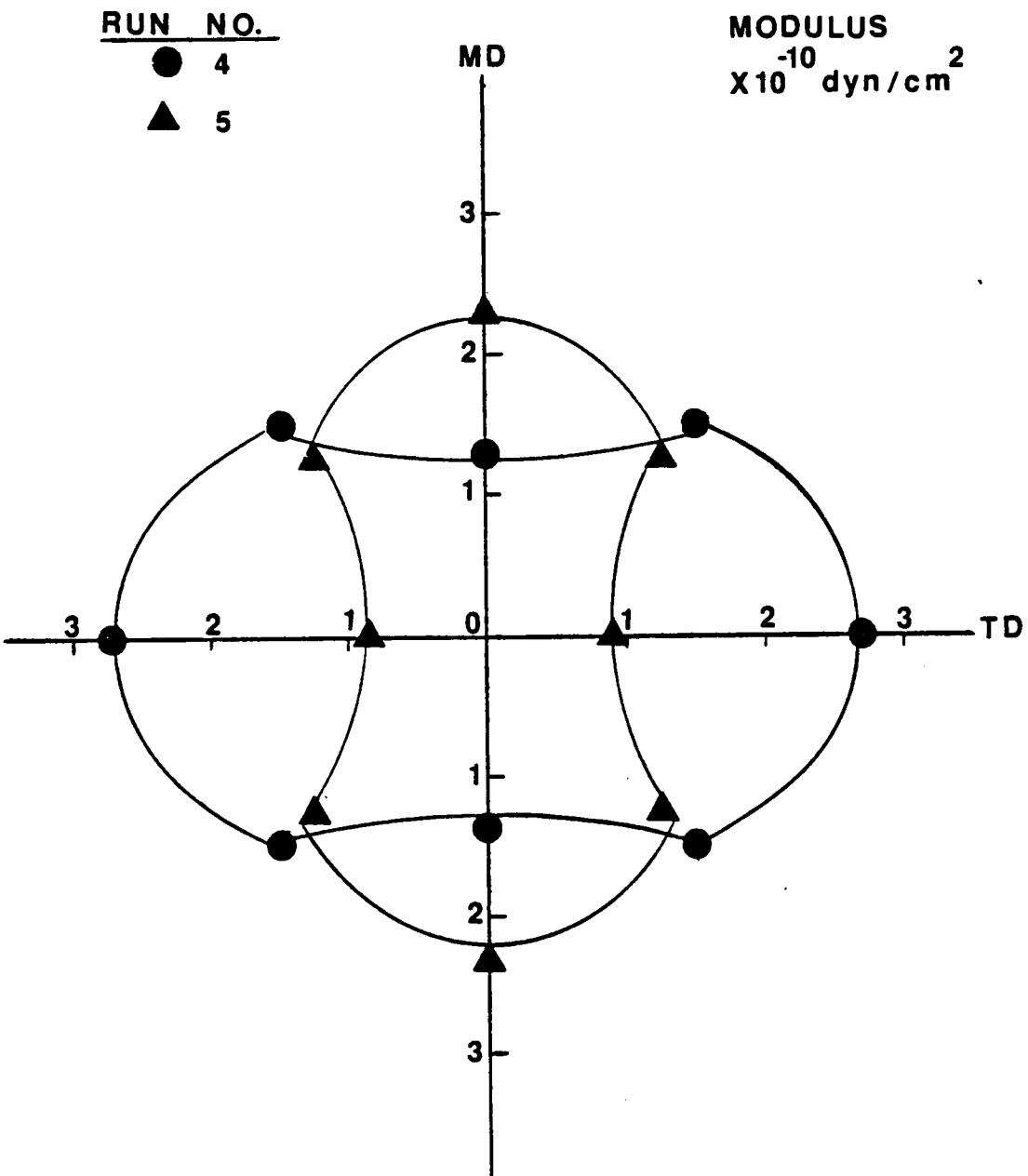


Figure VI. 5. Radial plot of modulus as a function of film direction for;
4. Mandrel processed
5. Annealed mandrel film

tensile modulus of this film is lower than that of the machine direction (see also Table VI-1). Since the modulus is expected to be the same in any direction of these films due to the biaxial orientation in them, these observation may be attribute to the experimental problems associated to the mechanical property measurements as a consequence of film thickness variation.All the films had some thickness variation. Biaxial film exhibited a greater degree of variation than either the uniaxially drawn or undrawn films. The mandrel processed films were always thicker in those sections extruded below the die entrance and thinner in those sections opposite the die entrance. Such a thickness variation therefore introduces some error into the initial modulus as well as the stress data. On the other hand, these data were obtained by averaging the results of three tests for each sample as was mentioned in Chapter III.

Tensile Strength

Radial plots of tensile strength versus film direction for all five films are shown in Figure VI-6 and VI-7. The values for tensile strength, modulus, and elongation to break are summarized in Table VI-1. The general shape of the plots for uniaxially drawn films two and three is also an oval, once again with the long axis in the machine

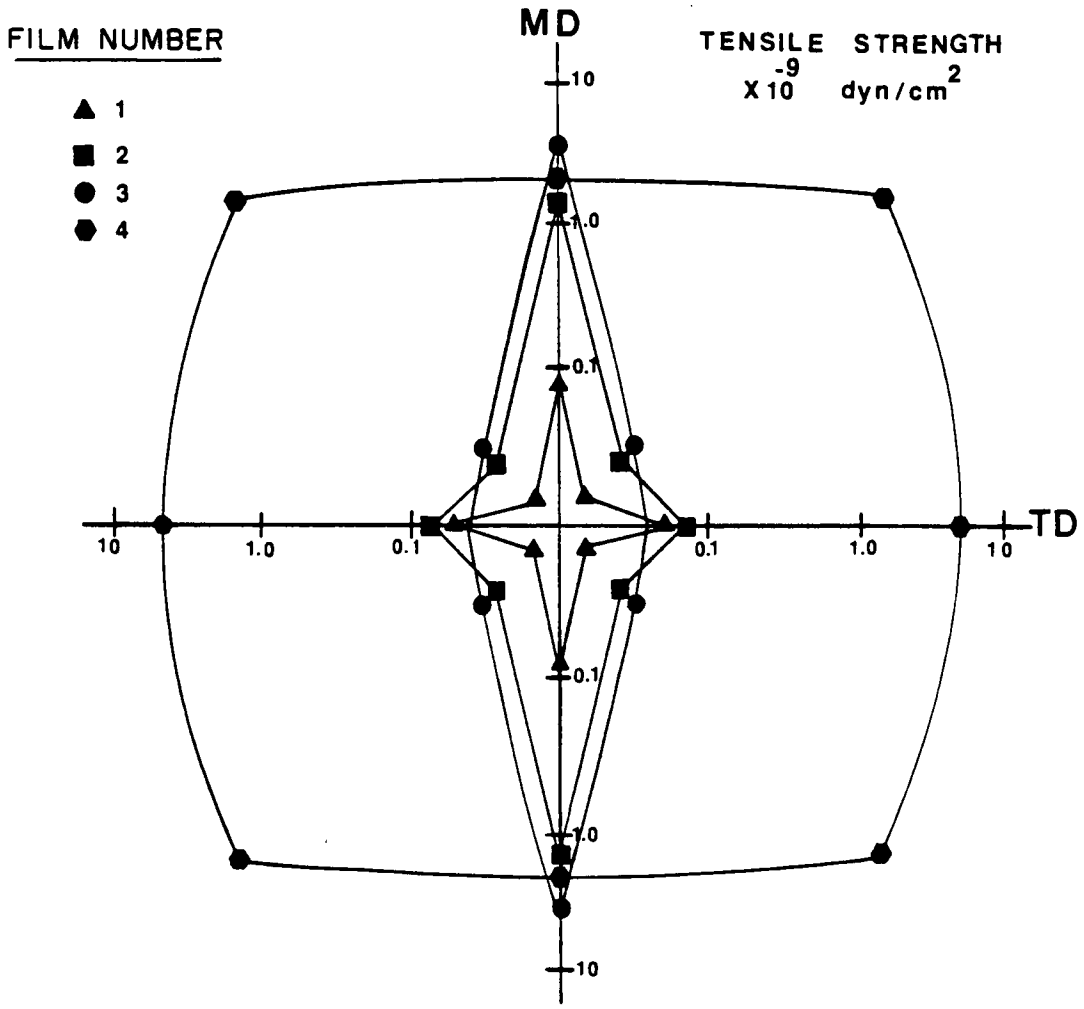


Figure VI. 6. Radial plots of tensile strength as a function of film direction for;
1. Extruded
2. Uniaxial low drawdown
3. Uniaxial high drawdown
4. Mandrel processed

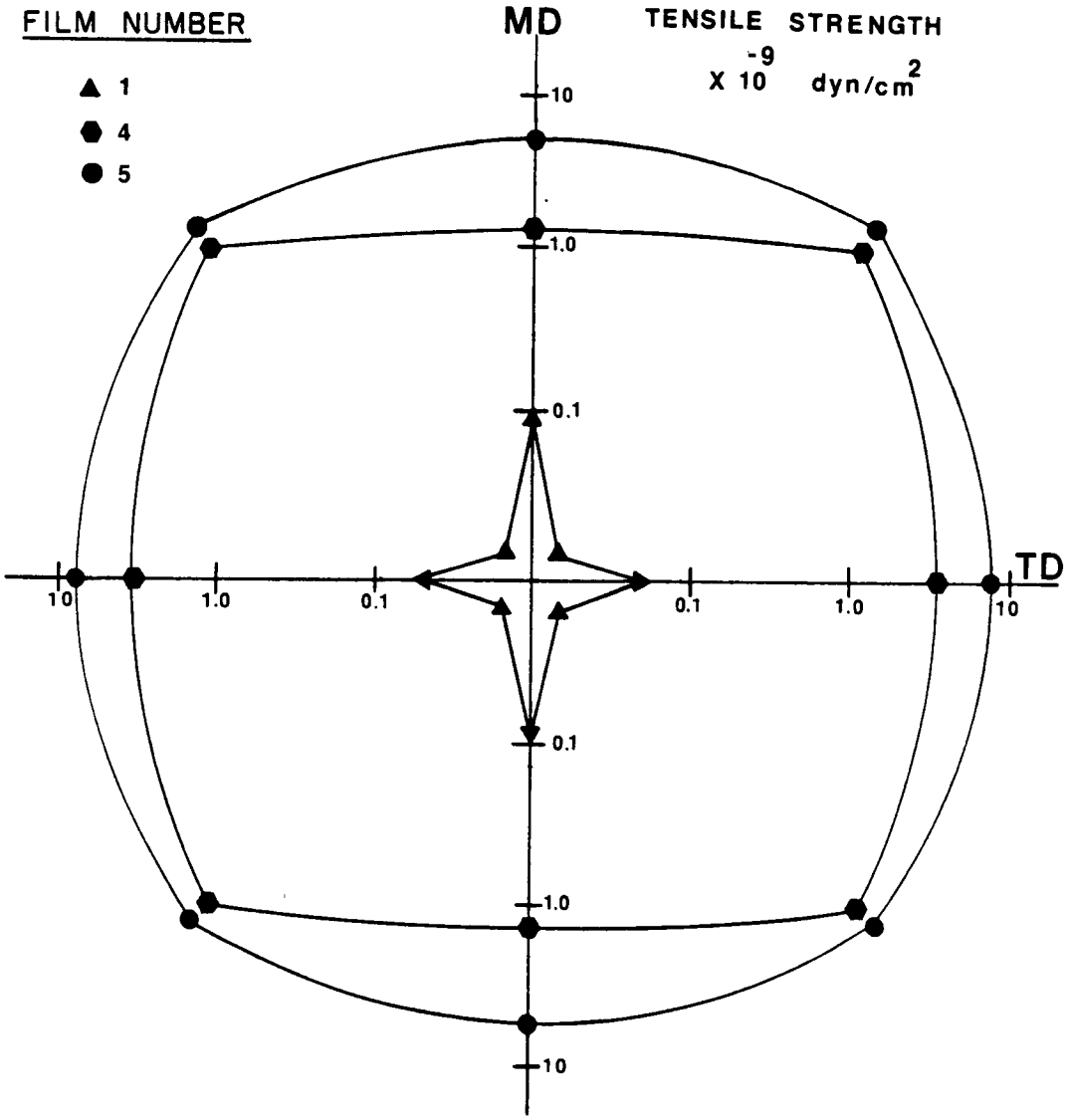


Figure VI. 7. Radial plots of tensile strength as a function of film direction for;
1. Extruded
4. Mandrel processed
5. Annealed mandrel films

direction. These plots are similar to the initial modulus plots, indicating uniaxial orientation in the machine direction. The extruded film one has twice the tensile strength in the machine as in the transverse direction. The uniaxially drawdown films two and three exhibit an order of magnitude greater machine direction tensile strength than for the extruded film. The transverse direction tensile strength is about the same.

It should be noted that extruded film one exhibits tensile strength in the 45° direction less than that of the transverse direction.This gives a star shape to the plot. This phenomenon is also the opposite of what would be expected and may be due to some internal flaw which shows up only on the 45° samples. Moreover, there is also an experimental problem associated with undrawn films; an extreme amount of wrinkling occurs in the machine direction upon drying. These wrinkles can be seen from the SEM photomicrographs of this film in Chapter IV. However, this makes measuring average thickness difficult and further, the wrinkles pull out slightly under the load leading to some expected error during these evaluations. The wrinkles together with the voids present in this film (see Figure V-1 page 192) act as defects which result in early failure.

The mandrel produced film four has about the same

machine direction tensile strength as the uniaxially drawn film (see Table VI-1). The transverse direction tensile strength for this film is slightly higher than the machine direction value. It is an order of magnitude higher than that of extruded and drawdown films. The annealed mandrel fabricated film five exhibits the same tensile strengths in the machine and transverse directions, which are remarkably higher than the results for initial film.

However, the general shape of the tensile strength plots for biaxially expanded film four and five is round as compared to oval for the uniaxial films. This may indicate that the orientation in these films is the same in all direcions.

Percent Elongation to Break

Percent elongation to break did not show a consistent pattern in terms of film direction, though plotting percent elongation as a function of film direction were not done for any of the films. However, the percent elongation values for all the films can be seen from the Table VI-1. In all but one case the percent elongation was no higher than seven percent and is as low as two percent. Extruded film one shows an elongation to break about the same in all three directions. Uniaxial drawdown films two and three have similar

elongations to break in the 45° angle direction while film three exhibits values in both machine and transverse directions as compared to film two. Both biaxially expanded film four and five show elongation to break of about 4 percent in all directions.

Discussion

The mechanical properties of the films are similar to those reported by Flood, et al (63). Extruded film has poor mechanical properties compared to the other films; see Table VI-1. As was seen in the orientation functions, WAXS pattern, and pole figures, the degree of orientation of this film is much lower than either the uniaxially drawn films or biaxially expanded films.

The uniaxially drawdown films are highly anisotropic especially with regard to tensile strength. The highest values obtained were for film three where the tensile strength is 2.3×10^9 dyne/cm^2 and modulus is 4.5×10^{10} dyne/cm^2. Obviously, these values are much smaller than those reported for Kevlar^R 29 fibers. Kevlar 29 in the fiber form has a tensile strength of 36×10^{10} dyne/cm^2 and a modulus of 8.3×10^{11} dyne/cm^2. These differences may partially be due to conditions that would not allow the film to be drawn as highly as the fibers, since no air gap was present as in the fiber process. Another

possibility could be due to the degradation in the films during processing or after coagulation.

Comparing the mechanical properties of uniaxially drawn film two and three to the extruded or undrawn film one sees a dramatic difference in tensile strength and modulus as a function of drawdown ratio. As the drawdown ratio increases both tensile strength and modulus increase in the draw or machine direction. The transverse direction properties are very weak for all three cases;see Table VI-1.

The uniaxial character of films two and three as demonstrated by the orientation functions, pole figures, and WAXS patterns is supported by the mechanical properties, where relatively high strength in the machine direction indicate of c-axis orientation in the stretching direction and low strength in the transverse direction.

The films produced on the mandrel have approximately equal mechanical behavior in all directions. The general level of properties achieved in the mandrel film (sample four) is superior to those reported by Flood (63). However, the mechanical properties of this film compared fairly well with orientation functions, pole figures,and WAXS pattern. Tensile strengths are relatively uniform in all directions indicative of biaxial orientation, The modulus is somewhat higher in the transverse direction of this film.

A substantial improvement in mechanical properties was achieved by heat treatment at 350°C. This corresponds to the results of Kwolek (102) and later investigators of PPTA fibers. The procedures of these investigators involved much higher temperatures for shorter periods. One notices the improvement observed in this study can be rationalized from the increased orientation and greater density of annealed film five versus original unannealed film four. This points out the importance of not only the character of the fluid stresses just prior to coagulations but also the need to study thermally enhanced structural changes in the solid state.

B. CTA Films

Figures VI-8 and VI-9 show typical stress strain behavior for the uniaxially drawn and biaxially expanded films respectively. The tensile modulus, tensile strength, and elongation to break of all CTA films in the machine, transverse and 45 degree angle are summarized in Table VI-2.

Uniaxially drawdown films, as indicated in the stress strain curves in Figure VI-8, exhibit variation in tensile strength, modulus, and elongation at break as a function

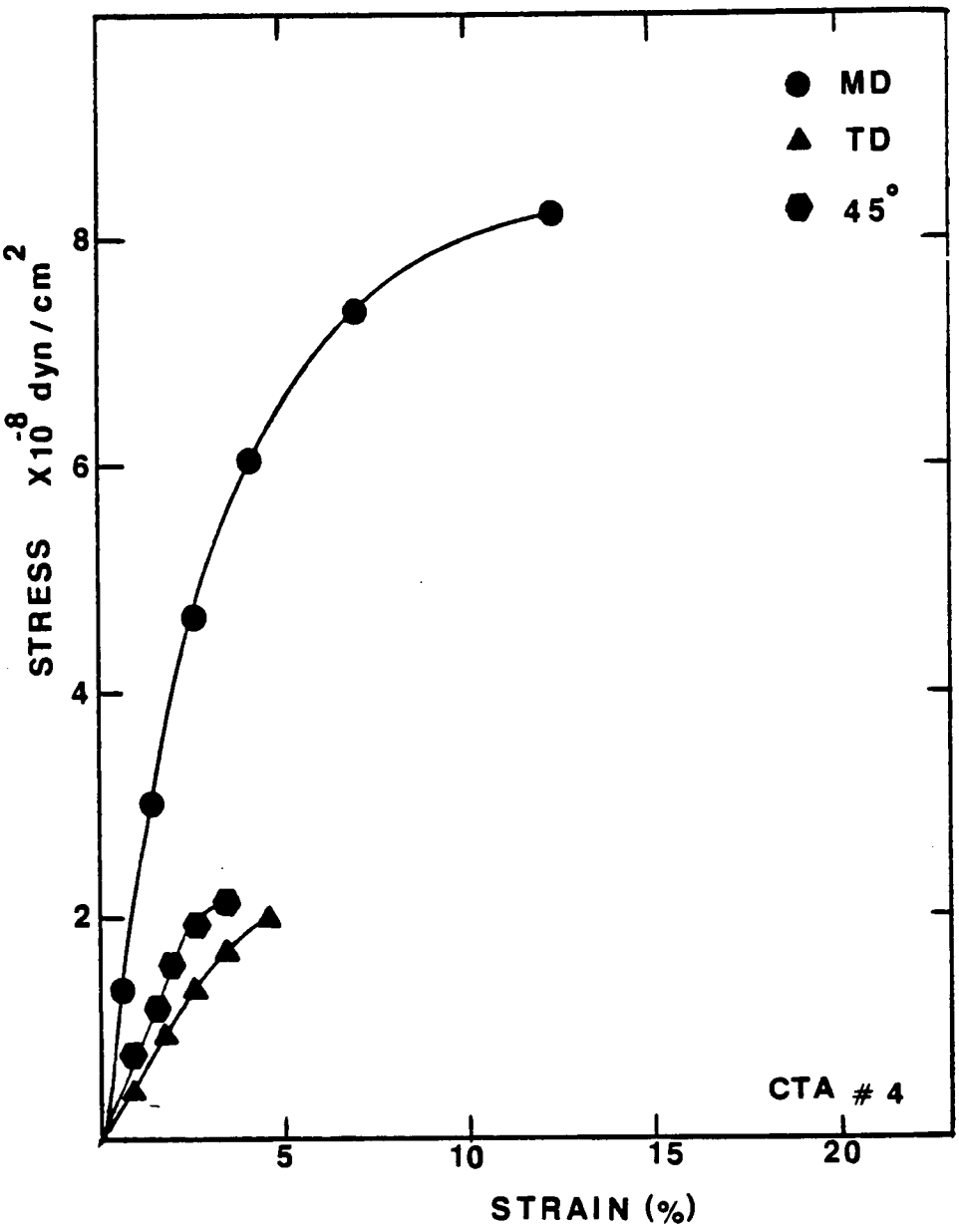


Figure VI. 8. Typical stress-strain curves for uniaxially drawn films as a function of film direction.

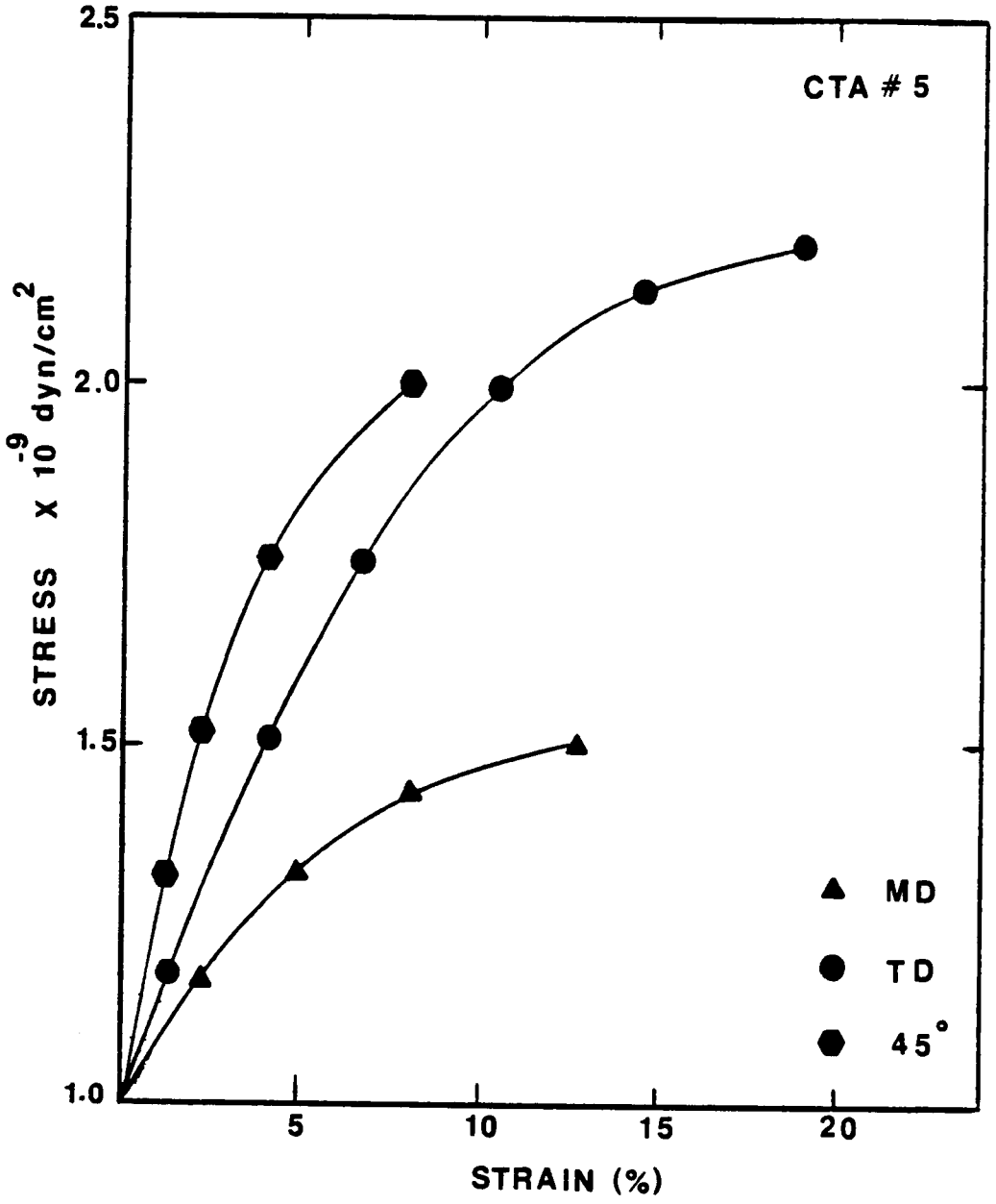


Figure VI. 9. Typical stress-strain curves for biaxially expanded films as a function of film direction.

TABLE VI·2. MECHANICAL PROPERTIES OF CTA FILM

Sample No.	Mean Thickness (nm)	Young's Modulus $\times 10^{9}$ (dyn/cm^2)			Tensile Strength $\times 10^{8}$ (dyn/cm^2)			Percent Elongation		
		MD	45°	TD	MD	45°	TD	MD	45°	TD
1	0.11	10	12	10	8.0	8.1	7.7	10	9.1	11
2	0.19	4.2	2.5	2.3	3.1	1.2	3.3	25	15	24
3	0.07	14	14	13	9.0	9.3	9.7	9.5	10	12.5
4	0.13	9.1	6.9	6.8	8.2	1.8	2.0	12.5	3.5	4.5
5	0.04	18	23	20	15	20.	22	12.5	8	19
6	0.12	4.9	7.2	9.3	7.5	3.0	2.5	13	3.1	4.0
7	0.04	13	29	25	18	17.5	14	11.5	5.0	7.5
8	0.04	60	60	63	31	30	24	6.5	3.2	5.0
9	0.05	16.9	16	15.2	10.3	9.1	9.6	18.1	13	17.3
10	0.05	29.3	28.2	29.3	9.4	8.5	8.8	5.8	4.8	5.2

of film direction. The tensile strength is much greater in the machine direction than both the transverse and 45° angle. Percent elongation at break is almost three times higher in the machine direction than transverse direction and 45° angle. The shapes of the curves for all three directions do not indicate well defined yield points, though they end in brittle failures.

Biaxially expanded films also reveal variation in tensile strength, modulus, and percent elongation (see Figure VI-9). Breaking strengths range from 7.7×10^{8} (isotropic film) dyne/cm^2 to 22×10^{8} dyne/cm^2 (anisotropic film) with no great loss of strength in any direction. Modulus values ranged from 10×10^{9} for isotropic film to 25×10^{9} dyne/cm^2 for an anisotropic film. A remarkable increase in breaking stress and modulus is observed as a function of annealing (see Table VI-2).

Percent elongation to break goes from three percent to about 25 percent. There is no appearance of any distinct yield point, and all the failures are brittle fractures.

Initial Modulus

Plots of initial modulus as a function of film direction for film one through four are shown in Figure VI-10. The general shape of the plots for uniaxial

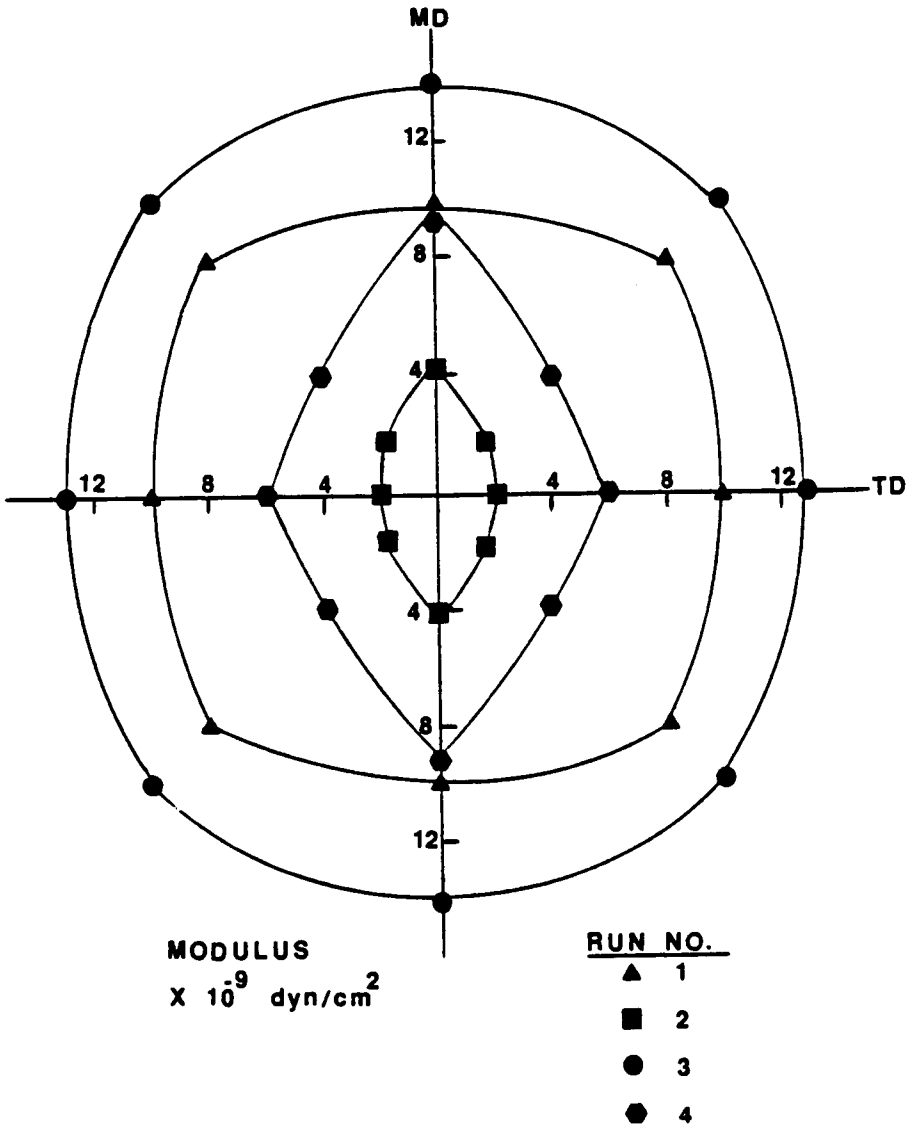


Figure VI.10. Radial plots of modulus as a function of film direction for films 1 to 4.

films two and four is an oval with the long axis in the machine direction. Both films have approximately twice the modulus in the machine direction as in the transverse direction. Uniaxial film six has almost the same values for modulus as compared to film four (see Table VI-2). However both film four and six exhibit an order of magnitude greater tangent modulus than for film two.

The biaxially expanded films one and three produced from 23 and 25 percent concentration respectively, exhibit isotropic moduli as a function of film direction. The general shape of these plots is round as compared to oval for the uniaxial films. The modulus of isotropic film one is 10 x 10^9 dyne/cm^2 in both machine and transverse direction. The modulus in the 45 degree angle of this film is 12 x 10^9 dyne/cm^2. The modulus for all three directions of film three produced from 25 percent concentration are higher than those of film one. These are 14 x 10^9 dyne/cm^2 in both 45 degree angle and machine direction and 13 x 10^9 dyne/cm^2 in transverse direction. The modulus data for films five and seven including annealed film eight are shown in Figure VI-11 and also Table VI-2. Film five and seven produced from 28 and 30 percent concentration exhibit much higher modulus than film one and three. This indicates that the modulus seem to increase as solution concentration is increased. The

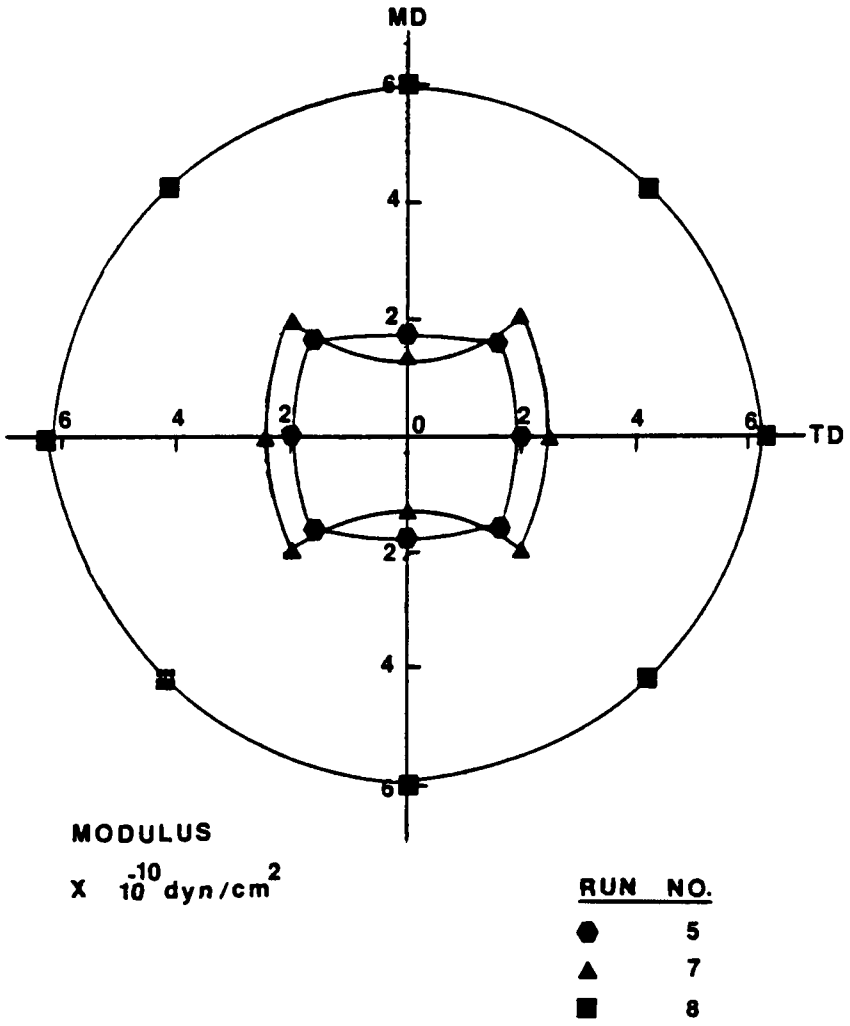


Figure VI.11. Radial plots of modulus as a function of film direction for films 5, 7, and 8.

annealed film shows a significant increase of modulus in all directions as compared to original unannealed film seven.

Figure VI-12 summarizes the modulus of commercial casted film nine and methanol treated film ten versus film direction. Removing the plasticizers (triphenyl phosphite) from the commercial film increased the modulus as shown in this figure.

Tensile Strength

Radial plots of tensile strength versus film direction for CTA films are shown in Figure VI-13 through VI-15. The values of tensile strength may also be seen from Table VI-2. The general shape of the plots for uniaxial film four is an oval, once again with the long axis in the draw direction. This film produced from 28 percent concentration exhibits four times the tensile strength in the machine direction as compared to the transverse direction (see Figure VI-13 and Table VI-2). The results for uniaxial film six are not drawn in these figures, since they were very similar to the values obtained for film four. However, as it is apparent from Table VI-2, film six (30 percent concentration) has three times the tensile strength in the machine direction as in transverse direction. The film two (25 percent

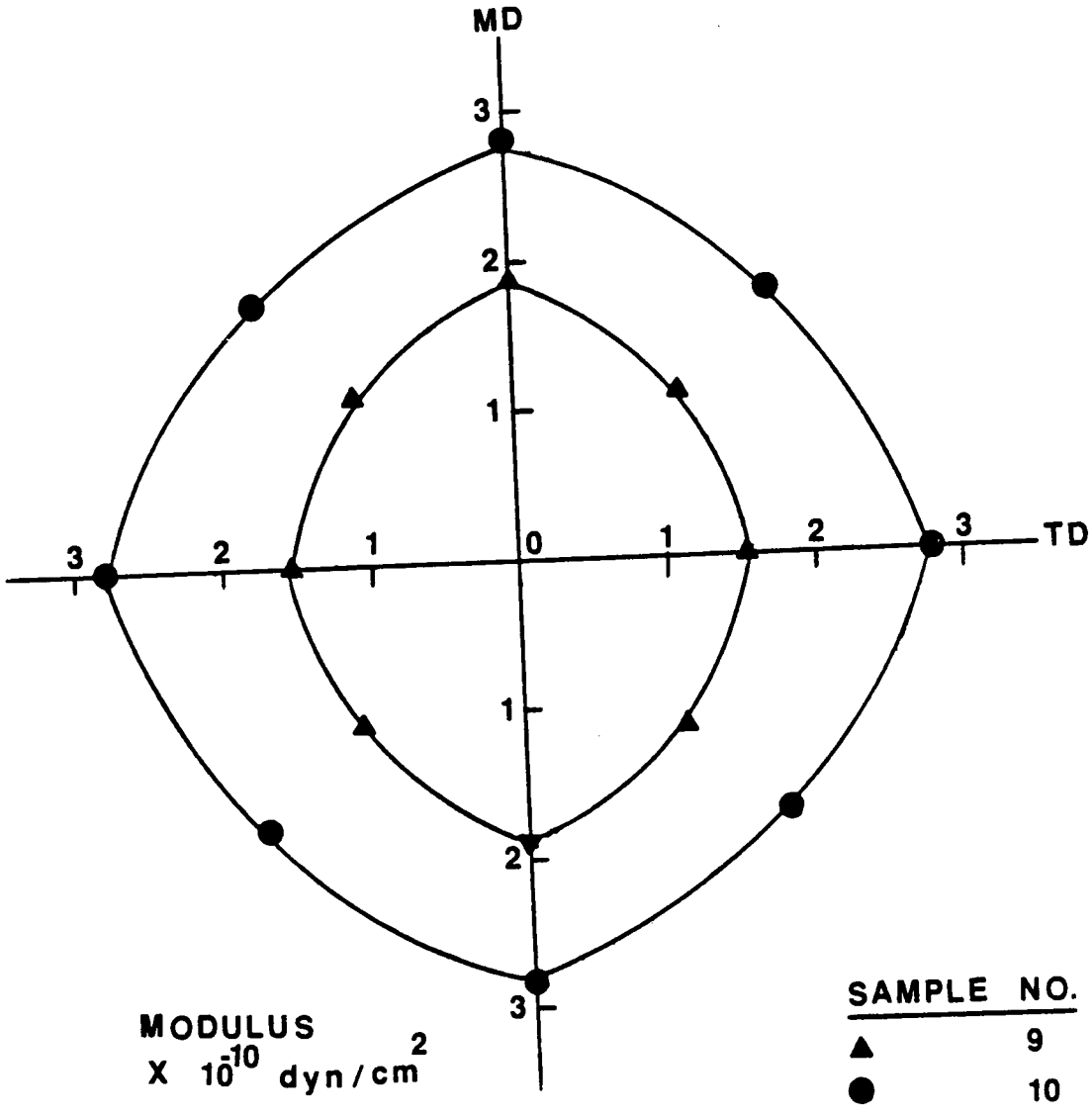


Figure VI.12. Radial plots of modulus as a function of film direction for films 9 and 10.

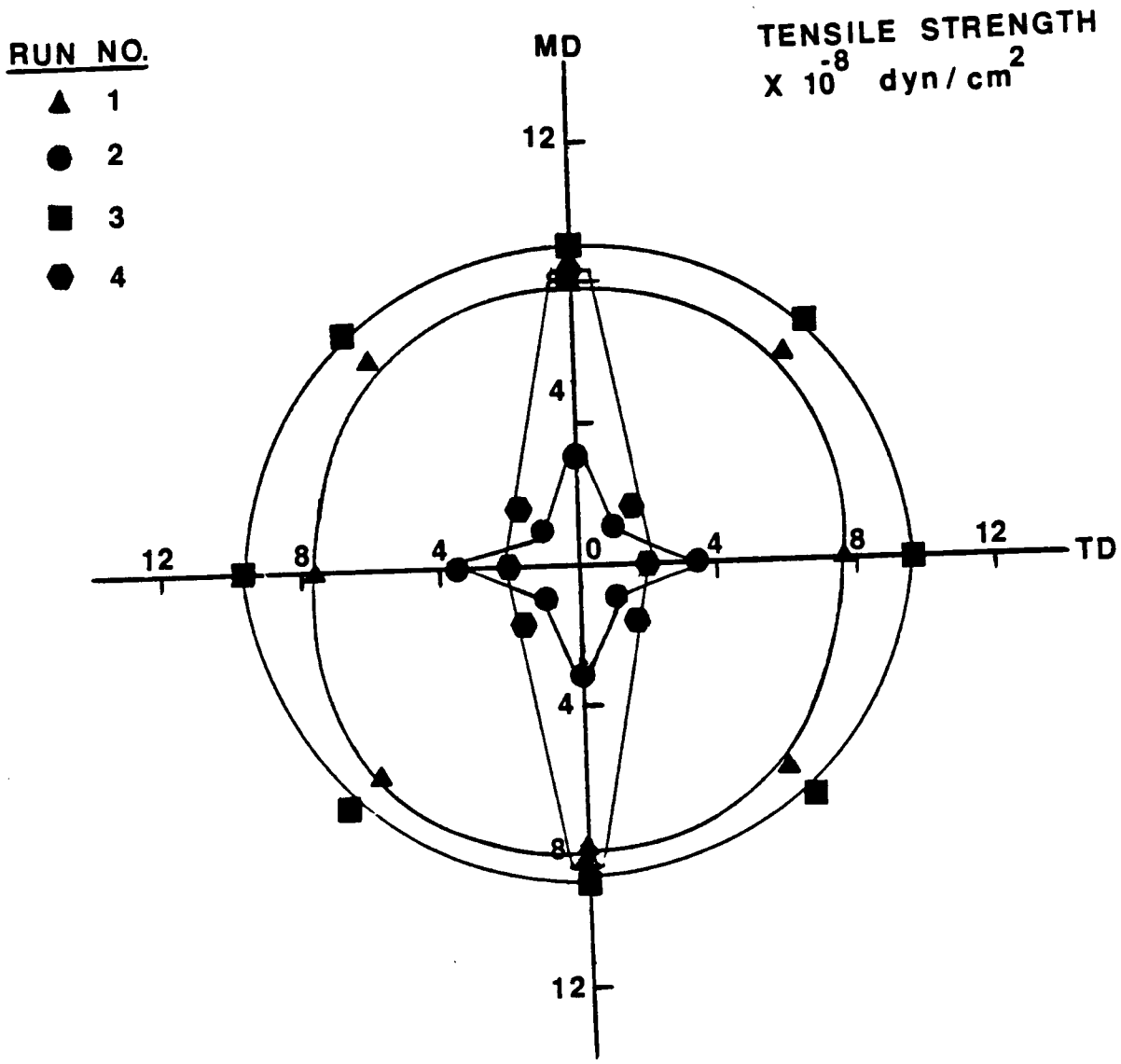


Figure VI.13. Radial plots of tensile strength as a function of film direction for films 1 to 4.

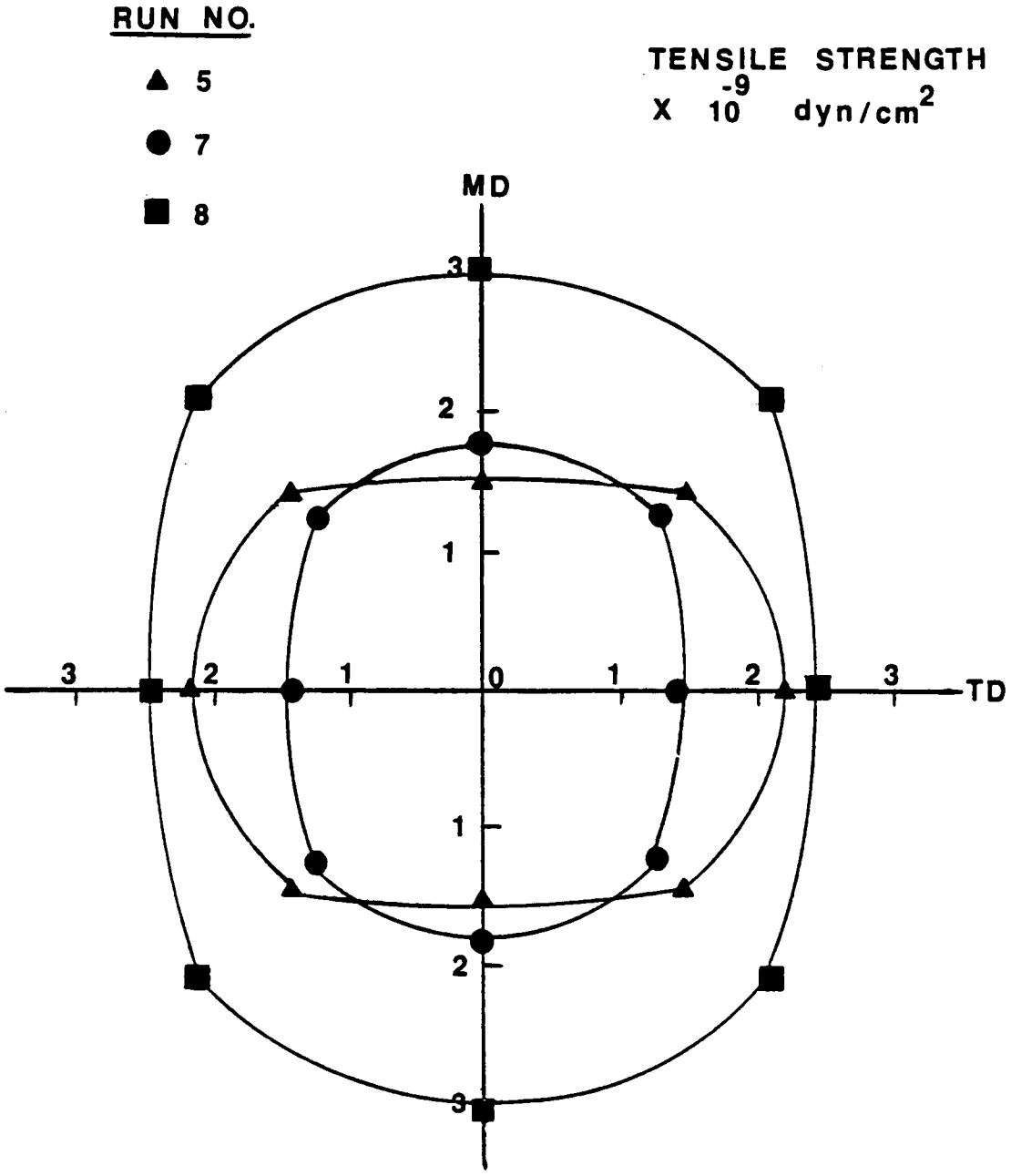


Figure VI.14. Radial plots of tensile strength as a function of film direction for films 5, 7, and 8.

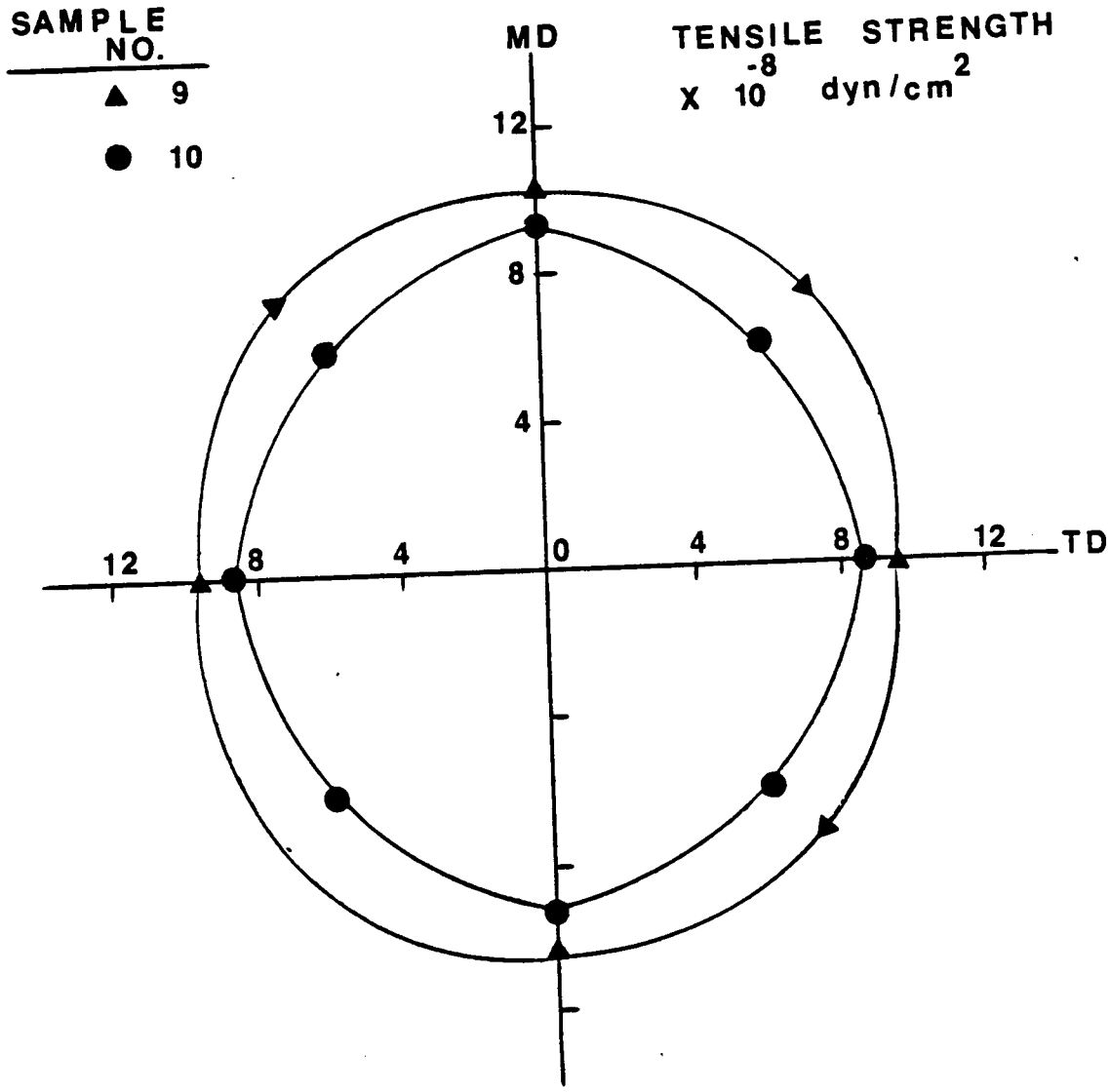


Figure VI.15. Radial plots of tensile strength as a function of film direction for films 9 and 10.

concentration) somewhat did not show any preferred tensile strength in any direction (see Figure VI-13). This is probably due to the fact that this film is the thickest among other films and also exhibits a very low level of orientation (see Table V- 6).

Biaxially expanded film one exhibits almost the same tensile strength in all directions. The biaxial film three (25 percent concentration) also shows about the same strength in all directions, but these are higher than those of isotropic film one (see Figure VI-13). Figure VI-14 exhibits the results for biaxial films five, seven, and heat treated film eight. The general shape of these plots again is almost round as compared to the oval shape seen for uniaxial films. Here, the biaxial film five (28 percent concentration) shows somewhat higher strength in the transverse direction than for the film seven (30 percent concentration). This is reversed in comparison of the machine direction tensile strengths of these samples, where film seven has higher machine direction strength than film five. The annealed sample eight shows a substantial improvement in tensile strength in all three directions.

The effect of the extraction of triphenyl phosphite additive from the commercial casted film nine on the tensile strength is appeared from Figure VI-15. The

tensile strength decreased from 10.3, 9.1, 9.6 dyne/cm^2 to 9.4, 8.5, 8.8 dyne/cm^2 for machine, 45° angle and transverse directions respectively.

Elongation to Break

Table VI-2 gives the values of percent elongation to break for the films. These ranges from three to 15 percent for 45 degree angle and three to 25 percent in both machine and transverse directions.The uniaxially drawn film two (25 percent concentration) shows similar elongation to break in both machine and transverse directions. Percent elongation in the 45 degree angle direction of this film is much smaller than those of machine and transverse directions.

Film four and six produced from 28 and 30 percent concentrations exhibit about three times higher elongation to break in the machine direction than the transverse direction. The percent elongation in 45 degree angles for these films are slightly smaller than those of transverse directions.

Biaxially expanded films one and three show elongation to break about the same in all three directions. Films five and seven exhibit much smaller values in 45 degree angle as compared to machine and transverse directions.

A decrease in percent elongation may be seen as a function of annealing in all three directions of film eight. A substantial decrease in elongation to break is observed for methanol treated film ten. Removing the triphenyl phosphite from film nine resulted in a decrease from 18.1, 13, 17.3 percent to 5.8, 4.8, 5.2 percent for machine, 45° angle, and transverse directions of the film respectively.

Discussion

The mechanical properties of the films except heat treated film eight are similar to those of CTA films reported in the literature (230). The annealed film eight exceeds the mechanical property values of commonly available commercial films (see Table VII- 3). All biaxially expanded films have higher strength and modulus over uniaxially drawn films of given solution concentration. This significant difference is due to the slow coagulation of extruded films which would not allow the film to be drawn highly as compared to biaxially expanded films. The uniaxial films are thicker than the biaxially expanded films and have lower level of orientation (see Table V- 6 Page 301).

The uniaxially drawn films four and six produced from higher solution concentrations compared to uniaxial film

two are highly anisotropic especially with regard to the machine direction tensile strength. The highest values obtained for film four (28 percent concentration) where the machine direction tensile strength is 8.2×10^8 dyne/cm^2 and the machine direction modulus is 9.1×10^9 dyne/cm^2. Clearly, these values are much greater than those obtained for film two (25 percent concentration). Uniaxial film two has a machine direction strength of 3.1×10^8 dyne/cm^2 and the machine direction modulus of 4.2×10^9 dyne/cm^2. These differences are in good agreement with the birefringence results indicating increase of both tensile strength and modulus as a function of solution concentration. It is also important to note that the uniaxial film six did not show any increase in tensile strength and modulus compared to film four. This may be due to the presence of defective voids within this film as was seen in SEM, SAXS, and density data.

The biaxially expanded films have approximately equal mechanical behavior in all directions. The mechanical properties of these films compared fairly well with the WAXS patterns and birefringence.

A substantial improvement in mechanical properties were achieved by heat treatment at 275 ^{o}C for 30 seconds. This can also be rationalized from the increased orientation, crystallinity and greater density of annealed film

eight versus orignal unannealed film seven.

Removing the triphenyl phosphite additive from the commercial film increased the modulus, decreased the elongation to break alot and the tensile strength slightly. There is little difference between machine (treated or untreated) and transverse direction in the commercial films nine and ten.

It should also be noted that the CTA films processed in the present study have an order of magnitude lower tensile strength and modulus as compared to those of CTA films reported earlier by Omatete et al. (216). The highest value obtained for annealed film eight with the tensile strength of 31×10^8 dyne/cm^2 and modulus of 63×10^9 dyne/cm^2 which are much smaller than the values reported by Omatete for CTA film produced from 30 percent concentration. This film is reported to have a tensile strength of 12×10^9 dyne/cm^2 and modulus of 28.5×10^{10} dyne/cm^2.

CHAPTER VII

COMPARISON OF CTA FILMS TO PPTA FILMS

This chapter attempts to draw the last two chapters together to make a general comparison between CTA films and PPTA films. The differences between processing conditions used to fabricate both the CTA and PPTA films are pointed out and the resulting film properties as a function of certain processing parameters which have substantial influences on the structure property relationship are discussed. The mechanical properties of both CTA and PPTA films are also compared to some available commercial films.

A. Processing Conditions

The PPTA films and CTA films were produced under processing conditions summarized in Table IV-1 (Chapter IV), and Table V-1 (Chapter V) respectively. Both the uniaxially drawn CTA and PPTA film were processed in a similar manner. The procedures used for producing biaxially expanded films were different as described in Chapter III. However, the die used for PPTA films recieved the polymer from the side. In this case, the films were always thicker in those sections extruded below the die entrance and

thinner in those sections opposite the die entrance. Unlike this, the die used for CTA films recieved the polymer solution from the top with other features ensuring adequate backpressure and resulted in production of CTA films with better uniformity.

The coagulation for PPTA films was relatively faster than CTA films. A fast coagulant (25 percent H_2O/75 percent MeOH) is more desirable for producing biaxial PPTA films. The reason for this is that a fast coagulant prevents the film from ripping and possible uniaxial drawing after it is drawn over the mandrel. On the other hand, the mandrel process is not applicable for producing biaxial CTA films. It was found by Omatete (216) that the coagulants used for CTA solutions do not extract the solvent fast enough to permit orienting the uniaxial film by stretching, or freeze-in the orientation imparted on the film extruded over the mandrel. The film would adhere together during take-up. Therefore, a blow-up recycling procedure as described in Chapter III was used. This process together with using a slow coagulant (isopropanol) allowed deformation and coagulation simultaneously during the expansion of CTA films. The coagulation temperature was also different for CTA films than that of PPTA films. PPTA films were coagulated at room temperature ($\simeq 26^{\circ}C$) while, the CTA films were solidified at about zero degree centigrade. The latter selection was

based on the studies by Knudesn (101), Panar and Wilcox (132) and Zwick and Van Bochave (212). These authors found that lowering the bath temperature (from about 26°C to zero or 5°C) result in improvement of the mechanical properties.

Extruded, uniaxially drawn and mandrel processed PPTA films were all produced from 17 percent solution concentrations. CTA films on the other hand, were prepared from concentrations ranging from 23 to 30 percent. The mandrel process resulted in PPTA film with a blow-up ratio of 3.3X. The blow-up recycle process has an advantage over the mandrel process in that various blow-up ratios can be applied to the film. Thus, biaxially expanded CTA films were prepared under various blow-up ratios (see Table V-1).

Both CTA and PPTA films were heat treated for 30 seconds but annealing temperatures were different. These were 275 and 350°C for CTA and PPTA films respectively.

B. Void Characterization

The density data of PPTA films indicate an increase of density as a function of drawdown ratio for uniaxial films. The thickness of these films also decreased as drawdown ratio increased. SEM and SAXS results of the extruded and uniaxially drawn PPTA films revealed a decrease in voids as a function of draw ratio. In the

case of CTA uniaxial films, all the films were moderately drawn due to the slow coagulation of CTA extruded as discussed in Chapter V.However, a decrease in density was observed as a function of solution concentration. Unlike highly drawn PPTA film, the uniaxial CTA film produced from 30 percent concentration exhibited extensive voiding and fibrillation which is verified from the SEM, density and SAXS data of this film (see Chapter V). The voiding and fibrillation decreased as solution concentration decreased. Though the uniaxial CTA film produced from lower concentration (25 percent) shows higher density as compared to 30 percent concentration CTA film and SEM photomicrographs of this film are similar to those of uniaxial highly drawn PPTA film (compare Figure IV- 3 Chapter IV to Figure V-3 Chapter V).

A similar situation can also be observed from comparison on the mandrel process PPTA film to the biaxially expanded CTA films. In this case, it is reasonable to compare CTA film 7 to PPTA film 4, since both films were prepared with the same blow-up ratio (3.3X). Here, the microstructure seen in the cross-sectional view of biaxial CTA film 7 produced from 30 percent concentration are more defective than those observed for the mandrel processed PPTA film four. This differences clearly are due to the fact that PPTA biaxial film was produced from much lower concentration

(17 percent) as compared to CTA film (30 percent). Furthermore the biaxially expanded CTA films made from lower concentrations have also higher densities and smoother cross-sections as compared and discussed in Chapter V to those of film seven.

The SAXS quantitative analyses for both CTA and PPTA demonstrate that the shape of the voids in the SAXS range are similar in both CTA and PPTA films. These are prolate ellipsoids (long axis in machine direction) for uniaxial films and oblate ellipsoids (short axis in thickness direction) for the biaxially expanded films. Moreover, the sizes of the voids in uniaxially oriented films in general are in the same order for CTA films as compared to those of PPTA films. For example, the average dimension of the voids measured by the Guinier technique for uniaxial Kevlar film three are 26.3nm in the machine direction and 24nm in the transverse direction. These are 27.3nm and 20.4nm for uniaxial CTA film six (produced from 30 percent concentration) respectively. On the other hand, on the SAXS range the void sizes measured for biaxially expanded CTA film seven (30 percent concentration) when the beam is normal to the plane of the film are smaller compared to those measured in the same condition for the mandrel processed PPTA film four (see Table IV-4 and V-4). This suggests that the CTA film produced from 30 percent

concentration contains more macrovoids (as seen from SEM photomicrographs of this film which are not detectable by SAXS technique)than mandrel processed PPTA film. The void dimensions however, in both uniaxial and biaxial CTA films increased as solution concentration increased. Furthermore, the void fraction measured from the invariant analysis of SAXS for CTA films also revealed an increase in void fraction as a function of solution concentration.

A reduction in void size is observed for both CTA and PPTA film as a function of annealing. This is substantiated by SEM observations and an increase in the density of the films after heat treatment as described in Chapter IV and V.

The methanol treated commercial cast film exhibited a lower density, higher void fraction and smaller void dimensions as compared to untreated commercial CTA film (see Table V- 2 , V-3 and V-4 in Chapter V). The SEM surface photomicrographs of this film shows voids on the order of about 1μ created as a consequence of the extraction of triphenyl phosphite additive (Figure V-11). Moreover, the void sizes in untreated cast CTA commercial film are in the same ranges as those of isotropic processed CTA film 1,(see Table V-4).

C. Molecular Orientation

Clearly, a high degree of molecular orientation can be obtained through the processes used in the present study. The uniaxially drawn PPTA films produced considerable molecular orientation in the machine direction. This uniaxial orientation increased as a function of drawdown ratio. The CTA uniaxially drawn films qualitatively exhibit lower levels of orientation in the machine direction than uniaxial PPTA films. This is attributed to the slow coagulation of extruded CTA which prevents applying the necessary drawdown to impart substantial orientation in the uniaxial films. Quantitative comparison of orientation can not be made between PPTA and CTA films due to the fact that the orientation factors were not obtained for CTA films. Though the orientation of CTA films were obtained from birefringence measurements as explained in Chapter V. Birefringence also was not measured for PPTA films, since they were not transparent.

However, a high degree of biaxial orientation with the c-axis being approximately equally distributed between the machine direction and the transverse direction was achieved for the mandrel process PPTA films(refer to Chapter V).

The influence of the annealing process on the orientation of both PPTA and CTA films was observed with

an enhanced biaxial orientation (see Chapter IV beginning on page 228, and Chapter V beginning on page 295).

D. Mechanical Properties

Effects of processing conditions on the mechanical properties of PPTA and CTA films were explained and discussed in Chapter VI. In this section, the mechanical properties of typical CTA and PPTA films produced in the present study will be compared to films and fibers reported by other investigators (29,63,216) and in addition to some commonly available commercial films.

In Table VII-1, comparison is made for uniaxially drawn films and fibers.It is clear from this table that the mechanical properties for PPTA film is similar to those reported by Flood. It can also be seen that the uniaxial PPTA film has about three times higher tensile strength compared to uniaxial CTA film in the machine direction. As it was discussed in Chapter V, this is partially due to the slow coagulation of extruded CTA which does not allow the film to be drawn sufficiently. The transverse direction tensile strength of PPTA film is lower than CTA film which may indicate that this film is more uniaxially oriented than the uniaxial CTA film. The machine direction elastic modulus of uniaxial PPTA film is also higher than the uniaxial CTA film while, the

TABLE VII·1. MECHANICAL PROPERTIES FOR UNIAXIALLY ORIENTED FILMS AND FIBERS

Samples	Modulus $\times 10^{-10}$ (dyne/cm^2) MD	TD	Tensile Strength $\times 10^{-9}$ (dyne/cm^2) MD	TD	Percent Elongation MD	TD
*Uniaxial PPTA film 3	4.5	0.09	2.3	0.04	7.0	2.0
Uniaxial PPTA film of Flood et al (63)	8.3	0.06	2.6	0.01	9.5	3.9
Kevlar Fiber	83	-	36	-	4.0	
*Uniaxial CTA film 6	0.5	0.93	0.75	0.25		4.0
Uniaxial CTA film of Omatete (216)	33.6	1.2	113	2.4	7.3	22
CTA fiber of Bheda (29)	7.5	-	5.0	-	10.	-

* Films produced in the present study

elongation to break is lower in both the machine and transverse directions of PPTA films as compared to those of CTA film. However, these anisotropic mechanical properties seen for both uniaxially drawn CTA and PPTA are consistent with the results obtained from orientation measurements.

In both PPTA and CTA films tensile strengths and modulus values, though high for films, did not reach the values for the fibers as seen in Table VII-1. This can be attributed to conditions that would not allow the film to be drawn as highly as the fibers because no air gap was present as in the fiber process. Another reason seems to be due to possible degradation in the film before and after coagulation.

Tables VII-2 shows mechanical properties of biaxially oriented and cast films. The biaxial PPTA film has similar modulus and elongation to break in both machine and transverse direction to those reported by Flood (63). The tensile strength of this film is somewhat higher. Biaxial CTA film which was produced from 30 percent concentration and has the same blow-up ratio as mandrel processed PPTA film, exhibits similar modulus but lower tensile strength in both the machine and transverse direction as compared to those obtained for the biaxial PPTA film. This lower strength can be associated with the extensive voiding

TABLE VII.2. MECHANICAL PROPERTIES FOR BIAXIALLY ORIENTED AND CASTED FILMS

Samples	Modulus $\times 10^{-10}$ (dyne/cm^2) MD	TD	Tensile Strength $\times 10^{-9}$ (dyne/cm^2) MD	TD	Percent Elongation MD	TD
*Biaxial PPTA film 4	1.3	2.7	2.24	3.2	4.4	4.2
*Biaxial/annealed PPTA film 5	2.3	0.98	3.8	3.7	4.4	4.4
Biaxial PPTA of Flood et al (63)	1.5	2.7	0.7	0.9	6.5	5.9
*Biaxial anisotropic CTA film 7	1.3	2.5	1.8	1.4	11.5	7.5
*Biaxial/annealed CTA film 8	6.	6.3	3.1	2.4	6.5	5
*Biaxial Isotropic CTA film 1	1.	1.	0.8	0.77	10	11.
*Biaxial CTA film of Omatete (216)	28.5	13.87	12.3	3.9	6.2	3.8
CFC Casted Film	1.6	1.5	1	0.96	18.	17.
CFC Casted/ MeOH treated Film	2.9	2.9	0.94	0.88	5.8	5.2

*Films produced in the present study

present in CTA film which are not seen for mandrel processed film. Elongation to break for all CTA films are higher than those of PPTA films.

A substantial increase in both machine and transverse direction tensile strength and modulus was observed as a function of annealing for both CTA and PPTA films. Both films exhibited a decrease in elongation to break after heat treatment.

It should be noted that all CTA films studied in the present work have an order of magnitude lower tensile strength and modulus as compared to those of CTA films reported earlier by Omatete (216).

The commercial cast film has similar tensile strength and modulus as biaxial isotropic processed film one. The elongation to break of this film is higher in both machine and transverse directions. Removing the triphenyl phosphite plasticizer from this film increased the modulus, decreased the elongation to break alot, and the tensile strength slightly.

Mechanical properties of some commonly commercial films are also presented in Table VII-3. It is clear from this table that both heat treated PPTA and CTA films exceed the property values of these commercial films.

TABLE VII.3. MECHANICAL PROPERTIES OF SOME COMMON COMMERCIALLY AVAILABLE FILMS(230)

Film Type	Process Methods	Tensile Strength $x10^{-8}$(dyne/cm^2)	Percent Elongation
Cellulose Triacetate	Casting	7 - 11	10 - 40
Cellulose Acetate	Extruded or Casting	6 - 11	20 - 30
Ethyl Cellulose	Extruded	5.5 - 6.9	20 - 30
Cellulose Acetate Butyrate	Extruded or Casting	2.7 - 6.2	40 - 70
Polyvinyl Chloride	Calendering	0.5 - 11	100 - 510
Polyester	Extruded/ Biaxially Oriented	17.3 - 27.5	50 - 120

TABLE VII.3. (continued)

Film Type	Process Methods	Tensile Strength $x10^{-8}$ (dyne/cm^2)	Percent Elongation
Nylon 6	Extruded/Biaxially Oriented	22 - 24	100 - 120
Nylon 66	Extruded	6.9 - 8.3	300 - 400
Polypropylene	Extruded/Biaxially Oriented	17.3 - 20.7	45 - 85
Polyethylene (low density)	Extruded/Biaxially Oriented	8.3	200 - 800
Polyethylene (high density)	Extruded/ or Casting	1.4 - 4	10 - 650

CHAPTER VIII

CONCLUSIONS AND RECOMMENDATIONS

In this chapter the major conclusions resulting from the experimental study are summarized below and are followed by recommendations for further study.

In this research, the major goal was to produce various uniaxially and biaxially oriented films from solutions of PPTA and CTA and study the effects of void structure and orientation on the mechanical properties as a function of processing conditions. As a preliminary to this, a circular tube was designed in order to produce biaxially oriented CTA films. A series of eight CTA films were prepared from isotropic and anisotropic solutions of CTA. These together with five PPTA films which were prepared from liquid crystalline PPTA/Sulphuric acid solutions and two CFC commercial casted films were characterized using various techniques. SEM, density, and SAXS were carried out to investigate void characterization. WAXS and birefringence were used to study the molecular orientation.

The main results are;

1. Films extruded without drawdown exhibit some polymer chain orientation in the machine direction. This is increased by uniaxially drawing down films.

2. Films produced using a lubricated conical mandrel and a coagulant recycle blow-up process show approximately equal biaxial orientation. The biaxial orientation appears to increase with increase in blow-up ratio.

3. It was found that birefringence for uniaxial CTA films are in the order such as $\Delta n_{13} \simeq \Delta n_{12} > \Delta n_{23}$ and for biaxial CTA films, these are as, $\Delta n_{13} \simeq \Delta n_{23} > \Delta n_{12}$. The birefringence could not be measured for PPTA films since, they are not transparent, and CFC commercial films did not show any birefringence.

4. Density of uniaxial films increased with increased drawdown ratio and decreased with increased solution concentration. An increase in density is also observed as a function of annealing.

5. The void volume fraction increased with increased solution concentration and decreased with increased drawdown ratio. A decrease in void fraction is observed as a function of annealing. These results are consistant with SEM photomicrographs.

6. Fibrillar structure was observed for "peeled" uniaxial CTA films. This is increased with increase in solution concentration. Biaxial films however, did not peel due to biaxial orientation developed in them.

7. Extensive voiding is present in all films. Void shape is dependent on the film process used. SAXS indicates void sizes which are roughly prolate ellipsoids (long axis in MD) for uniaxial films and oblate ellipsoids (short axis in thickness direction) for biaxial films.
8. SAXS quantitative analysis exhibit the existance of a void size distribution in all the films. Average void sizes measured using Debye and Bueche method were smaller than those obtained from Guinier analysis.
9. The uniaxially oriented films show highly anisotropic mechanical properties, while biaxial films show fairly high modulus and tensile strength in all directions.
10. Heat treatment under tension contributes greatly to enhancement of orientation and mechanical properties. Annealing also resulted in a significant decrease in voids and increased surface smoothness.

Recommendation for further study include the following;

1. All the films exhibited some thickness variation in the transverse direction as a consequence of the die design. This needs further modifications.
2. As described in Chapter III, the polymer solutions were degassed in an oven and left under vacuum for about 24 hours. There seems to be some degradation

as the solution, anisotropic before degassing becomes biphasic or sometimes isotropic. The degradation may be minimized by reducing the time for degassing. A new quicker method is needed to remove the air bubbles to help reduce polymer degradation.

3. The coagulation rate is relatively slow for production of highly oriented uniaxial film from CTA/DCA/FA in cold isopropanol. No systematic attempt at optimization has been made with the solvent mixture ratio, coagulant mixture or coagulant temperature. More complete investigation of this would be useful.
4. With improved film quality, using the previous suggestions, a higher level of uniaxial orientation may be achieved and also take-up rates could precisely be controlled.
5. A more complete investigation of crystal structure of CTA films is needed to better understand the role of both orientation and voids in the observed mechanical properties.
6. A solid state drawing of uniaxial CTA films is necessary to improve their mechanical properties and further understand the crystal structure of CTA under various draw ratio and draw temperatures.

7. Annealing at lower temperatures for longer duration or higher temperatures for shorter times would seem useful.

LIST OF REFERENCES

LIST OF REFERENCES

1. Acierno,D., Francesco,P.L.M and Giolio,P., Am. Chem. Soci.,15(5), 1455 (1982)

2. Adams,E.B., Whitehead,J.C. and Bogue,ICHE,J., 11, 1026 (1955)

3. Aharoni,S.M., Mol. Cryst., Liq.,Cryst., 56, 237 (1980)

4. Aharoni,S.M., Macromol, 12, 94 (1979)

5. Aharoni,S.M., J. Poly. Sci., Poly. Phys. Ed., 18, 1303 (1980)

6. Aharoni, S.M., and Sibila,J.P., SCA, Poly. Prepr. 20(1), 118 (1979)

7. Aharoni,S.M., Polymer, 21, 1413 (1980)

8. Aharoni,S.M., J. Macromol. Sci., Physo., B21,287 (1982)

9. Alexander,L.E., "X-ray Diffraction Methods in Polymer Science",R.E. Krieger Publishing Company, N.Y. (1979)

10. Alfrey,T., SPE Trans., 5,68 (1965)

11. Allen,S.R., Filippov, A.G., Farris,R.J., Thomas,E.L., Wong, C.P., Berry,G.C. and Chenevey,E.D. Macromol, 14,1135 (1981)

12. Aoki,H., Onogi,Y., White,J.L. and Fellers,J.F., Poly. Eng. Sci., 20(3),221 (1980)

13. Aoki,H., White,J.L. and Fellers, J.F., J. Appl. Poly. Sci., 23, 2293 (1979)

14. Arpin,M.and Strazielle,C., Polymer, 18, 597 (1977)

15. Asada,T., ACS Poly. Preprints, 20(11),70 (1979)

16. Asada,T., Matsumoto,H. and Onogi,S., J. Soc. Rheo. Japan, 6, 130 (1978)

17. Ast, W., Kunststoffe, 63,427 (1973), ibid 64,146, (1974)

18. Avakian, P., Blume,R.C., Gierke,T.D., Yang, H.H., and Panar, M., Poly. Prepr. Am. Ahcm. Soci., Div. Poly. Chem., 21, 8 (1980)

19. Bair, T.I., Morgan, P.W., and Killian,F.L., Macromol., 10,1396 (1977)

20. Bair, T.I., Morgan,P.W., U.S. Patent No.3, 673,143 (1972)

21. Baird,D.G., and Wilks,G.L., Poly. Eng. Sci., 23, 632 (1983)

22. Baird,D.G., "Liquid Crystalline Order in Polymer", Academic, N.Y., 273-259 (1978)

23. Baird,D.G., J. Rheo.,24,465 (1980)

24. Ballard, D.G., Griffiths, J.D. and Watson,J., U.S. Patent No., 3, 121,766 (1971)

25. Ballard, D.G., U.S. Patent No., 3,089,742 (1963)

26. Ballou, J.W., Poly. Repr., 17, 75 (1976)

27. Barnes, H.M., Skaar,C., and Luner,P., J. Appl. Poly. Sci., 21, 1085 (1977)

28. Bassett, D.C., "Principles of Polymer Morphology", N.Y., (1981)

29. Bheda,J., "Characterization and Fiber Formation of Liquid Crystalline Cellulose Derivatives", M.S. Thesis in Poly. Eng. Univ. of Tenn., Knoxville, Tenn., (1980)

30. Bheda,J., Fellers, J.F. and White, J.L., J. Appl. Poly. Sci., 26,3955 (1981)

31. Blackwell, J., and Gutierrez,G., Polymer, 23,671, (1982)

32. Blades,H., U.S. Patent No., 3,767,756 (1973)

33. Blumstein,A., Billard,J. and Blumstein,R., Mol. Cryst. Liq. Cryst., 25, 83 (1974)

34. Blundell, D.J., Polymer, 23, 359 (1982)

35. Bodaghi,H., "Spin-Draw Interaction Effects on Fibrillation of Polypropylene", M.S. Thesis in Poly. Eng., Univ. of Tenn., Knoxville, TN (1982)

36. Bonart,R. and Hosemann,R., Kolloid-Z, Polymer, 186, 16 (1962)

37. Brandenberger,J.E., U.S. Patent No., 1,601,289 (1926)

38. Brewster,D., Pil. Trans. R. Soc., 16, 156 (1816)

39. Bur, A.J. and Roberts, D.E., J. Chem., Phys., 51(7), 406 (1969)

40. Burchard,W., Macromol. Chem., 67,182 (1963)

41. Calundam, G.W., U.S. Patent No., 4,067,852 (1978)

42. Chandrasekhar, S., "Liquid Crystals", London, Eng., Chambridge Univ. Press, 42 (1977)

43. Chazy, H., Peguy, A., Chaunis, S., and Monzie,P., J. Poly. Sci., Poly. Phys. Ed, 18,1137 (1980)

44. Cheney, G.W. and Hughes,F.T., U.S. Patent No., 3,170,001 (1965)

45. Cichelli,M.T., U.S. Patent No., 2,987,765 (1961)

46. Ciferri,A., Valenti,B., "Ultra-High Modulus Polymers", Cifferri,A., Ward, I.M., Eds., Applied Sci. Publishers, London (1979)

47. Cifferri,A., Krigbaum, W.R. and Meyer, R.B., "Polymer Liquid Crystal", Academic Press,N.Y. (1982)

48. Cohoe, W.P., U.S. Patent No., 1,163,740 (1915)

49. Crank,J. and Park,G.S., "Diffusion in Polymers", Academic Press, London (1968)

50. Davies, G.T. and Taylor,H.S., Text. Res. J., 35, 405 (1965)

51. Dayan,S., Maissa,D., Vallutini, M.J. and Sixbu,P., J. Poly. Sci., Poly. Lett., 20, 33 (1982)

52. Debye,P. and Bueche, A.M., J. Appl. Phys., 20, 518 (1949)

53. Demus,D. and Richter,L., "Textures of Liquid Crystals",Weinhein, N.Y., Verlag Chemis (1978)

54. Dobb, M.G., Johnson,D.J. and Saville,B.P., J. Poly. Sci., Poly. Phys.Edn., 15,2201 (1977)

55. Dobb, M.G., Johnson, D.J., Majeed, A. and Saville,B.P., Polymer, 20, 1284 (1979)

56. Doi,M., J. Poly. Sci., Poly. Phys. Edn., 19, 229 (1981)

57. Donald, A.M. and Windle, A.H., Colloid and Polymer Sic., 261, 793 (1983), Polymer, 24,155 (1983)

58. Doulmadge,W.J., Nature, 172, 1053 (1953)

59. Dupre,D.B and Samulski,E.T., "Polypeptide Liquid Crystals", the fourth state of matter, Saeva, F.D., Ed., N.Y., Marcel Dekker, Inc. (1979)

60. Elliott,A. and Ambrose,E.J., Disc. Faraday Soc., 9, 246 (1950)

61. Fallwell, E.L., U.S. Patent No., 3,092,874 (1963)

62. Farber,R. and Dealy,T.M., Poly. Eng. Sci., 14, 435 (1974)

63. Flood,J.E., White, J.L. and Fellers,J.F., J. Appl. Poly. Sci., 27,2965 (1982)

64. Friedel, G. Ann. Phys., 18, 273 (1922)

65. Gerow, M.R., U.S. Patent No., 3,170,001 (1965)

66. Gilbert, R.D. and Patton, P.A., Prog. Poly. Sci., 9, 115 (1983)

67. Gray,G.W. and Winsor, P.A., "Liquid Crystals and Plastic Crystals", Vol.1, Wiley, N.Y. (1974)

68. Gurnee, E.F., J. Appl. Phys., 25, 1232 (1974)

69. Gutteridge, P.A., J. Non-Newt. Fluid Mech., 4, 73 (1978)

70. Guinier,A. and Fournet,G., "Small Angle Scattering of X-rays"Wiley, N.Y. (1955)

71. Guinier, A., "X-ray Diffraction", W.H. Freeman and Comp., San Francisco and London (1963)

72. Han, C.D., "Rheology in Polymer Processing",Academic Press, N.Y. (1976)

73. Hancock, T.A., Spruiell, J.E., and White, J.L., J. Appl. Poly. Sci., 21, 1227 (1977)

74. Hancock, T.A., White, J.L. and Spruiell, J.E., Poly. Eng. Sci., 20,1126 (1980)

75. Happey, F.J., Text. Inst., 41, T381 (1950)

76. Haraguchi,K., Kajiyama, T. and Takayanagi,M., J. Appl. Poly. Sci., 23, 915 (1979)

77. Hermans, P., Heikens, D and Weldinger,A., J. Poly. Sci., 35, 145 (1959)

78. Hermans, J.Jr., J. Colloid Sci., 17,638 (1962)

79. Henry, N.F.M., Lipson,H. and Wooster, W.A., "The Interpretation of X-ray Diffraction Photographs", McMillan and Co., Ltd. London (1960)

80. Hess, K., and Trogus, C.Z., Physik. Chem., B15, 157 (1932)

81. Hill, H.W. and Kwolek, S.L., U.S. Patent No., 3,006,899 (1961)

82. Hopfenberg, H.B., "Permeability of Plastic Films and Coatings", Vol. 6, Plenum Press, N.Y. (1974)

83. Horio, M., Ann. Report Res. Inst. Chem. Fibers, 35,87 (1978)

84. Howsman, J.A and Sisson, W.A., In Cellulose and Cellulose Derivatives (high polymers, Vol. V), N.Y. Interscience, 338 (1954)

85. Iasoski, S.W. and Cobbs, W.H., J. Poly. Sci., 36, 21 (1959)

86. Ide, Y. and Ophir,Z., Poly. Eng. Sci., 23(5), 261 (1983)

87. Ito, Y., Kobunski, Kagaku, 19, 412 (1962)

88. Jackson, W.J. and Kuhfuss, H.F., J. Poly. Sci., Poly. Chem. Ed., 14,2043 (1976)

89. Jackson, W.J., British Poly. J., 154 (1980)

90. Jackson, W.J. and Kuhfuss, H.F., J. Appl. Poly. Sci., 25, 1685 (1980)

91. Jellinek, M.H., Solomon, E. and Fankuchen, J., Ind. Eng. Chem., Anal. Ed., 18, 172 (1946)

92. Jerman, R.E. and Baird, D.G., J. Rheol., 25, 275 (1981)

93. Jennings, B.R. and Brown, B.L., Eur. Poly. J., 7, 805 (1971)

94. Kaneda, T. Ishikawa, S., Dimon,H., Katsura,T., Udea, M., Oda, K., and Horio, M., Macromol. Chem., 183,417 (1982)

95. Kelker,H. and Hatz, R., "Handbook of Liquid Crystals", Weinheim, Germ. Verlag Chemie, (1980)

96. Keller, A. and Machin, M.J., J. Macromol. Sci. Phys., B1, 41 (1967)

97. King, F.W., U.S. Patent No., 3,079,219 (1963)

98. Kiss,G. and Porter, R.S., Mol. Cryst. Liq. Cryst. 60,276 (1980)

99. Kiss,G. and Porter,R.S., J. Poly. Sci. Symp., 65, 193 (1978), J. Poly. Sci., Phys. Ed., 18,361 (1980)

100. Kleinschuster, J.J., U.S. Patent No., 3,991,014 (1976)

101. Knudesn, J.P. Text. Res. J., 33,14 (1963)

102. Kwolek, S.L., U.S. Patent No., 3,671,542 (1972)

103. Kwolek, S.L., Morgan, P.W., Schaefgan, J.R. and Gulrich, L.W., Poly. Prepr., 17,53 (1976) Macromol., 10,1390 (1977)

104. Kratky, O. and Miholic, G., J. Poly. Sci., C2, 449 (1963)

105. Krueger, D. and Yehi, G.S.Y., J. Macromol. Sci. Phys., B6, 431 (1972)

106. Kuhfuss, H.F. and Jackson, W.J., U.S. Patent No.,3, 804,805 (1974)

107. Lehmann, O.Z., Physik. Chem., 4, 462 (1889), 5, 427 (1890)

108. Lodge, A.S., Trans. Farday. Soc., 52,120 (1956)

109. Lonsdale, H.K., Merten,U. and Riley, R.L., J. Appl. Poly. Sci., 9,1341 (1965)

110. Matheson, R.R., Macromol., 13, 643 (1980)

111. Matsumoto, T. and Bogue, D.C., J. Poly. Sci., A215, 1663 (1977)

112. Maxwell, J.C., Proc. Roy. Soc., 22, 46 (1873)

113. McFarlane, F.E. and Davis, T.G., U.S. Patent No. 3,890,256 (1975)

114. McGregor, R., "Diffusion and Sorption in Fibers and Films", Academic Press., N.Y. (1974)

115. Meeten, G.H., Navardi, P. Dept. of Phys. Sch. of Sci. and Tech., London Polytechnic, London,UK Jan. 1983

116. Michaels, A.G. and Hausselein, R.W., J. Poly. Sci., C10,6 (1965)

117. Middleman, K., "Fundamental of Polymer Processing", MdGraw Hill, N.Y. (1977)

118. Millich, F., In Adv. Poly. Sci., 19,117 (1975)

119. Miyoshi,A., Sasaka, A., Iku,K. and Suzuki,Y., Japanese patent application 549-87683

120. Morgan, R.J., Pruneda, O. and Steele, W.J., J. Poly. Sci., Poly. Phys. Ed., 21, 1757 (1983)

121. Morgan, R.J., Mones, E.T., Steele, W.J., and Deutscher, S.B., Am. Chem. Soc. Poly. Chem., 21, 264 (1980)

122. Morgan, P.W., Killan, F.L. and Bir, T.L. Macromol., 10(6), 1381 (1977)

123. Mori, N., Uematsu,Y. and Uematsu,I., Rept. Prog. Poly. Phys. Japan, 16,612 (1974)

124. Naray, S. and Susich,G.Z., Physik. Chem., B4, 268 (1928)

125. Navard, P. and Haudin,J., Br. Poly. J.,12, 174 (1980)

126. Nomura,S. and Kawai, H., J. Poly. Sci., A28, 383 (1970)

127. Onogi, Y., White, J.L. and Fellers, J.F., J. Poly. Sci. Poly. Phys. Ed., 18,663 (1980)

128. Onogi, Y., White,J.L. and Fellers, J.F., J. Non-Newt. Flu. Mech., 7, 121 (1980)

129. Onogi, Y.and Asada, T., "Rheology", Vol.1, Astarita, G., Marrucci, G. and Nicolais,L., Eds., Pleumum, N.Y. (1980)

130. Page,L. and Adams, N.E., "Electrodynamics",Van No Strand, N.Y. (1940)

131. Panar, M., Avakian, P., Blume, R.C., Gardner, K.H., Gierke, T.D. and Yang, H.H., J. Poly. Sci., Poly. Phys. Ed., 21, 1955 (1983)

132. Panar, M. and Willcox, O.B., German patent No., 2,705,382 (1977), French patent no. 2,340,344 (1977)

133. Panar, M. and Beste, L.F., Acs. Poly. Prepr., 17(1),65 (1976), Macromol, 10, 1401 (1977)

134. Papakov, S.P., Kulichikin, V.G., Kalmykova, V.P. and Malkin, A.Y., J. Poly. Sci., Poly. Phys. Ed., 12,1752 (1974)

135. Patel, D.L. and Dupre, D.B., Mol. Cryst. Liq. Cryst., 53,323 (1979)

136. Patel, D.L. and Gilbert, R.D., J. Poly. Sci. Poly. Phys. Ed., 21,1079 (1983), 19, 1231 (1981)

137. Paulos, J.P. and Thomas, E., J. Appl. Poly. Sci., 25,15 (1980)

138. Pearson, J.R.A. and Petrie, C.J.S., J. Fluid Mech., 42,609 (1970)

139. Pennings, A.J. and Pijpers, M.F.J., Macromolecules, 3, 261 (1970)

140. Pennings, A.J., J. Poly. Sci., C16,1799 (1967)

141. Peterlin, A., Macromol. Sci. Phys., B11(1), 57 (1975)

142. Philippoff, W. and Troniquist, G.M.,J. Poly. Sci., 23,881 (1968)

143. Philippoff, W., J. Appl. Phys., 27,984 (1956)

144. Pincus, P. and de Gennes, P.G., J. Poly. Sci. Poly. Symp. Ed., 65,85 (1978)

145. Pletcher, T.C., U.S. patent no., 3,991,013 (1976)

146. Porod, G., Kolloid-z, 125,51 (1951), 124,83 (1951)

147. Porter, R.S. and Johnson, J.F., "Rheology", Vol. 4, Eirich, F.R., Ed., Academic N.Y. (1967)

148. Priestley, E.B., Wojtowicz, P.J., and Sheng,P., "Introduction to Liquid Crystals",Plenum Press N.Y. (1974)

149. Rehage,G. and Frenzel,J., "Thermal and Mechanical Properties of Polymer",a lecture given at Inst. of Physical Chem., TU Clausthall, 3392, Clausthal Zellerfeld, FRG (1982)

150. Reinizer,F.,Moatsh, 9,421 (1889)

151. Robinson, C., Trans. Faraday Soc., 52, 571 (1956), Tetrachedron, 13, 219 (1961)

152. Robinson, C., Ward, J.C. and Beevers, R.B., Disc. Faraday Soc., 25, 29 (1958)

153. Richie, C.A. and Scalora, A.J., U.S. Patent No., 3,142,865 (1964)

154. Rogers, C.E., Stannett,V. and Szware,M., J. Poly. Sci., 45, 61 (1960)

155. Ronald, N.D., J. Appl. Poly. Sci., 28, 1805 (1983)

156. Samuels, R.J., J. Poly. Sci. Poly. Phys. Ed., 7, 1197 (1969)

157. Samulski, E.T. and Tobolsky, E.V., in "Liquid Crystals and Plastic Crystals",Gray, G.W. and Windsor, P.W., Ed., Wiley, N.Y. (1980)

158. Samulski, E.T. and Dupre, D.B., "Polymer Liquid Crystals",in Adv. Liquid Crystals, Brown, G.H., Ed., Academic N.Y. (1979)

159. Schafgen, J.R., Foldi, V.S., Logulls, F.M., Good, V.H., Gulrich, L.W., Killian, F.L. and Waroblak, M.T., Poly. Prepr., 17,69 (1976)

160. Schenk, B.H., U.S. Patent No., 2,461,976 (1949)

161. Shibaev, V.P., Talrose, R.V., Petrukhin, B.S. and Plate, N.A., Vysokemol, Soedid, A13,493 (1971), B-13, 4 (1971)

162. Shimamura, K., White, J.L. and Fellers, J.F., J. Appl. Poly. Sci., 26,2165 (1981)

163. Silver, F.M. and Black, W.B., J. Poly. Sci. Poly. Chem. Ed., 17, 3535 (1979)

164. Simmens, S.C. and Hearle, J.W.S., J. Poly. Sci. Poly. Phys. Ed., 18, 871 (1980)

165. Singleton, R.W., Sieminiski, M. and Sprague,B., Tex. Res. J., 31,917 (1961)

166. Slutsker, L.I., Chererskii, Z.Y., Ulerskii, L.Y., Kuzmin, V.W., Kalmykova, V.D., Sokolova, T.S., Volokhina, A.V. and Kudryavtsev,G., Vysokomol, Soedin, Ser. A., A17, 1569 (1975)

167. Slutsker, L.I., Uterskii, L.E., Chererskii,Z.Y. and Perepdkin, K.E., J. Poly. Sci., Poly. Symp., 58, 339 (1977)

168. Sprague, B.S., Riley, J.L. and Noether,H.D., Tex. Res. J., 28, 275 (1958)

169. Stannett, V. and Williams, J.L. J. Poly. Sci., C10,45 (1965)

170. Stannett, V., Koros, W.J., Paul, D.R., Lonsdale, H. K. and Baker, R.W., "Recent Adv. in Membrance Sci and Technology",Springer-Verlaz Berlin Heidelberg (1979)

171. Statton, W.O., J. Poly. Sci., 58,205 (1962), 22, 385 (1956)

172. Statton, W.O., "Newer Methods of Polymer Characterization",Ke, B. Ed., Interscience, N.Y. (1964)

173. Stein, R.S., J. Poly. Sci., 21,335 (1958)

174. Stein, R.S., Clough, S. and Van Aartsen, J.J., J. Appl. Phys., 36,3072 (1965)

175. Stein, R.S., Rubber. Chem. Technol., 49,458 (1976)

176. Stoll, R.G., Tex. Res. J., 25,650 (1955)

177. Suto, S., White, J.L. and Fellers, J.F., Rheol. Acta., 21,62 (1982)

178. Sweeny, W., U.S. Patent No., 3,287,324 (1966)

179. Tadokoro, Sen-i-Gakkaishi, J. Soc. Fiber. Sci. and Tech. Japan, 31, 27B (1975)

180. Takagi, Y., J. Appl. Poly. Sci., 9, 3887 (1965)

181. Takahaski, K., Kajiyama, T. and Takayanagi, M., J. Appl. Poly. Sci., 23,903 (1979)

182. Tanford,C. "Physical Chemistry of Macromolecules", Wiley, N.Y. (1961)

183. Tobolsky, A.V. and Samulski, E.T., Macromol, 1, 555 (1968)

184. Tornberg, H.T., U.S. Patent No., 2,433,937 (1949)

185. Treloar, L.R.G., "Physics of Rubber Elasticity", 2nd Ed., Oxford, London (1958)

186. Vieth, W.R., Matulevicius, E.S. and Mitchell, S.R., Kolloid-Z, 220(1),49 (1967)

187. Viney, C., Donald, A.M. and Windle, A.H., J. Mat. Sci., 18,1137 (1983)

188. Warner, S.B. and Jaffe, M., J. Cryst. Growth, 48, 184 (1980)

189. Warner, S.B., Macromol., 13,450 (1980)

190. Werbowj, R.S. and Gray, D.G., Mol. Cryst. Liq. Cryst. 34,97 (1976)

191. Wessling, R.A. and Alfrey, T., J. Trans. Soc. Rheo., 8, 85 (1964)

192. Wessling, R.S., Trans. Soc. Rheo., 9,95 (1965)

193. White, J.L. and Fellers, J.F., J. Appl. Poly. Sci. Poly. Symp., 33, 137 (1978)

194. Williams, J.L. and Peterlin, A., J. Poly. Sci., Part A-2, 9, 4483 (1971)

195. Williams, R.J., Chem. Phys., 39,384 (1963)

196. Wissbrun, K.F., J. Rheol., 25,619 (1981)

197. Wissbrun, K.F. and Griffin, A. C., J. Poly. Sci. Poly. Phys. Ed., 20,1835 (1982)

198. Wissbrun, K.F., "Observations on the Melt Rheology of Aromatic Polyesters", a paper presented at the Leeds Symp. of Liquid Cryst. Polymers, Leeds, Eng. (1980)

199. Wolfe, J.F. and Arnold, F.E., Macromol. 14,909 (1981), 14,915 (1981)

200. Wooten, W.C., McFarlane, F.E., Gray, T.F. and Jackson, W.J., "Ultra High Modulus Polymers", Appl. Sci., London (1979)

201. Wunderlich, B., "Macromolecular Physics", Vol. 2 Academic, N.Y. (1976) Chapter 6

202. Wunderlich, B., "Macromolecular Physics", Vol. 1 Academic, N.Y. (1973) Chapter 3.

203. Wyckoff, H.W., J. Poly. Sci., 62,83 (1962)

204. Yasuda, H. and Peterlin, A. J. Appl. Poly. Sci., 18, 531 (1971)

205. Yoshiaki, I. and Zohar, O., Poly. Eng. Sci., 23(5), 261 (1983)

206. Yoshida, C., Vematsu, Y. and Vematsu, I. Rept. Prog. Poly. Phys., Japan, 15,645 (1972)

207. Zachariades, A.E., Economy, J. and Logan, J.A., J. Appl. Poly. Sci., 27,2009 (1982)

208. Zachariades, A.E. and Logan, J.A., Poly. Eng. Sci., 23, 797 (1983)

209. Kuhn W. and Grun, F., Kolloid-Z, 101, 248 (1942)

210. Oda, K. White, J.L. and Clark, E.S., Poly. Eng. Sci., 18,53 (1978)

211. Northolt, M.G., E.U. Poly. J., 10,799 (1974)

212. Zwick, M.M. and Van Bochaue, C., Text. Res. J., 34,117 (1964)

213. Franks, N. and Varga, J., U.S. Patent No., 4,145,532 (1979)

214. Stein, R.S., J. Poly. Sci., 24, 383 (1957)

215. Meeten, G.H. and Howard, P., Polymer, 23,483 (1982)

216. Omatete, O.O. and Fellers, J.F., A report written in Production and Characterization of Cellulose Triacetate Film from Liquid Crystalline Solution", Poly. Eng., Univ. of Tenn., Knoxville, TN (1982)

217. Tung, L.H. and Taylor, J. Poly. Sci., 21,140 (1956)

218. Wiley, R.E., Plastics Technology, 83,(1963)

219. Heffelfinger, C.J. and Burton, R.L., J. Poly. Sci. 47, 289 (1960)

220. Longman, G.W., Wignall, G.O., Hemming,M.and Dawkins, J.U. Colloid and Poly. Sci., 252,298 (1974)

221. Debye, P. Anderson, H.R. and Brumberger, H., J. Appl. Phys., 28,679 (1957)

222. Gwie, J.M.G. and Ranson, R.J., Die Makromol. Chemis, 143,105 (1971)

223. Takahashi, A., Kawaharada, T. and Kato, T., Poly. J., 11(8), 671 (1979)

224. Arneri, G. and Sauer, J.A. Poly. Eng. Sci., 15(11), 795 (1975)

225. Fedyakova, N.A. and Gembitskii, Khimicheskie Volokna, No. 1 , 24 (1983)

226. Stein, R.S., Rhodes, M.B. and Porter, R.S., J. Colloid and Interf. Sci., 27,336 (1968)

227. Hayashi, N.T, Murakami, Y., Moritani, M., Hashimoto, T. and Kawai, H., Poly. J., 4,560 (1973)

228. Hashimoto, T. Yamaguchi, K. and Kawai, H. Poly.J. 9, 405 (1977)

229. Liang , B., Fellers, J.F. and White, J.L., "A Basic Study of Ribbon/Cast Film Extrusion of Liquid Crystalline Cellulose Ethers", A report written to Proctor and Gamble, Poly. Eng., Univ. of Tenn., Knoxville, TN 1983

230. Schwartz, S.S. and Goodman, S.H., "Plastics Materials and Processes",Van Nostrand Reinhold Company, Inc. N.Y. (1982)

231. Zugenmaier, P., J. Appl. Poly. Sci., Appl. Poly. Symp., 37, 223 (1983)

232. Stipanovic, A.J. and Sarko, A. Polymer, 19, 3 (1978)

233. White, J.L. and Spruiell, J.E. Poly. Eng. Sci., 21, 859 (1981)

234. Wilchinsky, Z.W., "Advances in X-ray Analysis", Vol 6, Plenum Press, N.Y. (1963)

235. Samuels, R.J."Structured Polymer Properties",Wiley, N.Y. (1974)

APPENDIXES

APPENDIX A

PREPARATION OF DENSITY GRADIENT COLUMN

A linear density gradient column is prepared as follows; two solutions a more dense one A and a less dense one B are kept in equal volume communicating vessels while a steady stream of the heavy liquid is continuously drawn to fill the column. The pressure differential caused by the depletion of solution A causes fluid to flow from the liquid B to the heavy solution A container so that the liquid levels of A and B remain the same. Solution B continuously dilutes solution A making it less dense. If the more dense side is kept well mixed, as the density gradient column is being filled, a linear gradient will result as a consequence of the linear variation of the density in vessel A with time (see Figure A-1). Preparation of a column for the CTA films will be explained in the following section. Two other columns made in this study were followed by the same procedure.

A. Calculations

1. Decide an appropriate range for the column to be constructed. This was selected for CTA to be from 1.10 to 1.35.

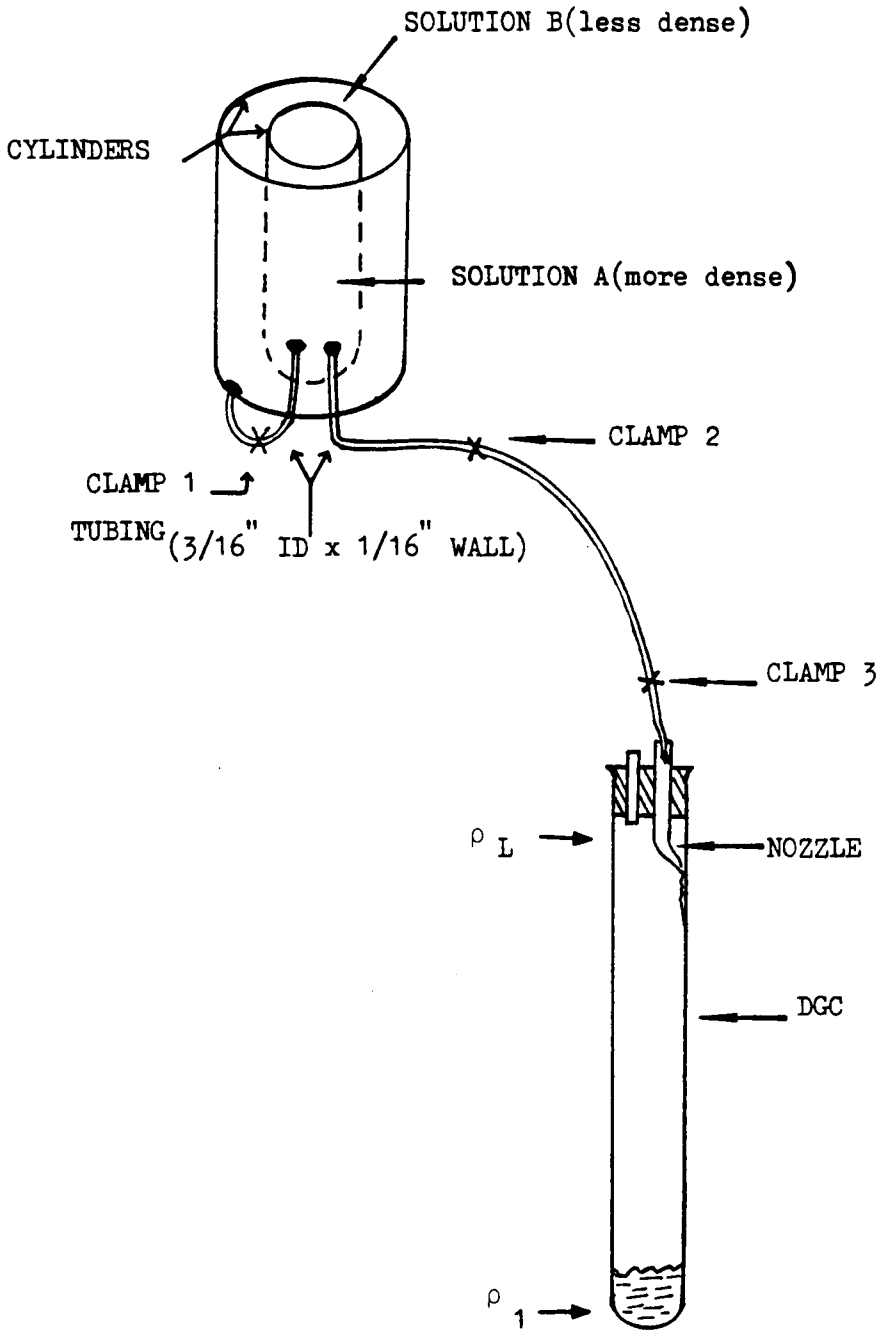


FIGURE A. 1. Schematic of the filling of a DGC.

2. Calculate the low density at 20 cm and the high density at 80 cm (this keeps the beads at the center of the column because the top and bottom of the column are the least accurate. However, this cut down on the overall range of the column).

3. Calculate the density at 0cm and at 100 cm (this is the full column range) as follows;

a) $\frac{(\text{High density-low density})\ \text{gm/cm}^3}{80\ \text{cm}} =$

$$\frac{(1.35 \times 1.10)}{80} = 3.125 \times 10^{-3} \qquad \text{(A-1)}$$

b) density on 20 cm is;

$$3.125 \times 10^{-3}\ \frac{\text{gm/cm}^3}{\text{cm}} \times 20\ \text{cm} = 0.0625\ \text{gm/cm}^3 \qquad \text{(A-2)}$$

c) density at 0 cm is;

low density- density for 20 cm

$$1.10 - 0.0625 = 1.0375\ \text{gm/cm}^3 \qquad \text{(A-3)}$$

d) density at 100 cm is;

high density + density for 20 cm

$$1.35 + 0.0625 = 1.4125 \qquad \text{(A-4)}$$

Let ρ_L = density at top of column (at 0 cm)

$\rho_L = 1.0375$

Let ρ_1 = density at bottom of column (at 100 cm)

$\rho_1 = 1.4125$

4. Choose solutions which when mixed, will yield this

density range from ρ_L to ρ_1 (1.0375 -1.4125) ASTMD 1505-68 gives some suggested solutions based on the density required.

Note; that the solution chosen must not react (swell, degrade, absorb, etc.) with the polymer.

5. Look up the density concentration data for the solutions. The concentration of A, X_A, corresponds to the density ρ_1 can be found in concentration-density tables such as those in the critical tables and CRC Handbook of Chemistry. This concentration for NaB_r/H_2O solution with a density of ρ_1 found to be X_A= 35 percent.

6. Calculate the solution density at the bottom of a 50 percent excess solution, (a 50 percent overall excess of solution is needed to maintain a pressure bead and for safety measures),

$$\rho_2 = \rho_L - \frac{\Delta P}{2} = 1.4125 - \frac{(1.4125 - 1.0375)}{2} \qquad \text{(A-5)}$$

the concentration of B, X_B, corresponds to density ρ_2. At this density the concentration of light solution X_B= 12 percent. This was determined by interpolation.

7. Calculate the average concentration, X_S, and the density at this concentation, ρ_S.

$$X_S = \left(\frac{X_B + X_A}{2}\right) = \frac{12 + 35}{2} = 23.5 \text{ percent} \qquad \text{(A-6)}$$

though

ρ_S = 1.2153 (use CRC tables and interpolation).

ρ_S represents the average density through out the column.

8. Calculate the mass of each solution, M, to fill the column.

$$M = \frac{M_c}{2} \qquad \text{(A-7)}$$

where, M_c is the mass to fill the column

M_c = (volume of the column) (50 percent excess solution (ρ_S) = (A-8)

(11.34.11 cm^3) (1.50) (1.2153 cm/cm^3)=2067.4gm

though

$$M = \frac{2067.4}{2} = 1033.713 \text{ gm} \qquad \text{(A-9)}$$

9. Calculate mass A. This is adjusted by 30 ml. The 30 ml volume is used to initially fill the tubing from the cylinder to the column.

$$M_A = M + (30)\ (\rho_1) \qquad \text{(A-10)}$$

$$= 1033.713 + (30)\ (1.35) = 1074.2 \text{ gm}$$

10. Calculate the mass of B. This is adjusted by four percent excess solution of X_B in order to help the establishment of flow from B to A.

$$M_B = M \cdot 1.04 \qquad \text{(A-11)}$$

$$= 10.33.713 \cdot 1.04 = 1075 \text{ gm}$$

11. Calculate the mass of solute and solvent in A and B.

Solution A

$M_{1A} = M_A X_A$; solute (A-12)

$M_{NaBr} = 1074.1 \times 0.35 = 375.97$ gm (A-13)

$M_{2A} = M_A(1-X_A)$:solvent (A-14)

$M_{H_2O} = 1074.2 \times 0.65 = 698.23$ gm (A-15)

Solution B

$M_{1B} = M_B X_B$; solute (A-16)

$M_{NaBr} = 1075 \times 0.12 = 129$ gm (A-17)

$M_{2B} = M_B (1-X_B)$: solvent (A-18)

$M_{H_2O} = 1075 \times 0.88 - 946$ gm (A-19)

B. Column Preparation

1. After the solutions are prepared and added to 1000 ml Erlenmeyer flasks, a vacuum is used to boil the solutions in order to remove the air bubbles.
2. The flasks (stoppered) are placed into a constant temperature bath at temperature of about 23° to equilibrate for at least two hours.
3. Place a clamp on each of the tubes leaving as it is shown in Figures A-1 (position 1,2, and 3).
4. Pour the heavier solution A, into the inner cylinder and light solution B, into the outer cylinder.
5. Add a stirring bar to the inner cylinder and place

the cylinder on a magnetic stirrer, about five to seven feet above the column (the higher the better for obtaining a constant flow rate).

6. The clamp one is now opened just a little to fill the tube from the inner to outer cylinders. The clamp two and three are opened enough to fill the tube from the inner cylinder to the column.
7. Adjust the speed of the stirring bar such that good mixing occurs. This is usually about one to two cm vortex.
8. The next few steps are critical and need to be performed quickly due to the fact that, once the filling process has started, it can not be stopped. A stop watch and a 10 ml graduated cylinder are needed before proceeding.
9. Remove both clamps one and two, so that solution begin to flow from the outside to the inside cylinder. Using the adjustable clamp three, adjust the flow rate to 15 mls per minute (7-8 ml/30 sec).
10. When the proper flow rate is established and at least 30 mls have been used, the nozzles placed into the top of the column and adjusted so that the stream of fluid runs down the inside wall of the column. The column will take about 75 minutes to fill depending on the solution and flow rate first established.

11. The flow rate is usually adjusted and monitored as the column fills. The time needed for the solution to fill one cm of the column (11.34 ml) should be about forty five seconds.
12. A periodic checking of the stirring is required in order to eliminate any possible displacement of the stirring bar that may occur during this procedure. If stirring stops, the column will be ruined.
13. When the column is filled to within about three centimeters of the top, close both clamps and drain the excess solution into a container. This will be used later to "wet" samples and to store the density gradient beads.
14. Place the beads in the wire mesh basket using a rubber tipped tweezer and position the basket at the top of the column. A clock motor is turned on to drive the basket into the column. Care must be taken not to trap any bubble under the basket. If this happens, raise and relower the basket with the motor.
15. When the basket reaches the bottom of the column, the motor is stopped and the line is taped to the outside of the column and the column is tightly stoppered.
16. After allowing twenty four hours for equilibrium, the position of the beads is plotted the results for three columns made in this study are shown in Figure A-2 to A-4.

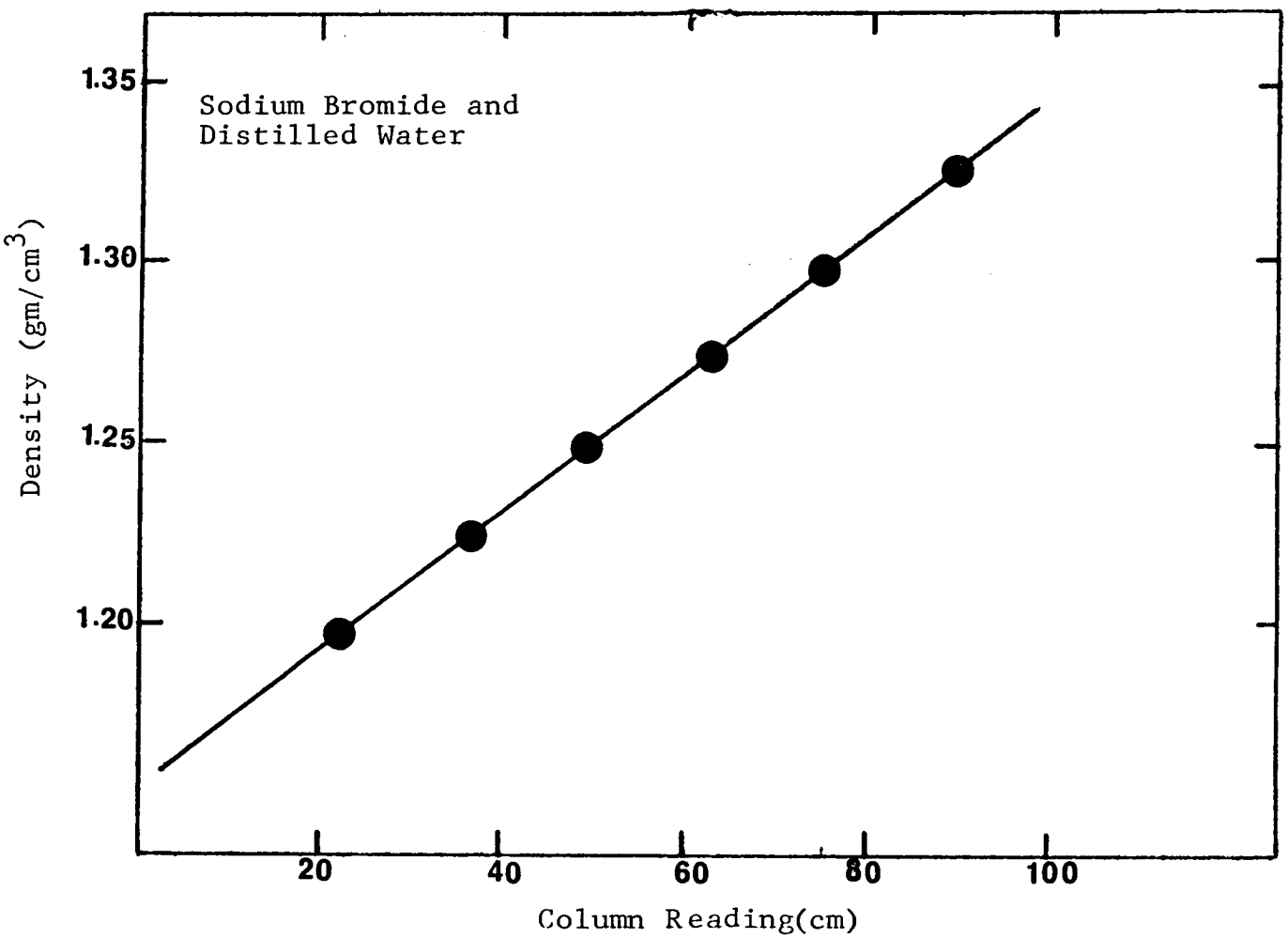


Figure A. 2. DGC calibration curve used for density measurements of CTA films.

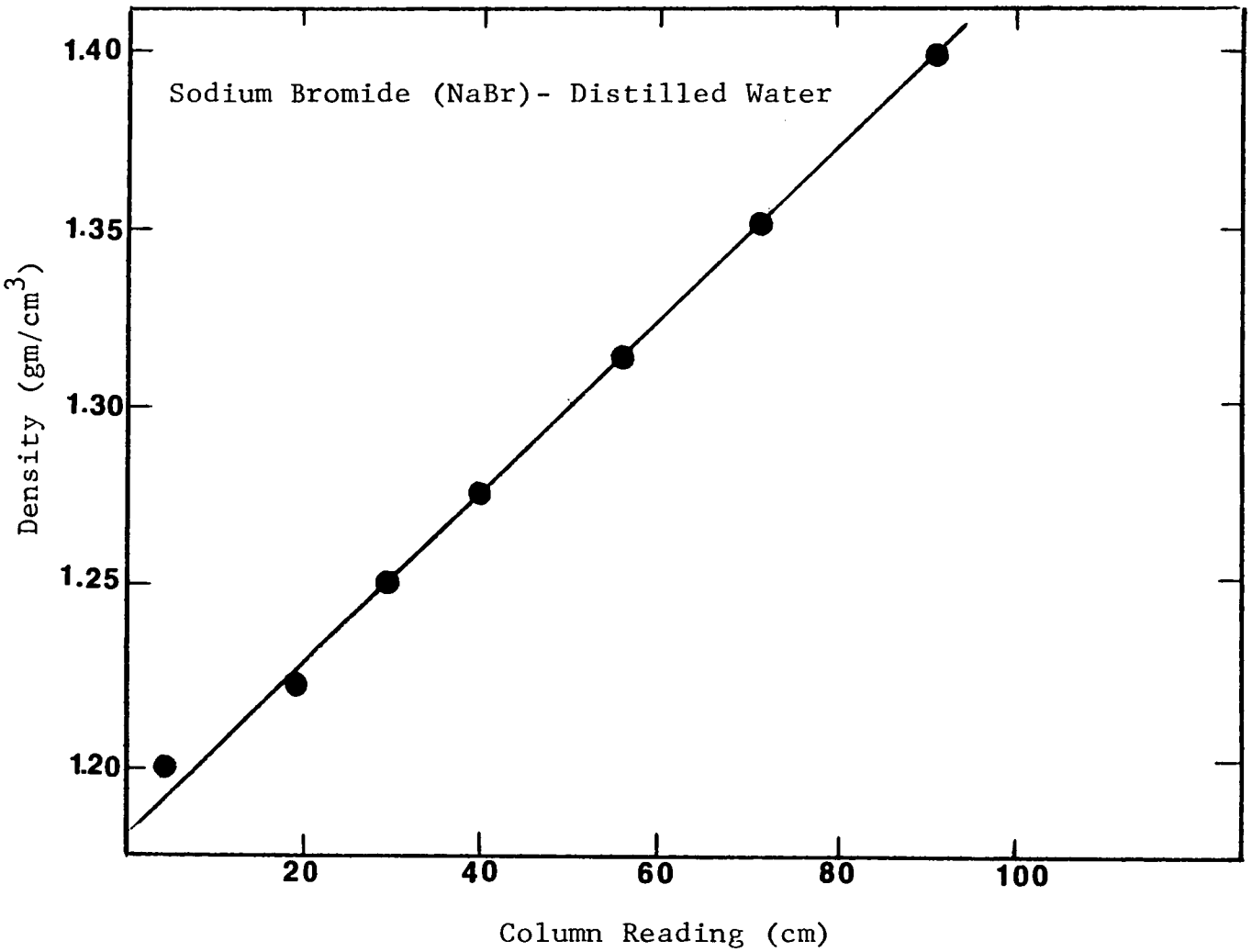


Figure A. 3. DGC Calibration curve used for density measurements of Kevlar film samples 2-5.

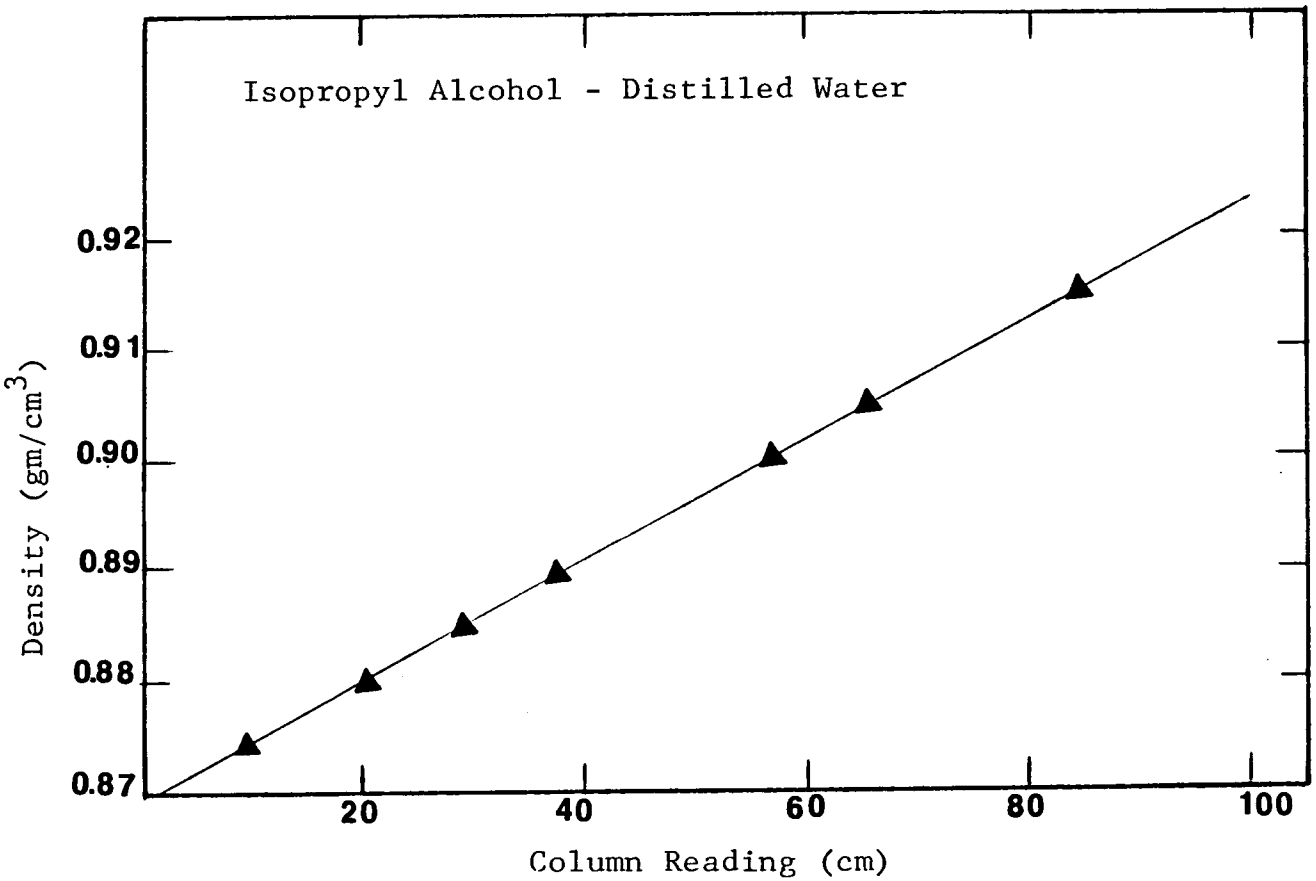


Figure A. 4. DGC calibration curve used for density measurements of Kevlar film sample 1.

17. The samples were wet in the container containing the excess solution and, placed into the columns. Each sample was held with a rubber tipped tweezer slightly below the liquid level in the column and released. Approximately, twenty four hours were allowed for equilibrium.

APPENDIX B

POLE FIGURES AND DETERMINATION OF BIAXIAL ORIENTATION FACTORS

A convenient means to describe and represent the degree of preferred orientation of the crystallites in textured specimens is the sterographic projection known as pole figure. Three-dimensional view of a pole figure is presented in Figure B-1. This is derived from a spherical projection and shows the density of crystallographic poles of a given set of planes as a function of orientation. In the absence of crystalline orientation, the poles will be distributed all over the stereographic projection. If orientation is present, the poles will tend to be concentrated in certain areas within the stereographic projection. As described in Chapter II pole figures from several planes are needed to determine the experimental values of $< Cos^2\theta >$ for the computation of orientation functions. (see Chapter II page 70 and reference 9). For PPTA films the planes used were the (110), (200), and (006) and biaxial orientation functions were obtained from $< Cos^2\theta >$ values generated from intensity data of the (110) and (200) pole figures. $< Cos^2\theta_{b,z} >$ and $<Cos^2\theta_{c,z}>$ were calculated for the PPTA orthorhombic unit cell. The model used for this analysis is shown below (9). The reference axis is the Z direction. The coordinate

Three-Dimensional View of a Pole Figure

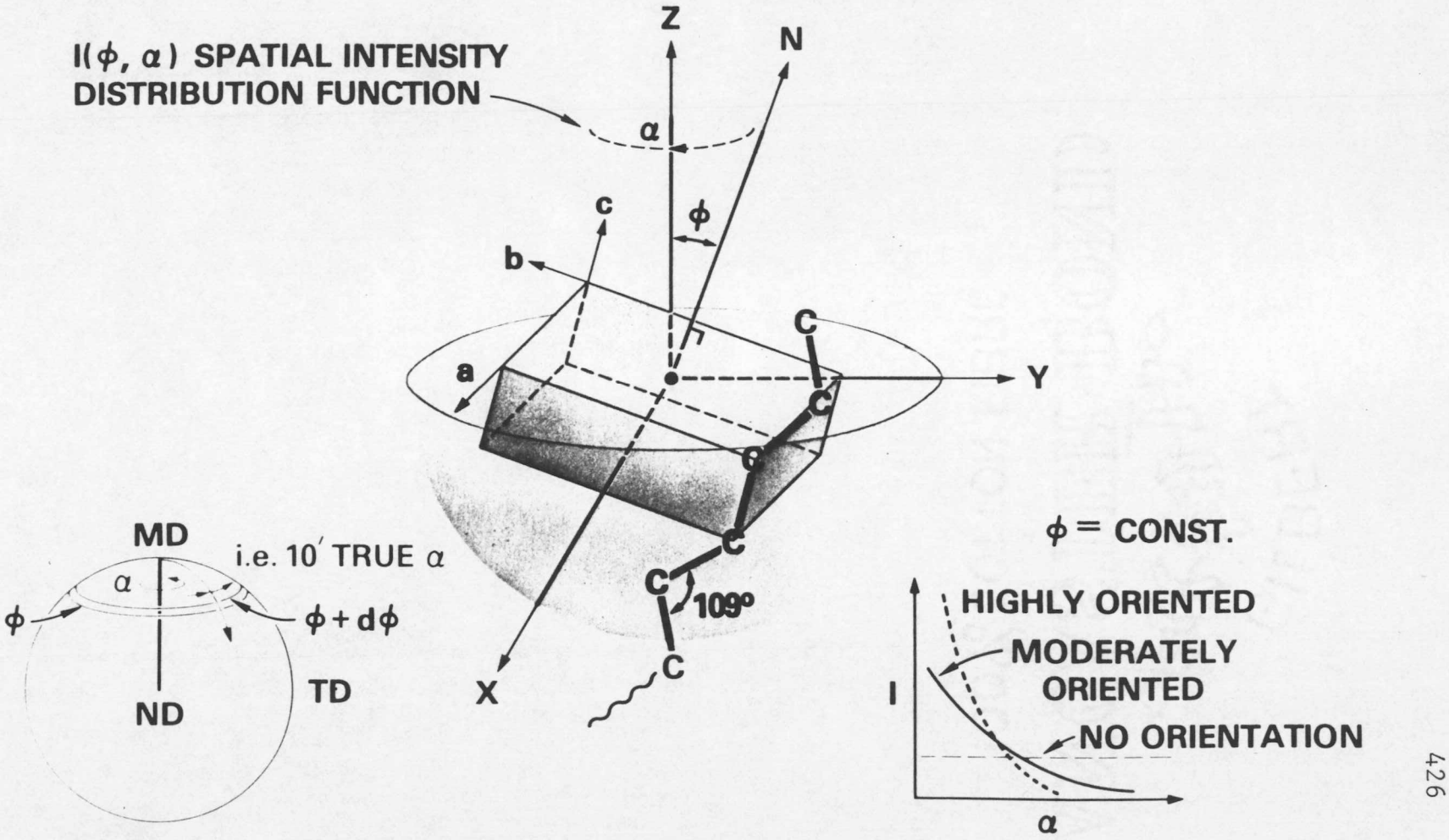
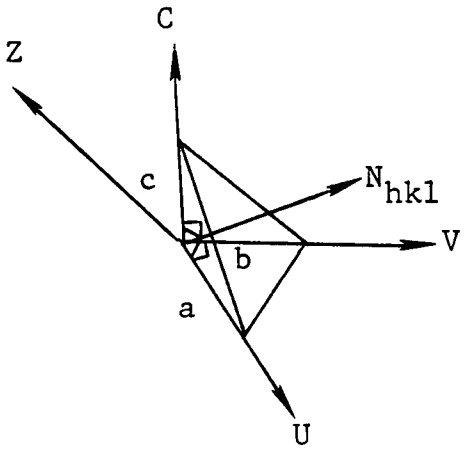


Figure B.1. Three-dimensional view of a pole figure.

system is Cartesian with U, V, and C as the axes. U and V, in this particular case of orthorhombic symmetry, coincide with the crystallographic axes a and b. The vector $\bar{N}$ is the normal to the set of planes being considered.



The Vector Z and N are expressed in the following manner (9);

$$Z = (\mathrm{Cos}\,\theta_{U,Z})\,i + (\mathrm{Cos}\,\theta_{V,Z})J + (\mathrm{Cos}\,\theta_{C,Z})K \qquad \text{(B-1)}$$

$$N = e\,i + f\,j + g\,k \qquad \text{(B-2)}$$

one can write the scalar product of A and N as follows;

$$N.Z. = \mathrm{Cos}\,\theta_{hkl,Z} = e\,\mathrm{Cos}\,\theta_{U,Z} = f\,\mathrm{Cos}\,\theta_{V,Z} = g\,\mathrm{Cos}\,\theta_{C,Z}, \qquad \text{(B-3)}$$

The mean-square cosine of $\theta_{hkl,Z}$ for the orientation distribution is given by;

$$\begin{aligned} \langle \mathrm{Cos}^2\theta_{hkl,Z} \rangle = {} & e^2 \langle \mathrm{Cos}^2\theta_{U,Z} \rangle + f^2 \langle \mathrm{Cos}^2\theta_{V,Z}, = g^2 \langle \mathrm{Cos}^2\theta_{C,Z} \rangle \\ & + 2\,ef \langle \mathrm{Cos}\theta_{U,Z}\,\mathrm{Cos}\theta_{V,Z} \rangle \\ & + 2\,fg \langle \mathrm{Cos}\theta_{V,Z}, \mathrm{Cos}\theta_{C,Z} \rangle \\ & + 2\,eg \langle \mathrm{Cos}\theta_{U,Z}, \mathrm{Cos}\theta_{C,Z} \rangle \end{aligned} \qquad \text{(B-4)}$$

For an orthorhombic unit cell, all cross product averages

are zero and for (hko) planes g=0 since, $f^2 + e^2 + g^2 = 1$. Then $f^2 = (1-e^2)$, and equation (B-4) simplifies to

$$\langle \cos^2\theta_{hkl,Z} \rangle = e^2 \langle \cos^2\theta_{U,Z} \rangle + (1-e^2) \langle \cos^2\theta_{V,Z} \rangle \quad \text{(B-5)}$$

In this case,

$$\langle \cos^2\theta_{U,Z} \rangle = \langle \cos^2\theta_{a,Z} \rangle \quad \text{(B-6)}$$

$$\langle \cos^2\theta_{V,Z} \rangle = \langle \cos^2\theta_{b,Z} \rangle \quad \text{(B-7)}$$

$$\langle \cos^2\theta_{hko,Z} \rangle = \langle \cos^2\theta_{(110),Z} \rangle \quad \text{(B-8)}$$

Substituting equations B-6, B-7, and B-8 into equation B-5 gives;

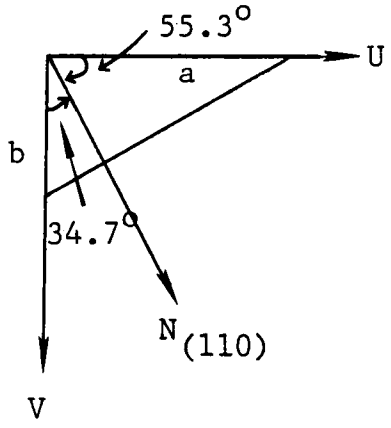
$$\langle \cos^2\theta_{b,Z} \rangle = \frac{\langle \cos^2\theta_{(110),Z} \rangle - e^2 \langle \cos^2\theta_{a,Z} \rangle}{(1-e^2)} \quad \text{(B-9)}$$

From the geometry of the unit cell for PPTA, it is easily found that the direction cosines for the two equatorial reflections are given by (refer to the following figure);

$e = \cos\theta_{(110),a} = \cos 55.3^\circ = 0.5693$

$f = \cos\theta_{(110),b} = \cos 34.7^\circ = 0.8221$

In the case of (200), e= 1,000 and f=0.0000



$a = 7.87\ \text{Å}$

$b = 5.18\ \text{Å}$

Using the value obtained from equation B-9, $< Cos^2\theta_{b,Z}>$ and for $<Cos^2\theta_{a,Z}>$ substitutes into the following equation for orthorhombic unit cell (9).

$$<Cos^2\theta_{U,Z}> + <Cos^2\theta_{V,Z}> + <Cos^2\theta_{C,Z}> = 1$$

gives $<Cos^2\theta_{C,Z,}>$

To determine orientation functions, the same analysis as above can be used to obtain $<Cos^2\theta_{b,y}>$ and $<Cos^2\theta_{c,y}>$ and also equation page 34 to 39, Chapter II.

APPENDIX C

MEASUREMENT OF BIREFRINGENCE

Birefringence results when a material is optically anisotropic, that is, when its refractive index is direction dependent. As was discussed in the background chapter, both "in-plane" and "out-of-plane" birefringence were measured. The "in-plane" birefringence represents the difference of index of refraction between the machine and transverse directions, Δn_{12}, and the "out-of-plane" birefringence represents the difference in index of refraction between the machine and thickness direction, ΔN_{13}. This was accomplished using an instrument equivalent to that of Stein (214) which allows a sample to be rotated and tilted in the incident polarized light beam.

The equipment consists of a telemicroscope, a Babinet compensator, a goniometer for sample orientation and a polarized filtered incandexcent light source. This instrument is shown in Figure C-1.

The procedure for this measurement is as follows;

1. The light source along the axis of the bench should first be aligned.
2. Before placing the compensator on the optical bench the polarizer and analyzer must be crosses and at 45° to the machine direction of the sample

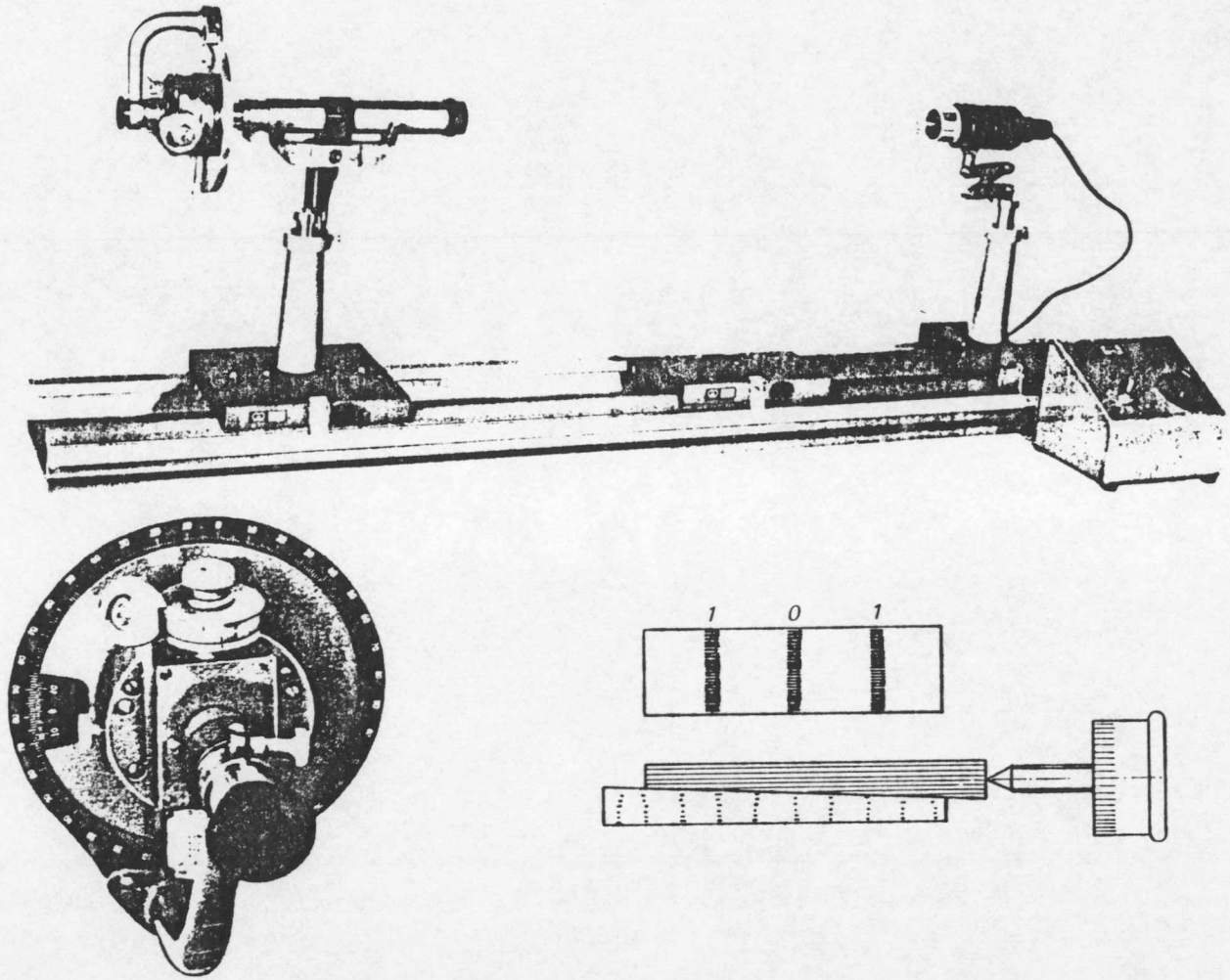


Figure C. 1. Illustration of Gaertner Polariscope and Compensator.

(typically vertical) that no light is transmitted.

3. The compensator is replaced and rotated until the fringe lines vanish. This is the point where the optic axes of the compensator line up with those of the analyzer and polarizer. The angle that this occurs at, can be read from the compensator holder. This angle should be 45°. If it is not, the polarizer is rotated slightly and the above repeated.
4. The sample is placed on the goniometer and focused through the microscope.
5. To find the optic axis of the sample, the compensator is removed and the sample is rotated slowly until the lowest light transmission through the sample is obtained.
6. Then the sample is rotated on opposite direction 45° from that was found in step 2.
7. The compensator is replaced and a reading is taken by turning the compensator now to set the dark fringe in between bifilars.
8. A second reading is taken by rotating the compensator 90°.
9. The values obtained from steps seven and eight allows one to calculate (Δn_{12}), "in-plane" birefringence. This is calculated as follows;

$$\Delta n_{12} = \frac{\lambda}{d} R_o \qquad \text{(C-1)}$$

where λ = wavelength of light used

d = sample thickness

R_o= optical retardation at ϕ =0

10. The "out-of-plane" birefringence (Δn_{13}) can be calculated using tilting technique (214). The governing equation is,

$$\Delta n_{13} = \frac{\lambda_o}{d_o} \frac{R_\phi \ (1 - \mathrm{Sin}^2\phi / n^2)^{\frac{1}{2}} - R_o}{\mathrm{Sin}^2\phi / n^2} \qquad \text{(C-2)}$$

Where n is the average index of refraction of the film

λ_o= wavelength of the light used

d_o= thickness of the film

R_o= the retardation of the film for incidence expressed in units of number of waves

R_ϕ= the retardation of the film tilted through the angle ϕ.

11. Then $\Delta n_{23} = \Delta n_{13} - \Delta n_{12}$ (C-3)

APPENDIX D

COMPUTER PROGRAM

This program calculate the integrated intensity (Q) and the mean square electron density fluctuation (MSEDF) presented in Chapter II.

```
      PROGRAM INVAR
C
C  GLOBAL COMMONS USED:
C     DATA #EFFC #1004
C     ONEDTA #EC80 #258
C     HEADER #EF00 #64
C     CSLOT #EFCC #18
C
C*********************************************************************
C*** PROGRAM TO CALCULATE THE INTEGRATED INTENSITY (Q) AND THE MEAN ***
C*** SQUARE ELECTRON DENSITY FLUCTUATION (MSEDF) FOR A CYLINDRI-    ***
C*** CALLY SYMMETRIC SAXS PATTERN ABOUT M1  (MU=0.0 DEG).          ***
C*** THE LOW ANGLE INTENSITY IS APPROXIMATED AS A CONSTANT         ***
C*** INTEGRATED OVER THE VOLUME OF AN ELLIPSOID ABOUT M1 IF DESIRE D.***
C*** ANISOTROPIC LIQUID SCATTER CORRECTION
C*** REQUIRES THREE VALUES OF FL AT 0, 45, 90 DEG AZIMUTHAL ANGLE.
C***    VERSION NOVEMBER 4, 1983
C***   IMPORTANT VARIABLES :
C***       CT = COUNTING TIME (SEC)
C***       TM = SAMPLE TRANSMISSION
C***       STH= SAMPLE THICKNESS (CM)
C***       CPCM=CHANNEL PER CM
C***       DIST2 = SAMPLE-DETECTOR DISTANCE (CM)
C***       XCH = NUMBER OF CHANNELS ALONG X
C***       YCH = NUMBER OF CHANNELS ALONG Y
C***       ICELL=NUMBER OF NEGATIVE CELLS
C***       IO=INCIDENT BEAM INTENSITY (COUNTS PER SECOND)
C***       MR1,MR2=Y,X LOW ANGLE LIMITS (MILLIRADIANS)
C***       MR3,MR4=Y,X HIGH ANGLE LIMITS (MILLIRADIANS)
C***       LAMBDA = XRAY WAVELENGTH (CM)
C***       AVOGAD = AVOGADRO'S NUMBER
C***       THOMSN = THOMSON'S NUMBER (CM**2)
C***       CX = X CENTER OF PATTERN (CHANNELS)
C***       CY = Y CENTER OF PATTERN (CHANNELS)
C***       FLS(I) = LIQUID SCATTER COUNTS AT 0,45, AND 90 DEGREES MU
C***       M1 = SCATTERING VECTOR MAGNITUDE IN Y
C***            DIRECTION ON DETECTOR PLANE (CM)
C***       M2 = SCATTERING VECTOR MAGNITUDE IN X
C***            DIRECTION ON DETECTOR PLANE (CM)
C***       SUM = M2 WEIGHTED INTEGRATED INTENSITY (CM CTS)
C***       SUMLA = LOW ANGLE INTEGRATED INTENSITY
C***       ISUMCL = NUMBER OF CELLS IN INTEGRATED INTENSITY
C***       Q = ABSOLUTE INTEGRATED INTENSITY (E**2 CM)
C***       MSDEF = MEAN SQUARED ELECTRON DENSITY FLUCUATIONS
C***             (MOLE ELECTRONS/CM**3)**2


C*********************************************************************
C
C
      DIMENSION IDATA(64,64)
      DIMENSION FINPT(3),FLS(3)
      REAL IO,LAMBDA,MR1,MR2,MSEDF,K,LS,MU,M1,M2,MR3,MR4
```

```
      INTEGER ANS(3),HEDREC(100),XCH,YCH
      COMMON/DATA/IDUM1,IDUM2,M,N,IDATA
      COMMON/HEADER/HEDREC
      COMMON/MANAGE/MAXREC,MXWRDS,LU,IDEM
      COMMON/CSLOT/NGC,NRTC,NHSCL,MSMS,NSMEM,NS8801
      EQUIVALENCE (NCDS,HEDREC(9))
      EQUIVALENCE (CPM,HEDREC(68)),(TM,HEDREC(52)),(DIST2,HEDREC(62))
      EQUIVALENCE (CX,HEDREC(42)),(CY,HEDREC(44)),(YCH,HEDREC(11))
      EQUIVALENCE (XCH,HEDREC(12)),(CTIME,HEDREC(36))
      DEFINE FILE 21(12992,200,L,NXTREC)
      LU = 21
      MAXREC = 12992
      MXWRDS = 100
      IDEM = 4100
      PI = 4.0*ATAN(1.0)
      P8 = PI/8.
      P38 = PI*3./8.
      AVOGAD = 6.0228E23
      LAMBDA = 1.5417E-08
      THOMSN = 7.94E-26
   20 CONTINUE
      WRITE(6,45)
   45 FORMAT(//,1H ,'--ANISOTROPIC INVARIANT PROGRAM',/,
     11H ,'  VERSION NOVEMBER 4, 1983',//)
      WRITE(6,40)
   40 FORMAT(1H ,'TYPE "1" IF DATA TO BE FETCHED FROM DATA BASE'/,
     &' TYPE "2" IF DATA FROM FLOATING POINT CAMAC STORAGE')
      CALL FREEFM(5,1,FINPT)
      ILOC=FINPT(1)
      IF(ILOC.EQ.2)GO TO 50
      WRITE(6,30)
   30 FORMAT(//,1H ,'ENTER DATA SET SEQUENCE NO.')
      CALL FREEFM(5,1,FINPT)
      ISEQ = FINPT(1)
      NERR = 0
      CALL FETCH(ISEQ,NERR,MAXREC,MXWRDS,LU,IDEM)
      IF(NERR .EQ. 0) GO TO 50
      GO TO 20
   50 ICELL = 0
C           CONVERT VARIABLES TO CENTIMETERS
      CPCM = CPM*10.0
      DIST2 = DIST2/10.0
      WRITE(6,60) HEDREC(1)
   60 FORMAT(1H ,'INVARIANT ANALYSIS FOR :',I6/)
      WRITE(6,70) (HEDREC(I),I=76,100)
   70 FORMAT(10X,' TITLE : ',25A2)
      IF(CX.NE.0..OR.CY.NE.0.) GO TO 75
      WRITE(6,72)
   72 FORMAT(1H ,  'CENTER THE PATTERN!   ENTER CX,CY:')
      CALL FREEFM(5,2,FINPT)
      CX=FINPT(1)
      CY=FINPT(2)
      IF(CX.NE.0..OR.CY.NE.0.) GO TO 75
      GO TO 295
   75 WRITE(6,80) TM,CPCM,DIST2,CX,CY
   80 FORMAT(1H ,'THE SAMPLE TRANSMISSION = ',11X,F8.3/
     X' THE CHANNELS PER CM = ',15X,F8.2/
```

```
109         X' THE SAMPLE-DETECTOR DISTANCE IN CM = ',F8.2/
110         X' THE CENTER OF PATTERN :          CX = ',F8.2/
111         X'                                  CY = ',F8.2//)
112          CT=CTIME
113          WRITE(6,82) CT
114   82     FORMAT(1H ,'THE COUNT TIME IN SECONDS =',F8.1,/1H ,'DO YOU WANT ',
115        1'TO CHANGE THIS? TYPE Y OR N...')
116          READ(5,230) ANS
117          IF(ANS(1).NE.'Y') GO TO 89
118          WRITE(6,84)
119   84     FORMAT(1H ,'INPUT THE COUNT TIME IN SECONDS')
120          READ(5,85) CT
121   85     FORMAT(F8.1)
122      89  WRITE(6,90)
123      90  FORMAT(1H ,'ENTER THE SPECIMEN THICKNESS IN CM')
124          CALL FREEFM(5,1,FINPT)
125          STH = FINPT(1)
126          WRITE(6,110)
127     110  FORMAT(1H ,'ENTER THE INCIDENT INTENSITY IN CPS')
128          CALL FREEFM(5,1,FINPT)
129          IO = FINPT(1)
130      55  WRITE(6,130)
131     130  FORMAT(1H ,'ENTER THE ORIGIN LIMITS IN MRAD IN X & Y DIR.')
132          CALL FREEFM(5,2,FINPT)
133          MR2 = FINPT(1)
134          MR1 = FINPT(2)
135          ANS(1)='N'
136          ISW=0
137          WRITE(6,135)
138     135  FORMAT(1H ,'APPROXIMATE THE LOW ANGLE INTENSITY?')
139          READ(5,230) ANS
140     230  FORMAT(3A1)
141          IF(ANS(1).EQ.'Y') ISW=1
142          WRITE(6,140)
143     140  FORMAT(1H ,'ENTER THE HIGH ANGLE LIMITS IN MRAD IN X & Y DIR.')
144          CALL FREEFM(5,2,FINPT)
145          MR4=FINPT(1)
146          MR3=FINPT(2)
147          MR3=TAN(MR3/1000.)*DIST2
148          MR4=TAN(MR4/1000.)*DIST2
149          MR1 = TAN(MR1/1000.)*DIST2
150          MR2 = TAN(MR2/1000.)*DIST2
151          WRITE(6,150)
152     150  FORMAT(1H ,'ENTER THE LIQUID SCATTERING COUNTS:',
153         &' 3 VALUES FROM POROD PLOT AT MU=0, 45, 90 DEG.')
154          CALL FREEFM(5,3,FINPT)
155          FLS(1) = FINPT(1)
156          FLS(2) = FINPT(2)
157          FLS(3) = FINPT(3)
158          ICELL=0
159          SUM = 0.0
160          TOTAL = 0.0
161          ISUMCL=0
162          TOTDAT=0.0
163   C*** CALCULATE SUM OF ALL DATA POINTS AND PI*SUM*M2 IGNORING DATA
164   C*** IN AN ELLIPSE ABOUT THE ORIGIN IF THE LOW ANGLE INTENSITY IS
165   C*** TO BE ESTIMATED (ISW=1) - OTHERWISE IGNORE A RECTANGLE
```

```
166         DO 190 J=1,YCH
167         DO 180 I=1,XCH
168         X=FLOAT(I)
169         Y=FLOAT(J)
170         M2=ABS((CX-X)/CPCM)
171         M1=ABS((CY-Y)/CPCM)


172   C*** CALCULATE SECTOR FOR LIQUID SCATTER CORRECTION
173         IF(M1.EQ.0.0) M1=0.00001
174         MU=ATAN(M2/M1)
175         IF(MU.GT.P8) GO TO 141
176         LS=FLS(1)
177         GO TO 145
178       141 IF(MU.GT.P38) GO TO 142
179         LS=FLS(2)
180         GO TO 145
181       142 LS=FLS(3)
182   C*** STORE LS CORRECTED DATA IN FLOATING POINT ARRAY
183       145 IF(ILOC.EQ.2) GO TO 155
184         RDAT=FLOAT(IDATA(I,J))-LS
185         CALL FPUT2(1,I,J,RDAT)
186         GO TO 156
187       155 RDAT=(FGET2(1,I,J))-LS
188       156 TOTAL=TOTAL+IDATA(I,J)
189         TOTDAT=TOTDAT+RDAT
190         IF(M1.GT.MR3.OR.M2.GT.MR4) GO TO 180
191               IF(ISW.EQ.1) GO TO 160
192         IF(M1.LT.MR1.AND.M2.LT.MR2) GO TO 180
193          GO TO 170
194       160 E=M1**2/MR1**2+M2**2/MR2**2
195         IF(E.LE.1.) GO TO 180
196       170 IF(RDAT.LT.0.0) ICELL=ICELL+1
197         ISUMCL=ISUMCL+1
198         SUM=SUM+PI*RDAT*M2
199       180 CONTINUE
200       190 CONTINUE
201         SUMLA=0.0
202         IF(ISW.EQ.0) GO TO 200
203   C***  APPROXIMATE THE LOW ANGLE INTENSITY AS AN AVERAGE OF
204   C***  THREE CELLS ON EACH SIDE OF THE X AXIS AND THREE ON
205   C***  EACH SIDE OF THE Y AXIS TIMES THE VOLUME OF AN OBLATE
206   C***  ELLIPSOID (CONSTANT VALUE APPROXIMATION)
207         I2=AINT(CX)
208         IC11=AINT(CY-MR1*CPCM+.5)
209         IC12=AINT(CY+MR1*CPCM+.5)
210         DAT11 = FGET2(1,I2,IC11)
211         DAT12 = FGET2(1,I2+1,IC11)
212         DAT13 = FGET2(1,I2-1,IC11)
213         DAT14 = FGET2(1,I2,IC12)
214         DAT15 = FGET2(1,I2+1,IC12)
215         DAT16 = FGET2(1,I2-1,IC12)
216         DAT1 = (DAT11+DAT12+DAT13+DAT14+DAT15+DAT16)/6.
217         I1=AINT(CY)
```

```
      IC21=AINT(CX-MR2*CPCM+.5)
      IC22=AINT(CX+MR2*CPCM+.5)
      DAT21 = FGET2(1,IC21,I1)
      DAT22 = FGET2(1,IC21,I1+1)
      DAT23 = FGET2(1,IC21,I1-1)
      DAT24 = FGET2(1,IC22,I1)
      DAT25 = FGET2(1,IC22,I1+1)
      DAT26 = FGET2(1,IC22,I1-1)
      DAT2 = (DAT21+DAT22+DAT23+DAT24+DAT25+DAT26)/6.
      SUMLA=4.*PI/3.*MR2**2*MR1*(DAT1+DAT2)/2.
  200 WRITE(6,210) ICELL
  210 FORMAT(//,1H ,'THE NUMBER OF NEGATIVE CELLS = ',I5)
  260 WRITE(6,270) TOTAL
  270 FORMAT(//1H ,'THE TOTAL INTEGRATED COUNTS = ',E15.6/)
      WRITE(6,275) SUMLA,SUM,ISUMCL
  275 FORMAT(/1H ,'THE LOW ANGLE INTENSITY = ',E15.6,
     +/1H ,'THE INTEGRATED INTENSITY = ',E15.6,


     +/1H ,'THE NUMBER OF CELLS IN INTEGRATED INTENSITY =',I4)
      WRITE(6,276) TOTDAT
  276 FORMAT(1H ,' THE TOTAL(COUNTS-LS)=',E15.6,//)
C***  CALCULATE Q AND MSEDF FROM THE SUM*M2 OF THE DATA ARRAY     ***
C*** CORRUN, DIFFER, AND OTHERS HANDLING FLOATING POINT DATA
C*** DIVIDE BY THE TRANSMISSION FACTOR. OLD BKC PROGRAM DOES NOT..
      TMM=TM
      IF(NCDS.NE.1) GO TO 279
      WRITE(6,277)
  277 FORMAT(1H ,'ACCORDING TO THE HEADER RECORDS, YOUR DATA HAS',
     11H ,'PREVIOUSLY BEEN DIVIDED BY THE TRANSMISSION FACTOR...',
     1/1H ,' DO YOU AGREE? TYPE Y OR N... Y WILL RESULT IN DATA',
     11H ,'NOT BEING DIVIDED BY TM IN THIS PROGRAM.')
      READ(5,230) ANS
      IF(ANS(1).EQ.1HY) TMM=1.0
  279 Q=(SUM+SUMLA)/((IO*CT)*TMM)
      K=1./(THOMSN*AVOGAD**2*STH*DIST2*LAMBDA**3)
      MSEDF=K*Q
      WRITE(6,280) Q,MSEDF
  280 FORMAT(1H ,'THE TOTAL ABSOLUTE INTEGRATED INTENSITY Q=',12X,E12.4,
     X' CM',/' THE MEAN SQUARED ELECTRON DENSITY FLUCTUATION = '
     X,E12.4,' MOLES OF E**2/CM**6')
      WRITE(6,290)
  290 FORMAT(//1H ,'DO YOU WANT TO RE-ANALYZE THIS DATA FILE?')
      READ(5,230)ANS
      IF(ANS(1).EQ.'Y') GO TO 55
  295 WRITE(6,300)
  300 FORMAT(//1H ,'DO YOU WANT TO ANALYZE A NEW DATA FILE?')
      READ(5,230) ANS
      IF(ANS(1) .EQ. 'Y') GO TO 20
      STOP
      END
TOTAL RECORDS WRITTEN =   267/     44
EXIT
$AVR CI 4
$END  LIST
$
```

VITA

The author, Hassan Bodaghi, was born in Dezege, Iran on June 2, 1952. He was brought up in an impoverished life-style. In order for him to continue elementary school, it was necessary for him to leave home at an early age. He attended Kharazmi high school in Tehran, and graduated in 1970. Then he entered Tehran Institute of Technology and graduated with a A.S. degree in 1972.

After two years serving in the military, in 1977 he came to the United States and studied English at E.L.S. Berkley, California. Continuing his studies, he graduated from the Philadelphia College of Textile and Science, Pennsylvania with a degree in Textile Engineering in 1979.

He accepted a research assistantship at the University of Tennessee's Polymer Engineering Department and recieved the Master of Science degree in Polymer Engineering on March 1982. Continuing in the polymer program, he received the Doctor of Philosophy degree in Polymer Engineering in December 1984.

On September 13, 1978 Hassan married Trisha Flynn. Their first son Kavous Kirk was born on November 30,1980 and their second son Pejmon Dustin was born on November 17, 1983.

The author is working as a senior development engineer for 3M Company in St. Paul, Minnesota.